The University of Cardiff

Axial Piston Pump

Leakage Modelling and Measurement

A thesis submitted for the degree of

Doctor of Philosophy

By

Jonathan Mark Haynes

November 2007

ProQuest LLC
789 East Eisenhower Parkway
P.O. Box 1346
Ann Arbor, MI 48106-1346

Abstract

This thesis is concerned with the dominant leakage characteristics of an axial piston pump. Results have been obtained from a combination of analysis, Computational Fluid Dynamics (CFD) and experimental work, and have added to existing knowledge in this field. The measurement of slipper leakage within an axial piston pump is impossible due to additional leakage from the pistons and between the cylinder barrel and port plate. It may only be determined by analysis and this aspect has been studied via a new CFD simulation.

Further progress has been made experimentally on slipper leakage. A new test apparatus was designed and developed by the author and comparisons have been made with parallel analytical work. Previous research in this area has concentrated on single-landed slippers and leakage rates from such slippers have been examined, however only under static conditions. The work in this thesis is the first to consolidate experimental studies on multiple-land slippers, and the first to measure slipper leakage under dynamic conditions. These results have been compared with both CFD simulations and a new theoretical study undertaken in parallel with this work. The new test apparatus allowed measurement of both leakage and groove pressure under a range of operating conditions. It was established that the presence of a groove reduces the restoring moment produced, and hence enables the slipper to operate with an appropriate angle of tilt, thus permitting hydrodynamic lift to more readily exist. However, this occurs at a cost of increased leakage.

In addition to the experimental work on slippers, the time-varying pressures within selected cylinders of an axial piston pump were measured. In parallel, a fully dynamic CFD model of a pump was produced. This model included all leakage paths from the pump. It was discovered that the port plate leakage dominated the overall leakage, with slipper leakage still being significant, but with piston leakage insignificant. This model was also used to predict the flow and pressure ripple from the pump and the predictions were compared with experimental measurements.

Acknowledgements

I would like to take this opportunity to thank the many people that I have worked with whilst studying as a post-graduate at Cardiff University.

Firstly, I would like to thank my supervisor, Professor John Watton for his guidance throughout the course of this research, and during the writing of this thesis. His academic experience, as well as his technical knowledge, has been invaluable to me. I would also like to thank Dr. Joseph Bergada (Polytechnic University of Catalonia, Spain), especially for his ideas and support during the experimental aspect of this work. The success of the experimental test apparatus would not have been possible without the experience and expertise of the following people: David Glinn, David Hobbs, Stephen Mead, and Malcolm Seaborne. I would especially like to thank Alan Griffiths and Robert Jones for making the practical side of this work so successful. I would also like to thank Dr. Mike Evans for the technical support he provided on the UNIX system that I used for CFD modelling.

Thanks are also due to my friends, who have made my time out of work so enjoyable. I would especially like to acknowledge the friendship of David Mapps, Adam Paul and Peter Theobald.

My greatest thanks, however, are reserved for my family. I would like to thank Georgina for her support and encouragement, especially during the writing of this thesis. My Mum and Dad have been a huge support to me, not only during this work, but throughout my studies at Cardiff University. I would like to take this opportunity to thank them for their continued support, advice and encouragement. It's truly appreciated.

To Mum and Dad

Contents

List of Figures

Chapter 1

Chapter 2

Chapter 3

Chapter 4

Chapter 5

List of Tables

Chapter 1

Chapter 3

Chapter 4

Chapter 5

Abbreviations

µm	micron
2-D	Two Dimensional
3-D	Three Dimensional
BSP	British Standard Pipe
CFD	Computational Fluid Dynamics
dB	Decibel
DC	Direct Current
ID	Inside Diameter
m	metre
min	minute
ml	millilitre
mm	millimetre
N	Newton
P.C.D	Pitch Circle Diameter
Pa	Pascal
PC	Personal Computer
Ra	Average surface roughness
rad	radian
rpm	Revolutions Per Minute
s	second
UDF	User Defined Function

Nomenclature

Symbol	Parameter	Unit
A	Displacement transducer A	-
A	Minimum load factor	-
B	Displacement transducer B	-
C	Displacement transducer C	-
C_A	Calibration for displacement transducer A	μm/Volt
C_B	Calibration for displacement transducer B	μm/Volt
C_C	Calibration for displacement transducer C	μm/Volt
C_a	Basic dynamic axial load rating	N
C_r	Basic dynamic radial load rating	N
D_P	Angular displacement of pump	$m^3.rad^{-1}$
E_v	Volumetric efficiency	%
F	Tension	N
F_a	Applied axial load	N
F_{am}	Required minimum applied axial load	N
F_r	Applied radial force	N
g	Gravitational constant	$m.s^{-2}$
L_{10}	Life in Millions of revolutions expected by 90% of a group of bearings	-
m	Length of porous region	m
n	Rotational speed	rpm
P	Pressure	$N.m^{-2}$
P_{ea}	Dynamic equivalent axial load	N
P_{in}	Inlet pressure	$N.m^{-2}$

P_L	Exponent of the bearing life equation	-
P_r	Dynamic equivalent radial load	N
Q_e	External leakage	$l.min^{-1}$
Q_{e1}	External leakage from high pressure side of pump	$l.min^{-1}$
Q_{e2}	External leakage from low pressure side of pump	$l.min^{-1}$
Q_i	Internal leakage	$l.min^{-1}$
Q_{in}	Inlet flow	$l.min^{-1}$
Q_{out}	Outlet flow	$l.min^{-1}$
R_e	Resistance to external leakage	$bar/l.min^{-1}$
R_i	Resistance to internal leakage	$bar/l.min^{-1}$
R_P	Radius of pulley	m
T	Torque	Nm
v	Velocity	$m.s^{-1}$
V	Volt	V
V_A	Output voltage from displacement transducer A	Volt
V_{AO}	Initial output voltage from displacement transducer A	Volt
V_B	Output voltage from displacement transducer B	Volt
V_{BO}	Initial output voltage from displacement transducer B	Volt
V_C	Output voltage from displacement transducer C	Volt
V_{CO}	Initial output voltage from displacement transducer C	Volt
X	Radial load factor	-
x_1	Radius of slipper face	mm
x_2	Radius of slipper array	mm
x_3	Distance between displacement transducers B and C	mm
Y	Bearing constant	-

y_1	Distance from centre of slipper to displacement transducer A	mm
y_2	Distance from centre of slipper to displacement transducers B and C	mm
z	Difference in height	m
Z_C	Central clearance	μm
Z_I	Inside edge clearance	μm
Z_L	Leading edge clearance	μm
Z_O	Outside edge clearance	μm
Z_T	Trailing edge clearance	μm
α	Angle of tilt of slipper about the x-axis	degree
β	Angle of tilt of slipper about the y-axis	degree
θ	angle	degree
ρ	Density	$kg.m^{-3}$
σ	Permeability of porous zone	m^2
μ	Viscosity	Pa.s

Glossary

Clamping ratio	Ratio of the load clamping the slipper to the swash plate to the maximum hydrostatic load carrying capacity of the slipper
Groove	Annulus cut in to the face of the slipper to produce multiple lands
Hydrodynamic lubrication	The geometry and relative motion of two surfaces creates a build up of pressure which is able to support an externally applied load
Hydrostatic lubrication	Pressurised lubricant is supplied between the surfaces by an external source, thus providing their separation and ability to support a load without surface contact
Land	Area of slipper face that would potentially contact with the surface of the swash plate
Leading edge	Front edge of slipper relative to direction of motion
Over clamped	The clamping force is greater than the hydrostatic load carrying capacity
Pool	Recessed area in the slipper face into which oil directly flows from the piston
Trailing edge	Rear edge of slipper relative to direction of motion
Under clamped	The clamping force is less than the hydrostatic load carrying capacity

Overview of Chapters

This thesis is divided into six main chapters. Below is an outline of the contents of each chapter:

Chapter 1

Chapter 1 introduces the axial piston pump, and contains a brief description of how it works, and describes the causes of leakage from within the pump.

Chapter 2

The axial piston pump has been the source of a significant amount of research. Chapter 2 contains a comprehensive literature review detailing both the theoretical and experimental studies that have been undertaken.

Chapter 3

An axial piston pump was simulated using the CFD software FLUENT. The models presented in Chapter 3 aimed to characterise the main sources of leakage from within the pump, and were validated by an experimental study. Pressure transients were measured experimentally and compared with the CFD derived pressure ripple.

Chapter 4

A test apparatus containing a 2:1 scale model of a slipper was developed in Chapter 4. This enabled the measurement of leakage, which is inherently difficult within an actual pump. The effect of tilt and clearance were observed as well as the pressure within the slipper groove.

Chapter 5

To further the work presented in Chapter 4, a CFD study was undertaken and is presented in Chapter 5. The geometries used within the CFD models replicated those used in Chapter 4, and thus a direct comparison between results was possible. In addition to the comparisons made between Chapter 4, different groove geometries and locations were explored.

Chapter 6

Presented in Chapter 6 are the main conclusions drawn from the work presented in this thesis. In addition, recommendations of how to develop this work in the future are presented.

Chapter 1. Introduction

1.1 Introduction

Hydraulic pumps can be divided into two general classes: Hydrodynamic and Hydrostatic. Hydrodynamic pumps use a rotating element, within a casing, to impart a radial velocity on the fluid. The fluid then exits the pump via a discharge nozzle. Hydrostatic pumps, also known as positive displacement pumps, displace a fixed volume of fluid per cycle. Hydrostatic pumps can be split into two categories: rotary and reciprocating. Rotary pumps work on the principle that a rotating vane, screw or gear collects fluid in its void on the suction side of the pump, and forces it to the discharge side. Reciprocating pumps, such as axial piston pumps, work on the principle that fluid is drawn into a void on the suction side of the pump, and then expelled on the outlet stroke, through the discharge port of the pump. An axial piston pump consists of the following major elements:

- Pistons and slippers
- Cylinder barrel
- Swash plate
- Port plate
- Pump casing

A sectioned view of an axial piston pump is shown in Figure 1.1. The nine pumping pistons are evenly spaced in a circular array around the cylinder barrel. The cylinder barrel is driven about its axis of symmetry via a shaft coupled to an electric motor or other drive such as a diesel engine on a mobile machine. Located behind the cylinder barrel is a swash plate. The swash plate is positioned at an angle to the axis of

rotation. Each slipper is constrained to follow the surface of the swash plate and hence the pistons exhibit a reciprocating motion as the cylinder barrel rotates. Located at the front of the pump is a stationary port plate, which the cylinder barrel bears against. The cylinder barrel is held against the port plate via a compression spring (not shown in Figure 1.1) located between the swash plate and the rear of the barrel.

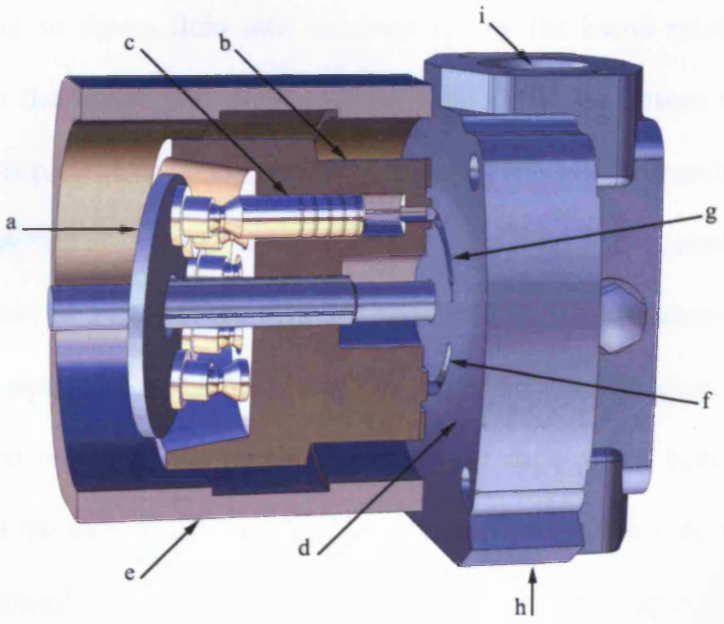

a) Schematic

(a) swash plate, (b) cylinder barrel, (c) piston assembly, (d) port plate, (e) pump casing, (f) suction port, (g) discharge port, (h) inlet line (not visible), (i) outlet line.

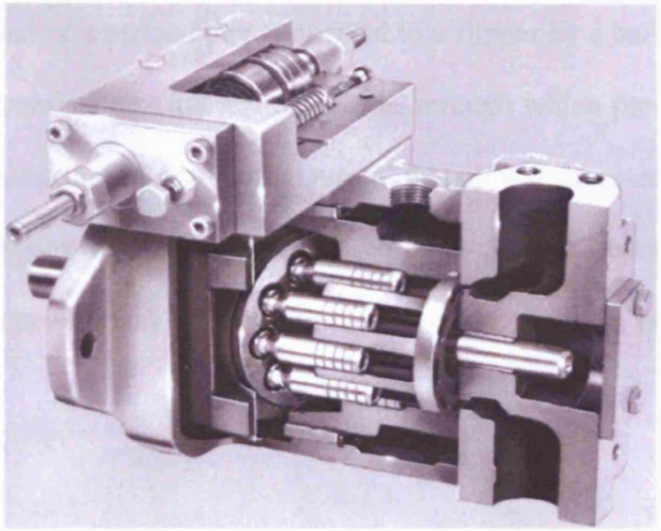

b) The Oilgear Towler pump used in this work (Oilgear Towler UK Ltd)

Figure 1.1 Main components within an axial piston pump

The port plate contains two kidney shaped ports which are each connected to the suction and discharge lines. The small gap between the rotating barrel and fixed port plate introduces a cross-port leakage and a leakage across the barrel edges to the internal casing, and ultimately back to tank. On the inlet stroke, the piston moves axially away from the port plate. During this time, the piston is located within the inlet port region, and so draws fluid into its chamber. As the barrel rotates, the piston moves through the outlet port region. During this time, the piston moves axially towards the port plate, and hence expels fluid out of the piston chamber. The pump contains nine pistons located at 40° intervals, and so fluid is constantly drawn into, and expelled from the pump as the cylinder barrel rotates. The instantaneous flow rate of the pump is equal to the summation of the instantaneous flow rates of the pistons within the outlet region of the pump. The shape of each piston bore changes to a kidney shape at the face of the barrel. This aids the flow between the port plate and each piston. Typically, four pistons will be contributing to the output flow rate at any one instant.

Each piston consists of a piston body connected to a slipper by a ball and socket joint. The slipper face consists of a lubrication orifice, through which pressurised fluid can flow, ultimately returning back to tank. During operation, a recessed pool in the face of the slipper contains a volume of pressurised fluid close to piston pressure on the supply side, and close to tank pressure on the inlet side. A piston assembly is shown in Figure 1.2.

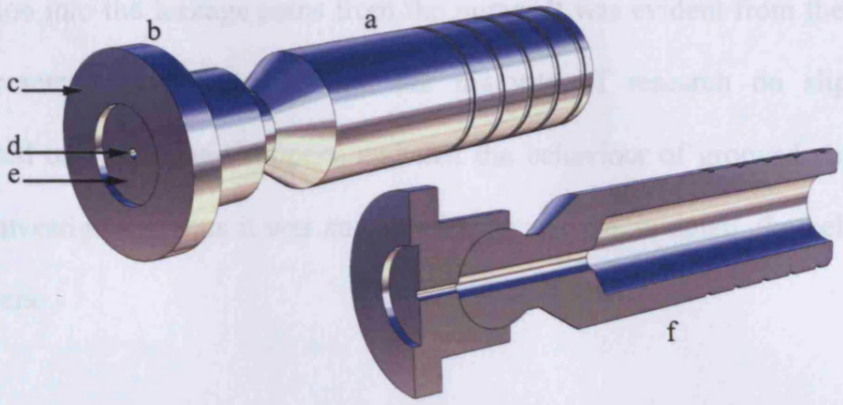

(a) piston, (b) slipper, (c) land, (d) lubrication orifice, (e) pool, (f) sectioned view

Figure 1.2 Piston assembly

Also shown in Figure 1.2 is a sectioned view, illustrating the hollow nature of the piston assembly. Table 1.1 shows the dimensions of the pistons used within the test pump.

Table 1.1 Test piston dimensions

Measurement	**Dimension**
Overall length	62.0mm
Length of piston body	42.0mm
Piston body diameter	14.7mm
Lubrication orifice diameter	1.0mm
Pool diameter	10.15mm
Slipper land outside diameter	20.5mm

Many axial piston pumps have a pressure compensator circuit, allowing the swash plate angle to be reduced as the load pressure increases above a prescribed limit, set by a load spring and associated spool. This makes the hydraulic system more efficient as only the required flow is produced by the pump at an otherwise excessive pressure. A pressure relief valve is still required at the pump outlet. For this study the pump had such a pressure compensator but a pressure range was selected to avoid its use. The main objective of the work presented in this thesis was to provide a detailed

investigation into the leakage paths from the pump. It was evident from the literature review presented in Chapter 2, that the majority of research on slippers had concentrated on single land slippers, and that the behaviour of grooved slippers had not been investigated. Thus it was an objective to analyse, in detail, the behaviour of such slippers.

Chapter 2. Background

2.1 Background

A considerable amount of research has been undertaken regarding the operation of axial piston pumps. Mathematical models have been developed to study many aspects of the axial piston pump including control systems and predicting pump dynamics [1-4]. Additionally, a variety of software has been used to model axial piston pumps. This ranges from purposely written simulation programs, to generic software packages, and commercially available Computational Fluid Dynamics (CFD) software.

Ivantysynova et al [5-10] developed a simulation tool specifically for axial piston pump analysis called "CASPAR". Based on the simulation of flow through self adjusting lubrication gaps within the axial piston pump, the losses due to friction and leakage could be determined. The gaps in axial piston pumps are self adjusting as the gap geometry is dependent on operating conditions, and not only the dimensions of mating parts. The simulation was applied to clearances between the pistons and their cylinder bores, between the cylinder barrel and port plate, and between the piston slippers and swash plate. Additionally, "CASPAR" was used for port plate timing optimisation [5]. In conjunction with "CASPAR", an experimental test apparatus was set up to measure instantaneous pressure within an individual piston chamber [6]. This worked by using a piezoelectric pressure transducer located within a cylinder bore. A telemetry system was used to transmit the data from the pump to a workstation. The simulation in "CASPAR" for transient pressure in the piston bore was validated by the pressures measured experimentally. The "CASPAR" software has also been used to predict the frictional forces between a piston and its corresponding cylinder [7, 8]. This was again validated experimentally, by means of a piezoelectric force sensor.

Here a force sensor was located on the peripheral of the cylinder barrel and connected to a floating bush encasing a single piston.

Armbruster et al used the "AMESim" software to simulate the dynamics of an axial piston pump [11]. "AMESim" is a modelling environment for performing simulation of engineering systems. It is a visual based application, where symbols represent components. In this case, each piston was modelled as a generic cylinder, with specific inputs for its operation. These related to the pistons movement and port timings. Whilst this model did not yield any significant results, it demonstrated the potential for the dynamics of an axial piston pump to be modelled using a generic software package. Gilardino et al [12] used the "AMESim" software to model a displacement control mechanism within an axial piston pump. Gilardino investigated the dynamic behaviour of the pump under transient conditions, enabling the delivery pressure and swash plate angle to be predicted. This enabled the response time of the pump to be characterised for changes in load.

A simulation program, "Bathfp" was used by Edge et al to simulate the dynamic behaviour of axial piston pumps [13, 14]. The simulations carried out enabled the forces acting on pistons in pumps with different port plate timings to be investigated. This has enabled the influence of port timing on fluid borne noise to be established. The simulations undertaken by Edge et al concentrated on the transition of a piston between the suction and delivery ports. As a piston travels through the port plate region between the suction and delivery ports, the delivery of oil is interrupted by the valve plate. For the geometry of the pump examined, this meant that the pressure in the cylinder rose transiently higher than the pressure in the delivery port. This

occurrence is known as a trapping and was previously investigated by Yamaguchi [15].

As a piston moves between the delivery and suction ports, the cylinder volume increases, and thus the trapped volume of fluid decompresses. This can lead to the onset of cavitation as confirmed by Wiklund's examination of suction dynamics [16, 17]. Cavitation is the collapse of bubbles within the fluid, and leads to the formation of pits and craters on the surface of the material. Evidence of wear due to cavitation on the port plate and piston slipper was presented by Fey et al [18]. Edge et al determined that a later suction port opening reduced the forces generated by the pistons, and hence reduced the noise potential. However it increased the possibility, and severity of cavitation [13]. Although reducing cavitation problems, Edge et al demonstrated that an increased inlet pressure increased air-borne noise [19, 20]. Consequently he suggested that the inlet pressure should be kept as low as possible whilst endeavouring to avoid cavitation.

The flow developed by an axial piston pump is determined by the contribution of the flows produced by each piston, and is hence fluctuating in nature. Within a pump containing nine pistons, there are always at least four pistons in the discharge region and contributing to the output flow. Manring et al [21] characterised the output flow ripple of axial piston pumps with different numbers of pistons. The theoretical kinematic fluctuation in flow as a percentage of mean flow for pumps containing different numbers of pistons is shown in Figure 2.1.

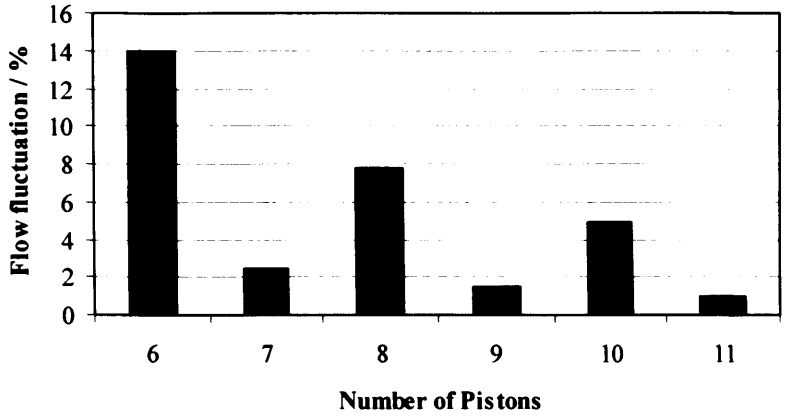

Figure 2.1 Kinematic flow fluctuation as a percentage of the mean flow

The general trend of Figure 2.1 suggests that increasing the number of pistons reduces the flow ripple amplitude. There is however, a significant difference in ripple amplitude between pumps with an even and odd number of pistons. The majority of commercially available pumps contain nine pumping pistons. This is largely because nine pistons provide a small flow fluctuation, with additional pistons providing no significant reduction in fluctuation, but requiring a larger diameter of barrel to accommodate them. When analysing the actual flow ripple, however, Manring found there was no significant difference in the flow ripple characteristics of pumps with even and odd numbers of pistons. This was in agreement with Jun and Yi [22] who concluded that, from a flow ripple point of view, a pump containing an even number of pistons may be as feasible as an odd numbered design. Masuda and Ohuchi [23] also investigated axial piston pumps with an even number of pistons, and developed a method of noise reduction for an eight piston pump. Their method involved porting the suction and delivery ports to control cylinders acting on the swash plate. This self compensation method reduced the airborne pump noise from 71dB to 64.5dB.

Further to the work carried out by Edge et al [13] and Wiklund [16, 17], Manring investigated the transition of a piston chamber between the discharge and suction ports. This research extended beyond simply the timing of the ports, as he proposed different geometries for the timing grooves. Timing grooves allow the pressure within a cylinder to be matched to the pressure of the advancing port by permitting restricted flow between the cylinder and the port. This helps restrict cavitation and over pressurisation from occurring. Helgestad et al gave a method for calculating pressure transients within an axial piston pump [24]. He concluded that if a pump operated at a constant pressure and flow, a port plate without silencing grooves could be used. He also found that a pump operating under variable operating conditions should utilise triangular silencing grooves. If the pump was expected to operate in both directions, a parallel slot design was desirable. Martin et al discussed the design of a port plate, also concluding that for a pump operating with a narrow range of conditions it was possible to design a port plate geometry that would work without timing grooves. However if a wide range of operating conditions was expected, silencing grooves would be required to assist in the matching of cylinder and port pressures. They also discussed design considerations which would assist in determining the optimum timing for a range of operating conditions [25]. Edge et al investigated the influence of groove dimensions on cylinder pressure and flow, concluding that the optimum design would consider both flow losses and pressure transient. In terms of reducing the pressure upon entry to the outlet port, a steeply sloping triangular geometry was found to be the optimum timing groove profile.

Manring found that a linearly varying timing groove was advantageous if the timing groove was short due to geometrical constraints. He also found that a slot with

constant area was shown to be most appropriate if the discharge area of the slot was limited [26]. Manring also investigated the possibility of removing timing grooves altogether [27]. The volumetric efficiency was calculated for a port plate with and without timing grooves, and Manring suggested that a trapped volume design may in fact offer improvements in operating efficiency.

Karkoub et al [28] produced a neural network to predict the steady state behaviour of an axial piston pump. For the training of the network, he used data obtained experimentally. The training data consisted of results obtained by measuring the pump discharge flow at different supply pressures, over a range of pump speeds. He then developed a neural network to predict the transient response of a pump with a pressure compensator circuit. Again this neural network used experimental data for training and validation. The actual dynamics of the pump were determined by measuring the transient pressures in the control cavities of the pressure compensator circuit. A solenoid activated control orifice was used to rapidly change the pump outlet pressure. The subsequent pressure response was measured using piezoelectric pressure transducers located within the control cavities. The resulting neural network consisted of two hidden layers, each consisting of five neurons. The steady state neural network was able to predict the characteristics of the pump with an error of less than 2%. The predicted values for the dynamic response of the pump also correlated well with the experimental data. The error between the predicted and experimental validation data was found to be less than 7%.

Manring et al investigated the control and containment forces required for both axially [29] and transversely [30] actuated swash plates. The primary difference between these is the direction, relative to the pump shaft, in which the containment force is

applied to the swash plate. Manring suggested that, for a transversely actuated swash plate, the angular length of the containment bearings should be as large as possible. Additionally, he suggested that from a performance point of view, axially actuated swash plates were superior, as they provide a more robust containment of the swash plate. Manring developed his work further by examining the impact of using a secondary swash plate angle [31, 32]. Predominantly used in the aerospace industry, a secondary angle allows the swash plate to be tilted about an additional axis, perpendicular to the conventional axis of tilt. By calculating the containment forces required to maintain the position of the swash plate, he determined that a secondary angle of tilt could reduce the required containment forces of the swash plate. Additionally, it was found that a secondary angle could increase the volumetric efficiency of the pump by approximately 3%. Manring also found however, that a secondary angle introduced a twisting moment on the swash plate about the pump axis. The presence of this additional load implied that additional containment of the swash plate was required.

CFD simulations were performed by Wiklund and Svedburg [16] using the "FLUENT" CFD package. They produced a two dimensional model to investigate the opening and closing phase of a piston within the suction region of a pump. The pump inlet manifold was modelled, with an adjacent region of cells representing the rotating cylinder block. The movement of the cylinder block was achieved by changing the porosity of groups of cells at each time step in the simulation. A "Pressure Inlet" boundary condition was applied to the region of the mesh representing the inlet of the pump. The areas of the mesh representing the pistons within the suction port were

allocated velocity boundary conditions. The velocity assigned to these boundaries was time dependent, and applied using a User Defined Function (UDF).

A two dimensional model generated results that assumed a square shaped cross sectional geometry. However, the opening of the piston into the inlet port is more accurately represented by the interaction of two curved surfaces. This fact was accounted for in the CFD simulation by determining the change in orifice geometry at any particular time, and then changing the porosity of cells within the model to replicate the flow area for each time step. Wiklund and Svedburg later developed a three dimensional pump model using the CFX CFD software [17]. This model was far more advanced than their previous model and used a dynamic change in mesh geometry to simulate the movement of pistons between each time step. Additionally, the pistons rotated about a central axis and therefore the change in geometry as the piston interacted with the inlet ports was simulated more effectively than the method used in the two dimensional model. Fairhurst later used the "FLUENT" package to develop a three dimensional pump model of an axial piston pump [33]. This was more advanced than the previous work reviewed, as an attempt was made to model the leakage from the cylinder barrel – port plate interface.

In order to simulate the motion of the pistons in his 3-D model, velocity inlets were used rather than deforming meshes. The pistons were therefore modelled as fixed volumes, with a reciprocating velocity applied to the end face of each via a UDF. To simulate the rotating cylinder barrel, the volumes of cells representing the pistons were given an angular velocity about a central axis. A sliding mesh was employed to facilitate the interface between the moving and stationary mesh volumes.

Using velocity boundary conditions to control the flow of fluid into and out of the piston chambers simplified the model to a degree, as it meant that no dynamic change in volume occurred. It also had the limitation that the leakage of fluid through the piston assembly could not be considered.

By introducing a narrow volume of cells, Fairhurst's model included the leakage across the cylinder barrel face. Here the separation was modelled using a region of cells with a depth of 2mm. These cells had a calibrated porosity to restrict the flow of fluid, thus simulating a smaller, more realistic clearance. This porous region was in fact two separate volumes. The first provided an external leakage from the piston side of the pump, with the other providing a leakage from the port plate side of the pump. The application of "Wall" boundary conditions to these two volumes meant that no fluid could flow between them directly. Fairhurst also attempted to create a 2-D axis-symmetric model of a single piston. The mesh was produced, but was non-convergent and hence results were therefore not obtained.

2.2 Lubrication within the Axial Piston Pump

2.2.1 The concept of lubrication

To maintain mechanical efficiency and maintain wear, mating surfaces within an axial piston pump have to be lubricated. The main areas requiring lubrication are:

- Cylinder barrel and port plate
- Pistons and respective bores.
- Piston slippers and swash plate

In order to provide complete separation between moving parts, axial piston pumps are designed to operate utilising a combination of hydrostatic and hydrodynamic lubrication. Boundary lubrication, however, is likely to occur under certain conditions [34]. Due to the nature of lubrication between mating surfaces, volumetric losses are inherent in axial piston pumps. These volumetric losses have been studied extensively, with the intent of optimising the overall volumetric efficiency of the pump whilst maintaining successful lubrication.

Hydrostatic lubrication relies on an external supply of pressurised fluid which is supplied between the bearing surfaces. In axial piston slippers, the fluid is bled from the high pressure side of the piston, through an orifice in the piston slipper interface as shown in Figure 1.2. This creates a pool of high pressure fluid beneath the slipper and hence produces a separation force between the slipper and swash plate. Slippers are generally designed so that they are slightly over clamped. Without motion, they are clamped to the swash plate when the piston bore is pressurised. During pump rotation, hydrodynamic lubrication develops between the slipper and swash plate, providing

sufficient additional force to generate separation. If pressure balance does not occur, it is possible that the slipper may tilt by a very small amount to provide the additional force due to a hydrodynamic contribution.

Hydrodynamic bearings are known as self acting. To create and maintain the hydrodynamic film, a relative motion is required between the two bearing surfaces. The surfaces must also be inclined to form a clearance in the shape of a wedge. This wedge converges in the direction of relative motion, and hence allows a pressure build up between the two surfaces, thus providing a separating force. Of course, hydrodynamic lubrication only occurs with a relative motion between the two surfaces, and so if the relative velocity is not sufficient, wear may occur due to contact between them.

Although designed to operate utilising hydrostatic and hydrodynamic lubrication, occasionally the oil film is too thin to provide complete separation between mating surfaces. This is known as boundary lubrication, and occurs, for example, at low speeds where hydrodynamic lubrication does not develop [35]. In addition, it may occur at low operating pressures, and during transient operating conditions such as when the pump starts or runs down [36]. To a degree, boundary lubrication is also likely to occur during the early use of the pump [37].

2.2.2 Lubrication between the cylinder barrel and port plate

Shown in Figure 2.2 are the areas in which axial forces act on the cylinder barrel. Highlighted in yellow are areas where pressurised fluid tends to clamp the cylinder barrel to the port plate. These areas occur where the cylinder bore changes in profile from circular to slot shaped. An additional clamping force due to the retaining spring

acts at the centre of the cylinder barrel. The face upon which this spring bears is shown in blue. Also shown in Figure 2.2 are the kidney shaped ports within the port plate.

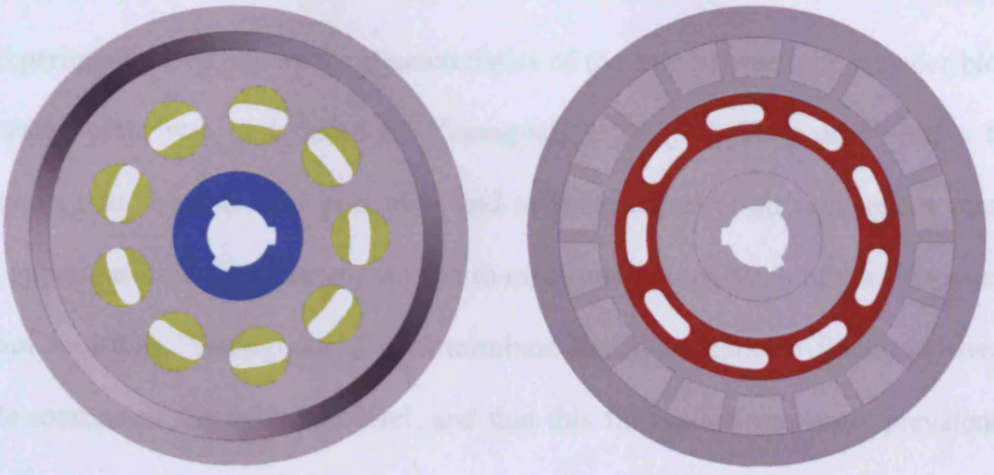

a) Swash plate side of the cylinder barrel b) Port plate side of the cylinder barrel

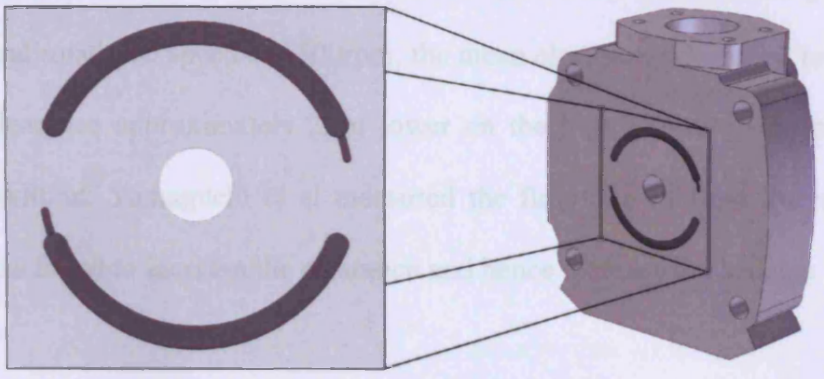

c) Suction and discharge ports on port plate

Figure 2.2 Axial forces acting on cylinder barrel

Shown in red is the contact land of the cylinder barrel, which bears on the port plate. During rotation a film of fluid develops between the two, tending to separate the cylinder barrel and the port plate. Although there is a fluid film around the entire land, the region of the barrel adjacent to the discharge port of the pump is subject to the highest pressure and thus greatest separation force. The area of the land radially inside and outside of the discharge port is also pressurised. This pressure reduces to

atmospheric at the radial extremities of the land [38]. Areas of the land between adjacent slots are exposed to the full working pressure of the pump when in the outlet port. Similarly, the clamping forces are greatest for the bores within the outlet port.

An experimental analysis on the characteristics of the film between the cylinder block and valve plate was undertaken by Yamaguchi et al [39]. They developed a test apparatus that simulated the port plate and cylinder barrel of an axial piston pump. This apparatus used eddy current sensors to measure the separation of the components in four locations. Yamaguchi et al determined that the clearance fluctuates over a single rotation of the cylinder barrel, and that this fluctuation was more prevalent at high pressures and at high speeds. In addition, they found that the cylinder barrel developed a small angle of tilt relative to the port plate. For a fluid pressure of 14.7MPa and rotational speed of 1500rpm, the mean clearance was found to be 15μm, with the clearance approximately 2μm lower on the high pressure side of the port plate. In addition, Yamaguchi et al measured the flow rate of fluid. Increasing the pressure was found to increase the clearance and hence increase the leakage flow rate.

Kim and Jung measured the cylinder barrel clearance by installing a single displacement sensor in the cylinder barrel of an axial piston pump [40]. The connecting cable was fed through the pump shaft and connected to a data acquisition system via a slip ring unit. Small fluctuations in clearance were found over the pumping cycle. These were similar to those found by Yamaguchi et al, and attributed to the pressure pulsations produced by the nine pistons. In contrast to Yamaguchi's findings, a significant difference in clearance was found between the suction and discharge ports. This difference could be due to differences between the two test

apparatus. Yamaguchi's apparatus was built to simulate the cylinder barrel, and the cylinder barrel was restrained radially by roller bearings. In contrast, the cylinder barrel used by Kim and Jung was in an actual pump, and was attached to the pump shaft via a splined section. Since splines have a relatively poor tolerance of clearance, they potentially provided less restriction in movement of the cylinder barrel. Furthermore the geometry and therefore effective pressurised areas for each apparatus are unknown. Therefore there could have been a significant difference between the forces acting on each cylinder barrel. It is therefore difficult to compare the two sets of results without further knowledge. At a pressure of 15MPa and speed of 1500rpm, Kim and Jung measured a minimum film thickness of 15μm. Under these conditions, the maximum film thickness, located at the inlet region of the pump, was found to be 35μm. The angle of tilt between the cylinder barrel and port plate was found to increase with an increase in discharge pressure. The clearance at the discharge region of the pump reduced with increasing pressure.

In addition to the tilting of a cylinder barrel, which has been shown to be characteristic of axial piston pumps under normal use, research has been carried out into the transient conditions that occur under certain operating conditions. Jacazio and Vatta [41] analysed the conditions leading to cylinder block lift in axial piston motors. Block lift results in the sudden movement of the cylinder barrel away from the port plate. This reduces the hydrodynamic pressure between the barrel and port plate, and is hence followed by reattachment of the cylinder barrel and port plate. Block lift is a transient condition and is most likely to occur when a motor is operating at, or past its design pressure. It can also occur at high rotational speeds, when the hydrodynamic

pressure arising between the rotating block and stationary port plate becomes critically high.

Parallel research at Cardiff is currently considering the leakage and pressure distribution between the barrel and port plate. This is currently determined from the Reynolds equation of lubrication in polar coordinates. When taking tilt and rotation into account, and assuming the flow moves in a radial direction, the Reynolds equation takes the form:

$$\frac{\partial}{\partial r}\left(rh^3\frac{\partial p}{\partial r}\right) = 6\mu\omega r\frac{\partial h}{\partial \theta} \tag{2.1}$$

Equation (2.1) can only be solved using some approximations for geometry due to the complex integrations needed. The two solutions for the inner and outer lands of the port plate are added together to give a solution for the leakage flow rate. Leakage due to the timing grooves should also be considered but this is insignificant when compared to the main grooves. The solutions are under development, but were not at the stage for comparison with the CFD results presented in this thesis.

2.2.3 Leakage around the peripheral of the pistons

For this particular case, equations may be developed and based on the one-dimensional Reynolds equation of lubrication, the Couette Poiseulle equation, and the continuity equation. Laminar flow is assumed, and each land and groove is modelled as a flat plate. Relative motion between the piston and cylinder barrel exists, and no eccentricity is considered. The one dimensional Reynolds equation of lubrication in Cartesian Coordinates can be written as shown in equation (2.2):

$$\frac{\partial}{\partial x}\left(\frac{h^3}{\mu}\frac{\partial p}{\partial x}\right)=0 \tag{2.2}$$

Earlier work at Cardiff has resulted in a complex solution to this equation, where piston position and barrel speed are considered [42, 43]. This leakage flow is negligible in comparison with slipper and port plate leakage.

Yamaguchi found that the leakage between a piston and its bore is more dependent on the velocity of the piston than the pressure differential along the bore [44]. He also found that using a tapered piston, with a smaller diameter at the high pressure side of the pump, tended to stabilise the pistons, restoring them centrally in the cylinders. Sadashivappa et al studied the effects of out-of-roundness and taper on piston performance [45]. Test pistons with out-of-round profiles were fabricated and, once measured, installed into a commercially available pump. The taper on these pistons was similar to the pistons considered by Yamaguchi, with a smaller diameter at the pressure end of the piston. Similarly, a set of pistons with a high level of roundness and consistent radial clearance was manufactured. Sadashivappa tested the frictional characteristics of each set of pistons and found that the out-of-round pistons produced a lower level of friction than the cylindrical pistons. The leakage flow rate was highest with the cylindrical pistons; however they operated with a higher clearance. Lasaar, used the "CASPAR" software to measure the flow of oil flow around a piston during pump operation [9, 10]. Like Yamaguchi, he found that the motion of the piston could cause fluid to flow back into the piston chamber. This effect was reduced with larger piston clearances or an increase in discharge pressure. Lasaar also investigated pistons with a cross section that reduced parabolically at both ends. The reduction in diameter was in the order of 10μm, and it was found that this profile could reduce both leakage

and frictional resistance. The radial movement of a piston in its bore was experimentally investigated by Tanaka et al. This was achieved by means of four eddy current position sensors installed in a cylinder bore [46]. This work demonstrated that the frequency of movement of a piston is dependent upon the operating conditions. Under conditions of high rotational speed and under high loads, the rotation of the piston was found to coincide with the relative movement of the swash plate. Under lower speed and reduced loads, the frequency of rotation of the piston was found to reduce to half of the rotational speed of the swash plate.

2.2.4 Lubrication of the pistons on the swash plate

The lubrication of slippers on the swash plate has been the subject of a significant amount of research, since their operation has a significant impact on wear, efficiency and overall reliability of the pump [47]. Fisher studied a hydrostatic single land slipper, with a rotating swash plate [48]. He determined the pressure distribution for both a flat and tilted slipper. From the pressure distribution he determined the load carrying capacity of the slipper. He showed that hydrodynamic effects increased the pressure at the trailing edge of the slipper, and hence tended to return the slipper to a flat position. Safar analysed the pressure distribution, load capacity and lubricant flow rate for a hydrostatic bearing when under tilted conditions [49, 50]. He demonstrated that for a parallel bearing, the pressure distribution is logarithmic in the radial direction, and symmetrical in the circumferential direction. For a slipper tilting forward, he found that negative pressures existed. As the tilt of the slipper increased, the magnitude of these negative pressures increased, and cavitation was possible. Iboshi and Yamaguchi, conducted both a theoretical and analytical analysis of slipper behaviour [51, 52]. They considered the transient nature of supply pressure to the slipper, and concluded that under certain conditions, the slipper could make contact

with the swash plate. This was especially likely to happen under high pressures and rotational speeds. Additionally they found experimentally, that under steady conditions, the slipper clearance fluctuated. Takahasi et al carried out a theoretical analysis based on laminar incompressible flow between parallel disks [53]. A varying gap between the bearing surfaces was modelled, as well as a varying, and constant flow rate of lubricant. This work was followed by an experimental analysis, where the slipper was moved perpendicular to the bearing faces via a cam drive mechanism.

Harris et al modelled a slipper pad's behaviour over an entire pumping cycle [54, 55]. As shown by Yamaguchi [51, 52], Harris established that contact between the slipper and swash plate was particularly likely to occur when the piston made the transaction from suction to delivery regions of the pump. This was shown physically by the location of witness marks on the swash plate of a dismantled pump. It was also shown that the slipper operates with small clearance in the delivery region of the pump, and with a greater clearance in the suction region. Additionally, the angle of tilt of the slipper was shown to dramatically increase when in the suction region of the pump. At high rotational speeds, the central clearance of the slipper was found to be consistent throughout the delivery stroke. However, at these higher speeds, the minimum clearance reduced and hence contact between the slipper and swash plate was more likely. In agreement with Harris, Manring [56] indicated that the greatest angle of tilt was likely to occur as the piston moved from the delivery to the suction region of the pump.

Kazama applied a mixed lubrication model to hydrostatic thrust bearings [36]. The effects of surface roughness, frictional torque and speed of rotation were considered. With a clamping ratio greater than unity, contact between the bearing surfaces was

possible. Contact between the surfaces led to greater levels of friction, and hence increased power losses. Conversely, clamping ratios less than unity led to higher flow rates, and hence a power loss due to fluid leakage. These characteristics were found to be more prevalent at high supply pressures. This research was followed by an experimental validation which demonstrated a high level of agreement with the theoretical results [57]. Canbulut developed an artificial neural network for the analysis of frictional losses of slipper bearings [58, 59]. In addition to his theoretical work he investigated the power losses experimentally. Different slipper geometries were investigated, and it was found that larger ratios of pocket to overall slipper diameter reduced the frictional power losses. Whilst reducing the frictional losses, slippers with a relatively large pool were shown to exhibit a larger fluid leakage characteristic. The clamping ratios explored in this work ranged from 2.27% to 68.36%. This range is well below the design boundaries of commercially available piston assemblies, which are usually designed to have a clamping ratio closer to 100%. Furthermore, the maximum pressure used was 30 bar, which is very low for an axial piston pump application.

Bergada and Watton [60], developed an approach for multiple land slippers. Previous work had either utilised a single land slipper, or assumed that the groove created no lift, with it being vented to atmospheric pressure [61]. Bergada demonstrated that for a flat slipper, the pressure profile was independent of clearance, and that the pressure drop radially across the groove was negligible. Overall, the presence of a groove, creating two lands, increased the leakage flow rate by approximately 7% when compared to a single land slipper with otherwise identical dimensions.

Hooke and Kakoullis measured the clearance between the slipper face and swash plate by installing displacement transducers within a swash plate [47, 62]. A cluster of four transducers was located in the centre of the high pressure region of the pump. By arranging the four transducers in a quadrant, an attempt was made to measure the clearance at the inside, outside, front, back and centre of the slipper as it passed through the measurement region. Although this was deemed to be representative of steady state conditions, measurement through swash plate mounted transducers only allowed the clearance to be measured at one specific location of the piston cycle. Repeatable results were obtained for individual pistons, however results between seemingly identical slippers were found to vary significantly. Reasons for this behaviour could only be attributed to small geometrical differences of the slipper surface and ball joint. Further experimentation was carried out by Hooke and Li using a test apparatus developed to analyse slipper behaviour under simulated conditions [63, 64]. A test rig was constructed using a stationary cylinder block and rotating swash plate. Slipper clearance was found to vary for different slipper geometries. However, all results indicated that the leading edge of the slipper had a greater clearance than the trailing edge. Additionally, it was established that the tilt perpendicular to the direction of motion was insignificant. For slipper with an 8mm land, the measured clearances were 22μm and 13μm for the leading and trailing edges respectively. For a slipper with a 2mm land, these clearances were reduced to approximately 4μm and 3μm for the leading edge and trailing edge clearance respectively

This work was extended by reproducing the couples experienced by the slipper whilst operating within a pump [65]. These couples are largely due to the centrifugal loads

from the pump rotation, friction within the assembly ball and socket joint, and drag between the slipper and swash plate surfaces. The couples were replicated by holding the slipper in the eccentric bore of a piston. A range of offsets were investigated by varying the rotation of the piston and eccentricity of the bore. Again, the displacement sensors were mounted in the rotating swash plate, and hence the slipper clearance was only measured at a specific angular location. In this work, however, the swash angle was zero, and thus the slipper to swash plate clearance was assumed to be continuous. It was found that the load offset had a large influence on the clearance that the slipper operated with. A centrally loaded slipper was found to operate relatively flat, however moving the load towards the rear of the slipper increased the angle of tilt. By moving the load towards the rear of the slipper, it was established that the clearance of the leading edge of the slipper increased, whilst the clearance measured at the trailing edge remained largely unchanged.

Koc et al [37], performed a further experimental investigation of the effect of clamping ratio and orifice size on the performance of slippers. He found that polishing of the running face optimised running conditions. Koc also discovered that slippers operate perfectly satisfactorily with no hydrostatic lift, for example, with the orifice blanked. In fact, the slipper was found to be more stable with the orifice blanked, and had maximum resistance to tilt when operating under these conditions. For all conditions, it was found that an oil flooded swash plate was essential. Removal of this oil substantially reduced the slipper clearance, especially with the lubrication hole blocked. Koc's research was carried out using a slipper with a single land and hence one with no groove.

Slipper clamp ratios were examined experimentally using a steady state slipper swash plate apparatus [61, 66]. This analysis found that slippers which are under clamped, with large orifice diameters, tend to operate with larger central clearances and tilts than slippers that are over clamped and have no orifice. Slightly over clamped slippers were shown to operate with a higher leading edge, with under clamped slippers being more unstable, operating with a larger clearance at the trailing edge. Over clamped slippers were found to give a consistent and predictable clearance characteristic over a range of offset distances. Conversely, under clamped slippers were found to be sensitive to offset loadings and demonstrated a relatively unstable mode of operation. This research was conducted for slippers with a single land, and hence the effect of a groove on the stabilisation of the slipper was not considered.

It has been shown that slippers with a single land operate move effectively with a slightly convex surface [67]. This enables the slipper to maintain hydrodynamic lift when the slipper is flat, as the leading edge produces lift, with the trailing edge cavitating. The minimum clearance of the slipper is relatively insensitive to the degree of non-flatness and this non-flatness is largely caused by wear and loading deformations during pump operation.

Manring et al [68, 69] developed a test apparatus to measure the pressure profile of the fluid supporting a slipper. In this work, there was no relative motion between the bearing surfaces. The test apparatus consisted of a piston within a bore. Hydraulic pressure was supplied to the piston bore forcing the piston against a stationary block. Several pressure taps were drilled into the block at different radial distances from the centre of the slipper. One of these was located under the pocket of the slipper, with five located across the area under the land of the slipper. These pressure taps were

connected to pressure gauges mounted around the peripheral of the block. A pressure profile was then determined and thus the load carrying capacity of the slipper was estimated for each inlet pressure. A flow meter located in the supply line of the test apparatus measured leakage of oil by measuring the flow rate of oil into the piston. The main aspect of this work was to investigate the characteristics of slipper bearings using different socket geometries. This was based on the idea that different socket geometries would affect the deformation of the slipper whilst under pressure, and hence impact the load-carrying capacity of the slipper. Manring found that lowering the contact point of the ball joint reduced the flow rate of oil across the face of the slipper. This suggested a reduction in deformation of the slipper face. Locating the contact point closer to the top of the joint tended to increase the load-carrying capacity of the slipper. However, no clear trend for this characteristic was present over the range of contact locations. All of the test specimens were geometrically identical to the original design slipper apart from the socket geometry. The range of socket geometries, however, was limited, with all of the test specimens exhibiting a significantly higher socket contact point than the original slipper. It was therefore concluded that raising the contact point did indeed increase the load-carrying characteristic of the slipper, but by doing so, greatly increased leakage. No optimal solution to socket geometry was found, as high levels of leakage are generally deemed undesirable.

Parallel research has considered an analytical solution with the assumptions of laminar flow in a radial direction. This work considers a tilted slipper operating under steady conditions where the slipper pocket, groove and slipper lands are flat. The rotation of the slipper is also taken into account. This then allows solution of the Reynolds equation as follows [70, 71]:

$$\frac{\partial}{\partial r}\left(rh^3\frac{\partial p}{\partial r}\right)=6\mu\omega r\frac{\partial h}{\partial \theta} \tag{2.3}$$

The solution is again complex, resulting in a generic equation capable of generating the pressure distribution equations for a slipper with any number of lands. Due to the complexity of the integral, equation (2.3) must be integrated numerically to determine the leakage. This is work being under taken with visiting researcher Dr. J.M. Bergada, and is shown in Appendix A1, as it is under publication review.

2.3 Water-Based Fluids

The research described previously has utilised hydraulic oil as the pumping, and hence lubricating fluid. However in recent years, the fluid power industry has re-examined the feasibility of using water and water-based oils as the hydraulic medium within piston pumps [33, 72-81]. This research has been driven primarily by the environmental, economic and safety advantages of using water in place of oil [73]. The main problems arising from using water in hydraulic pumps are corrosion and poor lubrication. The reduction in lubrication can lead to increasing levels of wear, reducing the volumetric efficiency and ultimately leading to failure of the pump [79].

A pure water axial piston pump was developed by Li et al [73]. In this pump, there were seals around each of the pistons, and hence the pistons and the port plate to cylinder barrel interface were lubricated with water, whilst allowing the shaft bearings and slipper to swash plate interfaces to be oil lubricated. There are complications associated with the sealing of the separate water and oil areas; manufacture cost and consequence of failure being of importance. These factors led to development of a pump using pure water as both a pumping medium and lubricant for all components. The poor lubrication properties of water were found to increase contact between mating parts, causing surface damage and wear. Furthermore, the low viscosity of water potentially increases the leakage rate, and hence reduces the volumetric efficiency of the pump. Consequently much of the research in the development of water axial piston pumps has concentrated on material selection and surface treatments, rather than the re-design of the mechanisms within the pump. Shudong [75] proposed splitting the slipper into two parts; the main body of the slipper made from stainless steel, with an inserted bearing pad made of a polymer. This

combination of materials ensured both structural rigidity of the ball joint and good lubrication properties of the slipper face. Shudong tested a range of materials for use on the slipper face, and concluded that a carbon fibre reinforced polyetheretherketon (PEEK) slipper insert pad offered the best wear performance. The resulting composite slipper was combined with a stainless steel swash plate. Li and Hooke [72] investigated composite slippers, finding that the analysis developed for predicting slipper behaviour under oil lubrication could be extended to water lubrication albeit with smaller clearances. Huanlong et al proposed a new slipper design, shown in Figure 2.3, which comprised of three cavities on the face of the slipper [80]. Here each of the cavities was connected to the lubrication orifice of the slipper and hence during operation contained high pressure fluid producing a hydrostatic separation force.

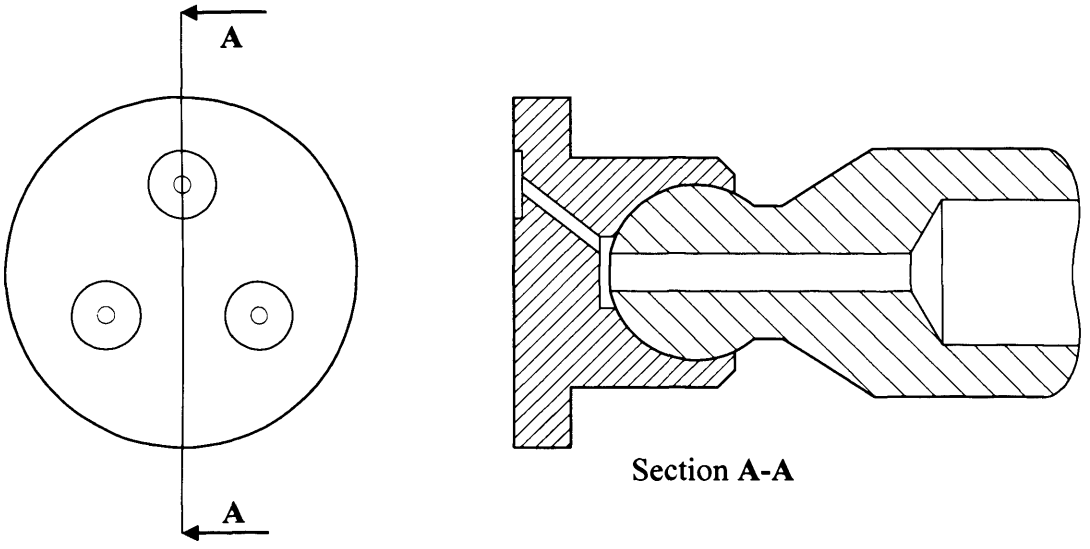

Figure 2.3 Multi-cavity slipper design

A CFD simulation of both a traditional single land slipper and the new multi-cavity slipper was performed. From the results, Huanlong concluded that the multi-cavity

slipper was more resistant to tilt, and had a lower leakage flow rate than the traditional slipper [80].

Due the poor lubrication properties of water, the use of water-based hydraulic fluids has been investigated [33, 73]. Water-based hydraulic fluids contain approximately 95% water, with the remainder being hydraulic oil. This oil-emulsion exhibits better lubrication properties than water, whilst maintaining some of the environmental and safety advantages of being predominantly made up of water. The extra lubrication properties enable pumps designed to work with mineral oils to be used without premature wear and failure occurring.

Chapter 3. Axial Piston Pump Analysis

3.1 Introduction

CFD simulations run by Wiklund [17] were successful in simulating the dynamic movement of an axial piston pump. This enabled regions of caviation to be identified. Later simulations by Fairhurst using the "FLUENT" software [33] had the capacity to model the volume of fluid between the cylinder barrel and port plate, and hence establish the leakage from this region, although the computation of output flow ripple was not pursued.

The work presented in this chapter aimed to produce a steady state CFD simulation of an axial piston pump, modelling leakage between the barrel and port plate, in addition to modelling leakage through the pistons. It was recognised that producing a CFD pump model that incorporated slipper leakage geometries would require a mesh with a substantial number of cells. Building and running such a model was beyond the processing capacity of the workstation available. Although this was somewhat limiting, the consequential model did include leakage through each slipper. This was accomplished by generating a separate mesh representative of a single slipper. Results obtained from this model were used to calibrate volumes of cells within the main pump model. Leakage past the face of the cylinder barrel was modelled using a similar approach to that implemented by Fairhurst [33]. Supplementary to the three dimensional models, a two dimensional axis-symmetrical mesh was produced which modelled the leakage of oil between a piston and its bore.

In addition to the CFD simulations, this chapter details an experimental investigation of an axial piston pump. An existing axial piston pump was modified, enabling pressure transducers to be installed in the cylinder chambers. Transient pressure

measurements from three of the nine piston chambers were subsequently obtained. In addition, the leakage from the pump was measured. Also presented in this chapter, is a comparison of experimental results with those obtained through the CFD simulations.

3.2 Materials and Methods

3.2.1 Pressure transducer fitment

In order to measure the transient pressure within an individual cylinder chamber, a pressure transducer had to be mounted in the discharge end of the piston bore. The key difficulty to overcome was the lack of space between the cylinder barrel and the inside of the pump casing. The radial clearance between the barrel and pump case was 14.5mm. The available pressure transducers measured 9mm in diameter and had an overall length of 24mm excluding the cable. A fitment was therefore designed which connected a pressure transducer to the relevant cylinder bore. This fitment enabled the transducer to be positioned on the peripheral of the cylinder barrel, aligned in an axial direction, parallel to the pump shaft. This fitment had to be robust enough to withstand the high cyclic pressures that it would experience during pump operation. This consideration affected the method of fitment to the cylinder barrel. In addition, an adequate flow path was required between the bore and the face of the pressure transducer, whilst limiting the dead volume to minimise compressibility effects on the pressure readings.

The fitment consisted of two parts. The first was a module that the pressure transducer screwed in to. This featured an internal annulus with porting to the face of the pressure transducer. The second component was the hollow bolt which secured the assembly to the cylinder barrel. This bolt featured two radial holes, which aligned with the annulus when assembled. This two part assembly enabled the bolt to be tightened to an appropriate torque, whilst ensuring the transducer body was aligned along the length of the cylinder barrel, and significantly, maintaining a flow path for

any angular position of the bolt. The assembly, shown in Figure 3.1 was manufactured from stainless steel and copper washers were used to seal the mating faces. Three of these assemblies were produced, enabling the pressure to be monitored in three of the nine cylinders. Before being installed within the pump, the three pressure transducer assemblies were tested statically, up to a pressure of 200 bar.

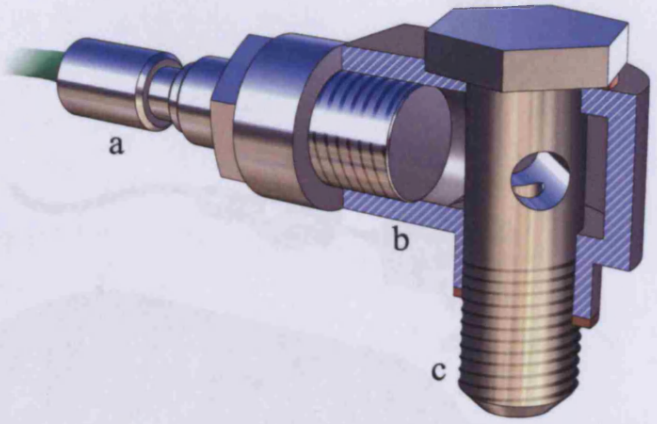

(a) pressure transducer, (b) transducer fitment (sectioned), (c) hollow securing bolt

Figure 3.1 Pressure transducer assembly

Once installed in the pump, the operating clearance between the top of each fitment and the inside of the case was approximately 2mm. It was intended that the symmetrical positioning of the transducers in every third cylinder bore would minimise rotational imbalance within the pump. The cylinder barrel, with an assembled and an exploded view of a pressure transducer assembly is shown in Figure 3.2.

In order to connect the sensors to charge amplifiers and an oscilloscope, a slip ring assembly was used. The cables from the three pressure transducers were threaded through a 2mm hole in the barrel, located between the ports of two consecutive piston bores. The pump shaft was modified so that the cables could then be threaded through the centre of it. Silicone sealant was used to seal the end of the pump shaft where the

three sensor cables protruded. This provided a semi-permanent seal for any oil within the pump shaft, whilst allowing easy disassembly. The pressure of oil in this area was low during operation, hence silicone sealant was considered adequate. The slip ring assembly was mounted onto the pump via a specially designed coupling.

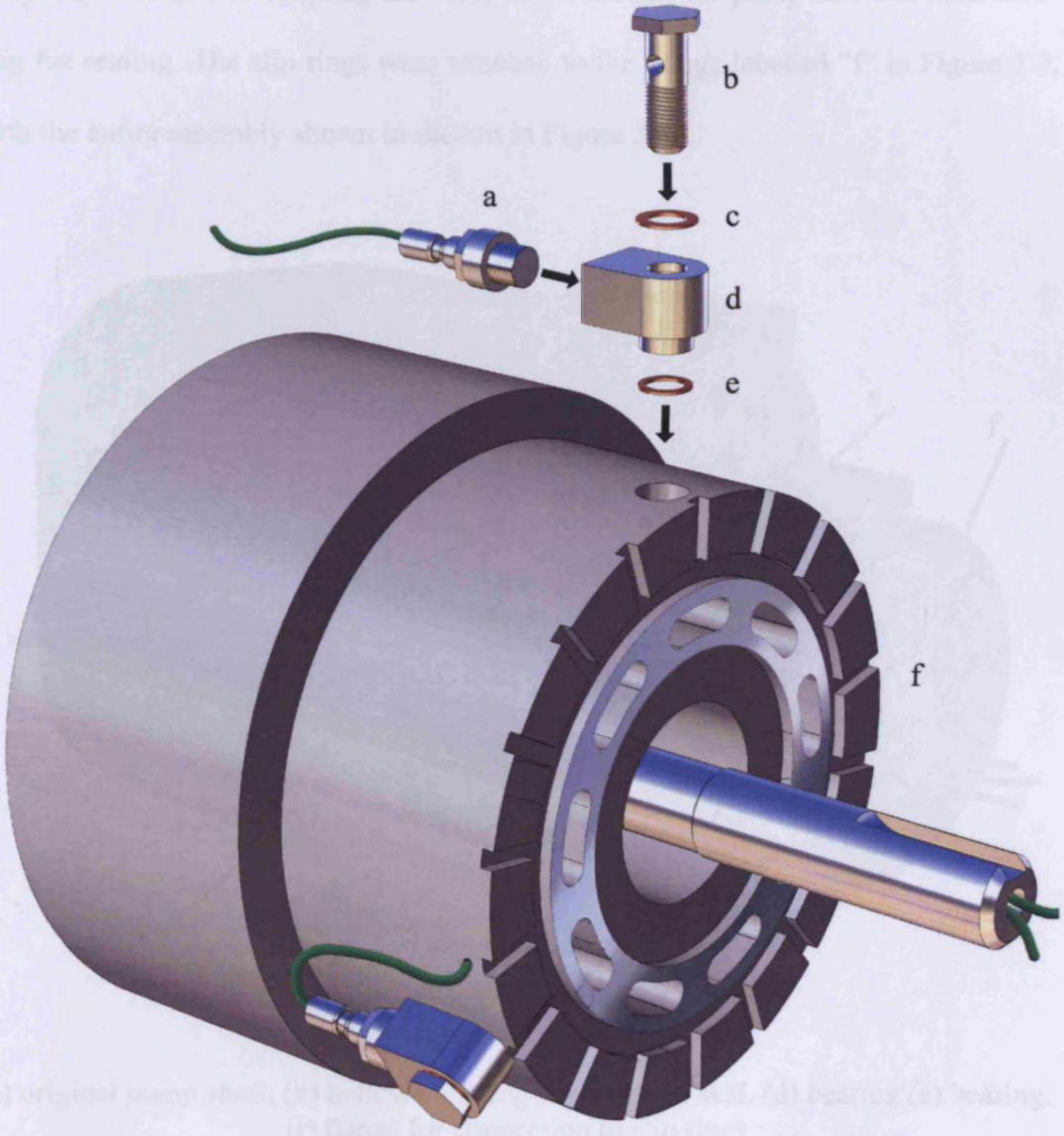

(a) pressure transducer, (b) hollow screw, (c) copper sealing washer, (d) assembly body (e) copper sealing washer, (f) cylinder barrel

Figure 3.2 Pressure transducer assemblies and cylinder barrel

The coupling assembly, shown in Figure 3.3, consisted of a cylindrical section which had a flange at each end. This coupling housed a short shaft, which connected to both the pump and slip ring shafts by means of keyways. The shaft was supported by a bearing at each end. Between these, a gaiter seal provided containment for the oil in the pump casing. The coupling assembly was bolted to the pump face and used an o-ring for sealing. The slip rings were attached to the flange labelled "f" in Figure 3.3, with the entire assembly shown in section in Figure 3.4.

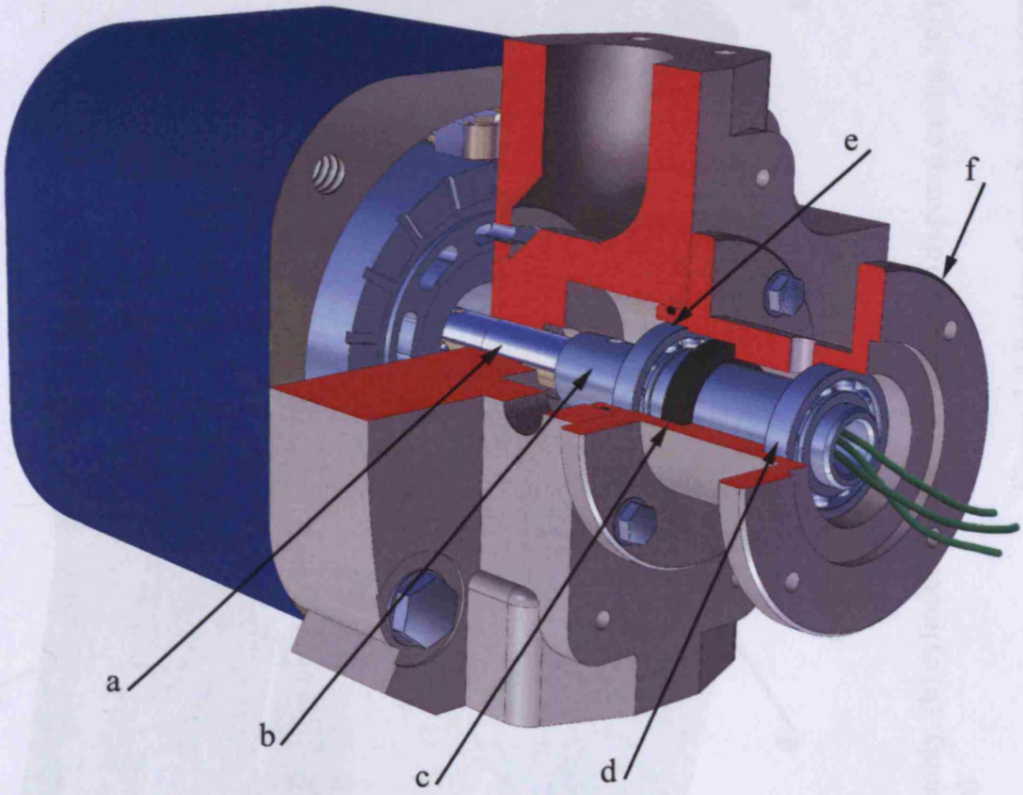

(a) original pump shaft, (b) hollow coupling shaft, (c) oil seal, (d) bearing (e) bearing, (f) flange for connection to slip rings

Figure 3.3 Coupling assembly: Sectioned surfaces in red

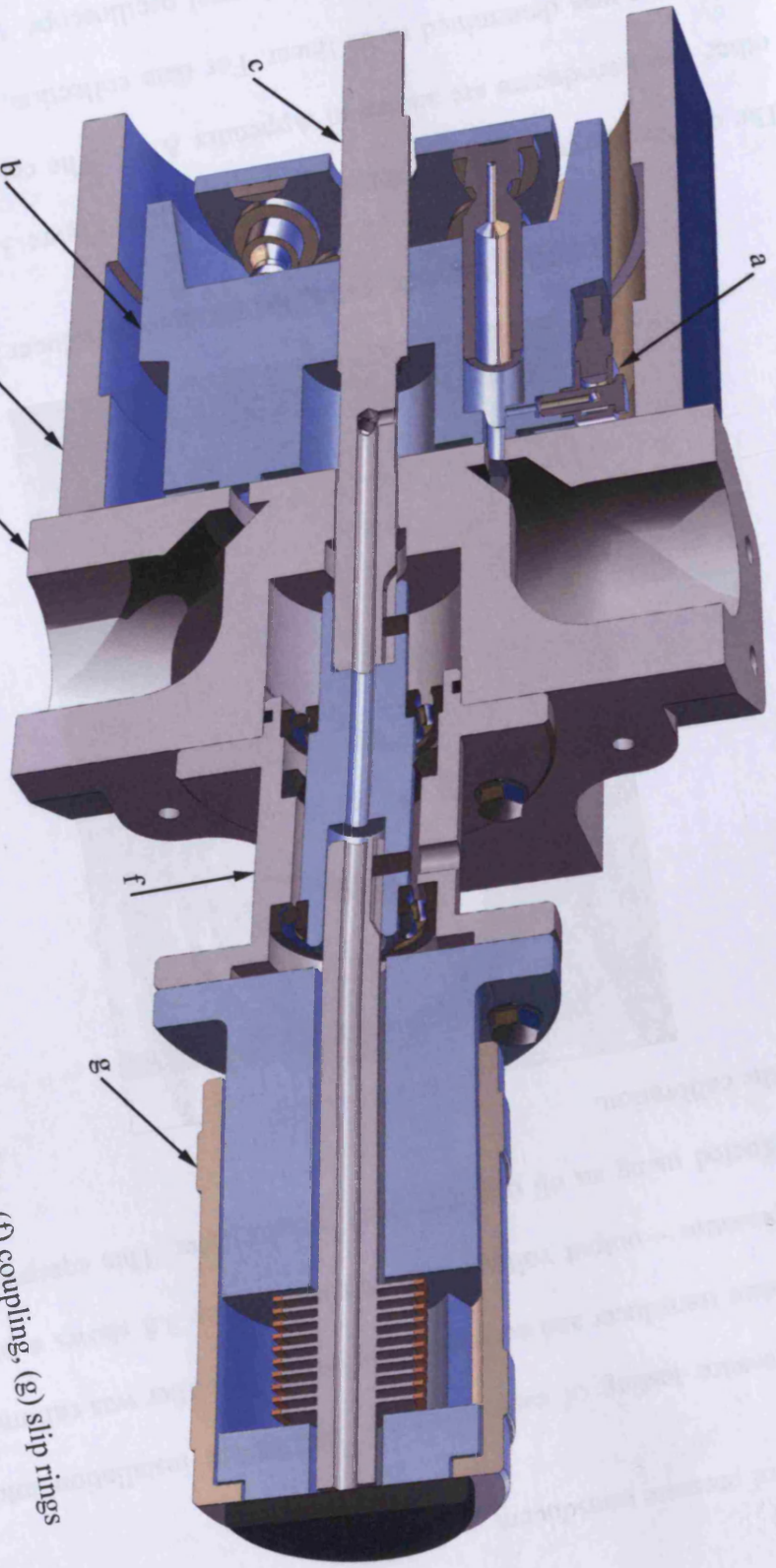

Figure 3.4 Section through pump assembly
(a) sensor assembly, (b) cylinder barrel, (c) pump shaft, (d) pump casing, (e) port plate, (f) coupling, (g) slip rings
(representation)

3.2.2 Calibration of pressure transducers

Following the pressure testing of each assembly, and before installation into the pump, each pressure transducer and corresponding charge amplifier was calibrated to determine the pressure – output voltage characteristic. Figure 3.5 shows a pressure test being conducted using an oil operated dead weight tester. This equipment was also used for the calibration.

Figure 3.5: Pressure testing the pressure transducer fitment

The calibration curve for one transducer is shown in Figure 3.6. The curves for the other two transducers are shown in Appendix A.2.1. The calibration curve for each transducer was determined to be linear. For data collection, two oscilloscopes were used. The first was a "Tektronix" 4 channel oscilloscope, which enabled data to be collected simultaneously from the three pressure transducers. In addition, this oscilloscope could be connected to a workstation via a serial port to allow data to be

analysed. The second oscilloscope was a PC based data logger (Pico Technology Ltd, UK) which combined with acquisition software, allowed data to be directly captured on to a Microsoft Windows based workstation. Although only two channel, this logger had a resolution of 12 bit, compared to the Tektronix resolution of 8 bit. Thus, it was able to detect a smaller change in signal amplitude.

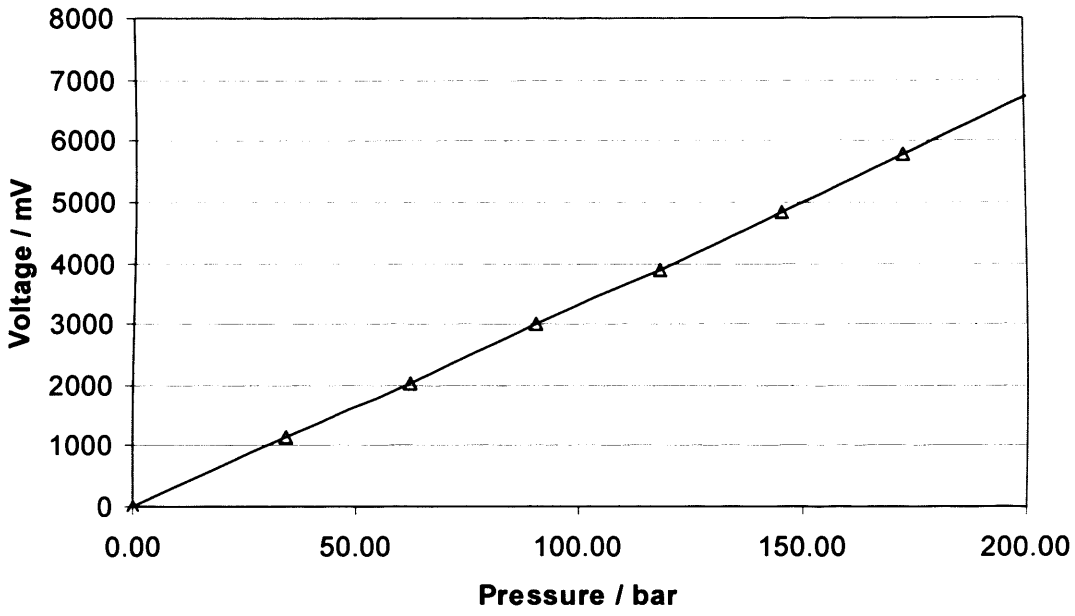

Figure 3.6: Calibration curve transducer 26766 and charge amplifier #1

3.2.3 Hydraulic circuit

Shown in Figure 3.7 is a schematic diagram of the hydraulic circuitry constructed for this research. The first circuit was the drive circuit. This consisted of a motor-driven gear pump which provided hydraulic flow to an axial piston motor. Prior to the inlet of the axial piston motor was a flow control valve. This was used to vary the flow rate of oil to the motor inlet, and hence could control its rotational speed. Directly coupled to the hydraulic motor was the axial piston pump equipped with the pressure transducers described above. The axial piston pump formed part of the second

hydraulic circuit which contained a relief valve. This relief valve, placed at the outlet of the pump, provided the capacity to adjust the load on the pump. The oil reservoir for the axial piston pump was placed with the oil surface at a height of 2.25m, thus providing a positive pressure at the inlet of the pump. By adjustment of the flow control valve and pressure relief valve, the axial piston pump could be run at variable speeds and loads.

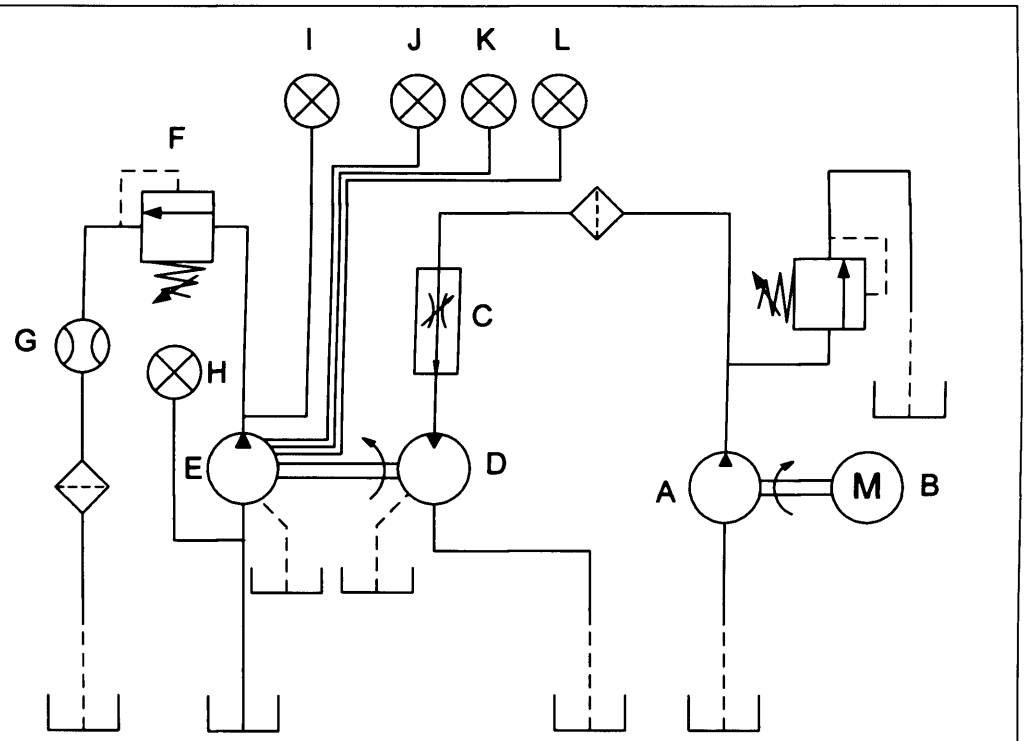

Label	Component
A	Gear pump
B	Electric motor
C	Flow Control valve
D	Axial Piston Motor
E	Axial Piston Pump
F	Pressure Relief Valve
G	Flow meter
H	Inlet pressure gauge
I	Outlet pressure gauge
J, K, L	Pressure transducers within cylinder bores of pump

Figure 3.7: Hydraulic circuit diagram

A pressure gauge was located between the outlet of the pump and the pressure relief valve. This enabled the mean outlet pressure to be monitored. A pressure gauge was later located just before to the inlet of the pump to confirm a steady inlet pressure. Since the tank was raised above the inlet, as shown in Figure 3.8, the inlet pressure was estimated using Bernoulli's Equation.

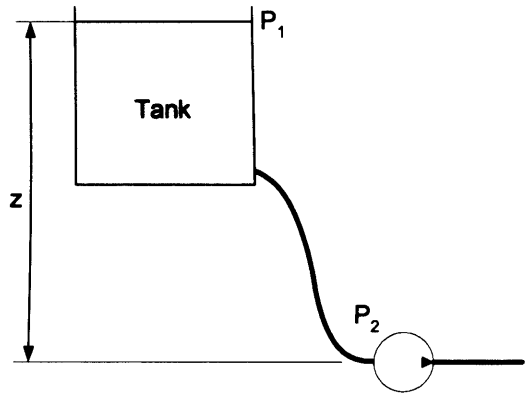

Figure 3.8 Tank height relative to pump

$$P_2 - P_1 = \rho g z - \tfrac{1}{2}\rho v^2 \tag{3.1}$$

Where, ρ is the fluid density, g is the gravitational constant, z is the height shown in Figure 3.8, and v is the velocity of fluid through the pump inlet hose. At a speed of 1100 rpm, the flow rate developed by the pump was 33.6 litres per minute. With a 32mm diameter inlet hose, this flow rate requires an inlet velocity of $0.7 m.s^{-1}$. Therefore, with the difference in height, z, of 1.25 metres, Equation (3.1) implies a pump inlet pressure of 0.105bar above atmospheric pressure. The Reynolds number of this flow was calculated to be 608 using Equation (3.2) confirming laminar flow [82].

$$\mathrm{Re} = \frac{\rho v d}{\mu} \tag{3.2}$$

Thus equation (3.3) could be used to determine the frictional pressure loss, which with a hose length (l) of 2m was determined to be 0.014 bar

$$\Delta P = \frac{128\mu l}{\pi d^4} Q \tag{3.3}$$

Thus an inlet pressure of 0.09 bar above atmospheric was assumed for the inlet pressure of the pump.

3.2.4 Flow rate measurement

Oil flowing through the outlet of the pump was measured by a Kracht flow meter, which worked on the gear motor principle. This flow meter was placed directly after the relief valve in the outlet line. Fluid leaking from the pump was initially intended to be measured using a Kracht flow meter. During operation leaked fluid accumulated in the pump casing, and hence was effectively at atmospheric pressure. This meant that the gear type flow meter used for the outlet flow could not be used, as it required a pressure differential of several bar to function: Installing such a flow meter in the leakage return line would have caused pressure to build up in the pump casing. This would have potentially caused leakage past the pump bearings, which were not designed to contain this level of pressure. Additionally it would have caused leakage past the shaft seal on the connecting slip ring assembly. The fluid collecting in the pump case was therefore measured by disconnecting the hose returning the leaked oil back to the tank, and collecting it in a measuring cylinder. The flow of oil was timed using a stop watch to determine the volumetric flow rate. Care was taken to maintain the height of the end of the hose during collection so as to ensure a steady flow rate of oil.

3.2.5 Shaft speed measurement

Shaft speed was measured using a hand-held optical speed sensor. This was used in conjunction with a strip of reflective material that was attached to the pump shaft.

3.3 CFD Pump Simulation

3.3.1 Mesh considerations

For 2-D models "FLUENT" can use meshes comprised of triangular or quadrilateral cells, or a combination of the two. 3-D models can comprise of a combination of tetrahedral, hexahedral, pyramid or wedge shaped cells. The appropriate grid type is dependent on the specific application, and the factors affecting the choice of mesh scheme are interrelated. The main factors to be considered were:

- Geometry of meshed area or volume
- Setup time
- Computational expense
- Numerical diffusion

3.3.1.1 Geometry of meshed area or volume

The actual geometry of the mesh will ultimately dictate the best meshing scheme. For example, a dynamic grid utilising layering requires quadrilateral cells in 2-D or hexahedral cells in 3-D. Furthermore, the direction of flow of the fluid should be considered when producing the mesh. Aligning the mesh with the flow will result in a quicker level of convergence at the processing stage. For meshes containing both small clearances and large volumes, the use of tetrahedral, pyramid and wedge shaped cells enables the transition between regions of differing cell density.

3.3.1.2 Setup time

Creation of grids consisting of quadrilateral or hexahedral cells can be very time consuming for complex geometries. Therefore, grids utilising triangular or tetrahedral cells are widely used for complex geometries. For simpler geometries time may not be saved by using triangular or tetrahedral cells so the cell type utilised will be more dependent on the other factors to consider.

3.3.1.3 Computational expense

When geometries are complex, a triangular or tetrahedral mesh can often be created with far fewer cells than the equivalent quadrilateral or hexahedral elements. This is because the triangular or tetrahedral mesh allows better control of the intensity of cells in specific regions. Conversely, quadrilateral or hexahedral meshes will offer less control by forcing cells to be placed in areas where they are not needed. One characteristic of quadrilateral or hexahedral cells is that they permit a much larger aspect ratio than triangular or tetrahedral cells. This makes them ideal for certain applications such as modelling a long thin duct. Utilising quadrilateral or hexahedral cells in this circumstance would result in far fewer cells than if triangular or tetrahedral cells were utilised with a similar aspect ratio. Due to computational processing restrictions, compressibility was not considered within the CFD models presented.

3.3.1.4 Numerical diffusion

Numerical diffusion is a consequence of representing the fluid flow in discrete form. The errors arising from numerical diffusion can be reduced by using the second order discretization scheme within "FLUENT". This helps reduce the effects of numerical diffusion on the solution. However, this sometimes results in reduced convergence.

An alternative solution is to refine the mesh by either employing quadrilateral or hexahedral cells which are inline with the fluid flow, or to increase the cell density.

3.3.2 2-D simulation of a single piston

A two-dimensional axis-symmetric model of a single piston was created using the "GAMBIT" software package, which is a pre-processor to the "FLUENT" CFD software. The mesh generated is shown below in Figure 3.9. This mesh was able to simulate the leakage through the lubrication orifice, and between the actual piston and its bore. A clearance of 10μm was assumed for the clearance of the slipper, whilst a radial clearance of 12μm was assumed for the piston bore clearance. The piston bore clearance was based upon measurements taken from a piston and corresponding cylinder bore, and was very similar to the clearance used by Lassar in his research on piston geometries [9]. The CFD model was created with the assumption that the piston was concentric within its bore, with no change in radial clearance along its length. Pistons have been shown to move radially during pump operation, however the difference in leakage between a tilted piston and a concentric one has been shown to be very small [83, 84]. A kinematic viscosity of $32mm^2.s^{-1}$, associated with an oil temperature of 40°C for an ISO 32 mineral oil, was assumed for all CFD models.

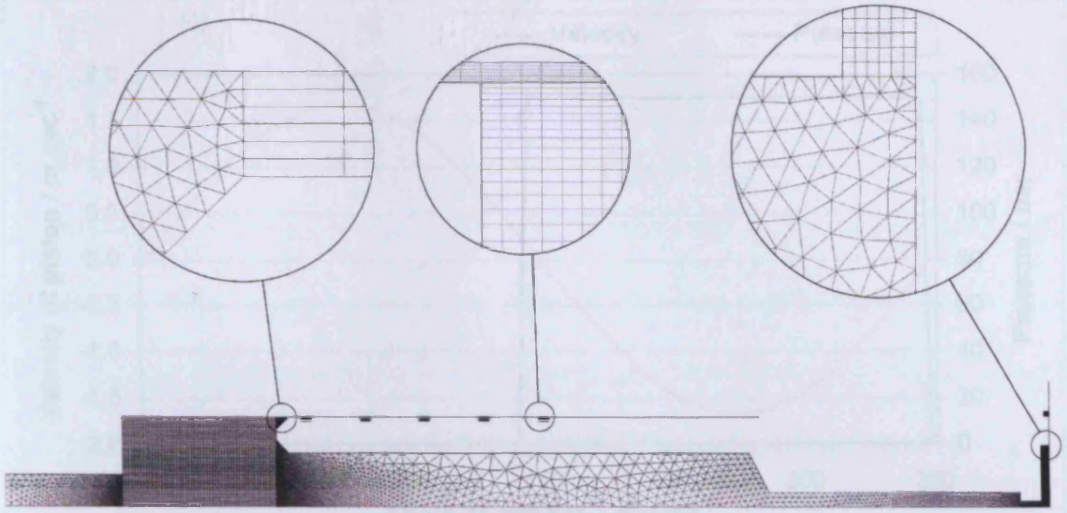

Figure 3.9 2-D Axis-symmetric mesh of a single piston

A time dependent UDF was implemented which controlled the pressure at the inlet to the cylinder bore, depending upon the hypothetical angular rotation of the piston bore. The velocity of the piston was also controlled relative to the angular rotation of the piston, and deforming zones allowed the volume of fluid within the piston to change accordingly. The pressure and velocity of the piston relative to the angle of rotation are shown in Figure 3.10, where the discharge stroke is denoted by a negative piston velocity.

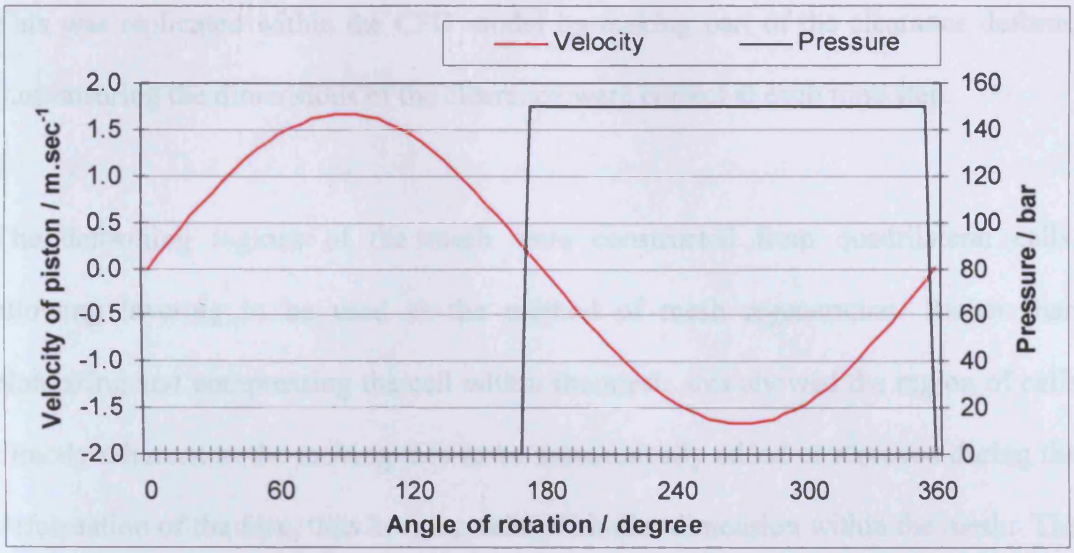

Figure 3.10 Variation of velocity and pressure

The end of the piston was observed to leave the cylinder bore during the suction stroke, as shown below in Figure 3.11. Thus the length of the leakage path along the length of the piston varied over time, being shortest at the end of the suction stroke.

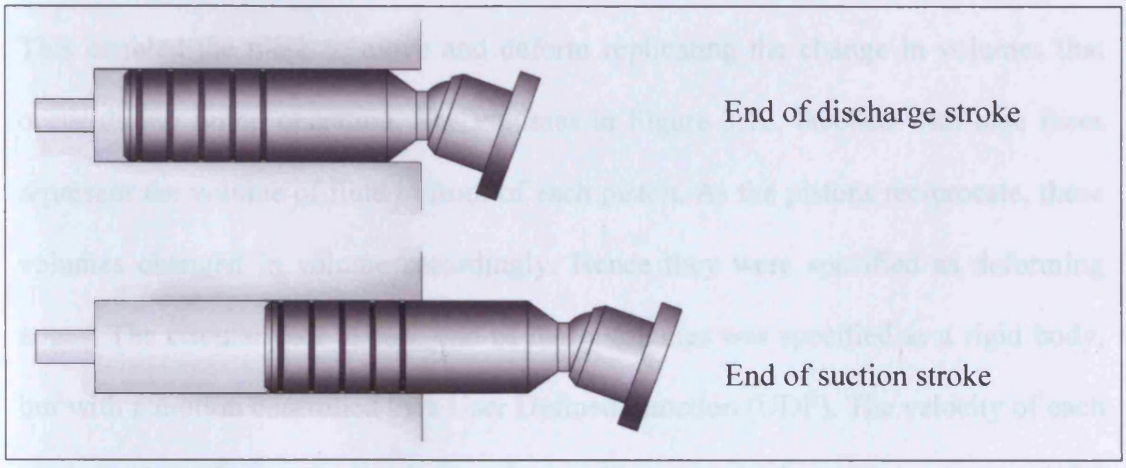

Figure 3.11 Piston at extremities of stroke

This was replicated within the CFD model by making part of the clearance deform, thus ensuring the dimensions of the clearance were correct at each time step.

The deforming regions of the mesh were constructed from quadrilateral cells, allowing layering to be used as the method of mesh regeneration. Rather than elongating and compressing the cell within the mesh, this allowed the region of cells directly adjacent to the moving face to be automatically added or removed during the deformation of the face, thus keeping cells of similar dimension within the mesh. The remainder of the mesh was constructed from triangular cells. "Pressure Outlet" boundary conditions were assigned to the edges representing the ends of the clearances, and these edges were monitored for flow rate when the model was run.

3.3.3 3-D pump model

A three-dimensional model of the pump was developed, also using "GAMBIT". This model replicated the pumping dynamics of the pump, and included the major leakage paths within the pump. The geometry produced is shown in Figure 3.12 and Figure 3.13. The geometry was produced from separate volumes, sharing common faces. This enabled the mesh to move and deform replicating the change in volumes that occur during pump operation. The volumes in Figure 3.12, labelled with blue faces represent the volume of fluid in front of each piston. As the pistons reciprocate, these volumes changed in volume accordingly. Hence they were specified as deforming zones. The circular face at each end of these volumes was specified as a rigid body, but with a motion controlled by a User Defined Function (UDF). The velocity of each piston is dependent on its angular location, and hence each piston was assigned a UDF representative of this. The UDF assigned to each piston is shown in Appendix A.2.2.1.

Dynamic layering was used in this model to maintain mesh integrity during deformation. This meant that the volumes representing the pistons had to be meshed using a hexahedral meshing scheme. Volumes shown to the right of the moving face in Figure 3.12, depicting the volumes within the hollow pistons, were specified as rigid. These volumes were assigned a velocity equal to that of the moving face on the adjacent deforming zone. In addition to the deformation and velocity settings, all volumes representing the pistons were assigned a rotational boundary condition, about the central pump axis. This combined with the reciprocating motion of each piston, replicated the pumping dynamics of the pump.

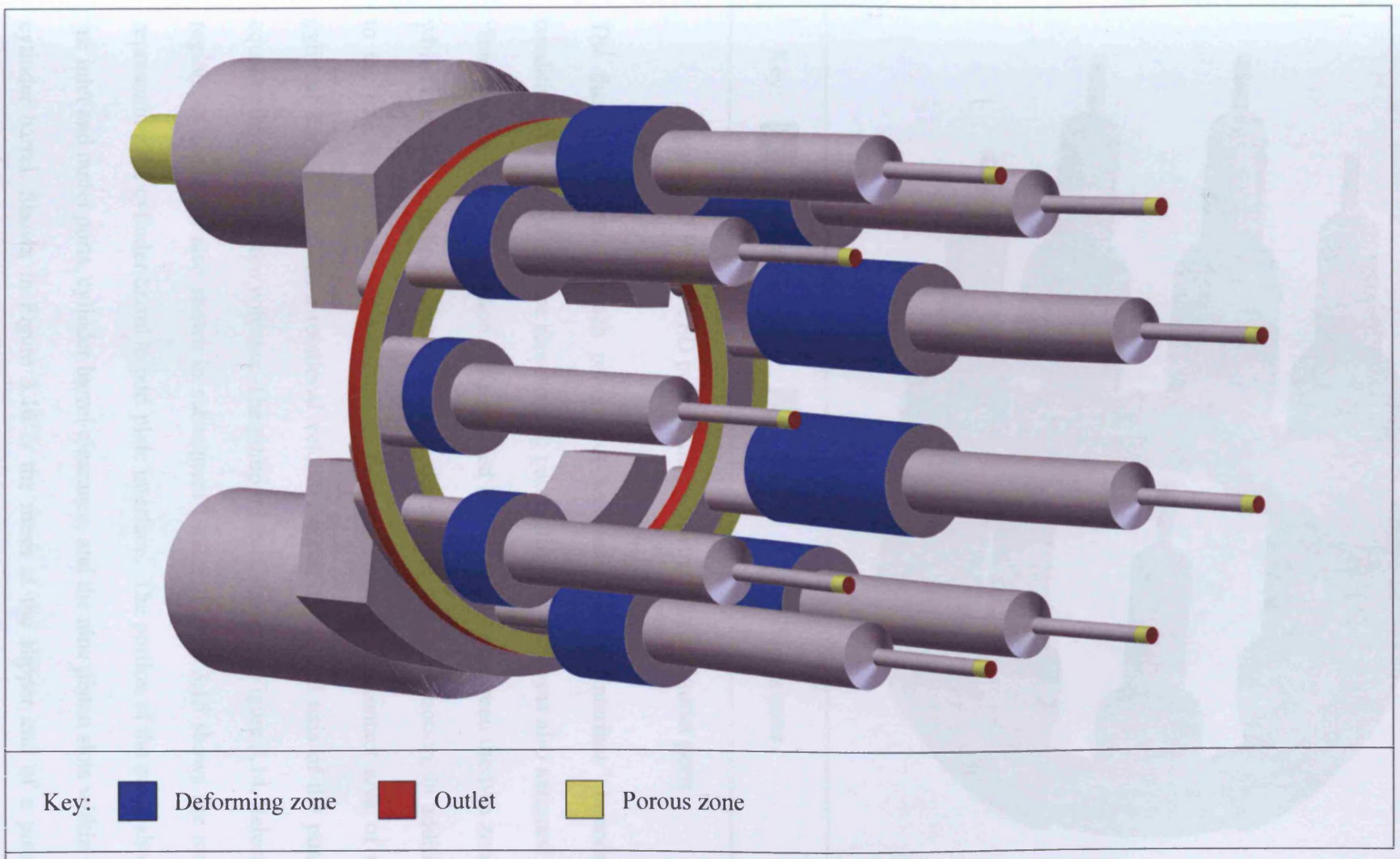

Figure 3.12 CFD pump model volumes

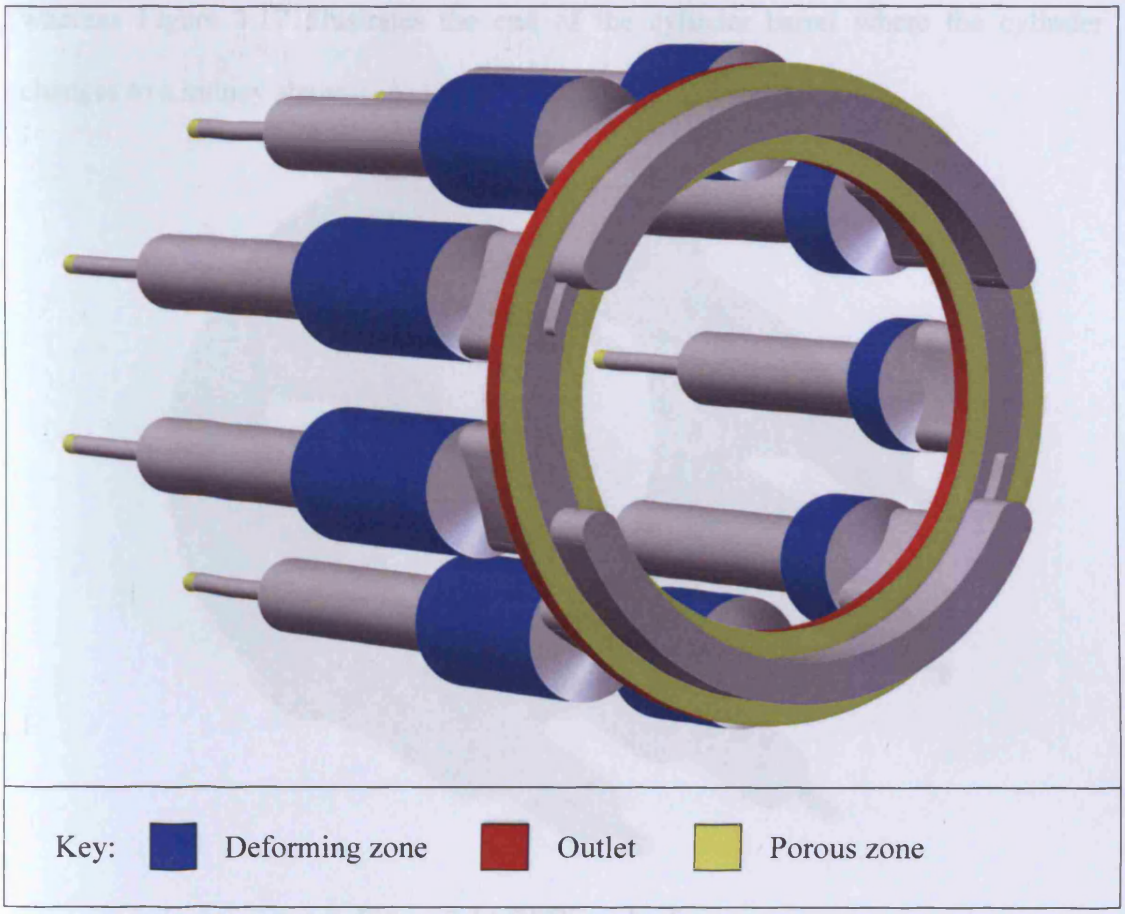

Figure 3.13 Partial CFD pump model showing inlet and outlet ports

The face on the end of each piston slot was assigned an "Interface" boundary condition. The adjoining face representing part of the port plate was also assigned an "Interface" boundary condition. This enabled flow continuity between the two zones, whilst allowing a sliding movement due to the relative rotational motion. In addition to the interface boundary condition, the face representing the contact area of the cylinder barrel was given a rotational velocity, about the central axis of the pump, equal to that of the piston volumes. The pump mesh is shown in Figure 3.14. Selected regions of mesh are also shown in subsequent figures. Figure 3.15 shows the mesh representing the cylinder barrel to port plate interface. The portion of the mesh shows the inlet and outlet ports, cylinder barrel clearance, and the nine piston slots within the cylinder barrel. Shown in Figure 3.16 is the mesh at the slipper end of a piston,

whereas Figure 3.17 illustrates the end of the cylinder barrel where the cylinder changes to a kidney shape.

Figure 3.14 CFD mesh of pump

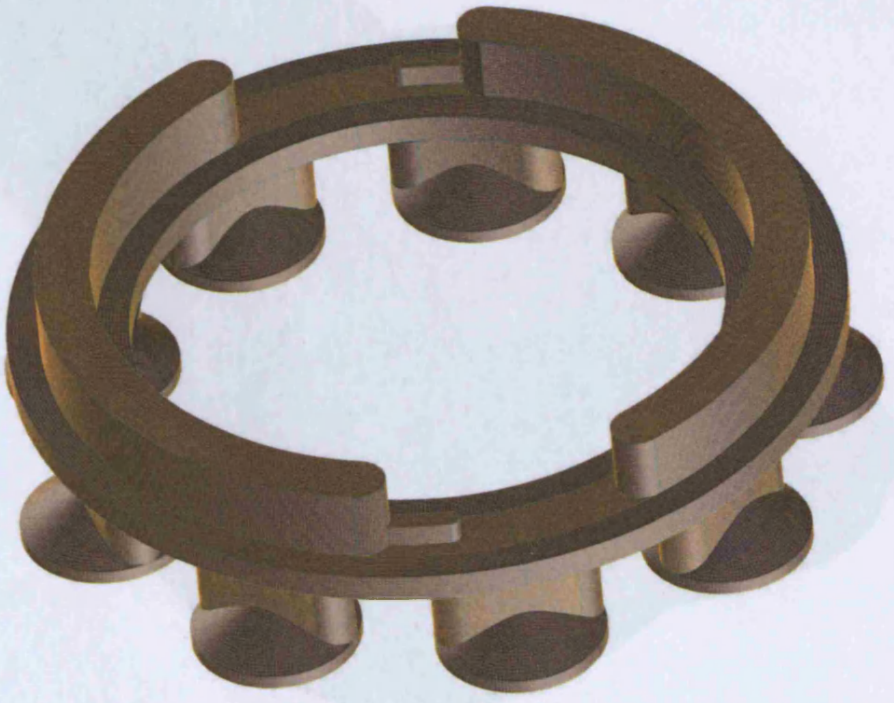

Figure 3.15 CFD mesh of piston slots and kidney shaped ports

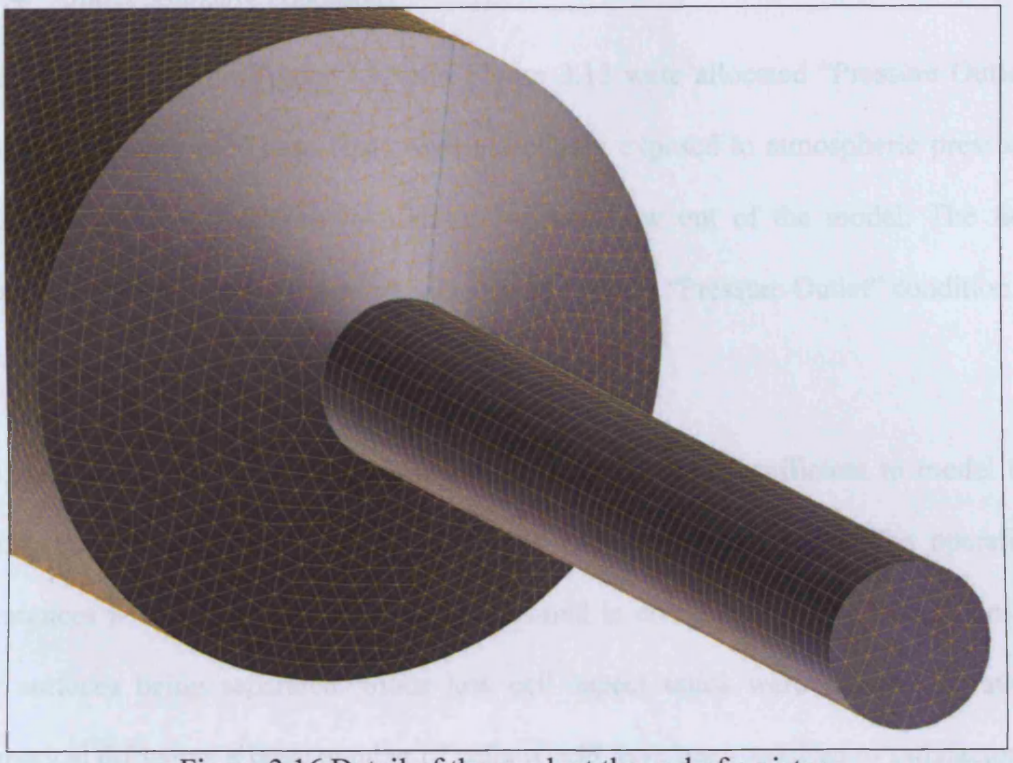

Figure 3.16 Detail of the mesh at the end of a piston

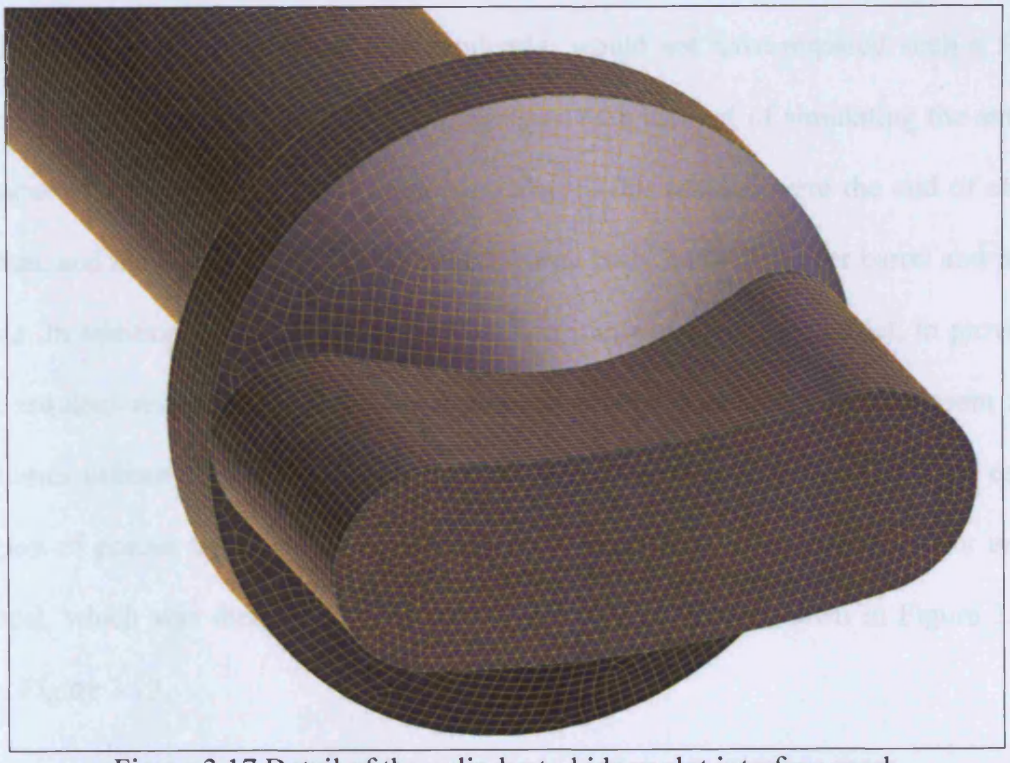

Figure 3.17 Detail of the cylinder to kidney slot interface mesh

3.3.4 Outlet boundary conditions

Faces labelled red on Figure 3.12 and Figure 3.13 were allocated "Pressure Outlet" boundary conditions. These faces were effectively exposed to atmospheric pressure, and were used as locations to monitor leakage flow out of the model. The face representing the outlet of the pump was also allocated a "Pressure Outlet" condition.

3.3.5 Porous zones

As stated previously, the computing power available was insufficient to model the entire pump including all of the clearances between mating parts. The operating clearances within an axial piston pump are small in comparison to the dimensions of the surfaces being separated. Since low cell aspect ratios were required to avoid numerical diffusion, a large number of cells would have been required to satisfactorily mesh volumes representing clearances within the pump. Additionally, a smooth transition was required between areas of different cell dimensions. This increases the cell density in volumes which, independently, would not have required such a fine mesh. Porous cells were therefore implemented as a method of simulating the small clearances within the pump. Regions modelled in this manner were the end of each piston, and the volume representing the clearance between the cylinder barrel and port plate. In addition, a region of porous cells was implemented at the outlet, to provide the required resistance to flow. Faces labelled yellow on Figure 3.12 represent the volumes utilising porous cells. Separate calibration models were produced for each region of porous cells and a resistance to flow coefficient was determined for each model, which was then applied within the main pump model shown in Figure 3.12 and Figure 3.13.

3.3.5.1 Porous zones at the end of each piston

A CFD model of a single slipper was produced. This slipper was assumed to operate with a central clearance of 10μm, which was based on experimental data for a slipper of similar dimensions [63]. A maximum cell aspect ratio of 5:1 was employed, with five cells spanning the gap between the face of the slipper and the swash plate. The leakage was determined for a range of pressures, and is shown in Figure 3.18.

From the gradient of the curve, a resistance coefficient was calculated, based on Darcy's Law of laminar flow through a porous media, and assigned to the porous boundary condition for each piston.

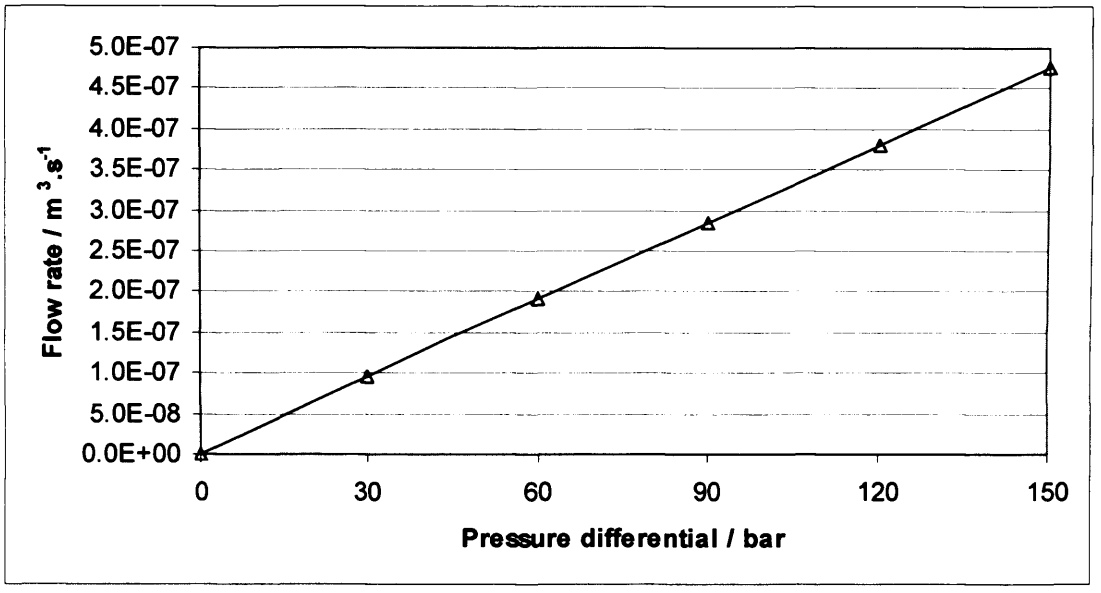

Figure 3.18 Calibration curve for piston leakage at angular velocity of 150 rad.s^{-1}

Through the length of the porous region, the pressure drop is defined by the following equation:

$$\Delta P = -\frac{\mu}{\sigma} v \cdot \Delta m \tag{3.4}$$

Where μ is the viscosity, v is the mean velocity (determined from the flow rate and cross sectional area of the porous region), Δm is the length of the porous region and σ is the permeability. The equation is negative as the pressure reduces in the direction of flow. The porous region for each piston had a diameter of 2.2mm and a length of 2mm. From Equation (3.4), a value for σ of $4.65 \times 10^{-13} m^2$ was calculated. This was applied in the direction of the z-axis, along the length of the piston.

3.3.5.2 Cylinder barrel and port plate clearance

Based upon experimental work, the operating clearance between a cylinder barrel and port plate has been shown to be approximately 15μm at a rotational speed of 150 $rad.s^{-1}$ [39, 40]. To determine the value of permeability for this zone, a volume of cells with cross sectional dimensions of 20mm by 15μm was produced. This volume had a length of 2.8mm, equal to the radial dimension from the piston slot across the land of the cylinder barrel. Once the flow rate had been determined for a range of pressures, as shown in Figure 3.19, Equation (3.4) was again implemented, this time making an adjustment for the fact that the porous region within the pump model had a thickness of 2.5mm, rather than 15μm. A value of $1.21 \times 10^{-13} m^2$ was thus derived for σ. This was applied in the directions of the x and y-axis only, so that there was only a resistance to flow in the radial directions.

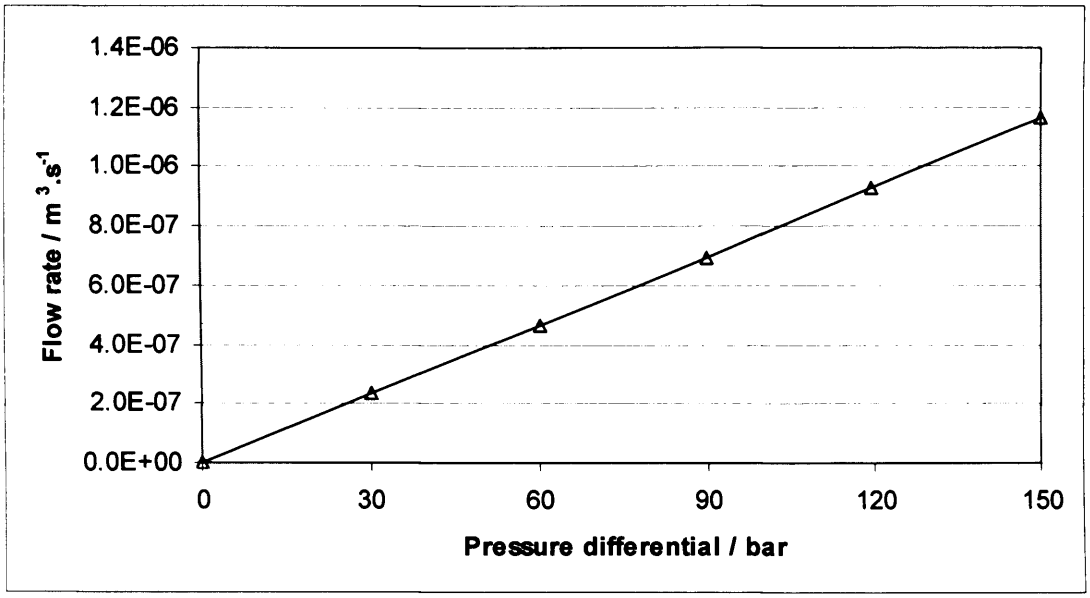

Figure 3.19 Calibration curve for port plate leakage

3.3.5.3 Pump outlet porous zone

The volume at the end of the outlet was calibrated in the same way as the other porous regions. The value calculated was such that the pump developed the desired pressure based upon the flow rate produced. The values required for the pump model to develop a range of discharge pressures are shown in Table 3.1.

Table 3.1 Porous outlet calibration values

Pressure / bar	**Value of σ / m^2**
20	2.68×10^{-09}
50	1.07×10^{-09}
70	7.67×10^{-10}
100	5.37×10^{-10}
120	4.47×10^{-10}
150	3.58×10^{-10}

3.4 Results

3.4.1 Experimental results

The output voltage from the charge amplifier is shown below in Figure 3.20. This voltage is shown at a speed of 1100 rpm, for a pump outlet pressure of 100 bar.

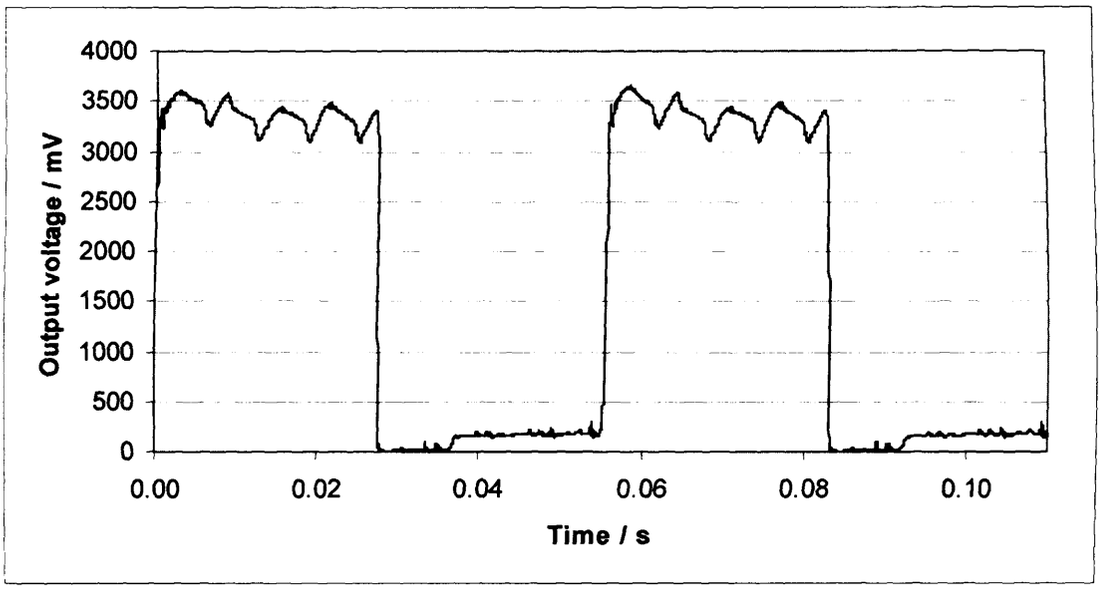

Figure 3.20 Typical output signal from charge amplifier

By using the calibration curve determined for each transducer, one of which is shown in Figure 3.6, the voltage signal was converted to represent the pressure experienced by the pressure transducer. By measuring the speed of rotation, the pressure could be plotted against angle of rotation rather than time. The resulting pressure characteristics for a several operating pressures are shown in Figure 3.21. The pressure transients observed were found to be very repeatable.

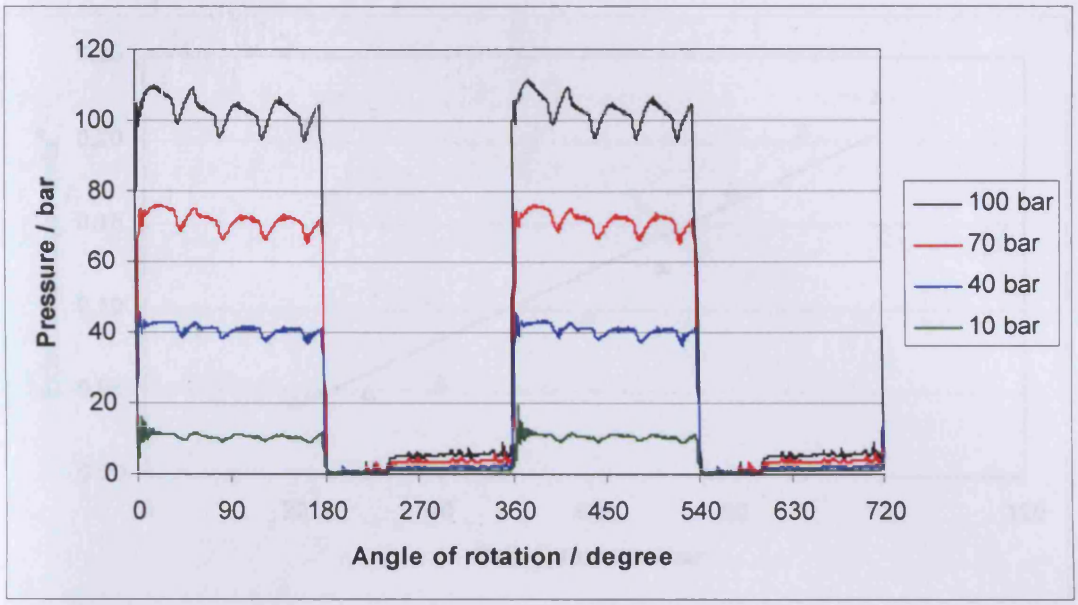

Figure 3.21 Transient pressure characteristics

The measured output flow from the pump is shown in Figure 3.22, with the external leakage shown in Figure 3.23. Although the output flow is relatively steady over the pressure range tested, a small reduction in flow was evident. This reduction in flow was partly due to the increase in external leakage, but also due to an increase in internal leakage between the discharge and suction ports.

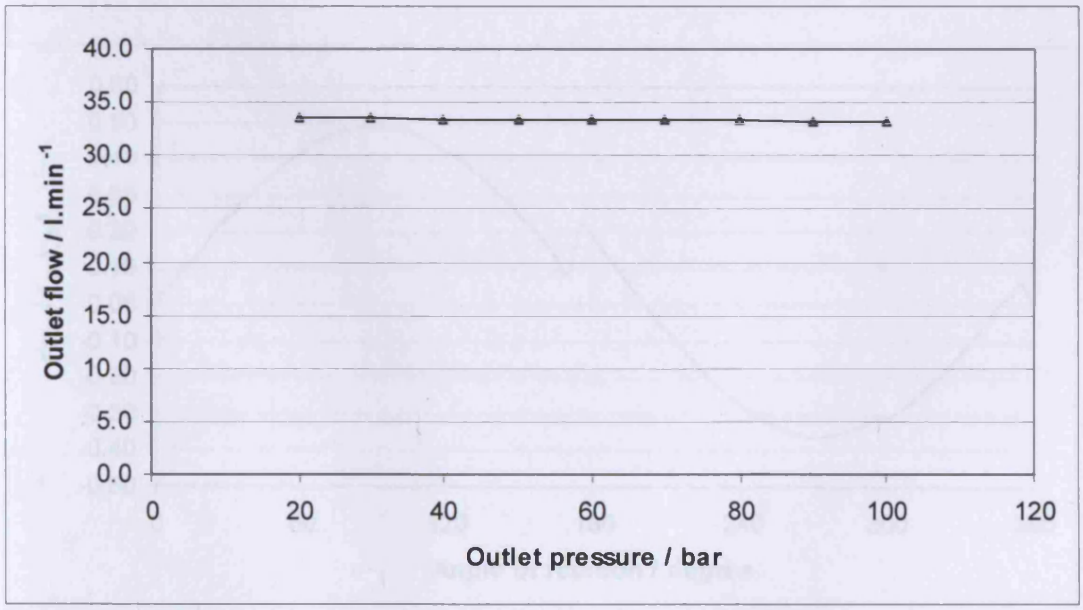

Figure 3.22 Experimentally measured output flow from pump

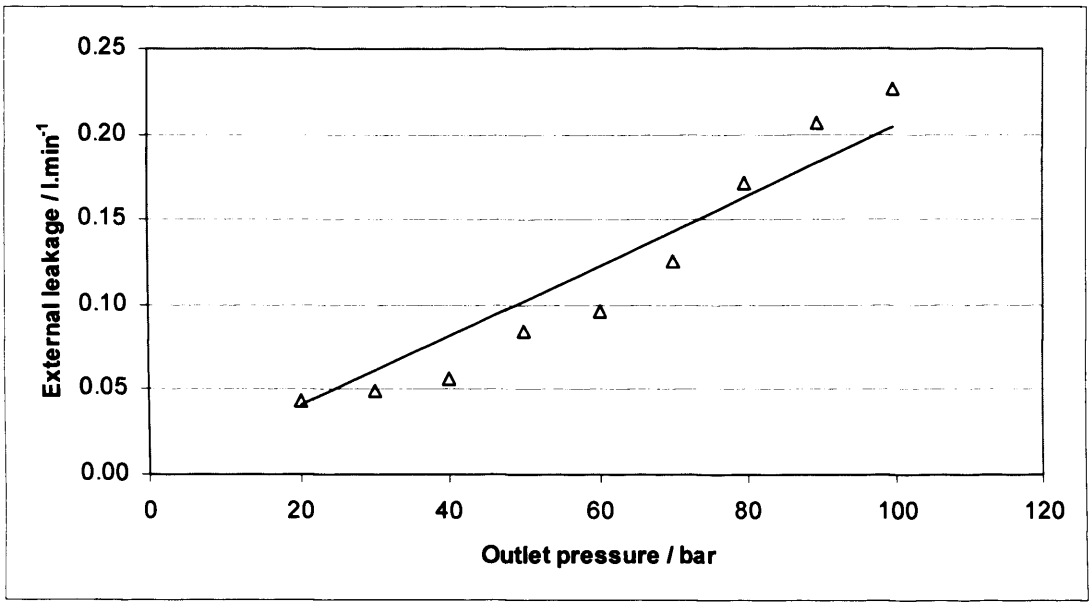

Figure 3.23 Experimentally measured external leakage from pump

The flow rates shown above are a mean calculated from four sets of results; however the flow rates we seen to exhibit a high level of repeatability.

3.4.2 CFD results

The flow rate of oil between the piston and its bore is shown below in Figure 3.24. The positive direction represents flow from the piston bore to the pump case.

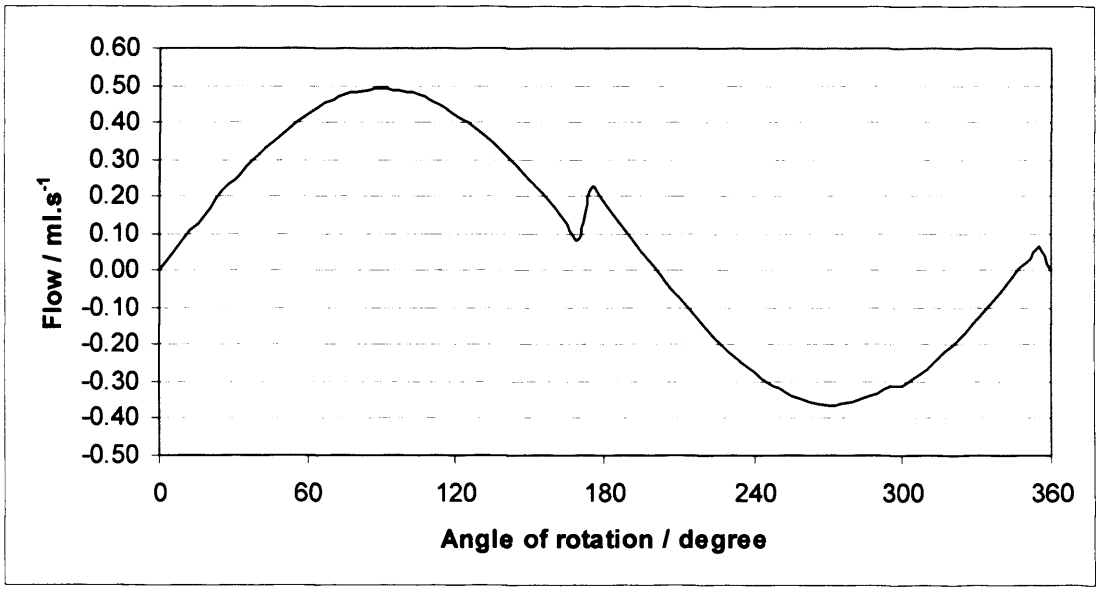

Figure 3.24 CFD derived flow through the gap between a piston and its bore, radial clearance of 10μm

The outlet flow of the pump, shown in Figure 3.25, suggests a fluctuating flow of 18 ripples per cycle of the pump. This ripple varies between 45.09 and 47.16 litres per minute, with a mean flow rate of 46.3 litres per minute. The pressure ripple at the outlet of the pump follows a similar trend, shown in Figure 3.26. This was expected and is due to the relationship between the flow and output pressure, as discussed when calibrating the porous zone at the outlet of the pump.

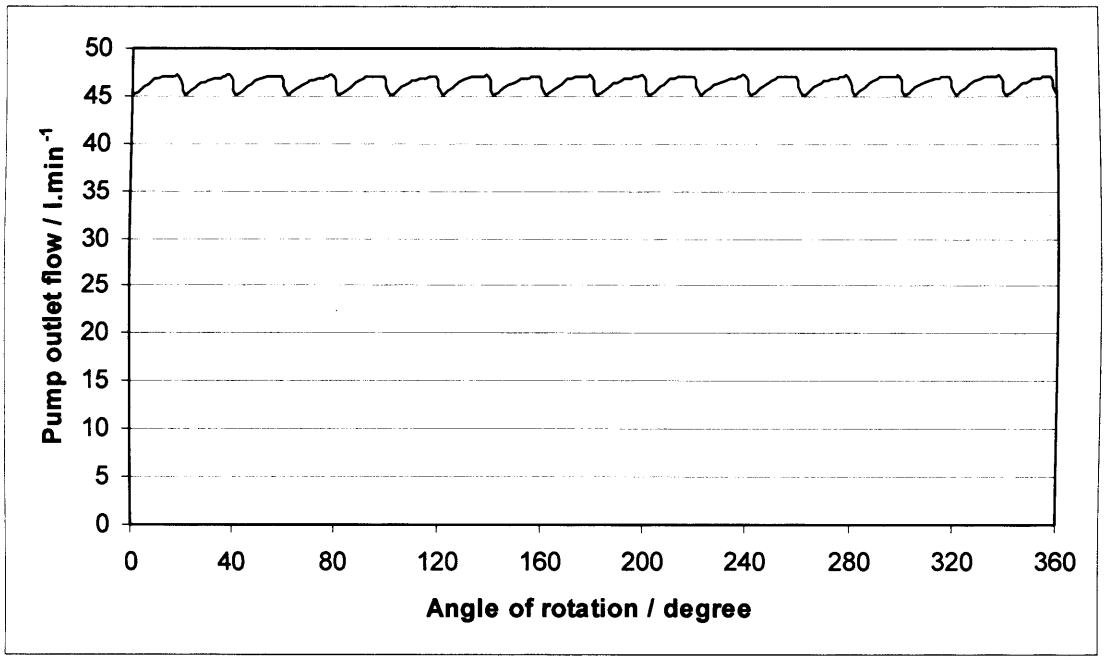

Figure 3.25 CFD derived outlet flow rate at 150 rad.s^{-1}

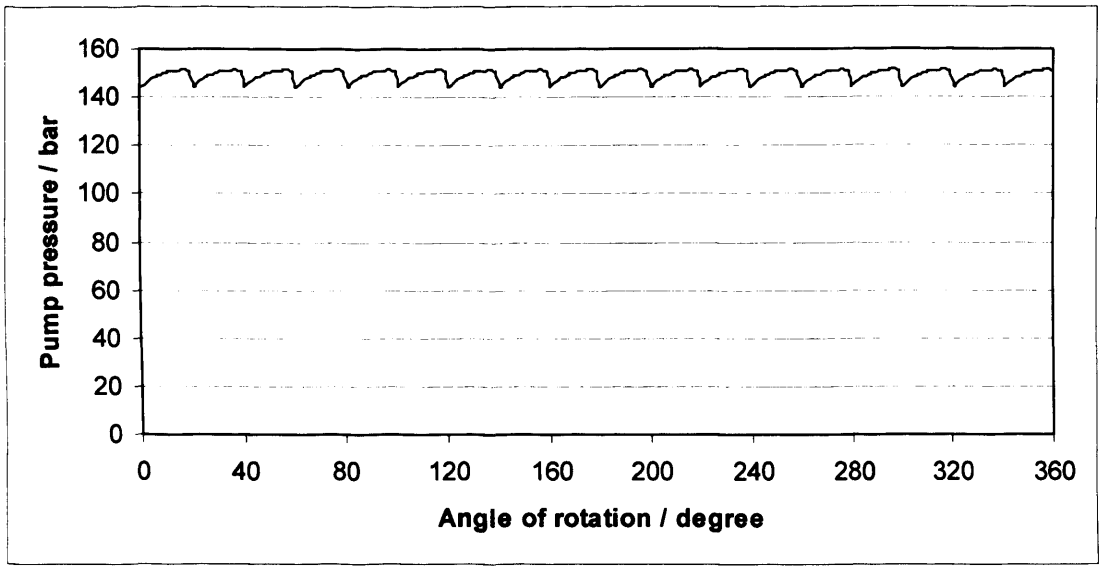

Figure 3.26 CFD derived pump pressure at outlet

A comparison between the CFD and experimental instantaneous cylinder pressure is shown in Figure 3.27 over two cycles. The regions of low pressure are when the cylinder is in the inlet region of the pump, with the high pressure being in the outlet region of the pump.

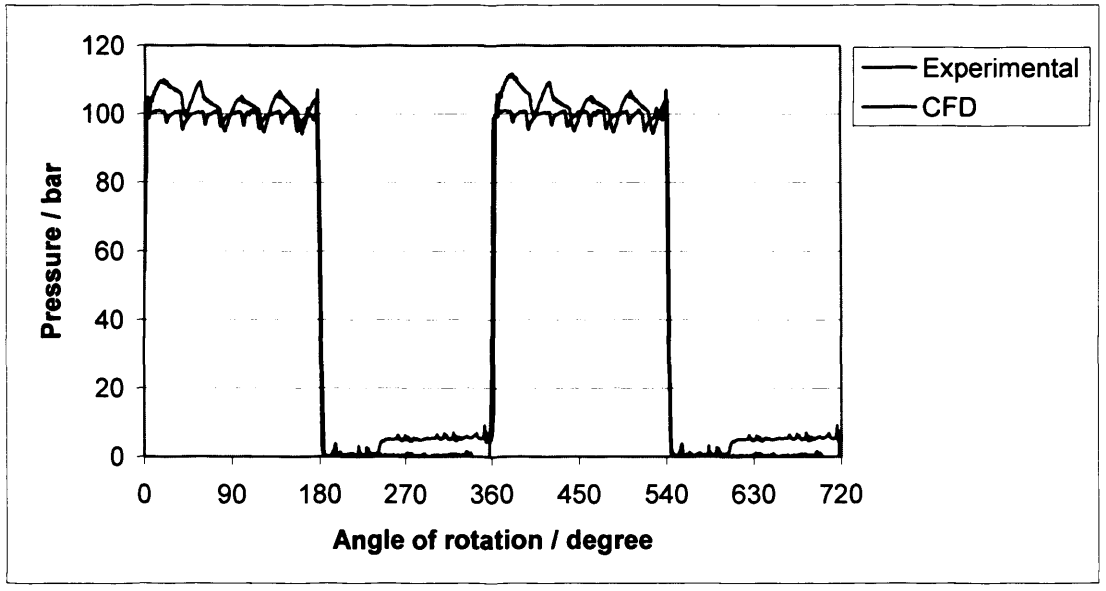

Figure 3.27 CFD calculation of a single cylinder pressure transient

The leakage through a single piston is shown in Figure 3.28. When in the high pressure side of the pump, the leakage was found to be 0.029 $l.min^{-1}$. This value was found to become negative just before the cylinder moved into the high pressure side of the pump. This is because a momentary negative pressure, as shown in Figure 3.27 occurred at this instant. This negative pressure is an indication of cavitation occurring, and the fact it is below zero bar absolute is a current limitation of the CFD package. A momentary increase in flow occurs as the piston moves from the high pressure side of the pump to the low pressure side. This is an indication of hydraulic trapping occurring. The overall leakage through the pistons is shown in Figure 3.29.

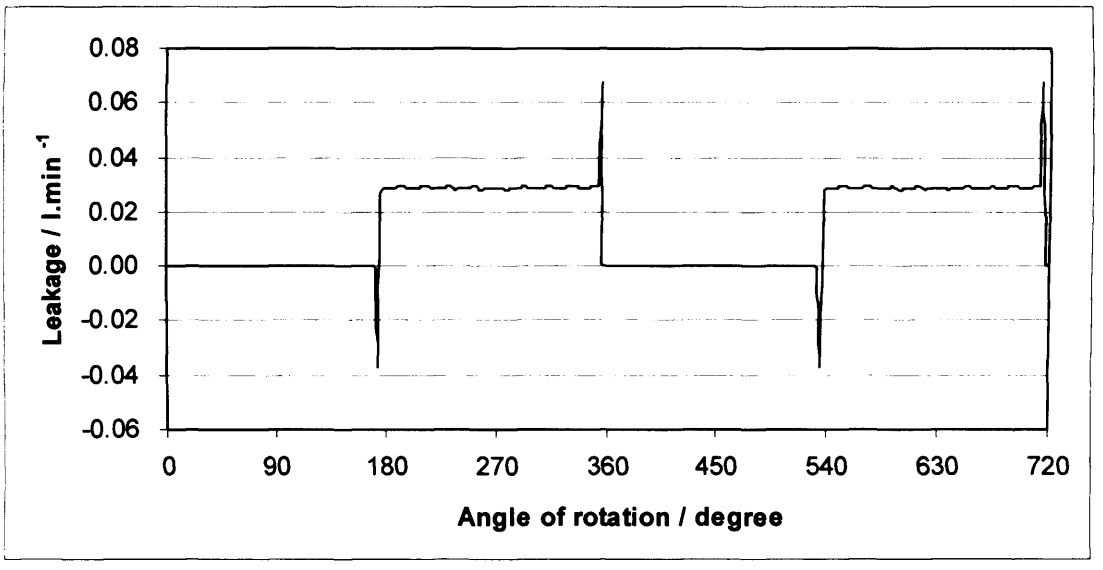

Figure 3.28 Leakage through a single piston

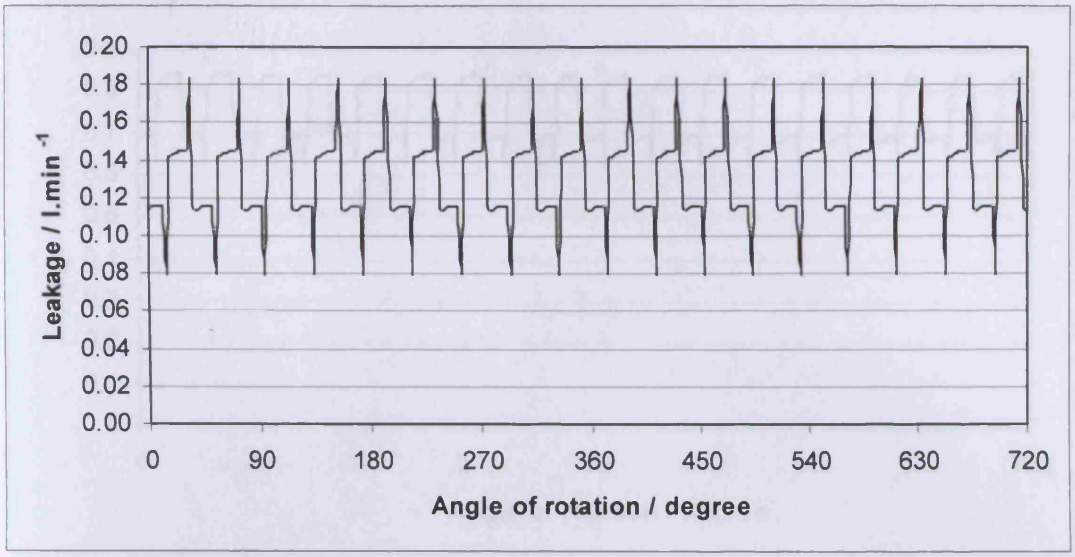

Figure 3.29 Total leakage through pistons

The leakage between the cylinder barrel and port plate is shown in Figure 3.30. The leakage from the outside surface was found to be greater than the leakage from the inside edge. This was expected, as the circumference of the cylinder barrel land was greater on the outside, thus creating a larger flow area.

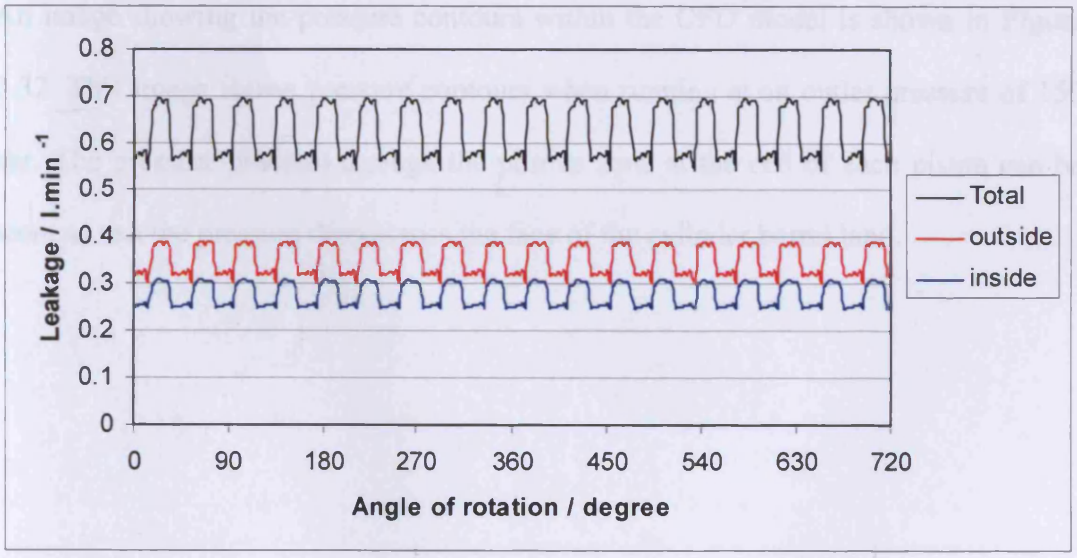

Figure 3.30 Leakage between cylinder barrel and port plate

By summating the leakage from the cylinder barrel and individual pistons, the overall pump leakage was determined. This is shown in Figure 3.31.

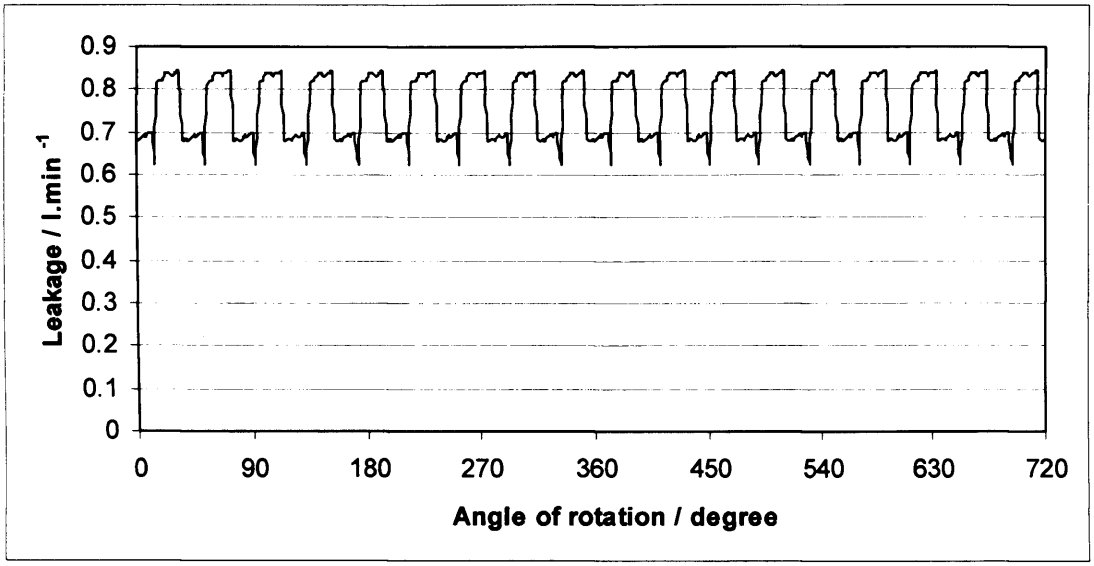

Figure 3.31 Total external leakage

By considering the overall leakage, and outlet flow rates, the volumetric efficiency of the CFD modelled pump was calculated to be 98.4% when operating at a discharge pressure of 150 bar.

An image showing the pressure contours within the CFD model is shown in Figure 3.32. This image shows pressure contours when running at an outlet pressure of 150 bar. The pressure gradient through the porous zone at the end of each piston can be seen, as can the pressure drop across the face of the cylinder barrel land.

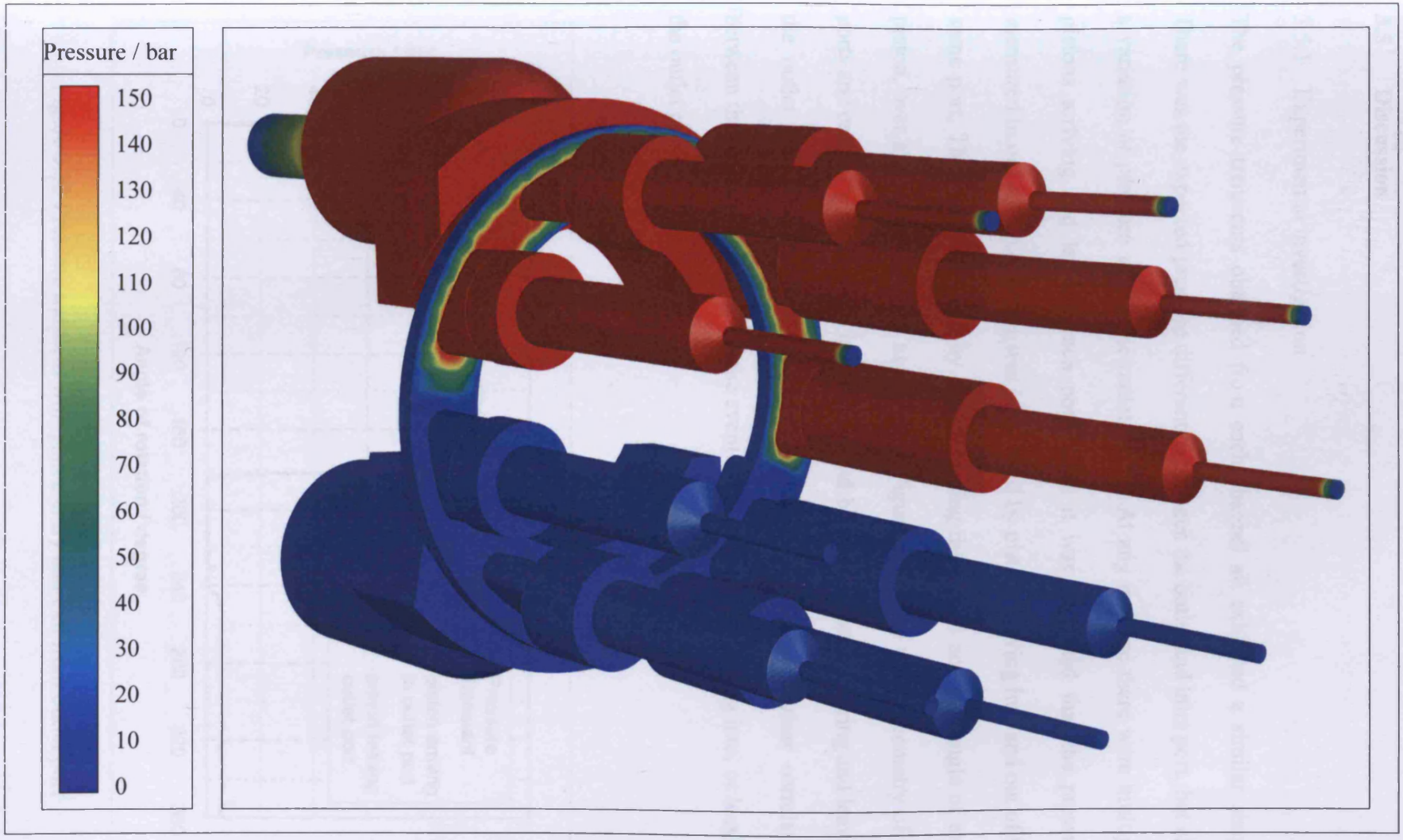

Figure 3.32 CFD pressure contours of pump model

3.5 Discussion

3.5.1 Experimental investigation

The pressure transients obtained from each channel all exhibited a similar shape. There was the expected pressure differential between the outlet and inlet port, but also a variation of pressure within the outlet stroke. At any instance there were multiple pistons arriving and leaving each port. Thus it was suggested that the pressure measured in one piston chamber was influenced by pistons moving into and out of the same port. This was confirmed by superimposing the arrival and exit angle of each piston, over a pressure transient as shown in Figure 3.33. Due to the geometry of the ports and each piston slot, there is a 20° interval between a piston entering and leaving the outlet port. The lines superimposed in Figure 3.33 show a clear correlation between the pressure variation and the event of a piston either arriving into, or leaving the outlet port.

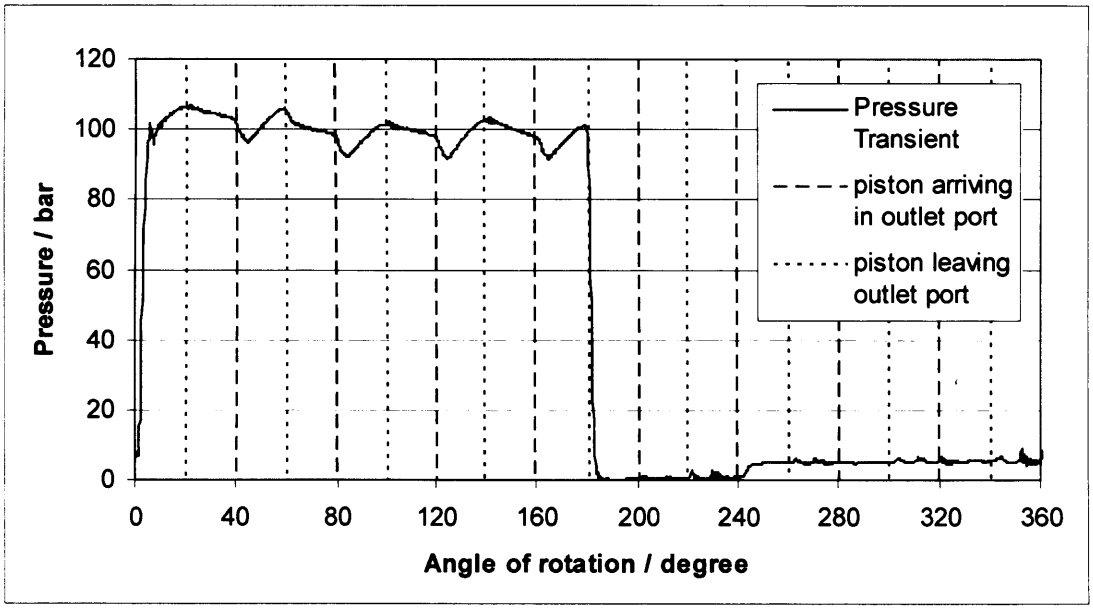

Figure 3.33 Pressure transient with piston entry and exit from outlet port

The fluid within the bore of piston leaving the inlet port is at inlet pressure, and thus when it moves into the outlet port, there is an equalisation of pressure. This has the effect of reducing the pressure of fluid in adjacent cylinders. This is apparent in Figure 3.33 at 40°, 80°, 120°, and 160°. Here pistons are entering the outlet port, which already contains the cylinder containing the pressure transducer. The reduction in pressure due the entry of a piston was found to vary with outlet pressure, and is shown in Figure 3.34. After the reduction in pressure, the pressure is then shown to increase. At the instant a piston leaves the outlet port, the pressure within the measured cylinder bore was observed to slightly reduce.

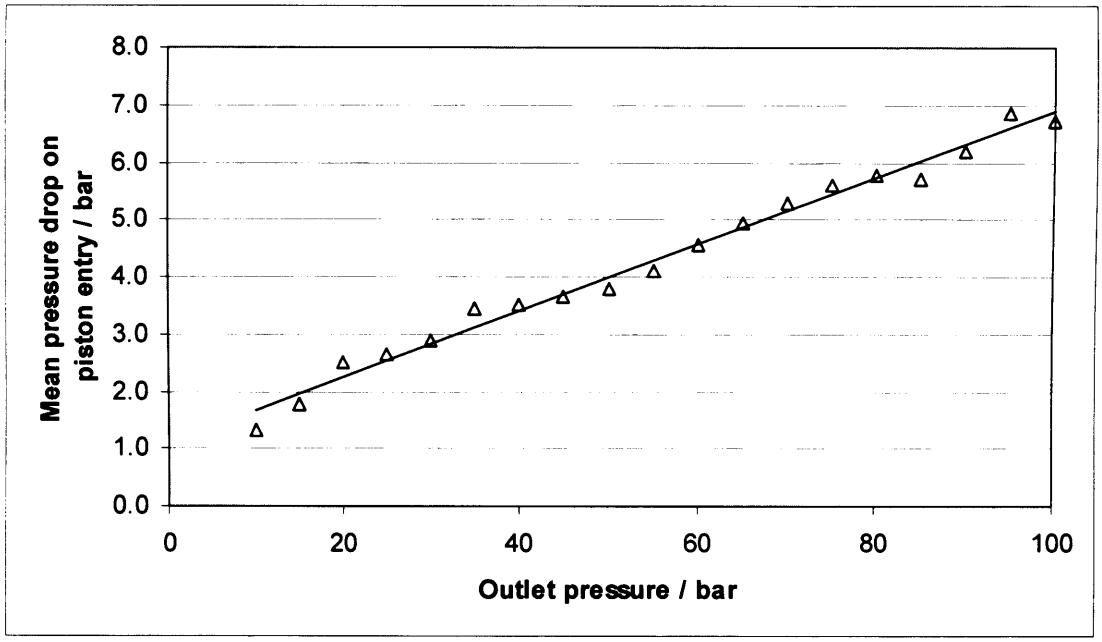

Figure 3.34 Pressure drop upon piston entry to outlet port

Shown in Figure 3.35 is a pressure transient indicating the arrival and exit angles of pistons moving through the inlet port. Of interest is the apparent increase in pressure which occurred when a cylinder moved through the inlet region of the pump. This pressure increase was found to be proportional to the outlet pressure, as shown in Figure 3.36.

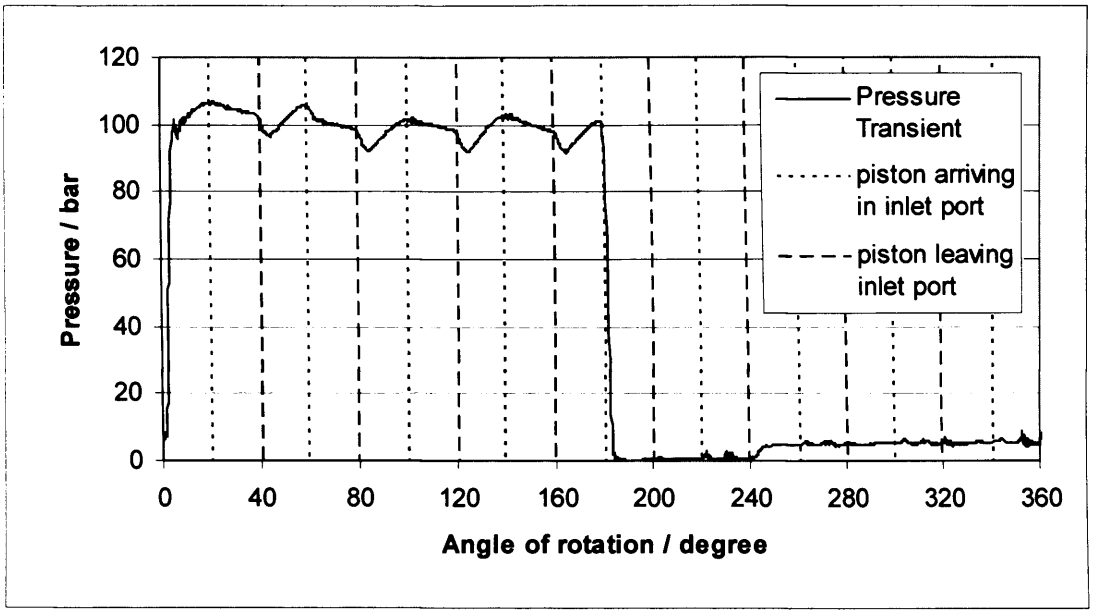

Figure 3.35 Pressure transient with piston entry and exit from inlet port

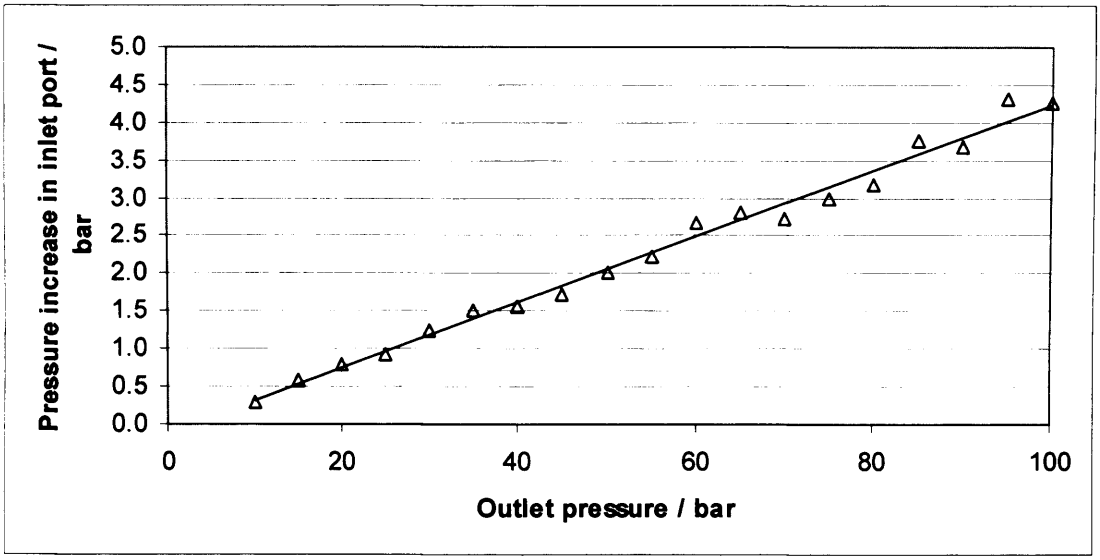

Figure 3.36 Pressure increase measured at a rotation of 240° in the inlet port

The cause of this pressure increase was not established; however it is possible that it was caused by fluid bleeding from the discharge port. A potential cause of this is vibration due to imbalance of the cylinder barrel.

From the pump output and external leakage characteristics shown in Figure 3.22 and Figure 3.23 respectively, the inlet flow to the pump and hence overall volumetric efficiency could be determined. Due to flow continuity, the flow into the pump is governed by Equation (3.5).

$$Q_{in} = Q_{out} + Q_e \tag{3.5}$$

Where: Q_{in} is the inlet flow rate, Q_{out} is the outlet flow rate, and Q_e is the external leakage from the pump. The resulting inlet flow rate is shown in Figure 3.37. The volumetric efficiency of the pump, calculated using Equation (3.6), is shown in Figure 3.38.

$$E_V = \frac{Q_{out}}{Q_{in}} x100\% \tag{3.6}$$

The volumetric efficiency of the pump was observed to reduce, with an increase in outlet pressure. This was clearly due to the increase in external leakage from the pump, but also due to an increase in internal leakage.

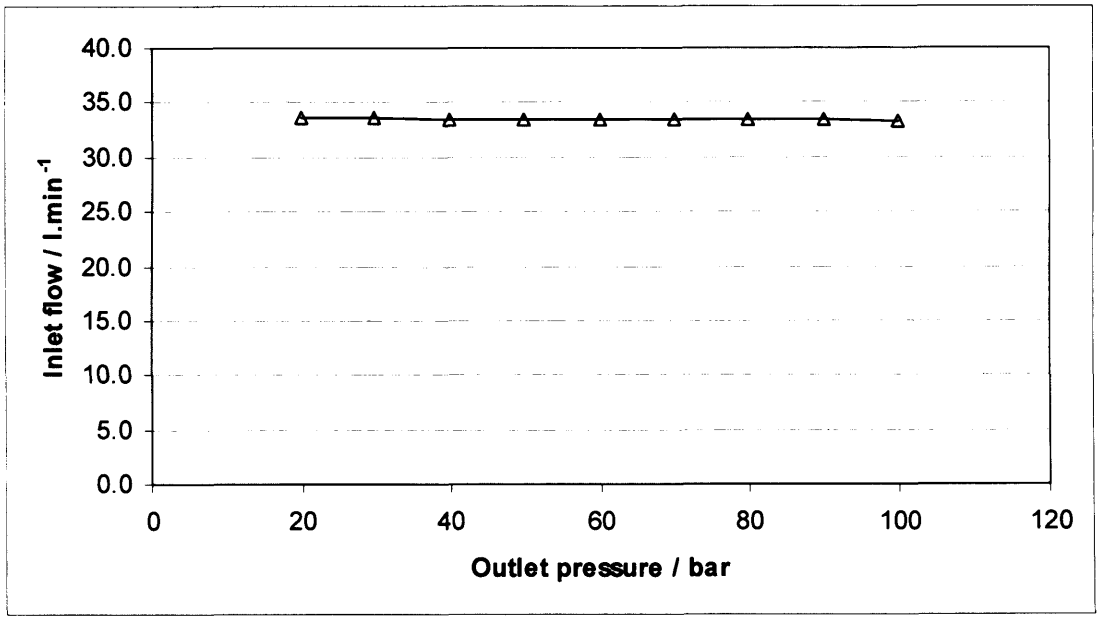

Figure 3.37 Calculated pump inlet flow

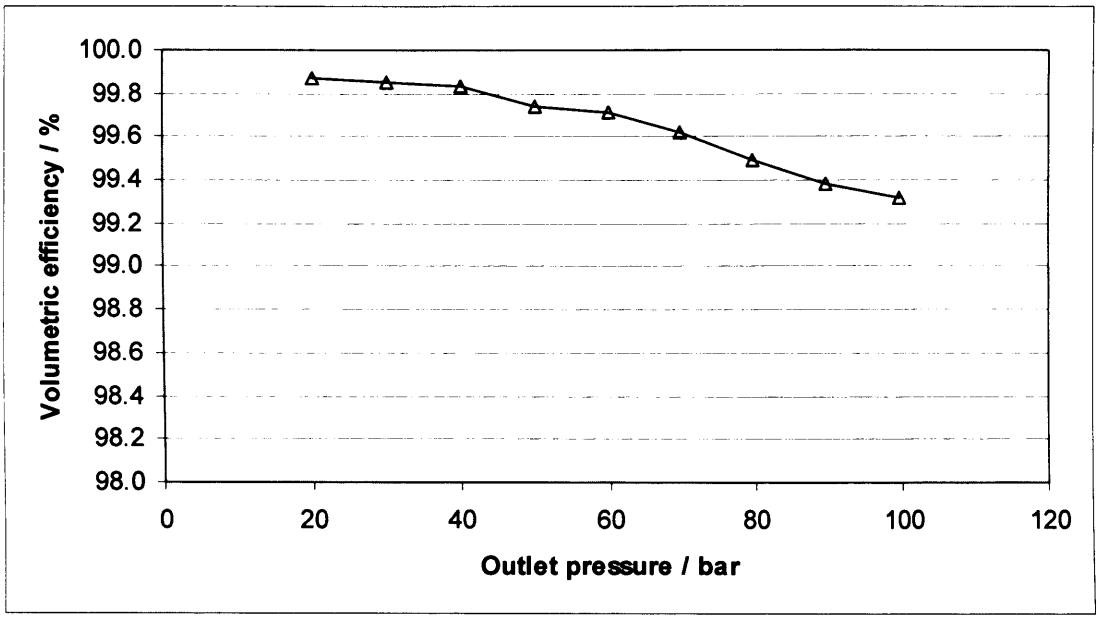

Figure 3.38 Volumetric efficiency of pump

The internal leakage within the pump cannot be measured experimentally. However, a set of equations developed by Watton [85], can be used to estimate the internal leakage. These equations assume that leakage rates are proportional to the pressure differentials producing them.

Figure 3.23 suggests that the external leakage from the pump may not follow a perfectly linear trend; however, a linear line of best fit can be applied to the figure for the data arrange obtained, providing a good approximation.

Shown in Figure 3.39 is a schematic diagram showing flows both into and out of the pump.

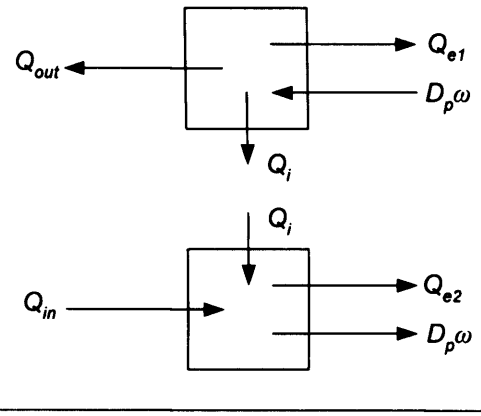

Label	Description
Q_{in}	Inlet flow
Q_{out}	Outlet flow
Q_i	Internal leakage
Q_{e1}	External leakage from high pressure side of pump
Q_{e2}	External leakage from low pressure side of pump
$D_p\omega$	Fluid transferred by piston bores

Figure 3.39 Schematic of pump flows

Both the high pressure and low pressure side are represented, and considering flow into and out of these regions, the following flow equations are generated:

$$Q_{in} = D_p\omega + Q_{e2} - Q_i \tag{3.7}$$

$$Q_{out} = D_p\omega - Q_{e2} - Q_i \tag{3.8}$$

Since it is assumed that flow is proportional to pressure differential, two resistance terms can be introduced, one for internal leakage, R_i, and one for external leakage, R_e. Thus, the leakage flows can be written as shown in Equations (3.9) to (3.11).

$$Q_i = \frac{(P - P_i)}{R_i} \tag{3.9}$$

$$Q_{e1} = \frac{P}{R_e} \tag{3.10}$$

$$Q_{e2} = \frac{P_i}{R_e} \tag{3.11}$$

By substituting Equations (3.9) and (3.10) into Equation (3.7), the following term for inlet flow is produced:

$$Q_{in} = D_p\omega + \frac{P_i}{R_e} - \frac{(P - P_i)}{R_i} \tag{3.12}$$

By substituting Equations, (3.9) and (3.11) into Equation (3.8), the following term for outlet flow is produced:

$$Q_{out} = D_p\omega - \frac{P}{R_e} - \frac{(P - P_i)}{R_i} \tag{3.13}$$

Subtracting (3.13) from Equation (3.12) produces an equation for Q_{leak}, the external leakage from the pump:

$$Q_{leak} = Q_{e1} + Q_{e2} \tag{3.14}$$

And finally substituting Equations (3.12) and (3.13) into Equation (3.14) provides an expression for the external leakage from the pump:

$$Q_{leak} = \left(\frac{P}{R_e}\right) + \left(\frac{P_i}{R_e}\right) \tag{3.15}$$

Thus, Equation (3.15) could be equated with the gradient of Figure 3.23, giving a value for R_e of 490.2 l.min^{-1}/bar.

Similarly re-arranging Equation (3.13) as shown in Equation (3.16) and equating with the gradient of Figure 3.22, the value for R_i could be found.

$$Q_{out} = D_p\omega - P\left(\frac{1}{R_e} + \frac{1}{R_i}\right) + \left(\frac{P_i}{R_i}\right) \tag{3.16}$$

This provided a value for R_i of 319.8 l.min^{-1}/bar. Thus using Equation (3.9), Figure 3.40 was produced. This suggests that at the maximum pressure tested, an internal leakage of approximately 0.3 l.min^{-1} occurred within the pump.

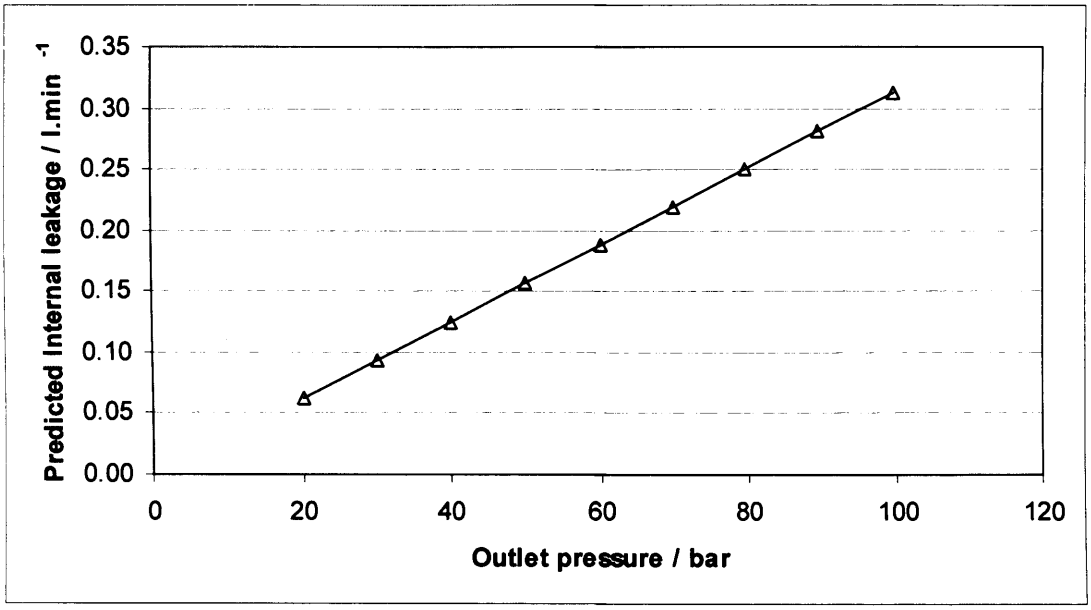

Figure 3.40 Calculated internal leakage

3.5.2 CFD analysis

From the 2-D axis-symmetric model, the leakage between a single piston and cylinder bore was modelled. The direction of flow was found to be largely dependent upon the velocity of the piston, and as such, the flow characteristic shown in Figure 3.24 closely resembled a sine-wave. Of interest is the fact that the flow could become negative, with oil flowing back into the piston chamber. This occurred during the discharge stroke despite the opposing outlet pressure of the pump, which independently tends to cause fluid to leak into the pump case. Further models were run with larger piston bore clearances. Under these conditions it was established that the negative flow reduced, as the pressure had an increased influence on the leakage. For a radial clearance of 24μm for example, the leakage was found to be largely in the direction of the pump case, except when the piston was at its maximum velocity on the delivery stroke, where a brief negative flow occurred as illustrated by Figure 3.41.

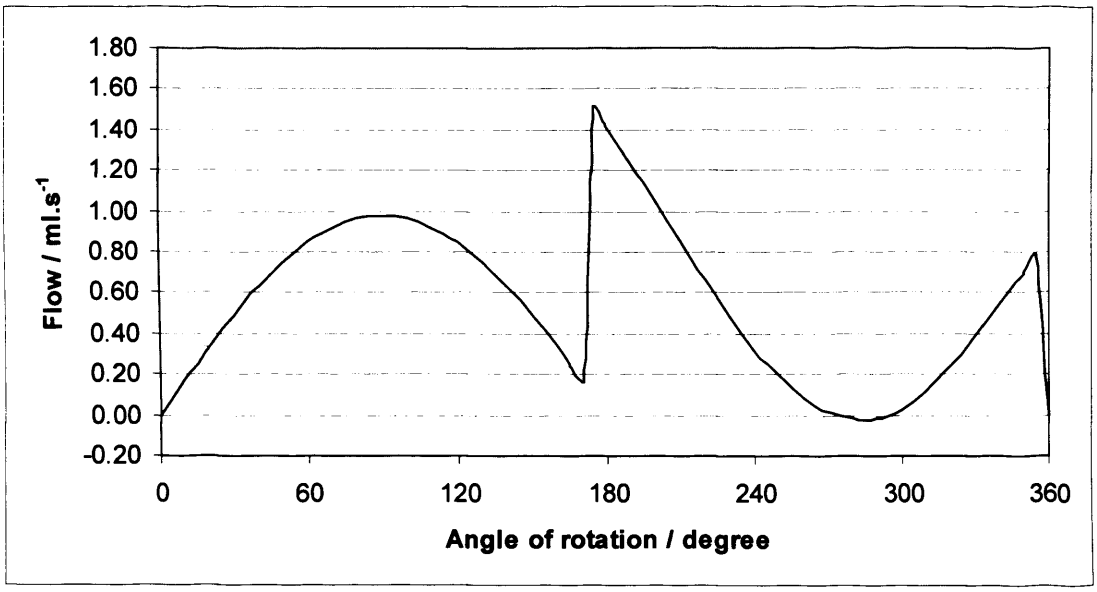

Figure 3.41 CFD derived piston / bore leakage at 24μm radial clearance

A comparison between the experimental and modelled volumetric efficiency of the pump is shown below in Figure 3.42. The efficiency was calculated from the full pump model, with the additional leakage from each piston (as shown in Figure 3.24), accounted for.

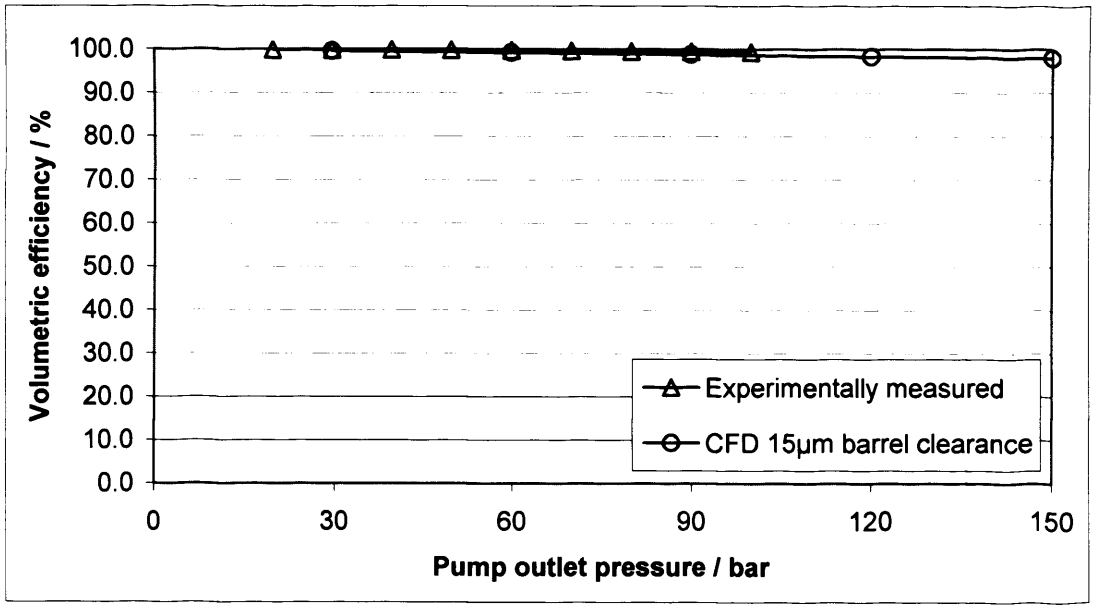

Figure 3.42 Volumetric efficiency of pump

The CFD simulations suggested a lower overall efficiency than the experimental study showed. The CFD simulations clearly suggested that the leakage between the port plate and cylinder barrel dominated the external leakage from the pump. This clearance was estimated based upon previous data from a similar pump.

Two further cylinder barrel clearances were simulated using the CFD pump model. The resulting volumetric efficiencies of the pump are shown in Figure 3.43. From this it is clear that a small deviation in cylinder barrel clearance can result in a significant change in port leakage and therefore overall pump efficiency.

The 12μm barrel clearance provided a higher volumetric efficiency. This value was closer to the experimental efficiency of the pump than the initial 15μm clearance. It is therefore likely that the cylinder barrel clearance within the pump was closer to 12μm, especially as the port leakage was seen to dominate the leakage from the pump.

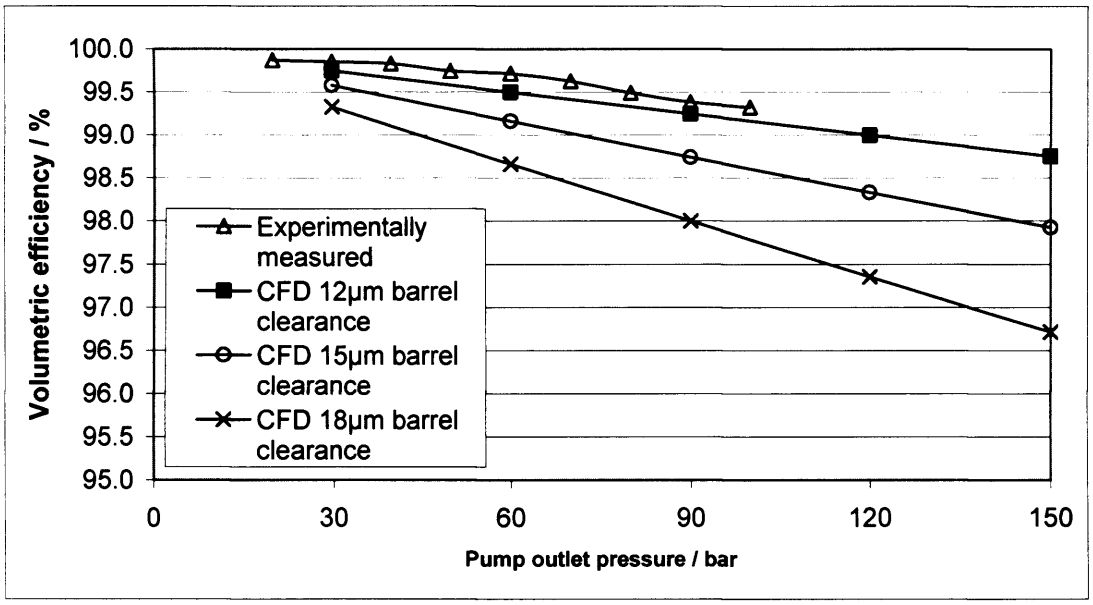

Figure 3.43 Volumetric efficiency with different varying cylinder barrel clearance

Contrary to the experimentally measured cylinder pressures, the CFD simulations did not show a reduction in pressure as a subsequent cylinder entered the discharge port. Cylinders entering the discharge port are at low pressure, and thus when a cylinder enters the region, the pressure in the other cylinders reduces as the pressures equalise.

The CFD model did not consider the compressibility of the oil, and thus the equalisation of pressure was instantaneous as a piston entered the discharge port. It should also be considered that the CFD model assumed that the cylinder was completely full of oil when it reached the discharge port. In reality this may have not have been the case, as air bubbles could have formed within the oil during the low-pressure suction stroke. A method of reducing the pressure ripple would be to add a boost pump in the inlet line. This would help to ensure that the cylinders were full of oil upon entry to the discharge port. The CFD model indicated that caviation occurred between the suction and discharge ports. This would also contribute to the pressure ripple identified in the discharge port.

3.6 Conclusions

The work in this chapter led to the following conclusions being drawn:

1. An experimental analysis of the pressure within an individual cylinder bore identified a pressure fluctuation whilst a cylinder was in the discharge port. This fluctuation was attributed to a pressure equalisation when subsequent pistons entered the discharge port.

2. A two-dimensional model of a single piston was effective in replicating the flow of fluid between a cylinder and its bore. It was discovered that the velocity of the piston was dominant in its influence over the direction of flow. As such, negative flow was identified under certain conditions. This flow occurred during the discharge stroke of the piston even with a high operating pressure opposing the negative flow direction. The negative flow was reduced by a larger piston clearance; however flow back into the cylinder is not undesirable as it reduces the overall leakage from the piston.

3. A three-dimensional CFD model of an axial piston pump was successfully developed using a porous mesh technique for modelling small clearances. This model incorporated cylinder barrel leakage as well as leakage through the pistons. Combined with the 2-D model, this allowed all major leakage paths from the pump to be modelled

4. The CFD model suggested that cavitation occurred between the suction and discharge port. This was not evident during the experimental analysis, probably due to the compressibility of the oil and the locality of the pressure transducers.

5. Previous experimental data from a similar pump was used for the cylinder barrel clearance. This provided a good estimate as the volumetric efficiencies determined experimentally and via CFD analysis correlated well. It was established that the cylinder barrel leakage dominated the overall pump leakage, and therefore had a considerable influence on the overall pump efficiency. A clearance of 12μm rather than the initially used value of 15μm provided a better agreement with the experimentally measured efficiency.

Chapter 4. Experimental Study of Slipper Behaviour

4.1 Introduction

Previous experimental and theoretical analyses of slipper bearings were predominantly based on slippers with a single land. Thus, the behaviour of slippers without a groove is well understood. Experimentally, the operation of slippers has been thoroughly examined. Multiple displacement transducers, mounted in a swash plate have been used to measure the clearance and tilt of a slipper operating in an actual pump [47, 62]. This quantified the momentary operating clearance of a slipper as it passed through the centre of the high pressure region of a pump. Yamaguchi used similar sensors located in the land of the slipper to provide a continuous measurement of slipper clearance [86].

Subsequent research concentrated on either replicating, or controlling the operating conditions of a slipper, and thus analysing the operation in specially designed test apparatus. The use of a rotating swash plate was the usual method of reproducing the relative motion between the slipper and swash plate surface. Additionally, mounting transducers in the swash plate was the sole method used for measuring displacement [37, 61, 63-66]. The pressure at different radial locations of a slipper has been measured for static conditions and the leakage of lubrication fluid has also been measured for static conditions [68, 69].

Leakage between the barrel and port plate, and around the peripheral of the pistons makes the measurement of slipper leakage impossible in an actual pump. In addition, there was no evidence to suggest that the measurement of leakage under dynamic conditions had been successfully accomplished in a fabricated test apparatus prior to

this study. Furthermore, no experimental studies have focused on the characteristics of a slipper with multiple lands.

The work in this chapter aims to characterise a two-land slipper operating over a range of conditions. A test apparatus consisting of a rotating swash plate and fixed slipper was developed. Eddy current displacement sensors, to measure separation, were mounted around the peripheral of the slipper in a manner that did not affect the flow of oil across the face of the slipper. The test apparatus designed and manufactured provided the capacity to measure slipper clearance and angle of tilt, leakage rates of lubrication fluid, and the pressure at four locations within the groove. Modifications were made to the test rig in an attempt to measure the lift that the slipper created.

The piston and slipper assembly that initiated this study is shown in Figure 4.1. The face of the slipper contains two lands, divided by a groove. Its dimensions are shown in Table 4.1.

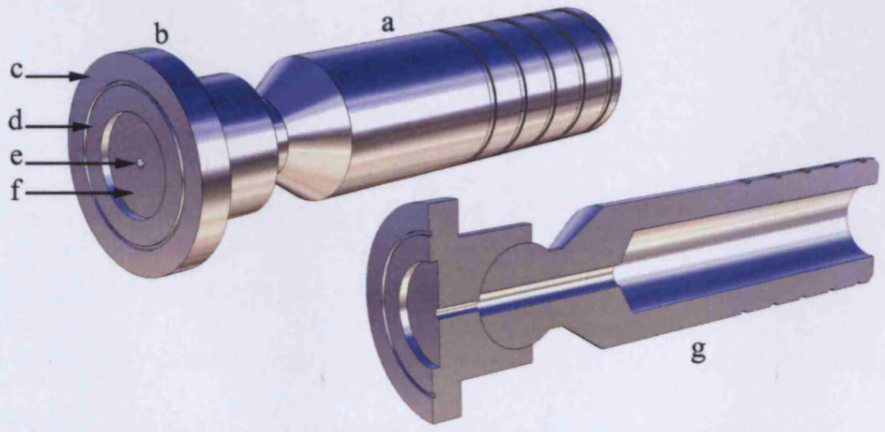

(a) piston, (b) slipper, (c) outer land, (d) inner land, (e) lubrication orifice, (f) pool, (g) sectioned view

Figure 4.1 Piston assembly with multi-land slipper

Table 4.1 Slipper dimensions

Measurement	**Dimension**
Lubrication orifice diameter	1.0mm
Pool diameter	10.15mm
Groove Diameter minimum	14.7mm
Groove Diameter maximum	15.7mm
Groove depth	0.4mm
Slipper overall diameter	20.5mm

4.2 Materials and Methods

4.2.1 Test apparatus

The following section describes the main components within the test apparatus as well as the main considerations taken during its development.

The apparatus consisted of a fixed slipper, with a rotating plate replicating the relative motion between the face of the slipper and the swash plate. A fixed slipper and moving swash plate were employed for several reasons, the foremost being that they enabled the required instrumentation to be attached in a simple manner. A single slipper rotating at speeds of up to 1500 rpm was expected to exhibit a high level of unbalance. This would potentially lead to vibration levels which could compromise the small clearances between the slipper and swash plate. The size of the slipper required to allow instrumentation to be connected would have only amplified this problem. Furthermore, making adjustments to the position of the slipper during operation would be impossible with a rotating slipper. Other considerations were the resources available to manufacture the test apparatus.

A means of controlling the slipper's location above the swash plate was developed, and instrumentation mounted on the slipper allowed the precise measurement of the clearance between the slipper face and swash plate. The components were fabricated from stainless steel and aluminium and a photograph of the test apparatus is shown in Figure 4.2. The materials selected for manufacture were partly as a result of the instrumentation requirements; however they also made the apparatus suitable for

further research into water-based hydraulic fluids. Photographs of the individual components within the apparatus are presented in Appendix A.3.4.

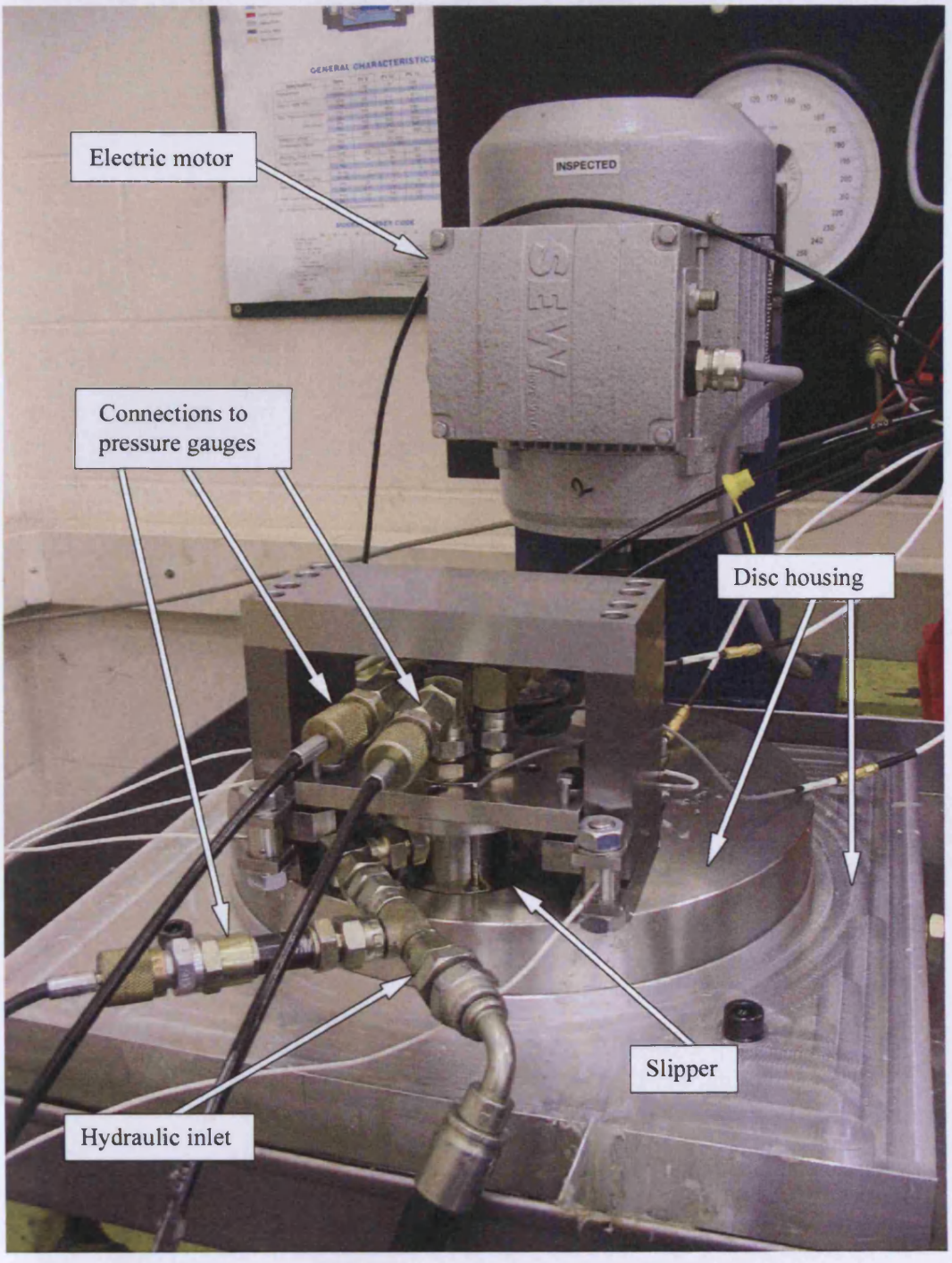

Figure 4.2 Experimental test apparatus with force measurement capability

A cut-away view of the test apparatus, showing the bearing assemblies and swash plate is shown in Figure 4.3

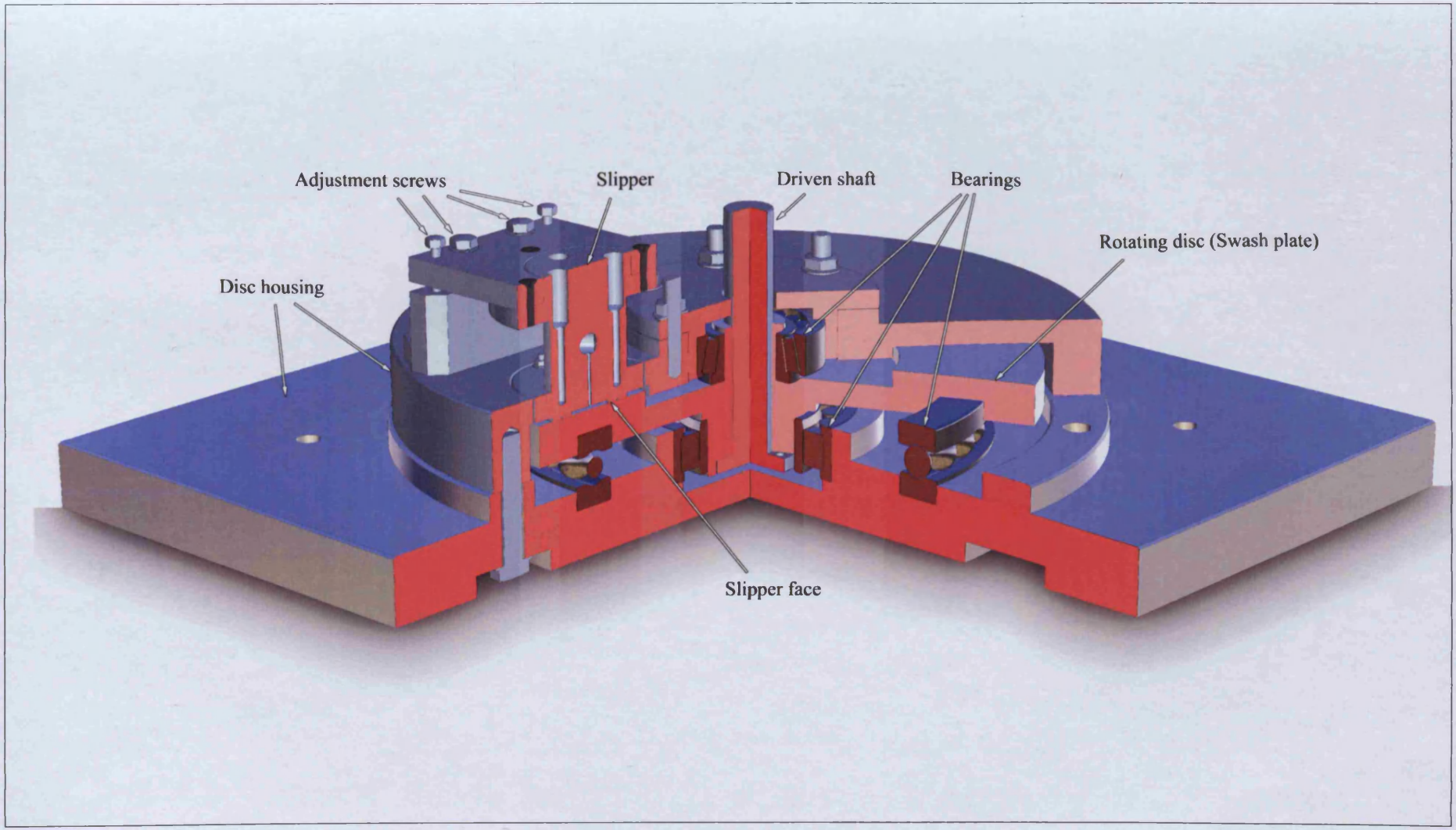

Figure 4.3 Sectioned view of hydraulic test rig

To ensure a continuous clearance between the slipper and swash plate, a high level of accuracy during manufacture was required. The accuracy of machining, and the components available were considered during the design of the test apparatus, and influenced the way in which it was developed. Of high importance was the stability of the rotating disc, both in terms of rigidity under load, and its axial run-out.

Run-out, the variation of axial location of the disc during rotation, was minimised by utilising three bearings. A thrust bearing underneath supported the disc in a vertical direction. This bearing also ensured that the disc could not move axially once hydraulic pressure was applied to the slipper. A roller bearing was used in conjunction with the thrust bearing, since the thrust bearing provided no radial support for the disc. This roller bearing was non-locating axially, and so ensured that all of the axial loads were supported by the thrust bearing. In addition, the swash plate was designed so that the bearing surfaces and face of the plate could all be machined without removing the plate from the lathe. This assisted in ensuring that all surfaces were parallel, minimising the potential of axial run-out.

A tapered roller bearing mounted above the disc provided additional radial support, but more significantly, enabled an axial preload to be applied to the thrust bearing. This preload was applied through a steel bearing flange, by tightening six lock-nuts onto studs mounted in the upper cover plate. The tapered roller bearing also provided radial support for the drive system. The races of all three bearings could be separated enabling easy assembly and disassembly of the rig. Calculations for the expected life of each bearing are presented in Appendix A.3.3.

4.2.1.1 The slipper

The slipper manufactured for use within the test apparatus was a 2:1 scale reproduction of the slipper found in the PVWH15 pump, and is shown in Figure 4.4. Although larger than the slippers within the pump which initiated this study, this size of slipper is not uncommon in larger pumps.

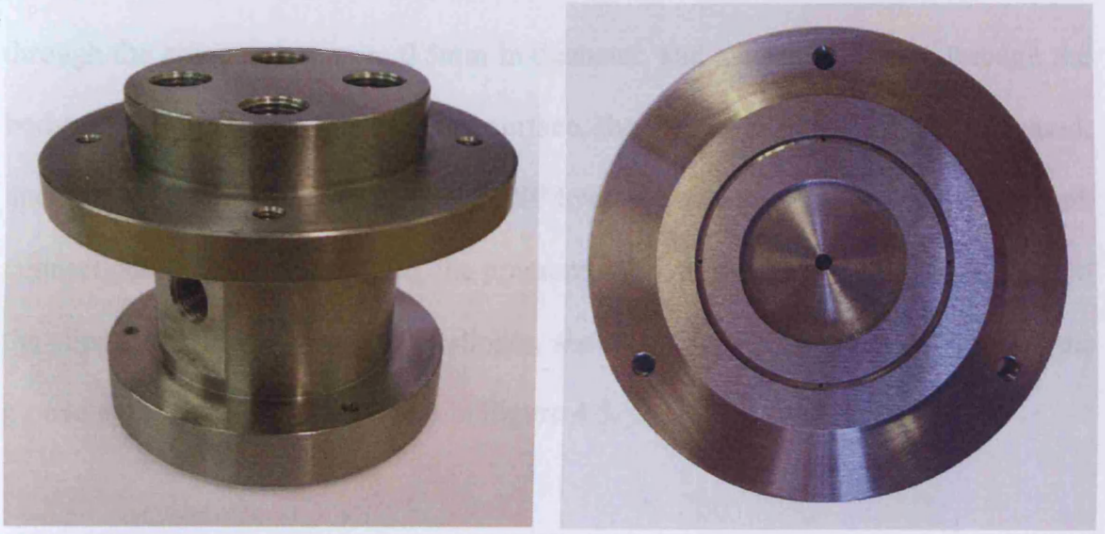

Figure 4.4 a: Slipper with hydraulic connections b: Slipper face

The full dimensions of the slipper face are shown below in Table 4.2.

Table 4.2 Test slipper dimensions

Measurement	**Dimension**
Inlet diameter	2.0mm
Pool diameter	20.3mm
Pool depth	1.4mm
Groove Diameter minimum	29.4mm
Groove Diameter maximum	31.4mm
Groove depth	0.8mm
Slipper outside diameter	41.0mm
Transducer mounting diameter	52mm P.C.D.

The slipper face resembled that of the actual slipper: It had a central hole through which hydraulic oil could flow, a central pool, and two lands divided by a groove. The remainder of the slipper was designed so that the required instrumentation could be installed and the slipper itself could be held and positioned appropriately above the rotating disc. In order to measure the pressure within the groove, holes were drilled through the slipper body, from the groove to the top surface. Where these holes broke through the groove, they were 0.5mm in diameter, and increased to 4mm through the body of the slipper. Close to the top surface, the diameters of these holes increased, and they were threaded to enable 1/8" BSP hydraulic fittings to be attached. Four such connections were made, enabling the pressure to be measured at the four quadrants of the slipper. A section through the slipper, showing two of the four holes joining the groove to the top surface, is shown in Figure 4.5.

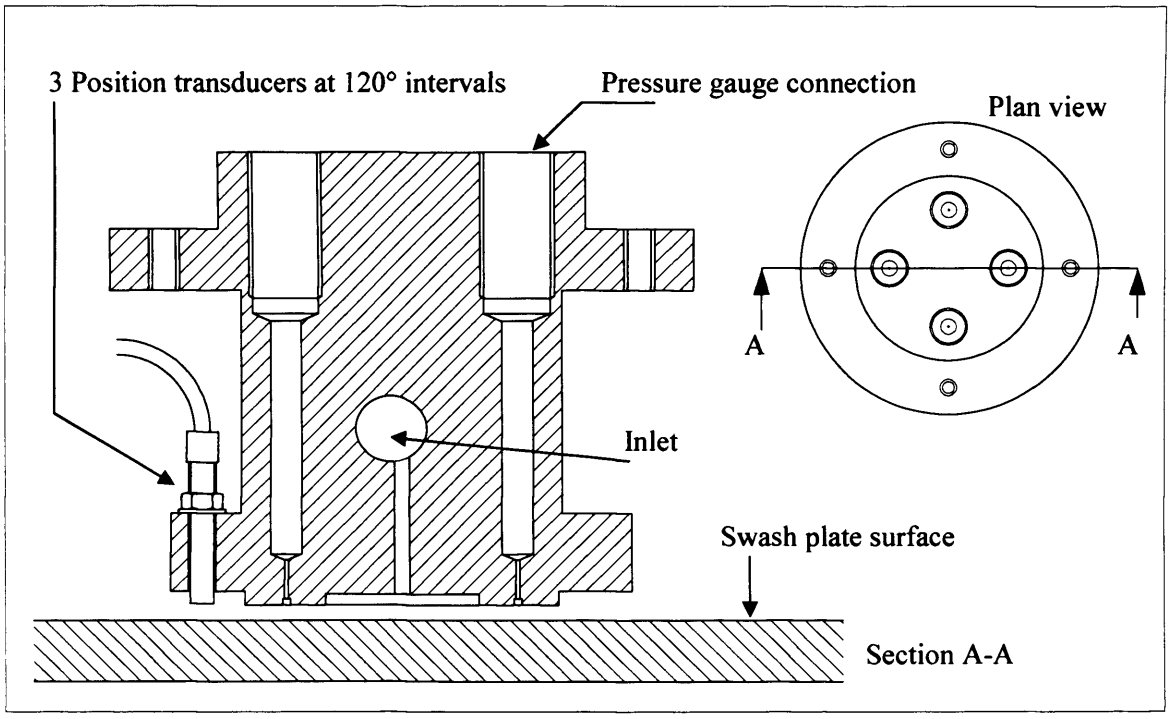

Figure 4.5 Cross section of slipper

At the top of the slipper was a flange which enabled the slipper to be mounted to the tilting mechanism. For space considerations, the hydraulic inlet was placed on the side of the slipper. This inlet connected to a 2mm diameter vertical hole running through the centre of the slipper. This hole connected to the pool in the centre of the slipper face.

Three precision Micro-Epsilon displacement transducers were mounted around the peripheral of the slipper on a flange recessed by 1.8mm. Mounting the transducers in this manner ensured that they did not affect the flow of oil across the slipper face. In addition, recessing the flange ensured it did not have any significant influence on oil emerging from the edge of the slipper. The displacement transducers were located at 120° intervals around the slipper. The three displacement transducers were sufficient to enable the angle of tilt and clearance of the slipper to be determined.

4.2.1.2 Slipper positional adjustment

The slipper was mounted under a rectangular plate, supported at either end by brackets fixed to the main body of the apparatus. The relative movement between the rectangular plate and the brackets provided the required movement of the slipper. This movement was controlled by pairs of opposing screws located in each corner of the rectangular plate. The outermost screw was threaded into the rectangular plate. The end of this screw impinged on the fixed bracket and tended to lift the slipper when tightened. Conversely, the inner screw of each pair was threaded into the bracket, and thus pulled the rectangular plate, and hence slipper, down when tightened. By careful adjustment of each pair of screws, the height of each corner of the plate could be precisely controlled, and therefore both the height and angle of the slipper, relative to

the swash plate, could be adjusted. A sectioned view of the slipper and tilting mechanism is shown below in Figure 4.6. In this view, the slipper assembly brackets and rig chassis are sectioned, revealing the swash plate beneath. Two of the four pressure monitoring points and the hydraulic inlet are sectioned. Two of the three displacement sensors are shown at the base of the slipper.

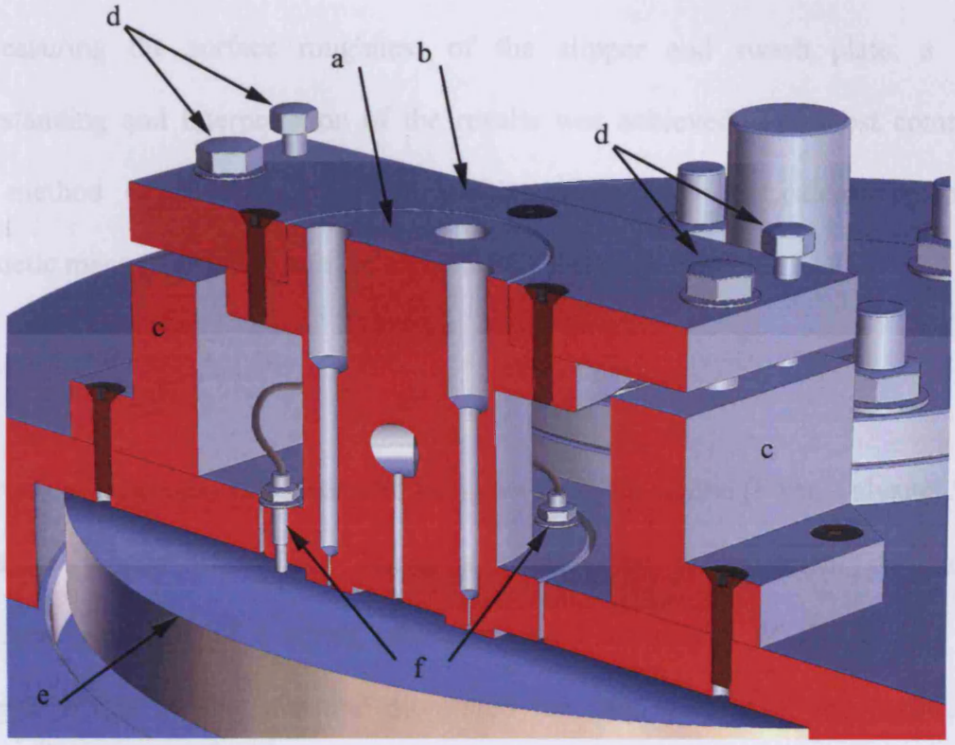

(a) slipper, (b) tilting plate, (c) mounting brackets, (d) adjustment screws, (e) swash plate, (f) position transducers (2 of 3).

Figure 4.6 Slipper assembly sectional view

Initially, the apparatus utilised 4mm diameter bolts to retain the slipper plate. The pitch of these screws (0.7mm) made these the original choice as it was envisaged that they would provide the highest level of control over the adjustment of the slipper. After preliminary tests, these bolts were replaced by 6mm diameter bolts, which although having a courser pitch (1.0mm), deformed far less under load. They were also easier to adjust than the 4mm bolts under load. The bolts that lift the slipper were

kept at the original 4mm as they were not load bearing under operation. It was deemed that the combination of the two sizes of bolts would ensure that a high level of control would be maintained over the position of the slipper. The load-extension characteristics for the 4mm and 6mm screws are shown in Appendix A.3.2.

4.2.1.3 Surface roughness

In measuring the surface roughness of the slipper and swash plate, a better understanding and interpretation of the results was achieved. The most commonly used method of classifying surface roughness involves the calculation of the arithmetic mean (Ra) of the surface asperities as shown in Equation (4.1).

$$R_a = \frac{1}{n}\sum_{i=1}^{n}|y_i| \tag{4.1}$$

The average roughness was measured using a Talysurf machine (Form Talysurf Series 2, Taylor-Hobson Ltd., UK). Being a contact-type measurement device, the instrument consisted of a stylus which followed the profile of the surface as it traversed across it. The machine monitored the displacement of the stylus, thus enabling the average roughness, Ra, to be determined. Five sets of measurements were taken from both the slipper and the disc: The sample length used for the slipper measurements was 4mm, with the disc measurements being 40mm long. The Ra value for each test was then calculated using Equation (4.1). The mean Ra value was then determined for each data set.

4.2.2 Instrumentation

4.2.2.1 Slipper to swash plate clearance measurement

The position sensors used to measure the clearance between the slipper and swash plate work on the eddy current principle. Each consisted of a coil cast in the sensor

housing. In operation, a high frequency alternating current flows through this coil, inducing a magnetic field. When a conductive target material is placed within proximity of the magnetic field, eddy currents are induced within it. The resulting eddy currents produce an alternating magnetic field of their own, and these attenuate the magnitude of the sensor's magnetic field. This attenuation is increased as the target material is moved closer to the sensor, and hence if the changes in current within the sensor are evaluated, the proximity of the target can be determined. According to the manufacturer, Micro-Epsilon, they work most effectively with a target made from a non-ferrous material [87], and hence the swash plate, which was the target, was constructed from aluminium. Each sensor was supplied with signal conditioning electronics which, once calibrated, provided a linear displacement – voltage relationship. The system was insensitive to temperature effects which also made it ideal for this application, where moderate temperatures were expected.

4.2.2.2 Calibration of sensors

Each sensor was calibrated using a digital micrometer calibration device shown in Figure 4.7. This utilised a threaded housing for the sensor which is shown on the left side of the figure. Adjacent to this was an aluminium target fastened to a non-rotating micrometer spindle. Each sensor was calibrated with an initial offset. This ensured that a false reading did not arise due to the sensor contacting the target. Additionally it ensured mechanical damage did not occur to the face of the sensor. Due to the linear relationship between target distance and output voltage, this offset did not affect the calibration, as it was the increase in voltage relative to the increase in distance that was of significance.

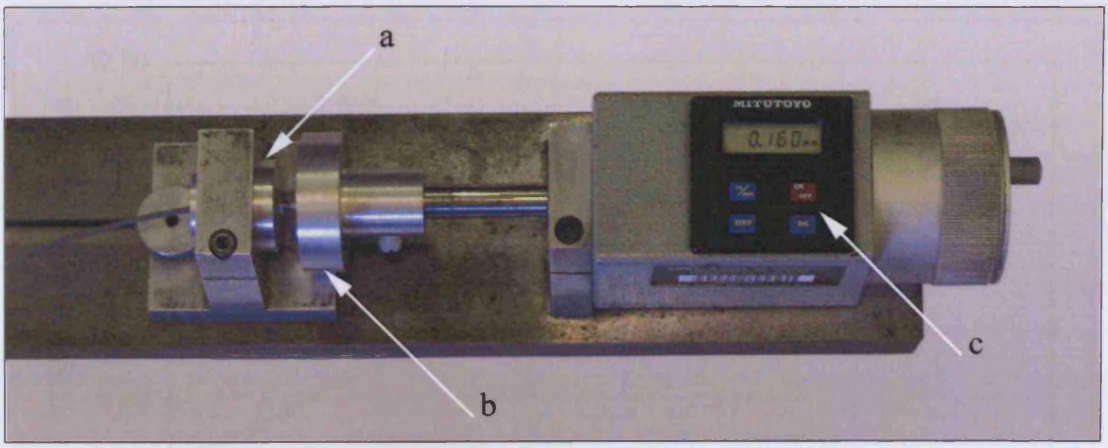

(a) transducer and mounting, (b) aluminium target, (c) digital micrometer

Figure 4.7 Calibration of eddy current sensor

Once each sensor was calibrated, it was installed in the slipper and the calibration was confirmed within the test apparatus by lifting the slipper using shims of varying thickness, and checking the change in output voltage. To avoid interference between the three transducers, synchronisation cables were used between each set of signal conditioning electronics.

The calibration curve for one of the sensors is shown below in Figure 4.8. A linear displacement – voltage relationship is displayed, with output voltage varying between 0V and approximately 10V for a displacement of 500μm. The calibration curves for the remaining two sensors are shown in Appendix A.3.1. All three sensors displayed excellent linearity characteristics. The accuracy of instrumentation to measure the small clearances between the slipper and swash plate was of prime importance. According to the manufacturer, the sensors had an accuracy of ± 0.5μm, with an effective working range of 0 - 500μm.

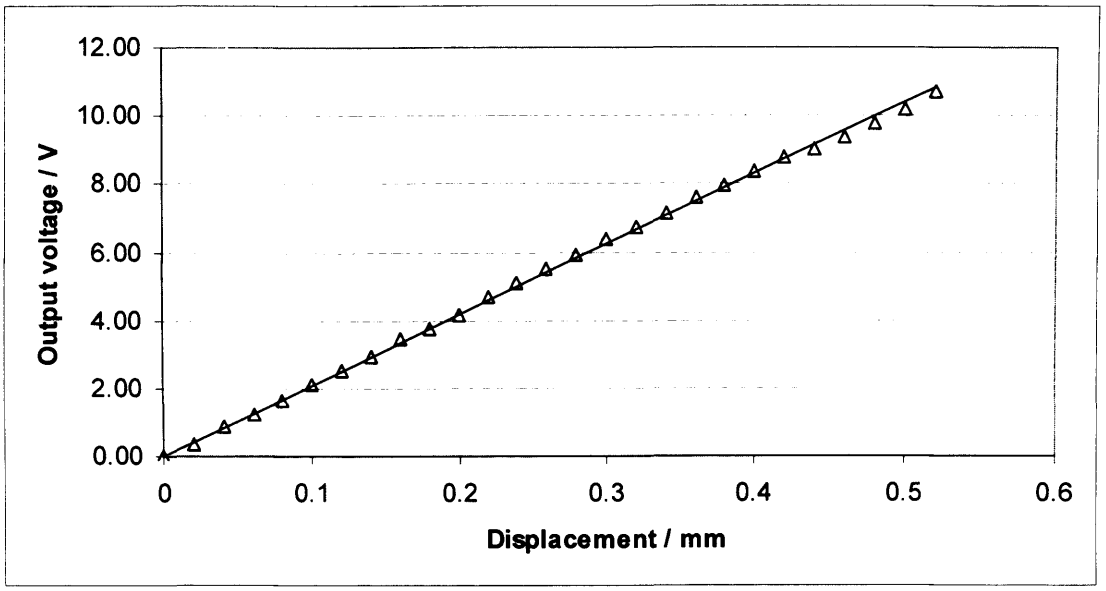

Figure 4.8 Calibration curve for eddy current displacement sensor (Serial # 25266)

4.2.2.3 Installation of sensors

It was accepted that eddy current displacement sensors may be influenced by an adjacent metallic object rather than just the target [87]. Thus the sensors had to slightly protrude beyond a metallic sensor mount, in this case the mounting on the slipper. Additionally, no metallic material could be within a diameter equal to three times the sensor diameter. Since the diameter of the sensor tip is 2mm, a metal free area of 6mm in diameter was required. Both of these specifications were followed during the design of the slipper. Once installed in the test rig, the eddy current sensors were used to measure the run-out of the disk. This was achieved by lowering the slipper within close proximity to the disc and rotating it with the hydraulic fluid disconnected. By determining the fluctuation in readings of the outer most sensor, the maximum run-out was measured to be 11μm. The variation in run-out around the peripheral of the disc is shown in Figure 4.9. The magnitude of run-out was confirmed using a contact type dial gauge with the slipper assembly removed.

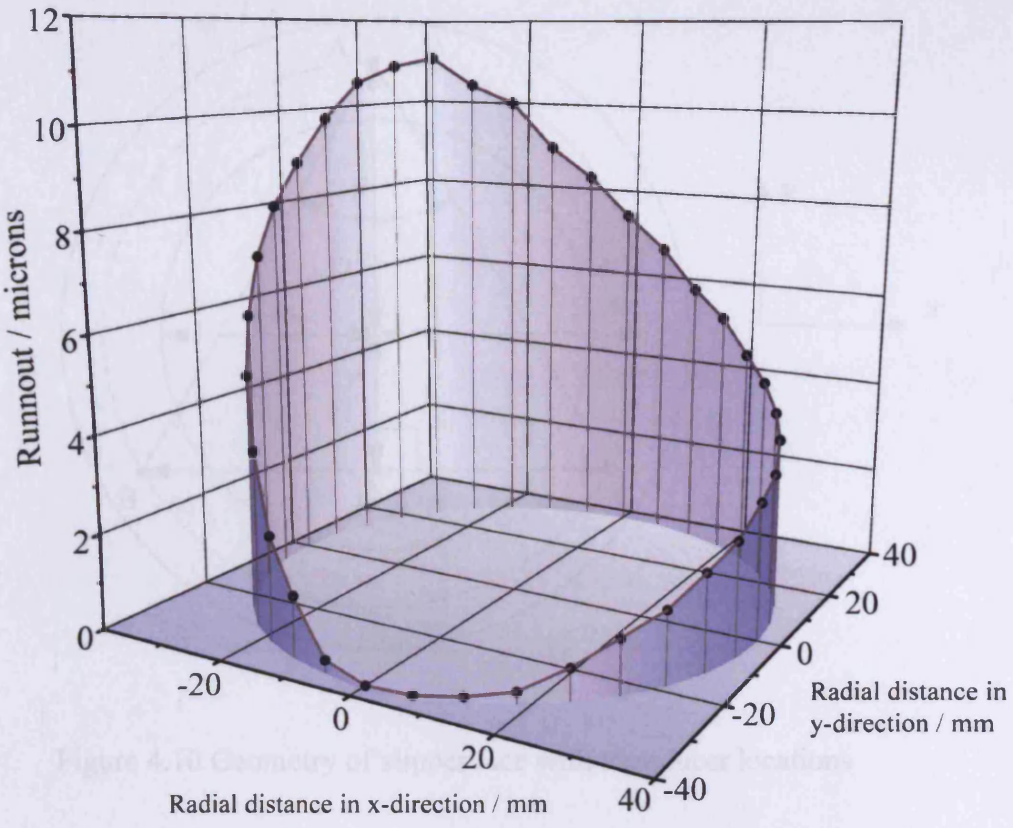

Figure 4.9 Run-out around peripheral of disc

4.2.2.4 Determination of slipper position and angle of tilt

The calculations performed to determine the proximity and angle of the slipper from the output voltages of the three displacement sensors are detailed below.

Figure 4.10 is a plan view of the slipper, and shows the location of the three displacement transducers labelled A, B and C. Table 4.3 contains details for each dimension and angle labelled.

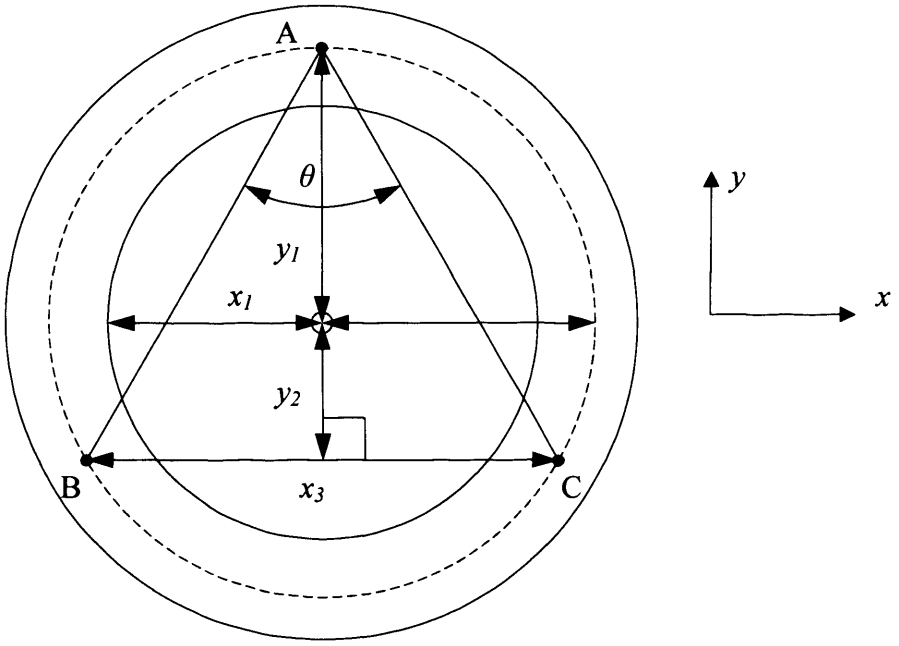

Figure 4.10 Geometry of slipper face with transducer locations

Table 4.3 Explanation of labels and dimensions

Symbol	**Parameter**	**Value**
A	Sensor	N/A
B	Sensor	N/A
C	Sensor	N/A
θ	Angle between sensors	60 °
x_1	Radius of slipper face	20.5 mm
x_2	Radius of sensor array	26.0 mm
x_3	Distance from sensor B to sensor C	See Eqn. 4-6
y_1	Distance from centre of slipper to sensor A	26.0 mm
y_2	Distance from centre of slipper to sensors B and C	13.0 mm

Figure 4.11 and Figure 4.12 illustrate the slipper in a tilted position, with the swash plate represented by the x and y axis in each figure. For ease of explanation, the magnitude of the clearance and angle of tilt in each diagram is exaggerated.

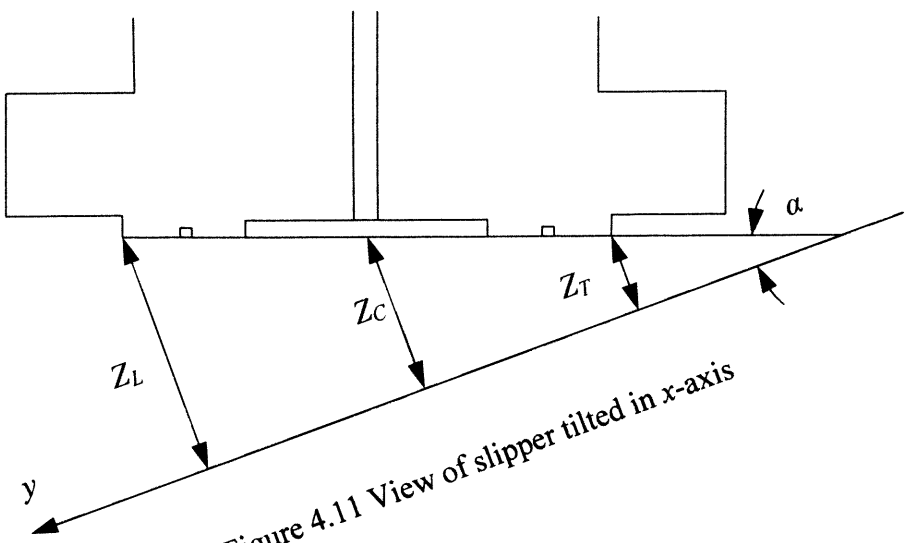

Figure 4.11 View of slipper tilted in x-axis

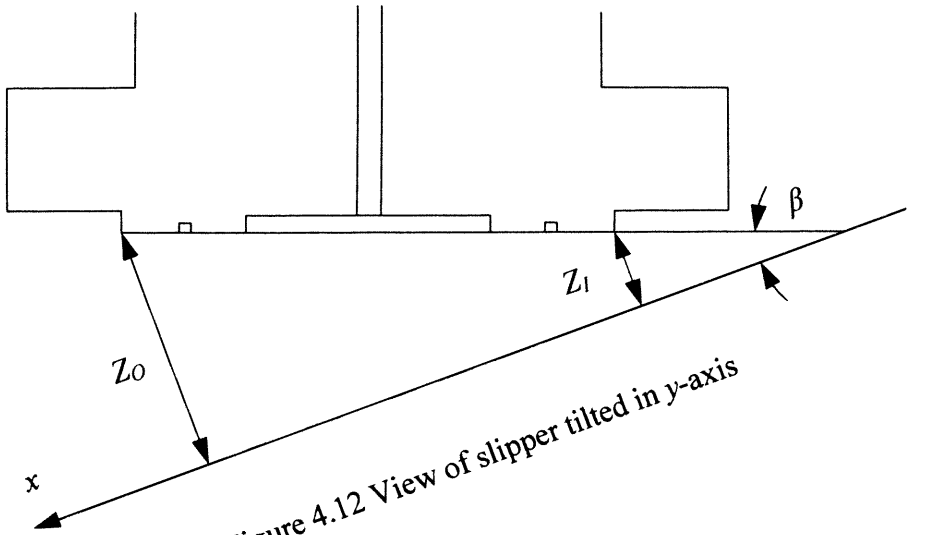

Figure 4.12 View of slipper tilted in *y*-axis

The measurements and angles identified in Figure 4.11 and Figure 4.12 are outlined in Table 4.4.

Table 4.4 Clearances and angles

Symbol	Parameter	Unit
Z_L	Leading edge clearance	μm
Z_T	Trailing edge clearance	μm
Z_O	Outside edge clearance	μm
Z_I	Inside edge clearance	μm
Z_C	Central clearance	μm
α	Angle of tilt about x-axis	degree
β	Angle of tilt about y-axis	degree

All angles and displacements were determined from the change in the voltage output from the three transducers. Clearly the transducers did not come in to contact with the swash plate, even in the situation when the slipper face was resting on the swash plate. It is for this reason that initial voltage readings were measured, and subtracted from subsequent voltages when the slipper was separated from the swash plate. The transducers were installed so that a reading of approximately 4 volts was measured at the output of each. This meant that the face of each transducer was approximately 0.2mm away from the swash plate. This prevented accidental contact whilst ensuring that the remaining working range of each transducer, approximately 0.3mm, was sufficient. The calibration values obtained for the three transducers are shown in Table 4.5

Table 4.5 Calibration constants for displacement transducers

Transducer	Notation	Serial Number	Calibration / μm / Volt
A	C_A	25266	48.56
B	C_B	25267	46.91
C	C_C	25268	47.38

The notation used for the calibration constants and voltage readings is displayed in Table 4.6.

Table 4.6 Voltages and relative displacements

Symbol	Parameter	Unit
C_A	Calibration for Transducer A	μm / Volt
C_B	Calibration for Transducer B	μm / Volt
C_C	Calibration for Transducer C	μm / Volt
V_A	Voltage reading from transducer A	Volts
V_B	Voltage reading from transducer A	Volts
V_C	Voltage reading from transducer A	Volts
V_{A0}	Initial voltage reading from transducer A	Volts
V_{B0}	Initial voltage reading from transducer B	Volts
V_{C0}	Initial voltage reading from transducer C	Volts
T_A	Relative movement of transducer A	mm
T_B	Relative movement of transducer B	mm
T_C	Relative movement of transducer C	mm

Equations (4.2) to (4.4) show how the relative movement of each transducer was calculated by subtracting the initial voltage reading from the final reading. When multiplied by the corresponding calibration constant, this yielded the relative movement in millimetres. All angles and displacements were determined based upon these three relative displacements.

$$T_A = C_A(V_A - V_{A0})/1000 \tag{4.2}$$

$$T_B = C_B(V_B - V_{B0})/1000 \tag{4.3}$$

$$T_C = C_C(V_C - V_{C0})/1000 \tag{4.4}$$

Using Figure 4.11, α, the angle of tilt about the x-axis was determined. This was calculated using Equation (4.5) and resulted in Equation (4.6).

$$Sin\alpha = \frac{(T_A - (T_B + T_C)/2)}{(y_1 + y_2)} \tag{4.5}$$

$$\alpha = Sin^{-1}\frac{(T_A - (T_B + T_C)/2)}{(y_1 + y_2)} \tag{4.6}$$

Angle β, the angle of tilt about the y-axis, illustrated in Figure 4.12, was calculated using Equations (4.7) to (4.9).

$$x_3 = \sqrt{\left(x_2^2 - y_2^2\right)} \tag{4.7}$$

$$Sin\beta = \frac{\left(T_B - T_C\right)}{x_3} \tag{4.8}$$

$$\beta = \sin^{-1}\frac{\left(T_B - T_C\right)}{x_3} \tag{4.9}$$

Once the relative angles and displacements were determined, the displacements at the critical slipper locations could be determined. These were the clearance at the centre, leading edge, trailing edge, outside edge and inside edge as shown in Equations (4.10) to (4.14)

Central Clearance:

$$Z_C = 1000\left(\frac{\left(T_B + T_C\right)}{2} + y_2 \sin\alpha\right) \tag{4.10}$$

Leading edge clearance:

$$Z_L = Z_C + 1000\left(x_1 \sin\alpha\right) \tag{4.11}$$

Trailing edge clearance:

$$Z_T = Z_C - 1000\left(x_1 \sin\alpha\right) \tag{4.12}$$

Outside edge clearance:

$$Z_O = 1000\left(\left(\frac{T_2 + T_3}{2}\right) + \left(x_1 \sin\beta\right) + \left(y_2 \sin\alpha\right)\right) \tag{4.13}$$

Inside edge clearance:

$$Z_I = 1000\left(\left(\frac{T_2 + T_3}{2}\right) - (x_1 \sin\beta) + (y_2 \sin\alpha)\right) \tag{4.14}$$

Using this method of calculation, the magnitude of the initial reading of each transducer was insignificant. By placing the slipper flat on the swash plate, the three initial voltage readings were noted. The final voltage readings required to obtain each slipper position were then calculated, and during the experimental procedure, alterations were made to the adjustment screws, until the three displacement transducers gave the required readings, and hence the desired clearance and angle of tilt relative to the swash plate.

4.2.3 Hydraulic circuit

The hydraulic circuit used in conjunction with the slipper apparatus is shown schematically in Figure 4.13.

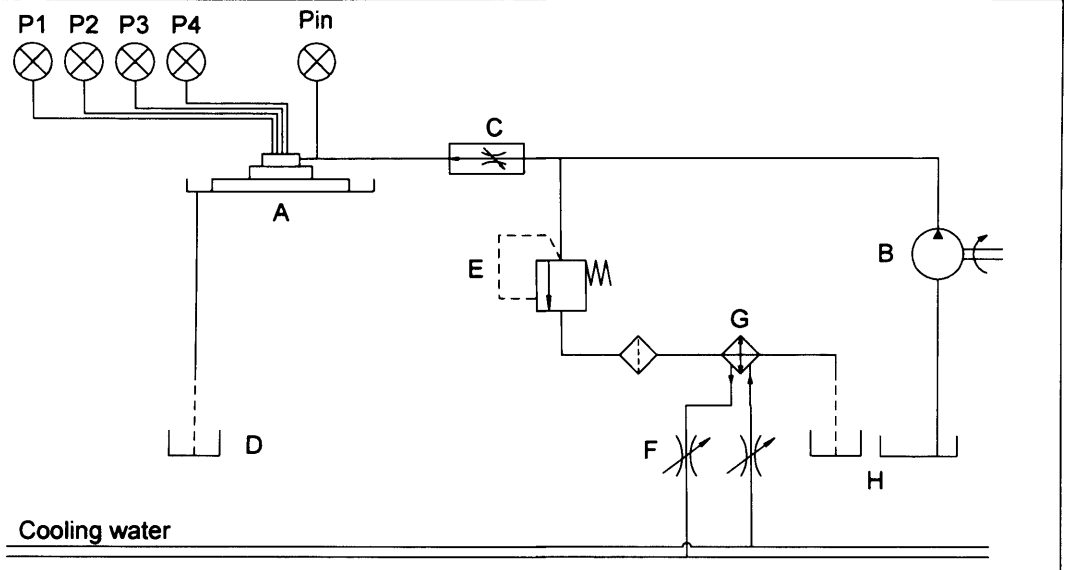

Label	Component
A	Hydraulic test apparatus
B	Gear pump providing hydraulic fluid
C	Flow control valve
D	Collected fluid from test apparatus
E	Pressure relief valve
F	Valves for cooling water
G	Heat exchanger
H	Main hydraulic tank
P_{in}	Pressure gauge at inlet to the apparatus
P_1, P_2, P_3, P_4	Pressure gauges for the four quadrants of the slipper

Figure 4.13 Hydraulic circuit

This circuit allowed the pressure supplied to the slipper face to be varied. Since the oil was circulated through a relief valve, the temperature of the oil was expected to rise over time. This heating effect was expected to be greater at higher operating pressures, and hence a variable cooling system was required. By regulating the flow rate of water through the heat exchanger, the cooling effect was controlled, and hence

the temperature of the oil could be maintained at a constant temperature of 40°C regardless of operating pressure and ambient room temperature.

4.2.4 Static tests

Initial tests concentrated on a static swash plate, and studied the leakage characteristics across the slipper at a range of clearances and angles of tilt. For all test conditions, a range of pressures were supplied to the inlet of the slipper. This set of tests enabled the hydrostatic lift generated by the slipper to be characterised. For each test, the pressure at each quadrant was recorded, as well as the temperature of the oil flowing into the apparatus. The oil flowing across the slipper face accumulated in a drip tray. This was collected in a measuring cylinder and its collection was timed using a stopwatch, thus enabling the flow rate to be determined. Static tests were carried out at clearances of 5, 10, 15, 20, 25, 30 and 50μm. For clearances of 5, 10, 15 and 20μm, several angles of tilt were studied, ranging from flat to fully tilted. For the tilted tests the leading edge of the slipper had a greater clearance than the trailing edge, whilst maintaining a continuous central clearance.

4.2.5 Dynamic tests

Dynamic tests on the slipper were carried out up to a maximum speed of 1400 rpm. A central clearance of 20μm was chosen for this, with tests for the slipper parallel to the swash plate, and inclined at an angle. As with the static tests, a range of supply pressures were used to find the slipper characteristics over a range of operating conditions.

4.2.6 Force measurement

The test apparatus was modified after the initial set of results was obtained. The modification was to enable four miniature load cells to be installed, to allow the lift

generated by the slipper to be measured. In order to incorporate the load cells, new mounting brackets were designed and manufactured. These utilised both the original mounting positions on the main chassis, and the original adjustment mechanism. The modified mounting bracket consisted of two parts. The first was screwed to the main apparatus chassis. The second part was attached to the slipper tilting plate via the four adjustment screws outlined in section 4.2.1.2. The load cells were situated between the two, with the end of each load cell passing through a hole in each mounting bracket, and being secured by nuts. This configuration meant that any load produced by the slipper was applied to the upper part of each bracket and transferred through the load cells. Figure 4.14 shows the load cells installed within the apparatus. The aim was to measure the lift generated by the slipper, as well as to calculate the torque generated by the slipper by taking moments using the four load cell readings.

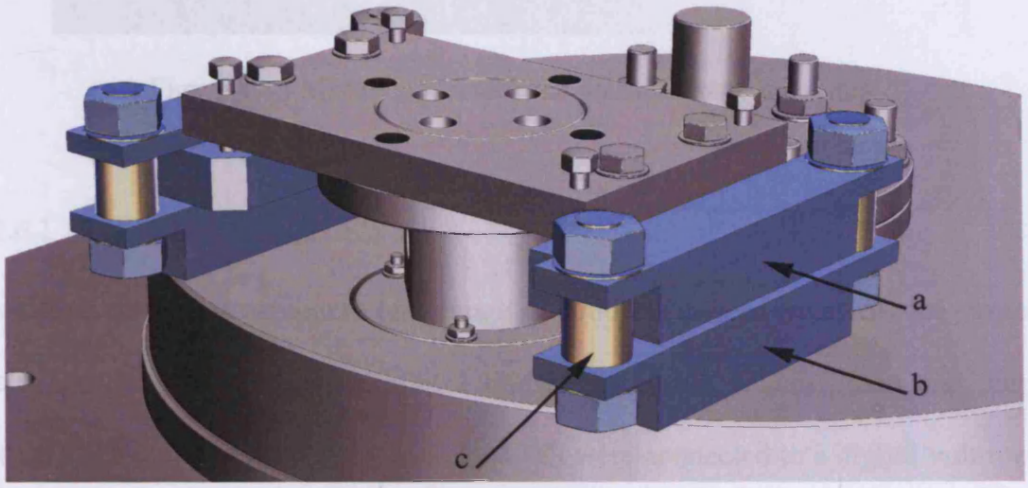

(a) top plate for slipper attachment, (b) mounting to chassis, (c) load cell (one of four)

Figure 4.14 Apparatus for force measurement.

Due to deformation under load, the mounting brackets were modified, as shown in Figure 4.15. This reinforcement effectively joined the two top mounting brackets, and hence reduced the deformation of them under load.

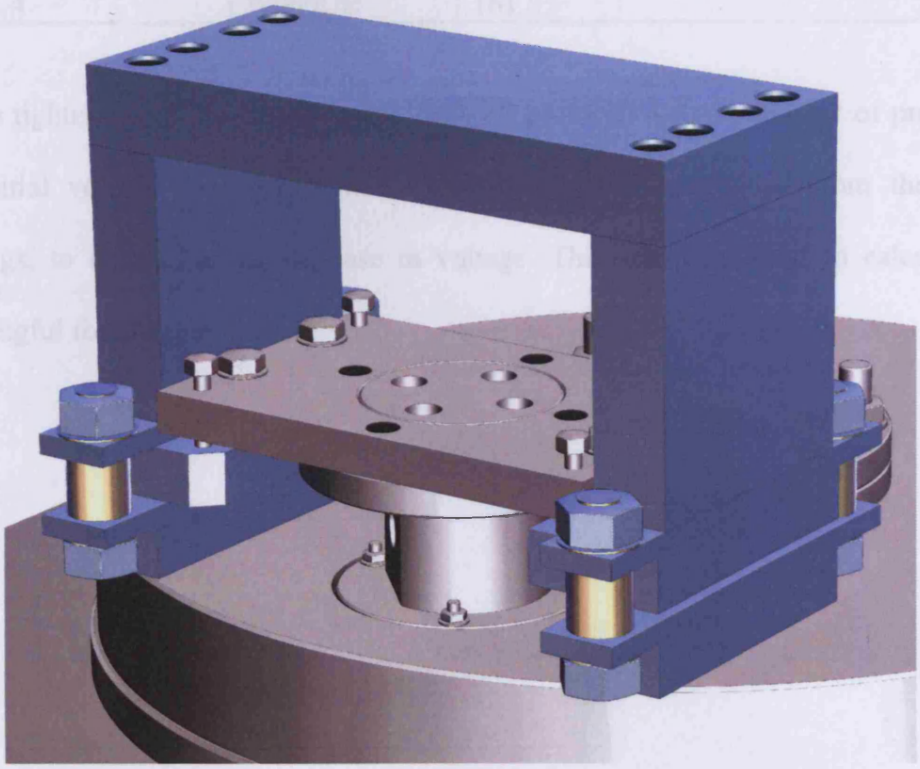

Figure 4.15 Modification to force measurement apparatus

4.2.6.1 Calibration of load cells

Each load cell had a maximum load range of 5000N. Powered by a 15V DC supply, each load cell was found to exhibit a linear relationship between load and output voltage. The output terminals on each load cell were connected to a digital volt meter to allow the voltage readings to be recorded. Table 4.7 indicates the voltage each load cell supplied when subjected to a load of 5000N. The results obtained during the calibration agreed with those stated on the manufacturers' certificate of calibration.

Table 4.7 Load cell maximum output voltage

Load cell	**Serial number**	**Full range output voltage / mV**
1	W060UB	174.1
2	W060UC	179.7
3	W060UD	177.3
4	W060UE	161.8

As the tightening of the nuts on each load cell provided a small amount of pre-load, the initial voltage readings from each load cell were subtracted from the final readings, to determine the increase in voltage. This was then used to calculate a meaningful force value.

4.3 Results

4.3.1 Surface roughness

The surface roughness of both the slipper and rotating disc were measured using a Form Talysurf machine (Taylor-Hobson Ltd., UK). The measurements across the land of the slipper were 4mm in length, with the disc measurements being 40mm long reflecting the diameter of the slipper contact area. The average Ra values are presented in Table 4.8.

Table 4.8 Surface roughness (Ra) values for slipper and disc

	Surface roughness, Ra / μm	
	Slipper	**Disc**
Test 1	0.445	0.571
Test 2	0.408	0.548
Test 3	0.389	0.571
Test 4	0.401	0.552
Test 5	0.399	0.538
Mean	**0.408**	**0.556**

The Ra values obtained indicate that the slipper had a superior surface finish than the disc. This was principally due to the fact that it was surface ground during manufacture. Surface profiles obtained from both the slipper and disc are presented in Figure 4.16 and Figure 4.17.

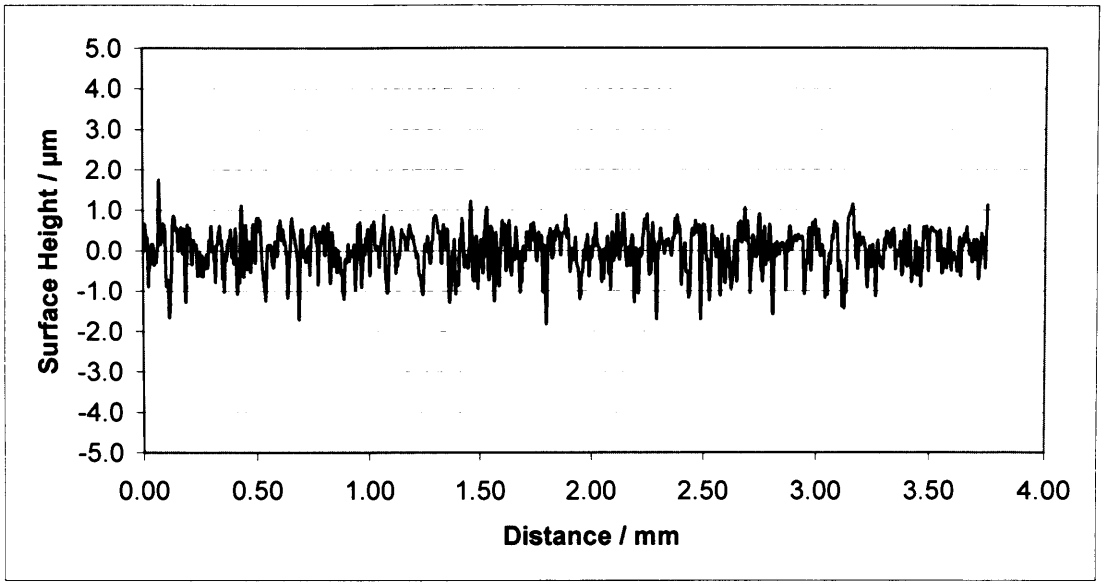

Figure 4.16 Surface profile of slipper land

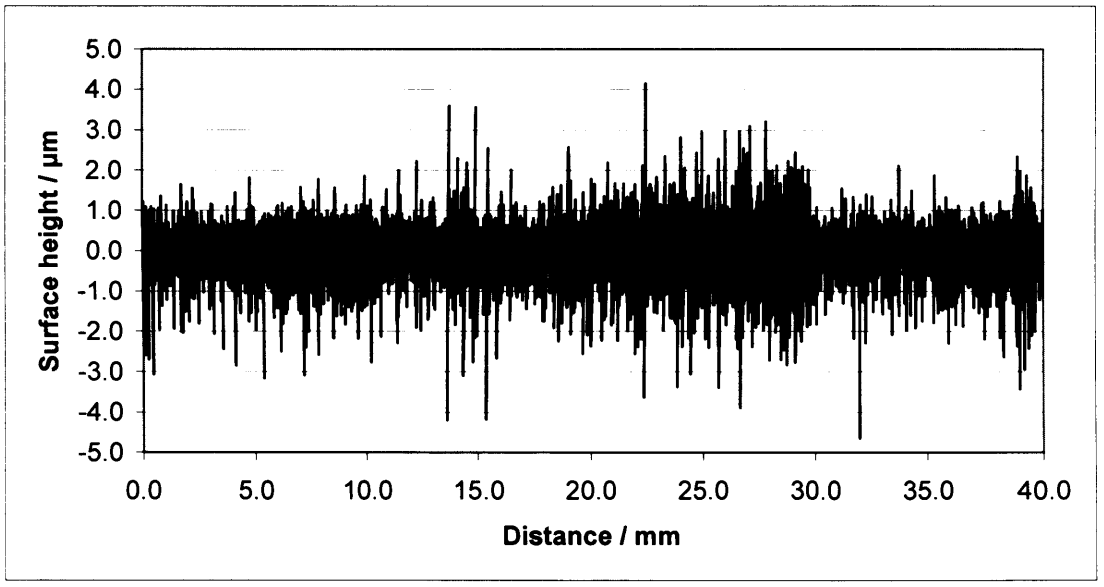

Figure 4.17 Surface profile of aluminium disc

4.3.2 Static tests

Preliminary tests were conducted for clearances ranging between 5µm and 30µm. During these tests, the flow rates and pressure within the groove were monitored for a range of inlet pressures. Each test was repeated four times, and a good repeatability of

results was apparent. The results presented are an average calculated from the four sets of results. By closely monitoring the temperature of oil within the tank, and adjusting the flow rate of cooling water accordingly, the oil temperature was maintained at 40° C, with a fluctuation of ±1° C. Additionally, the temperature of the region around the slipper was monitored using an infrared thermometer.

4.3.2.1 Flat slipper

Results obtained from the flat slipper, shown in Figure 4.18 and Figure 4.19 show a clear trend in leakage with both pressure and clearance.

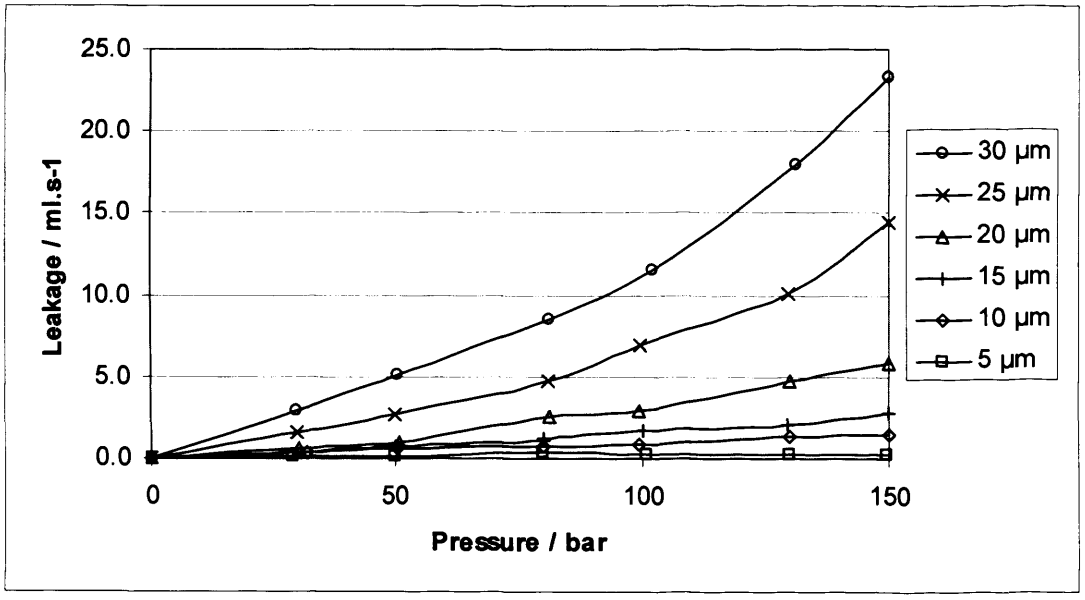

Figure 4.18 Clearance – leakage characteristics for a flat slipper

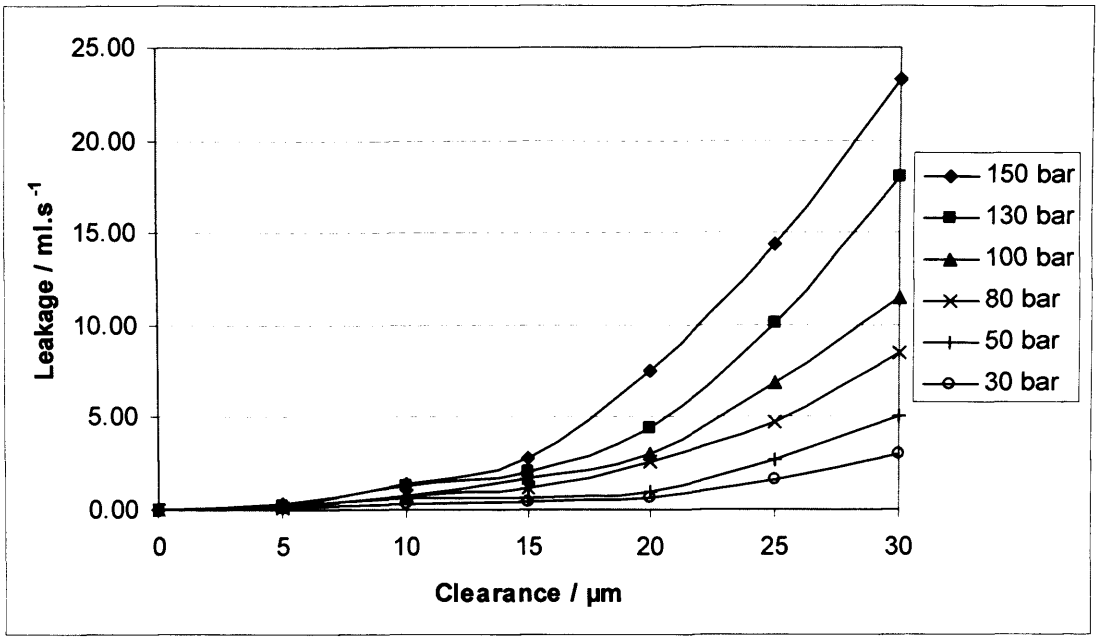

Figure 4.19 Variation in leakage with clearance

The mean pressure within the groove, determined by calculating the mean from the four pressure gauges is shown in Figure 4.20. An interesting observation was that the mean pressure within the groove exhibited a small decrease for larger clearances, especially at the higher pressures tested.

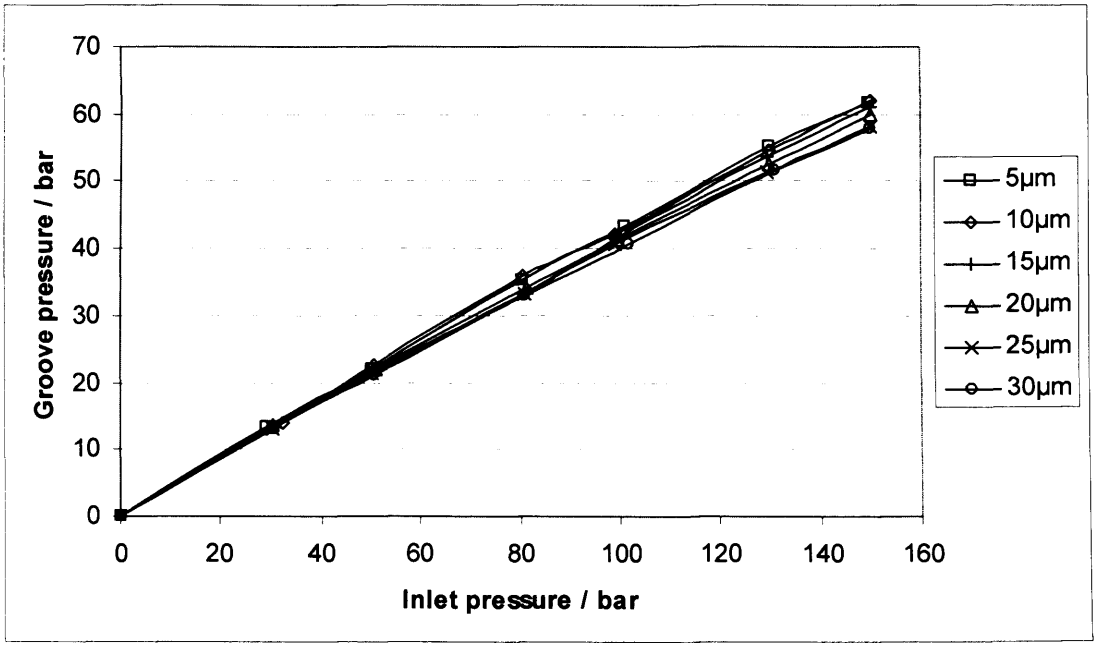

Figure 4.20 Variation in groove pressure with inlet pressure

4.3.2.2 Tilted slipper

For a stationary tilted slipper, it was found that increasing the angle of tilt, increased the leakage. This trend was observed for all clearances tested and is shown in Figure 4.21 to Figure 4.24. An interesting change in flow rate was found whilst working at a clearance of 10μm. Here the flow rate demonstrated a small decrease in leakage at a particular angle of tilt. This attribute was repeatable for all operating pressures. Multiple tests were run for this condition, all indicating the same angle – flow characteristic shown in Figure 4.22.

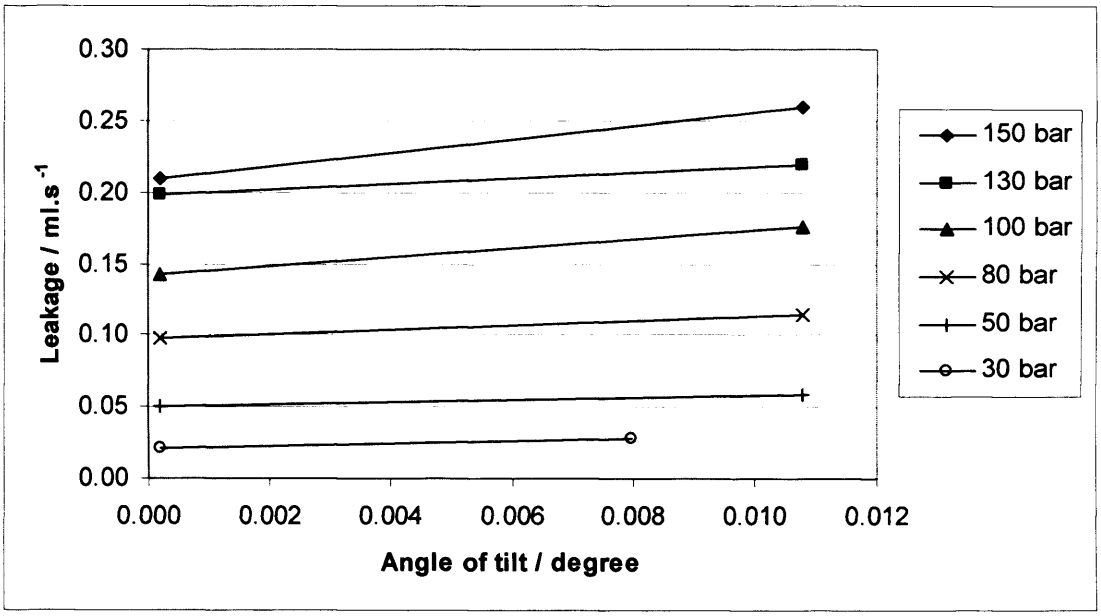

Figure 4.21 Leakage characteristics at a central clearance of 5μm

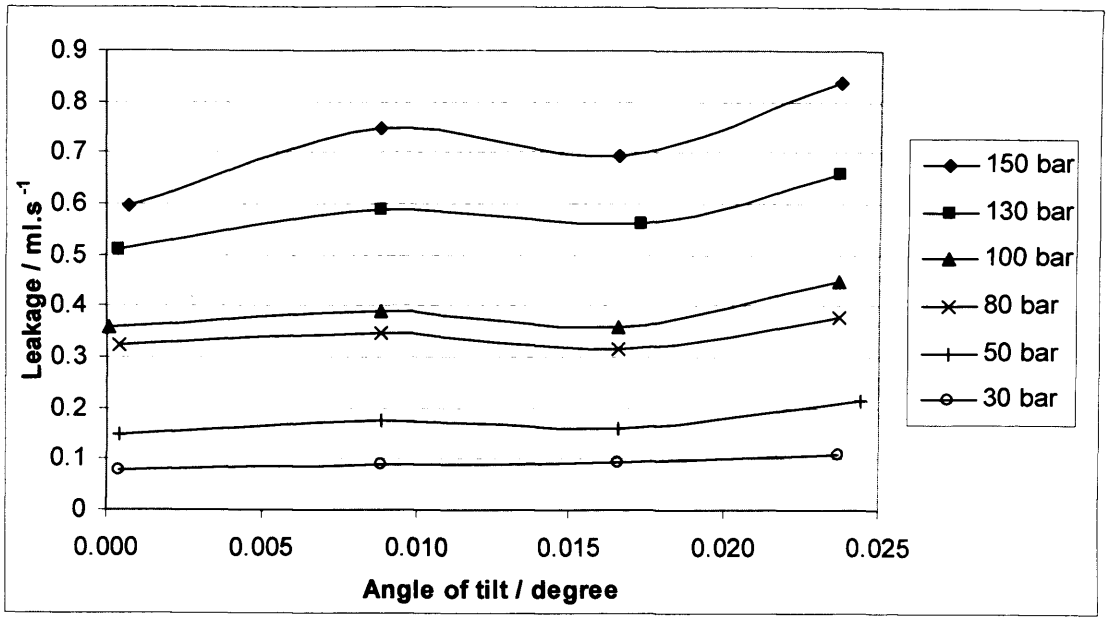

Figure 4.22 Leakage characteristics at a central clearance of 10μm

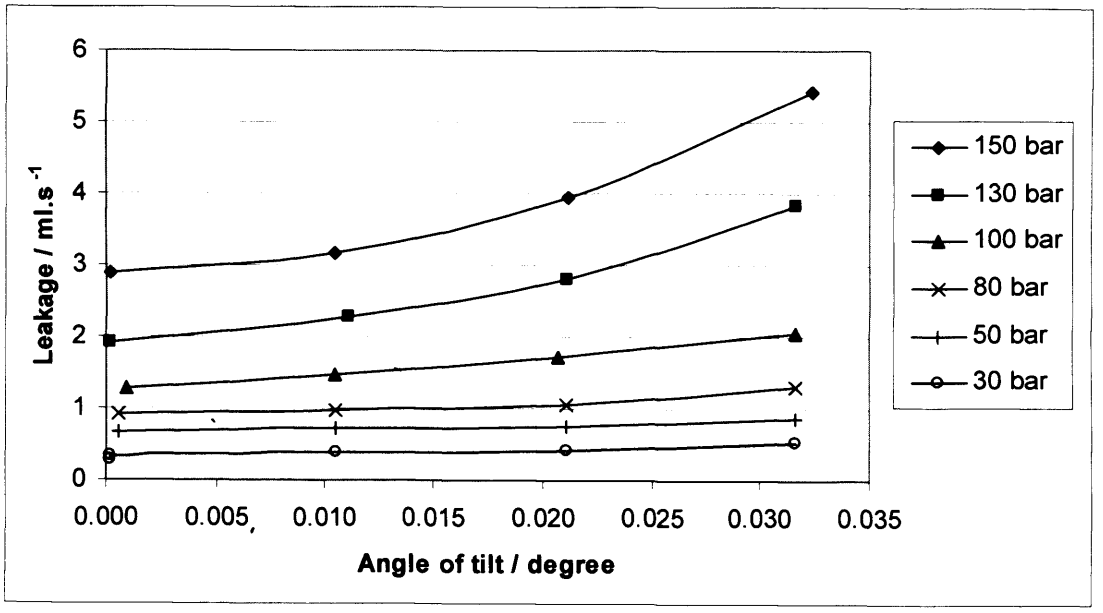

Figure 4.23 Leakage characteristics at a central clearance of 15μm

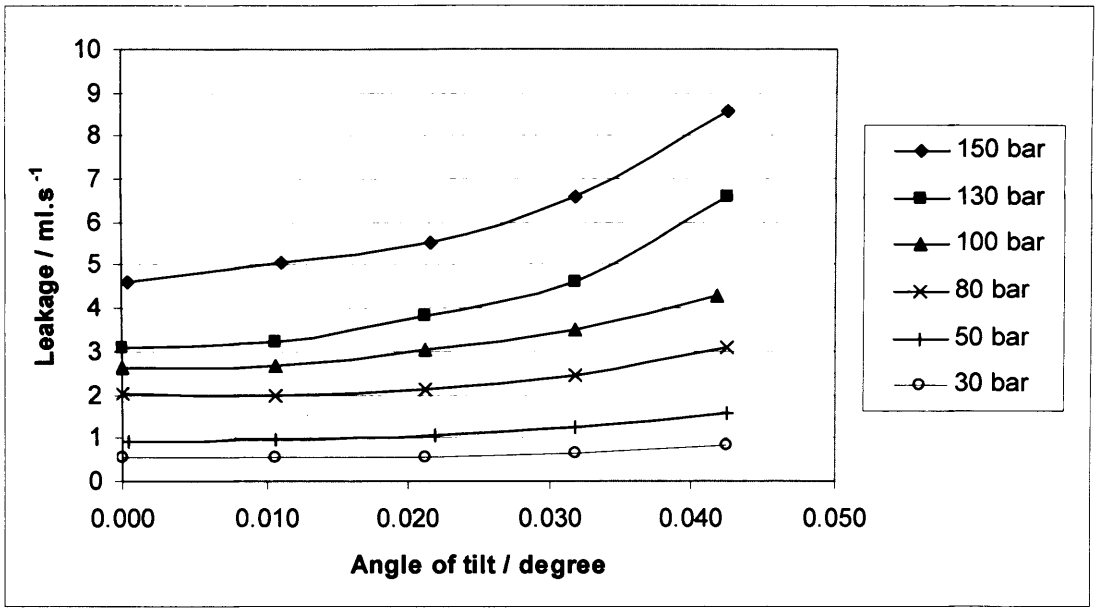

Figure 4.24 Leakage characteristics at a central clearance of 20μm

The mean groove pressure was found to reduce with an increased angle of tilt, as shown in Figure 4.25 to Figure 4.29. It was discovered that there was negligible pressure differential across the groove for clearances typical of those found under normal operating conditions. However, at higher clearances and tilt, for example at the maximum tilt allowed by a central clearance of 50μm, a pressure differential of approximately 1 bar was apparent. This was with an inlet pressure of 150 bar. The region of the groove with the highest clearance was found to exhibit a lower pressure than the region with the lowest clearance.

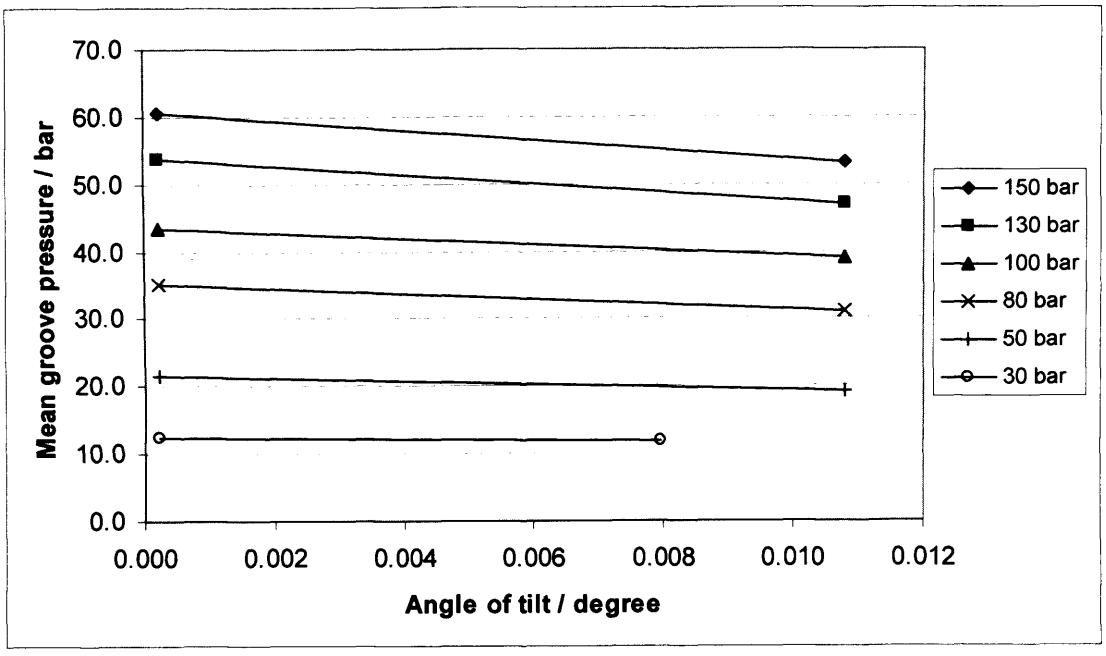

Figure 4.25 Variation of mean groove pressure with angle of tilt, 5μm central clearance

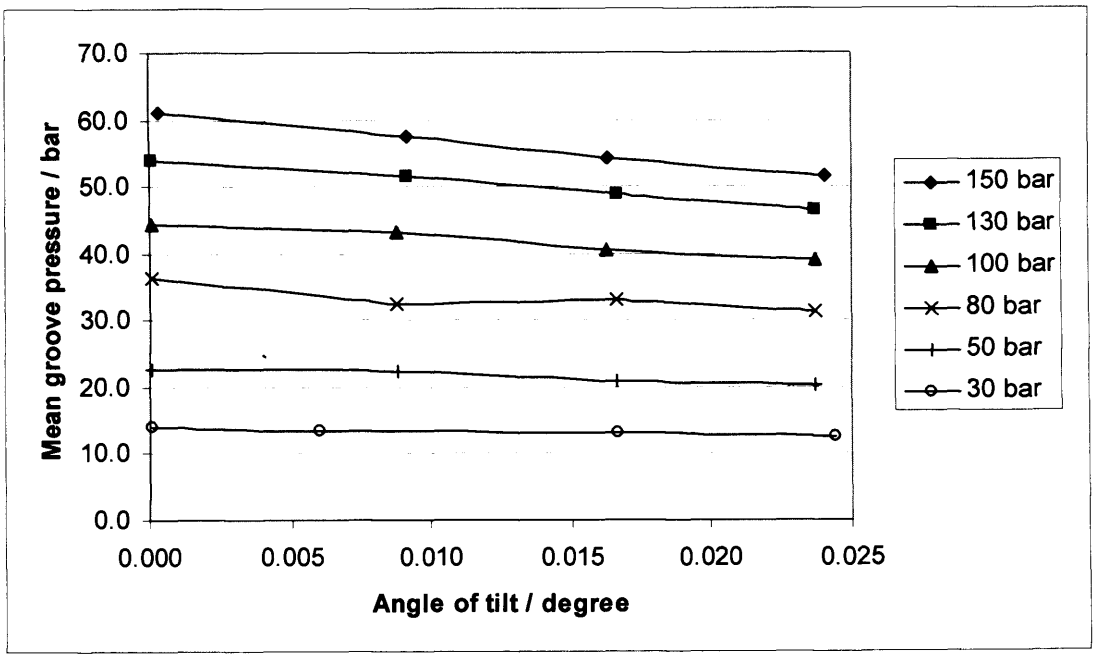

Figure 4.26 Variation of mean groove pressure with angle of tilt, 10μm central clearance

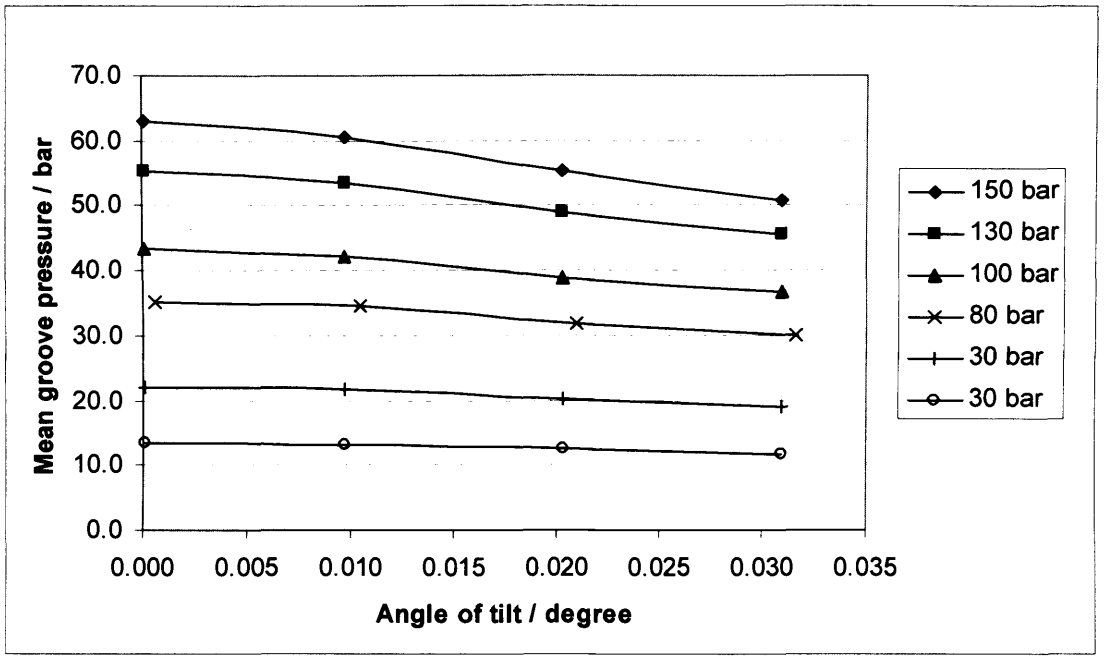

Figure 4.27 Variation of mean groove pressure with angle of tilt, 15μm central clearance

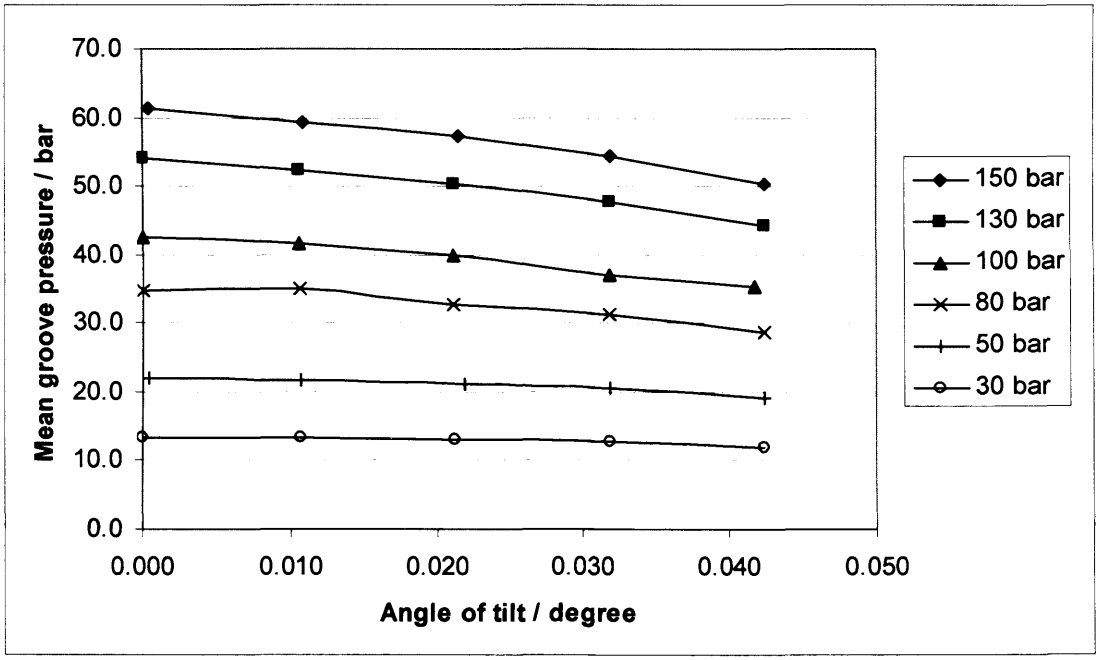

Figure 4.28 Variation of mean groove pressure with angle of tilt, 20μm central clearance

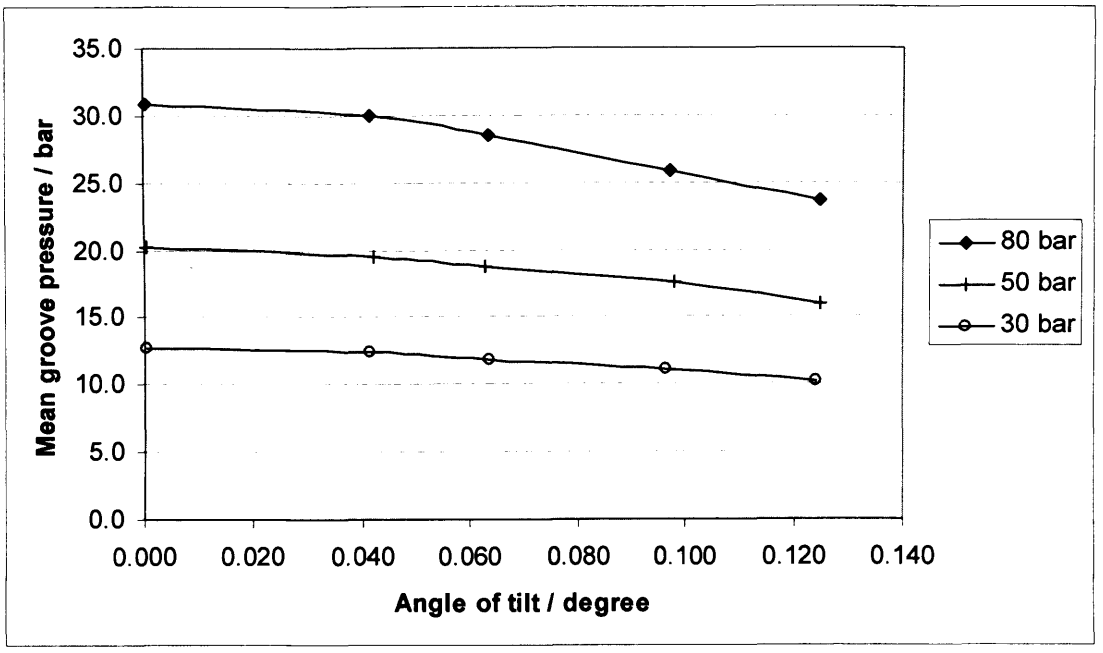

Figure 4.29 Variation of mean groove pressure with angle of tilt, 50μm central clearance

4.3.3 Dynamic tests

The leakage characteristics for a tilted slipper with a rotating swash plate are shown in Figure 4.30. As the rotational velocity increased, a reduction in leakage was evident. The mean groove pressure, however, increased with an increase in rotational velocity, as shown in Figure 4.31. For a flat slipper, the leakage was shown to exhibit a slight upward trend, as illustrated in Figure 4.32.

A small pressure differential within the groove was evident when under dynamic conditions. The portion of the groove closest to the trailing edge developed a slightly higher pressure than the region towards the leading edge. For a tilted slipper the pressure differential amounted to approximately 1.5 bar and occurred at the maximum speed tested. The pressure differential within the groove is shown in Figure 4.33.

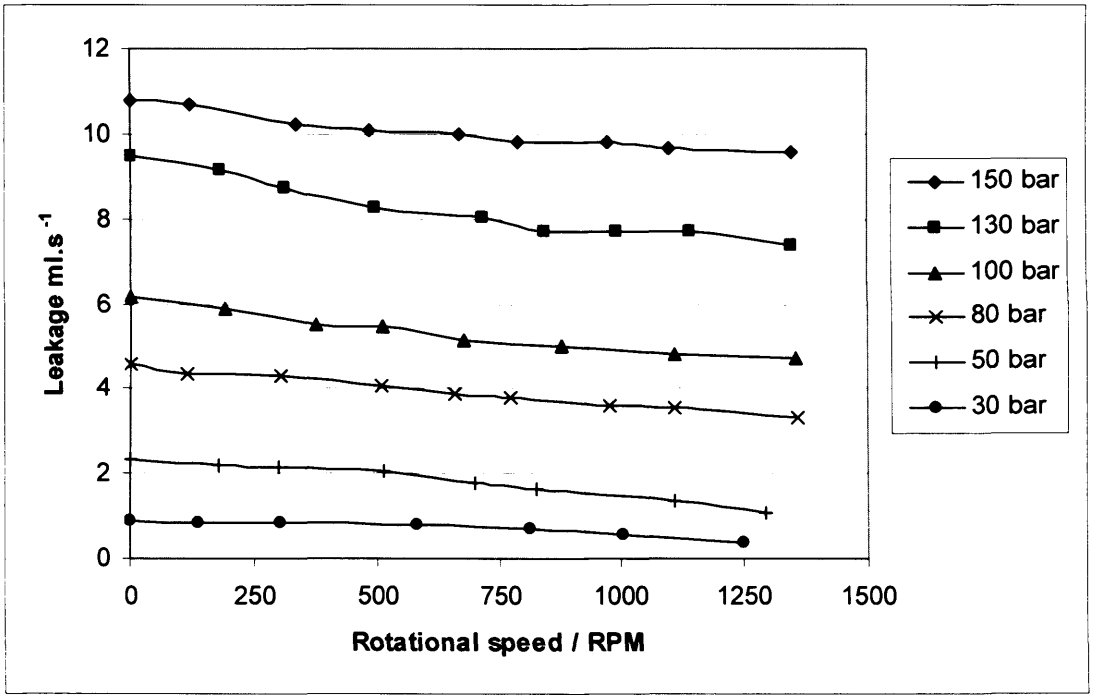

Figure 4.30 Leakage characteristics for a tilted slipper with velocity component

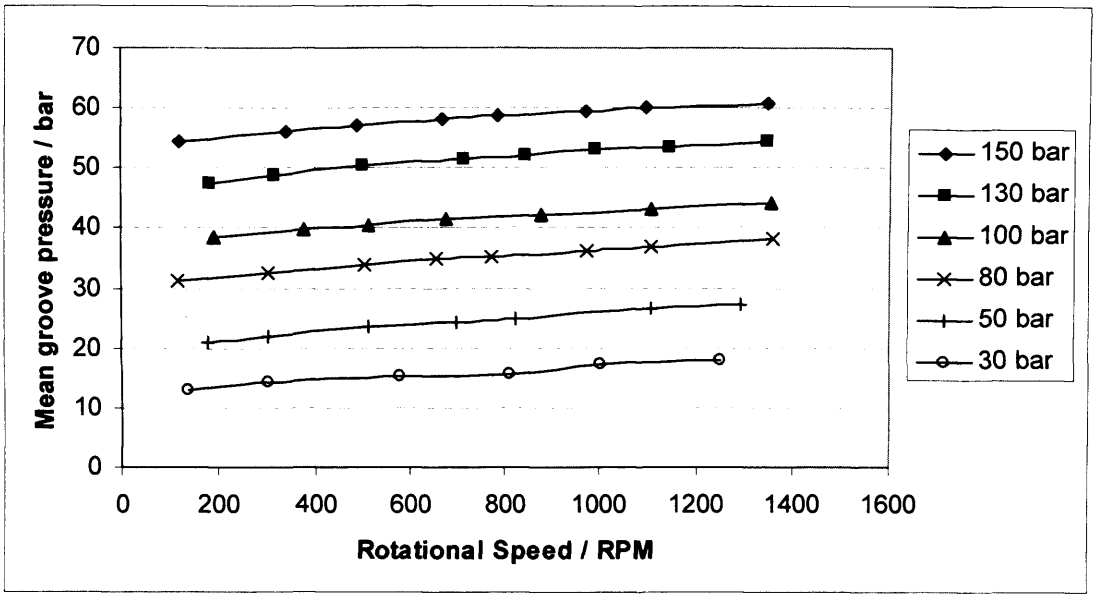

Figure 4.31 Variation of mean groove pressure with rotational speed

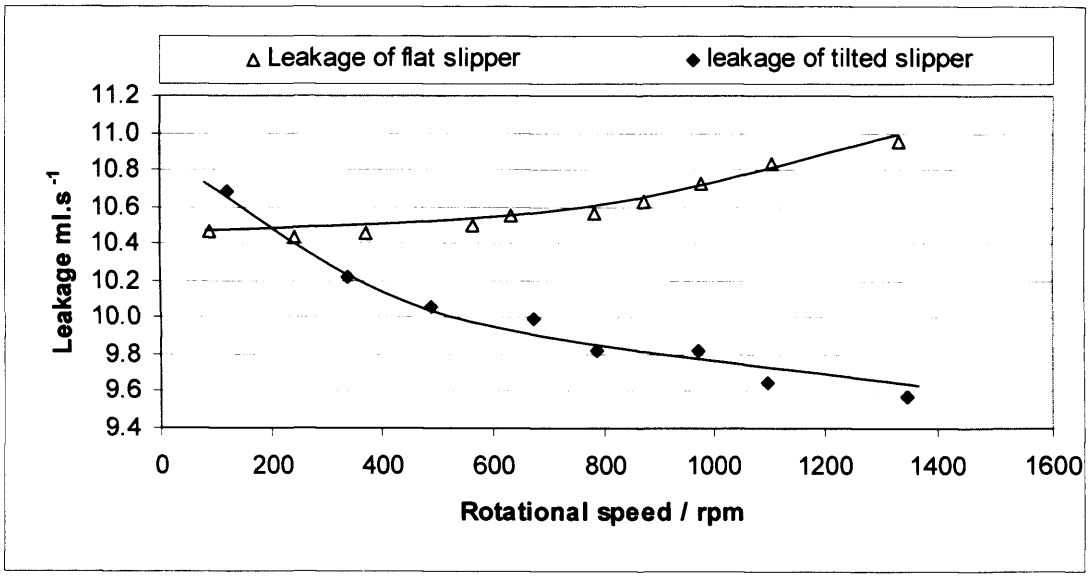

Figure 4.32 Leakage for a flat and tilted slipper at a pressure of 150 bar

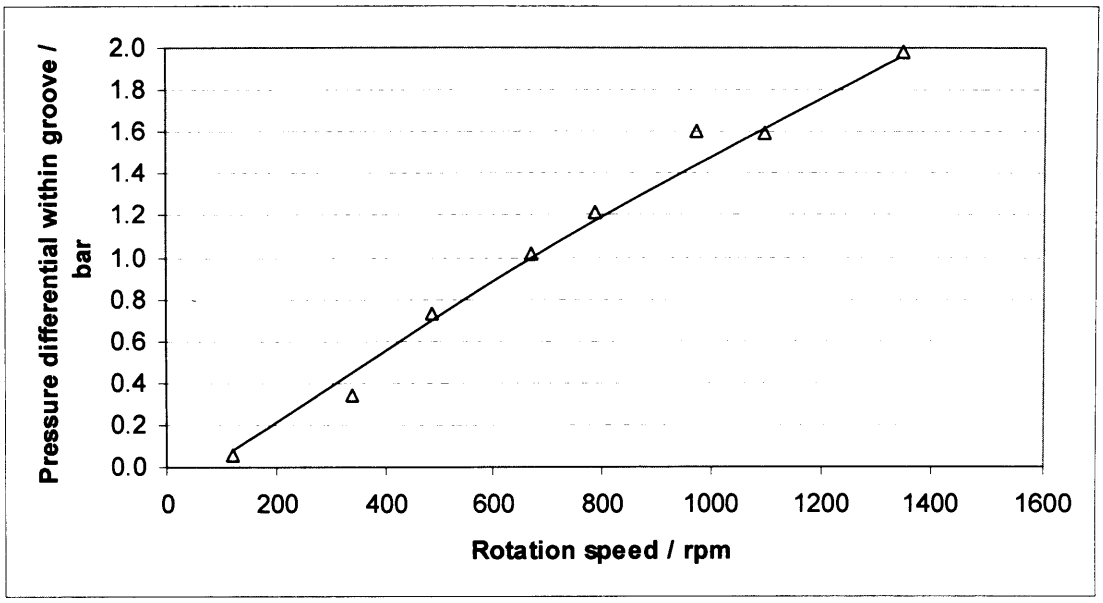

Figure 4.33 Pressure differential within groove for a tilted slipper with inlet pressure of 150 bar

4.3.4 Force measurement

Results for lift under static conditions are shown in Figure 4.34. The experimental values obtained for lift were all approximately 25% lower than the CFD values obtained for a slipper of identical dimensions. This is indicated by the linear trends of differing gradient. Results from the CFD study are detailed later in Chapter 5. Dynamically, the lift generated by the slipper was shown to increase with rotational speed, as depicted in Figure 4.35.

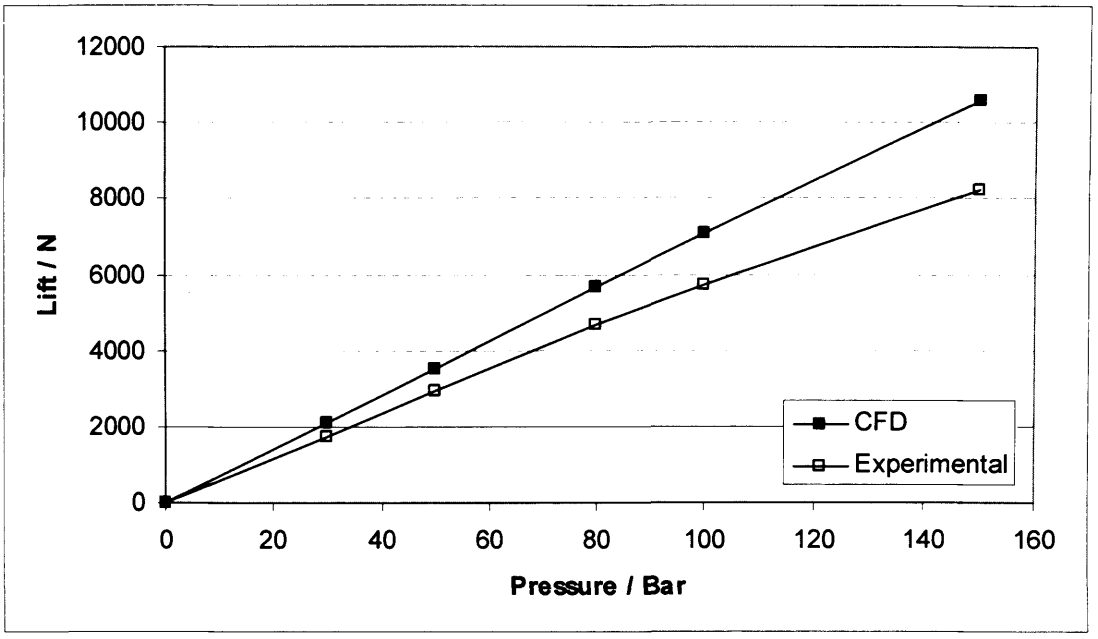

Figure 4.34 Comparison of experimentally obtained and CFD lift values, flat slipper 15μm clearance

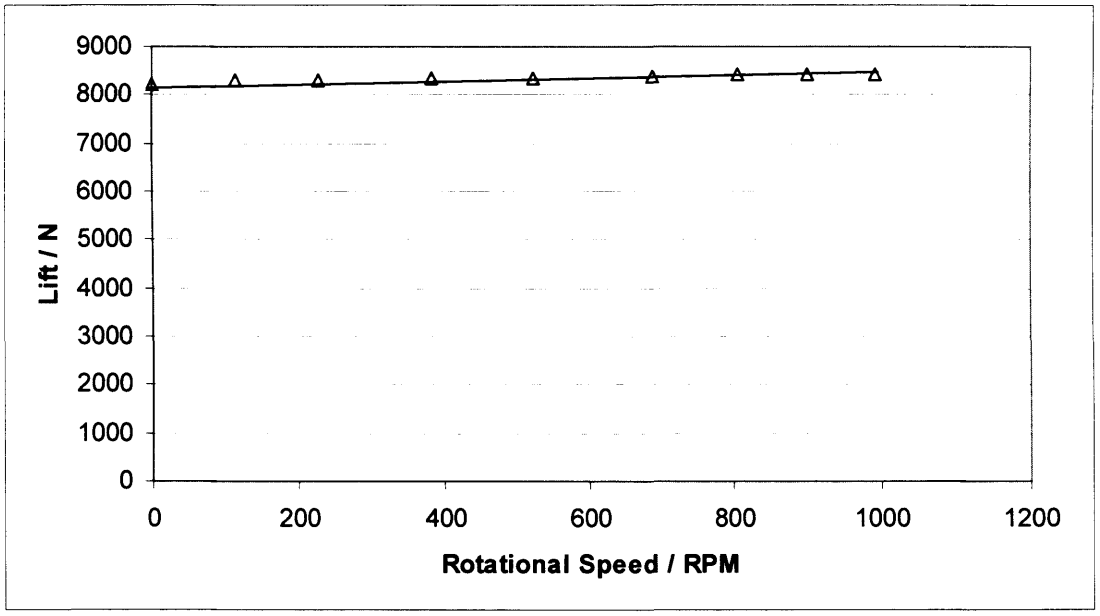

Figure 4.35 Relationship between lift and rotational speed for a tilted slipper

4.4 Discussion

The pressure within the groove was found to be largely proportional to the inlet pressure for all clearances examined. As the clearance increased, a small drop in pressure within the groove was evident. This equated to a reduction of approximately 6% when comparing the groove pressures at clearances of 5μm and 30μm.

Under static conditions and for central clearances of up to 30μm, the pressure measured in the four quadrants of the groove was found to be the same, suggesting that the pressure around the entire groove was constant. Conditions which created a pressure differential between the groove quadrant could be created, however these required a large angle of tilt. A large central clearance was required to permit these angles, and this was significantly larger than those expected to be found under normal operating conditions within a pump. CFD results, to be discussed in more detail later, have shown that with the groove removed, or reduced in depth, a significant pressure differential can exist between the four pressure measurement locations. It was clear that the groove within the test slipper was of sufficient size to allow the equalisation of pressure around the groove, especially whilst operating at clearances typically found during pump operation.

The angle of tilt at which the slipper operated was found to influence the leakage from the slipper. Under static conditions, large angles of tilt were found to increase the leakage, however at the small angles of tilt expected under normal operating conditions, the increase in leakage compared to a completely flat slipper, was found to be small.

As stated in section 4.2.2.3, the axial run-out of the disk representing the swash plate was found to be 11μm. This meant that during the dynamic tests, a consistent clearance could not be maintained. In fact the clearance during the dynamic tests ranged from 20μm to 31μm. This change in clearance over each revolution of the disc meant that the flow rate would be considerably higher than a similar test conducted at the minimum clearance of 20μm. A series of CFD models replicating the existence of run-out were produced to validate the results obtained experimentally. A comparison between these two sets of results is discussed later in Chapter 5.

Since the oil leaking from the slipper was collected in a drip tray before being collected in a measuring cylinder for measurement, there was a time delay before the rate of flow of oil from the drip tray equalled the rate of flow from the slipper. This time delay was kept to a minimum by reducing the available volume of the drip tray. This ensured the system reacted rapidly to changes in flow rate. This was of most importance when the swash plate was rotating due to the amount of heat produced by the bearings. The heat produced by the bearings resulted in heating of the disc, and subsequently the hydraulic oil. Due to the relatively small volume of oil in proximity of the disk, the warming effect was found to be significant, and it was anticipated that this caused a change in viscosity leading to an increased leakage flow rate. It is accepted that friction between the slipper and swash plate surfaces could cause a rise in temperature. However it was clear that a significant amount of heat originated from the bearings, as a temperature rise was apparent even when the slipper assembly was removed.

At high rotational speeds, an increase in temperature of the test rig was observed over time. Since flow rate measurement was required at a range of speeds, the influence of the heating effect became of importance, as it meant that a constant oil temperature could not be assumed. The approach adopted during measurement therefore was to run the apparatus as a constant speed of 700 rpm for a period between each test. Once the temperature of the rig had stabilised, the speed was increased or reduced to the required value. As soon as the flow rate from the apparatus had stabilised, measurements of flow, and pressure were recorded. During this time, the temperature was also measured to ensure it did not notably rise. The test apparatus was then run at 700 rpm again before being changed to the next value. This technique minimised the heating effect, and prevented the understandable trend in temperature caused by taking consecutive readings, each at an increased rotational speed.

Due to the time taken for the oil flow to stabilise, the effects of heating were not completely eliminated. However, the increase in temperature was small, with the entire set of dynamic data being obtained for a temperature range of 44 to 46°C.

As indicated by Figure 4.30, the flow rate of oil for a tilted slipper was shown to reduce with an increase in speed, regardless of the fact that the temperature of the oil was slightly greater at the higher speeds tested. For a flat slipper, the leakage showed a small upward trend with velocity. CFD results, explained later, suggested that this leakage should remain constant, and so it is possible that the residual heating effect of the apparatus was the basis for this small increase in leakage.

The first modification to the test apparatus to incorporate force measurement resulted in the requirement for further development. The brackets were found to deform under load, and this resulted in a large moment being applied to each load cell. It was clear that the load cells were sensitive to moments, and further tests outside of the test rig confirmed this. In addition, it was discovered that the angular location of the applied load had a significant influence on the magnitude of the output signal. A wide range of readings could be obtained for a load applied at different locations. However, for forces applied at the same angular location, the load cells exhibited a linear relationship between the applied force and output voltage, albeit not following the expected calibration trend.

From this it was concluded that the load cells had to be mounted in such a way that they were only subjected to tensile forces. A modification shown in Figure 4.15 was made to the test apparatus, to prevent the identified deformation from occurring. The amount of lift generated by the slipper under static conditions was found to be consistently 25% lower than values obtained through CFD simulation, regardless of the inlet pressure. Comparison of the CFD results with theory developed by Bergada (Appendix A.1) showed an excellent agreement for results of pressure, lift and flow.

A comparison of values obtained for the level of pressure within the groove is shown in Figure 4.36 for a clearance of 15μm. Any significant difference between these values would indicate that the CFD calculated pressure profile did not exist beneath the slipper in the test apparatus. Validation of pressure at this point therefore strongly suggests that the pressure profiles calculated during the CFD simulations indeed occurred in reality, especially for the lower clearances examined.

Hence, it is proposed that the consistently lower experimental values of lift were due to a systematic error in the force readings provided by the load cells. It is probable that this was due to a small amount of torque being applied to the load cells, which affected the readings. Time restrictions at the end of the project did not allow further development.

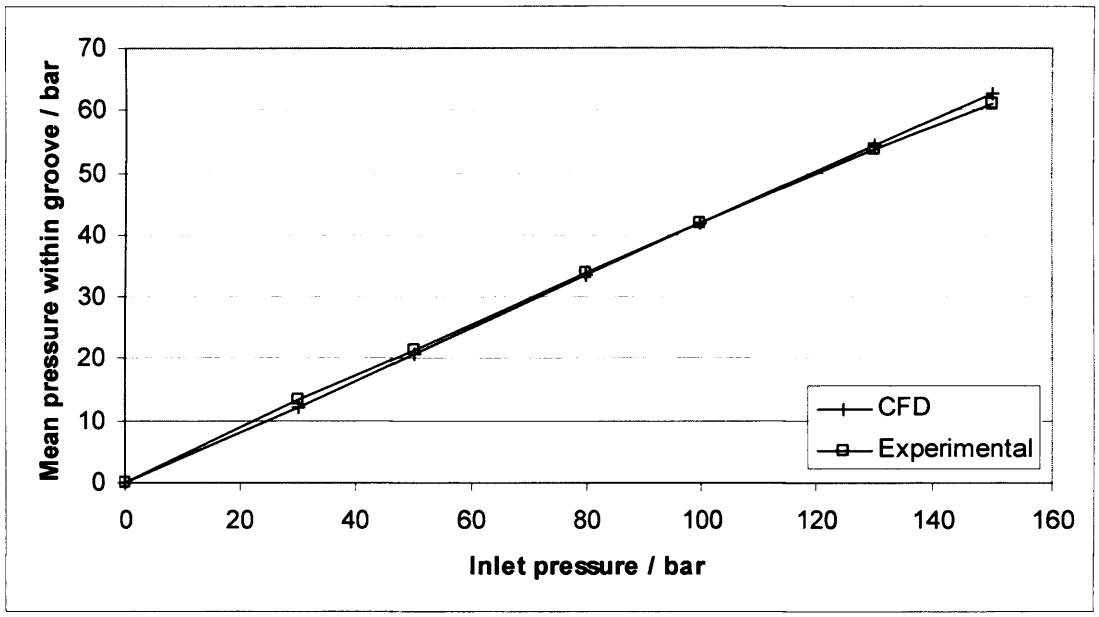

Figure 4.36 Comparison of experimental and CFD mean groove pressure 15μm clearance

The load cells did however provide a linear relationship between inlet pressure and lift. This was in agreement with the CFD simulations, and was in compliance with the fact that the load cells were shown to provide a linear relationship between force and output voltage when the load was applied at the same location. In terms of the lift under dynamic conditions, Figure 4.35 suggests that the lift did indeed increase with an increase in tangential velocity, confirming that hydrodynamic lubrication occurred under dynamic conditions.

4.5 Conclusions

The following conclusions can be drawn from the work presented in this chapter:

1. A test apparatus to investigate the operating characteristics of a slipper with a single groove was successfully designed and developed. Groove pressure and leakage rate were successfully measured for a range of clearances and angles of tilt.

2. Under static conditions, tilt was shown to affect the leakage from the slipper with large angles producing a greater leakage rate.

3. The mean groove pressure was shown to increase with an increase in rotational speed. Under large angles of tilt, a small pressure differential within the groove was detected. This increased as the rotational speed increased.

4. The variation of pressure within the groove was found to be negligible at clearances typical of those expected to be found under normal operating conditions. At higher clearances a small pressure differential was evident within the groove. These clearances, however, were greater than would be typically found in an actual pump. Therefore it was concluded that the groove was of sufficient size to be effective at equalising pressure.

5. With a relative tangential velocity, the leakage from a tilted slipper decreased as the rotational speed increased. For a flat slipper, a small increase in leakage was identified as the rotational speed increased. Both of these trends were

small and thus it was concluded that velocity had little impact on the leakage from the slipper.

Chapter 5. CFD Modelling of Slipper Behaviour

5.1 Introduction

The work presented in this chapter aims to simulate slipper behaviour using CFD simulations. A number of the results obtained were used to validate results obtained experimentally, and presented previously in Chapter 4.

A series of CFD models was produced to measure the pressure profiles, lift and moment generated in addition to the leakage flow rates. These models used dimensions identical to those of the slipper in the test apparatus discussed in Chapter 4. Geometries with varying clearances, and angle of tilt were generated. A range of inlet pressures and rotational speeds were explored using these models.

In addition, CFD slipper models with varying groove depths were produced, and the pressure around the groove was analysed for a range of operating conditions.

CFD models were produced to replicate the run-out identified in the hydraulic test apparatus developed in Chapter 4. This enabled the flow rate due to variation in clearance to be quantified and offered validation for the test apparatus

5.2 Slipper Models

Geometries representing the fluid beneath a slipper were created in the "GAMBIT" software package for processing in "FLUENT". A typical geometry is shown in Figure 5.1.

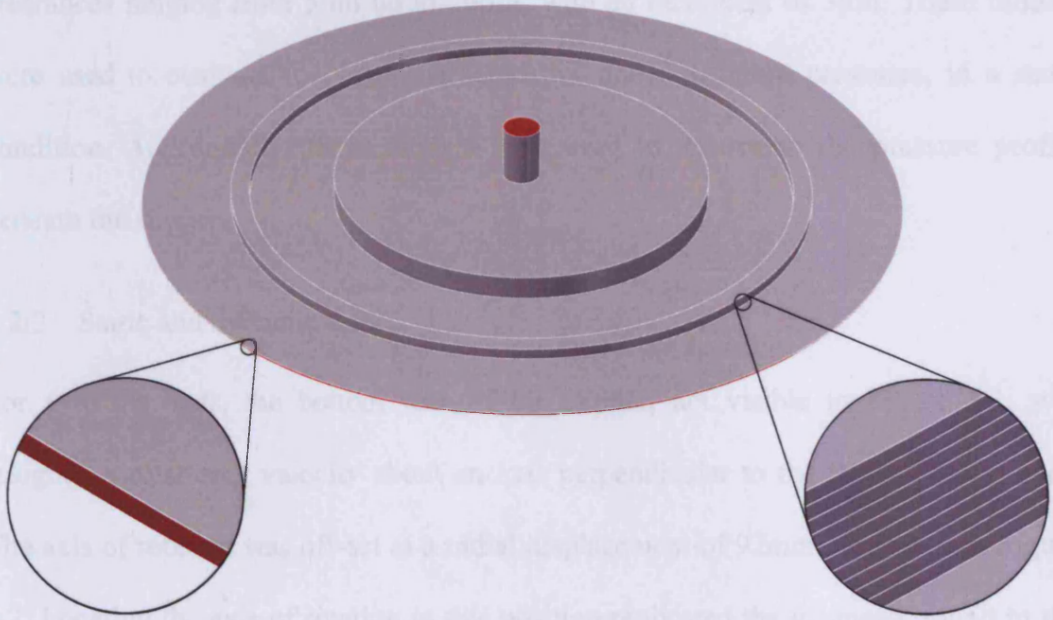

Figure 5.1 CFD geometry of a slipper

The circular face shown in red in the centre of the slipper was assigned a "Pressure Inlet" boundary condition. The curved face around the peripheral of the slipper was assigned a "Pressure Outlet" boundary condition equal to atmospheric pressure. The flow across this face was monitored. A kinematic viscosity of $32mm^2.s^{-1}$ was assumed for the static models. This reflected the viscosity of the ISO 32 mineral oil at a temperature of 40°C. This was the temperature maintained during the static tests presented in Chapter 4. For the dynamic tests, where a temperature rise was noted experimentally, the viscosity was adjusted accordingly. Here a viscosity of $26.4mm^2.s^{-1}$ was assumed reflecting a temperature of 45°C. The full viscosity –

temperature characteristic for the ISO 32 hydraulic oil used experimentally is shown in Appendix A.4.1 [88].

5.2.1 Clearance

A series of meshes representing different clearances was produced. These meshes had clearances ranging from 5μm up to 29μm, with an increment of 3μm. These models were used to evaluate the flow characteristics under different pressures, in a static condition. Additionally, these models were used to determine the pressure profile beneath the slipper.

5.2.2 Static and dynamic tests

For dynamic tests, the bottom face of the slipper, not visible in Figure 5.1, was assigned a rotational velocity about an axis perpendicular to the face of the slipper. The axis of rotation was off-set at a radial displacement of 92mm, as shown in Figure 5.2. Locating the axis of rotation in this position replicated the geometry found in the test apparatus developed in Chapter 4. The axis of rotation created a tangential velocity gradient across the face of the slipper. At an angular velocity of 150 $rad.s^{-1}$, the tangential velocity ranged from 10.7 $m.s^{-1}$ on the inside edge of the slipper, to 16.9 $m.s^{-1}$ on the outside edge.

All images of the slipper presented in this chapter have the axis, and direction of rotation as illustrated in Figure 5.2. The slipper was tilted about an axis labelled A-A, with the leading edge generally greater than the trailing edge. For static tests, the boundary condition of "Stationary Wall" was allocated to the bottom face.

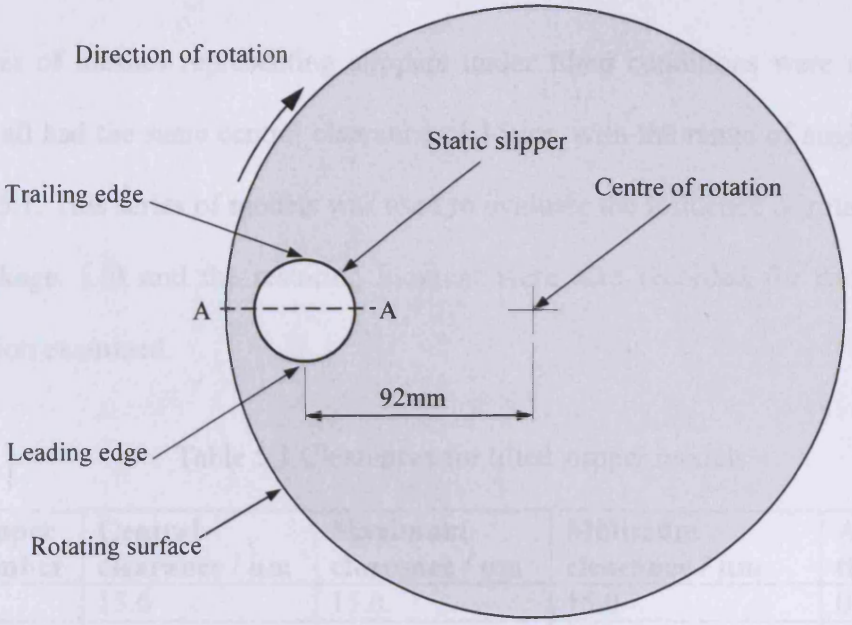

Figure 5.2 Slipper axis of rotation

Figure 5.4 shows part of the meshed slipper geometry. This portion shows the part of the edge of the slipper film. The thickness of this particular mesh in this location was 15µm. The vertical face was assigned a "Pressure Outlet" boundary condition and was used to monitor the volumetric flow rate of fluid leaving the slipper.

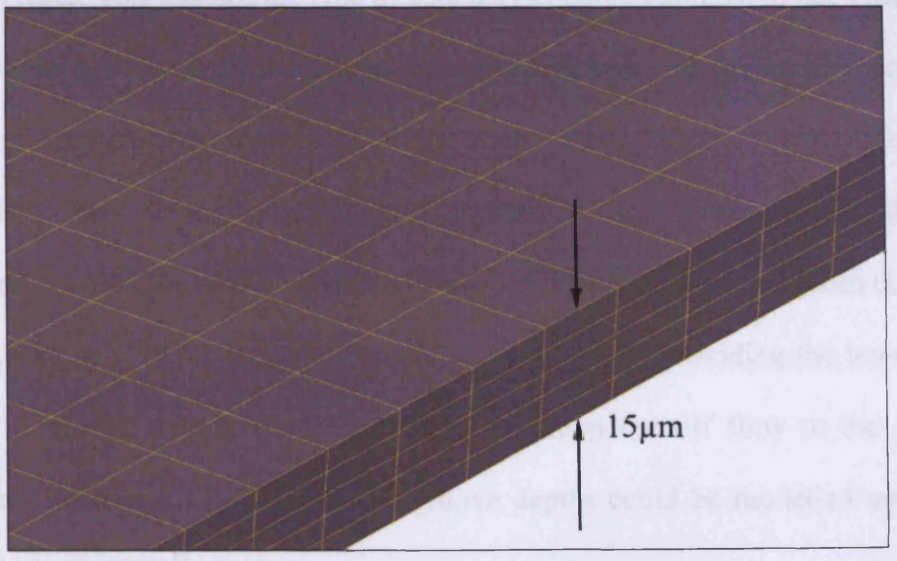

Figure 5.3 Part of CFD mesh around edge of slipper

5.2.3 Tilted conditions

A series of meshes representing slippers under tilted conditions were also created. These all had the same central clearance of 15μm, with the range of angles shown in Table 5.1. This series of models was used to evaluate the influence of rotational speed on leakage. Lift and the restoring moment were also recorded for each operating condition examined.

Table 5.1 Clearances for tilted slipper models

Slipper number	Central clearance / μm	Maximum clearance / μm	Minimum clearance / μm	Angle of tilt / °
1	15.0	15.0	15.0	0.0000
2	15.0	18.0	12.0	0.0084
3	15.0	20.0	10.0	0.0140
4	15.0	22.0	8.0	0.0196
5	15.0	24.0	6.0	0.0252
6	15.0	26.0	4.0	0.0307

5.2.4 Groove depth

In each model of the slipper, the groove was made up of ten layers. These collectively formed the full groove depth, with adjacent layers, each a separate volume, sharing common faces. This enabled the type of boundary condition applied to each face to be adjusted during the processing stage in "FLUENT". By changing the boundary conditions, the effective groove depth of the slipper could be varied, without creating a completely new mesh for each groove depth. For a full groove depth, all faces within the groove volume were given an "Interior" boundary condition, with the upper most face given a "Wall" boundary condition. Conversely, providing the lowest face within the groove with a "Wall" boundary condition cut off flow to the groove, effectively removing it. In total eleven groove depths could be modelled using this

approach, ranging from zero to 0.8mm in depth. Part of the groove mesh is shown below in Figure 5.4.

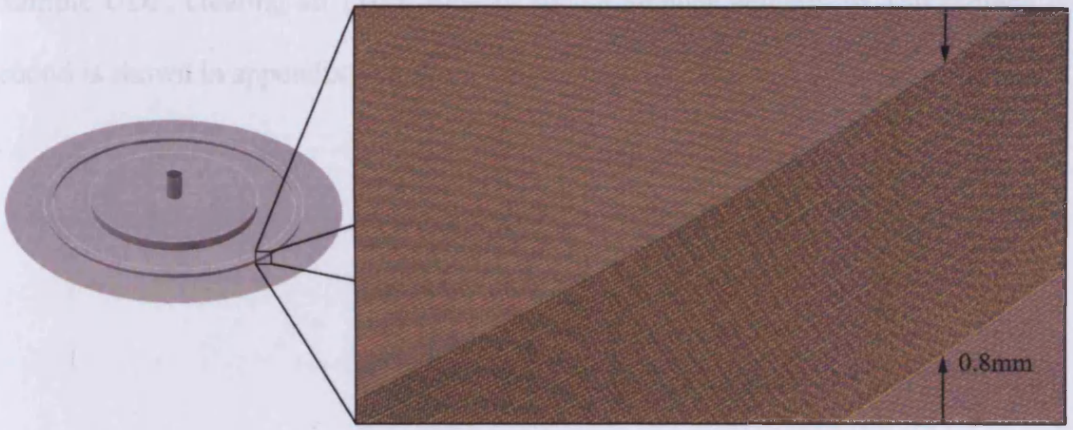

Figure 5.4 CFD mesh showing groove area

5.2.5 Groove location

The impact of the radial location of the groove was also investigated. In total nine groove locations were modelled, each dividing the face of the slipper in a different place. The leakage and lift characteristics of the slipper were determined for each groove location.

5.2.6 Modelling of variable clearances

An attempt was made to simulate the axial run-out identified in the test apparatus used in Chapter 4. This was achieved by utilising a time-dependent-velocity UDF. The UDF controlled the velocity of the lower face of the geometry, in a direction parallel to the axis of rotation. The volume directly above this face, representing the film of fluid between the slipper lands and swash plate deformed accordingly, thus simulating the effect of axial run-out. The flow rate of oil from the slipper was then compared to the flow rates obtained experimentally.

This UDF was modified when simulating different angular velocities, thus providing the correct velocity amplitude and cyclic frequency for the velocity simulated. An example UDF, creating an 11μm run-out for an angular velocity of 150 radians per second is shown in appendix A.4.2.

5.3 Results

5.3.1 Clearance

Presented in Figure 5.5 is the pressure profile for a flat slipper. Since the slipper was flat, the pressure profile was symmetric about the centre of the slipper. The pressure profiles shown below were generated at a clearance of 10μm, however they were found to be identical in profile for any clearance. As the pressure profile was found to be constant, the lift generated was also found to be constant, and hence independent of clearance.

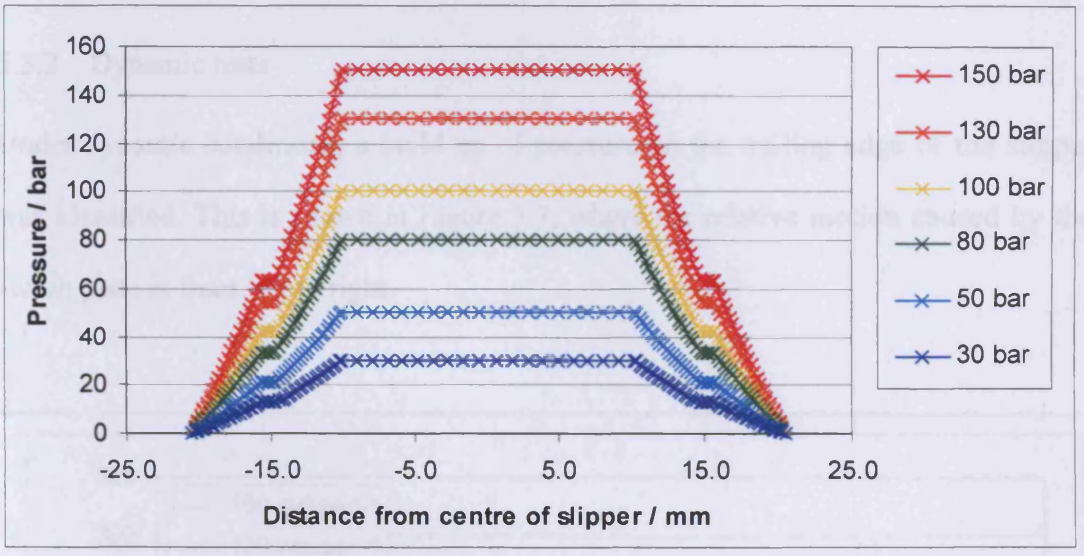

Figure 5.5 Pressure profiles at fixed clearance

The leakage, however, was found to increase dramatically with clearance as shown in Figure 5.6, and typically proportional to clearance^3 as predicted by well-established hydrostatic theory. Also plotted in Figure 5.6 are the leakage rates calculated utilising the theory developed by Bergada. A high level of correlation between these results was expected, as only radial flow occurs with a flat slipper, as assumed by Bergada's theory.

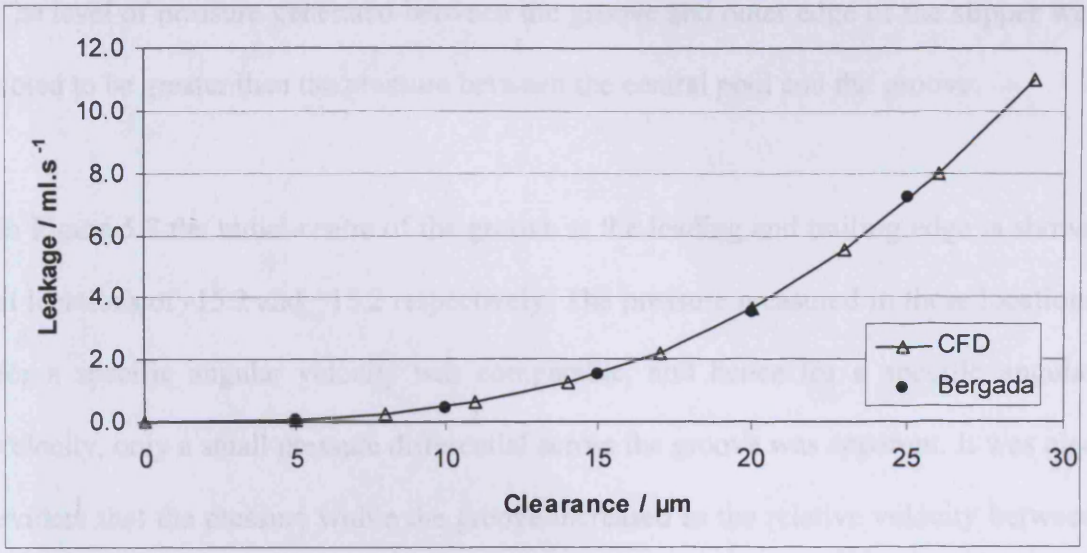

Figure 5.6 Clearance - leakage characteristics at 150 bar

5.3.2 Dynamic tests

Under dynamic conditions, a build up of pressure on the trailing edge of the slipper was identified. This is shown in Figure 5.7, where the relative motion caused by the swash plate is from left to right.

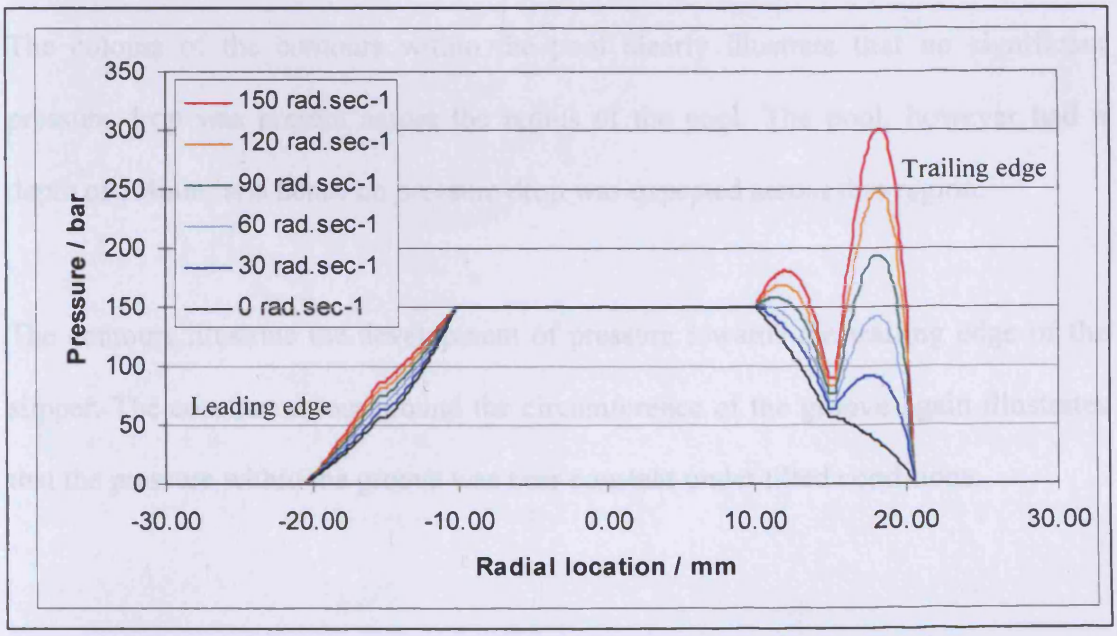

Figure 5.7 Pressure profile in direction of motion with tilt of 0.0307°

The level of pressure generated between the groove and outer edge of the slipper was noted to be greater than the pressure between the central pool and the groove.

In Figure 5.7 the radial centre of the groove at the leading and trailing edge is shown at locations of -15.2 and +15.2 respectively. The pressure measured in these locations for a specific angular velocity was comparable, and hence for a specific angular velocity, only a small pressure differential across the groove was apparent. It was also evident that the pressure within the groove increased as the relative velocity between the slipper and swash plate increased.

Pressure contours for a number of angular velocities are shown in Figure 5.8. The centre of rotation of the swash plate is to the right of the diagrams, and relative swash plate rotation is in a clock-wise direction. The lubrication orifice, pool, and groove have been superimposed over the contours to illustrate their positions.

The colours of the contours within the pool clearly illustrate that no significant pressure drop was present across the radius of the pool. The pool, however had a depth of 1.4mm, and hence no pressure drop was expected across this region.

The contours illustrate the development of pressure towards the trailing edge of the slipper. The constant colour around the circumference of the groove again illustrates that the pressure within the groove was near constant under tilted conditions.

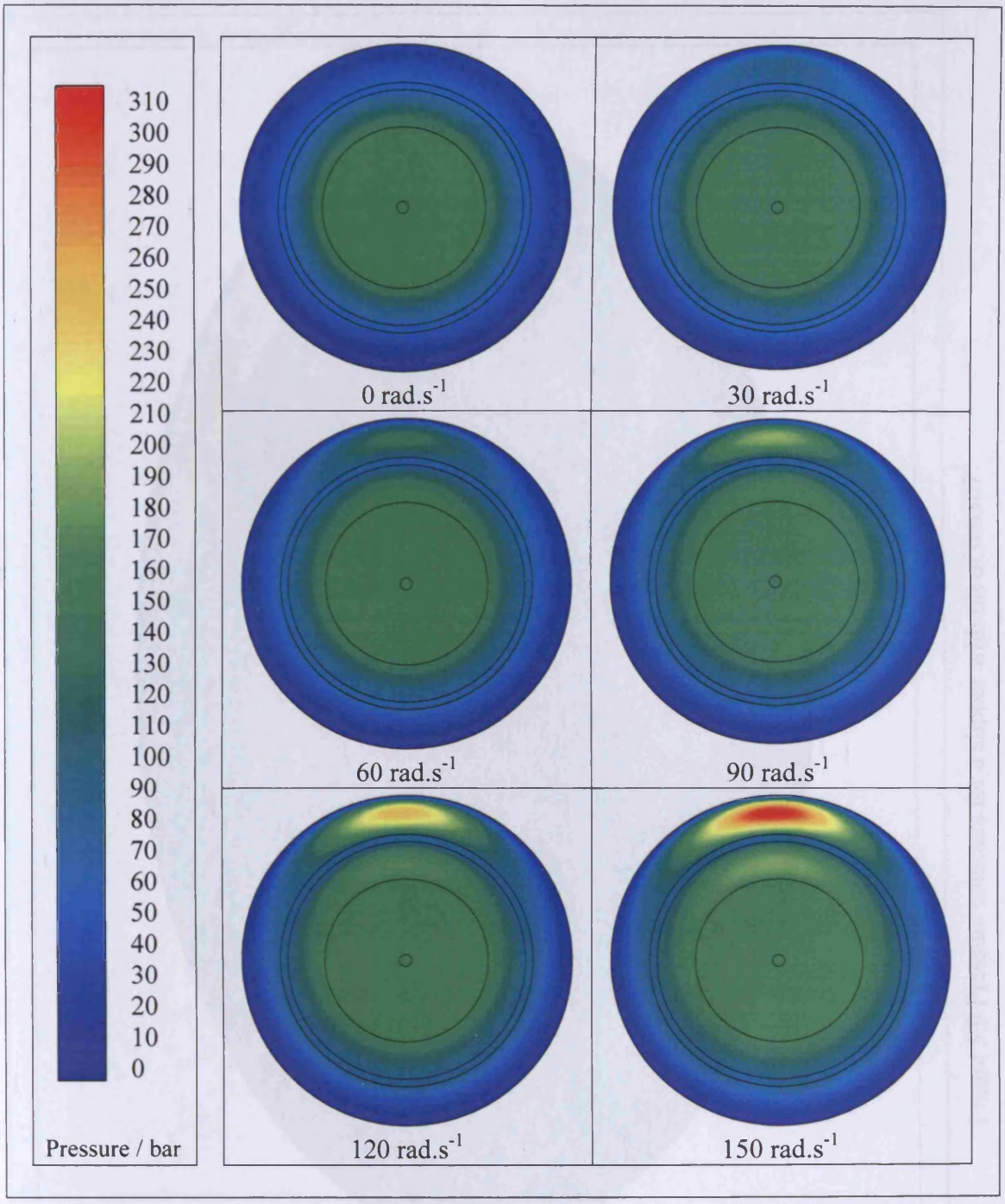

Figure 5.8 Pressure contours with velocity component for tilt of 0.0307°

A three-dimensional view of a slipper is shown in Figure 5.9. When the slipper was tilted, the build up of pressure at the trailing edge of the slipper created a moment which tended to restore the slipper to a horizontal condition.

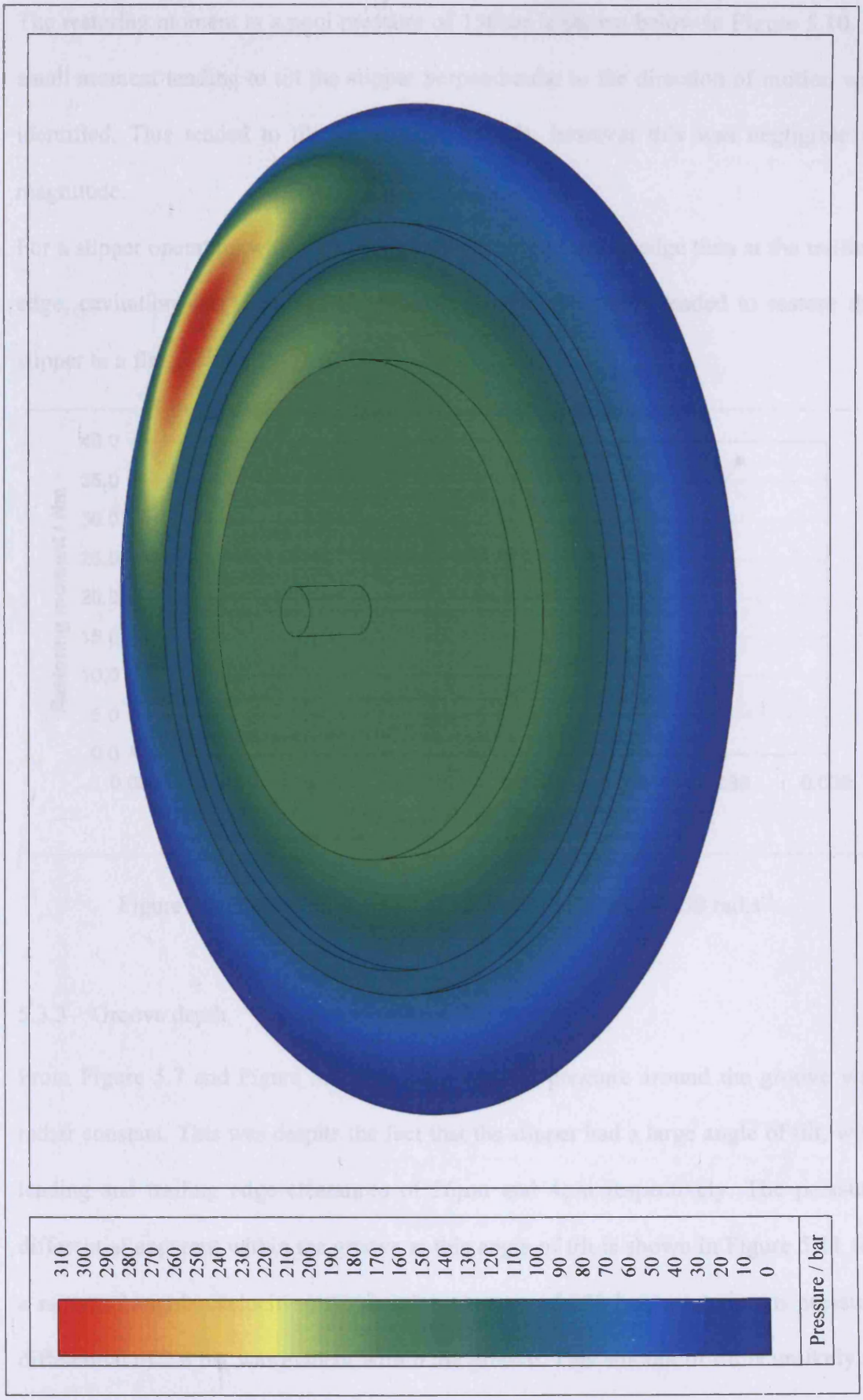

Figure 5.9 Pressure contours for a slipper with tilt of 0.0307°

The restoring moment at a pool pressure of 150bar is shown below in Figure 5.10. A small moment tending to tilt the slipper perpendicular to the direction of motion was identified. This tended to tilt the slipper inwards, however this was negligible in magnitude.

For a slipper operating with a smaller clearance at the leading edge than at the trailing edge, cavitation was identified near the front edge. This also tended to restore the slipper to a flat position.

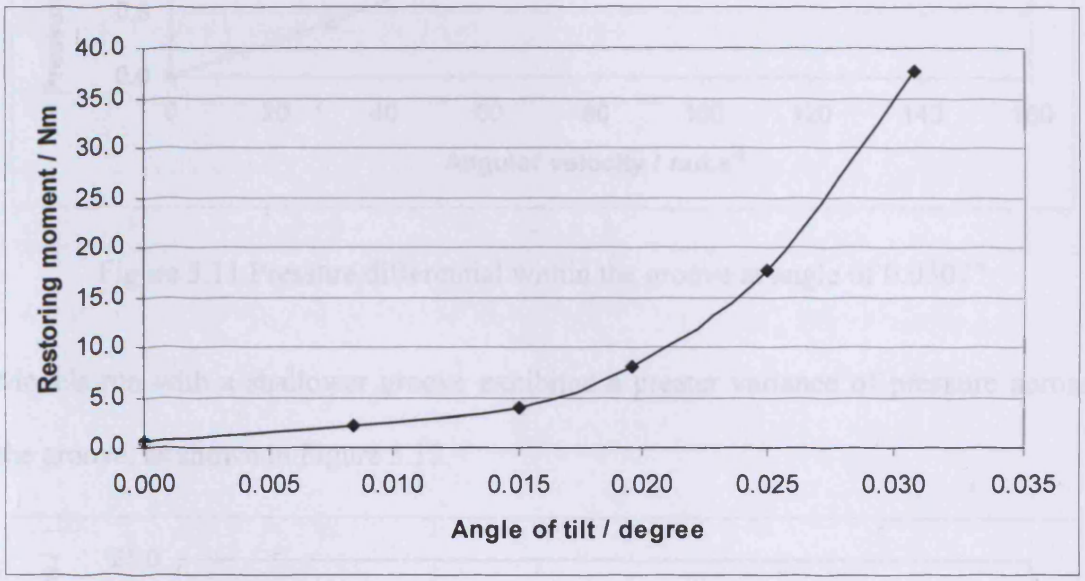

Figure 5.10 Restoring moment at tangential velocity of 150 rad.s^{-1}

5.3.3 Groove depth

From Figure 5.7 and Figure 5.8, it is clear that the pressure around the groove was rather constant. This was despite the fact that the slipper had a large angle of tilt, with leading and trailing edge clearances of 26μm and 4μm respectively. The pressure differential apparent within the groove at this angle of tilt is shown in Figure 5.11 for a range of angular velocities. At an inlet pressure of 150 bar, a maximum pressure differential of 2.6 bar was evident within the groove. This amount of tilt is unlikely to

occur under normal operating conditions, but illustrates the fact that the groove was efficient at maintaining a constant pressure.

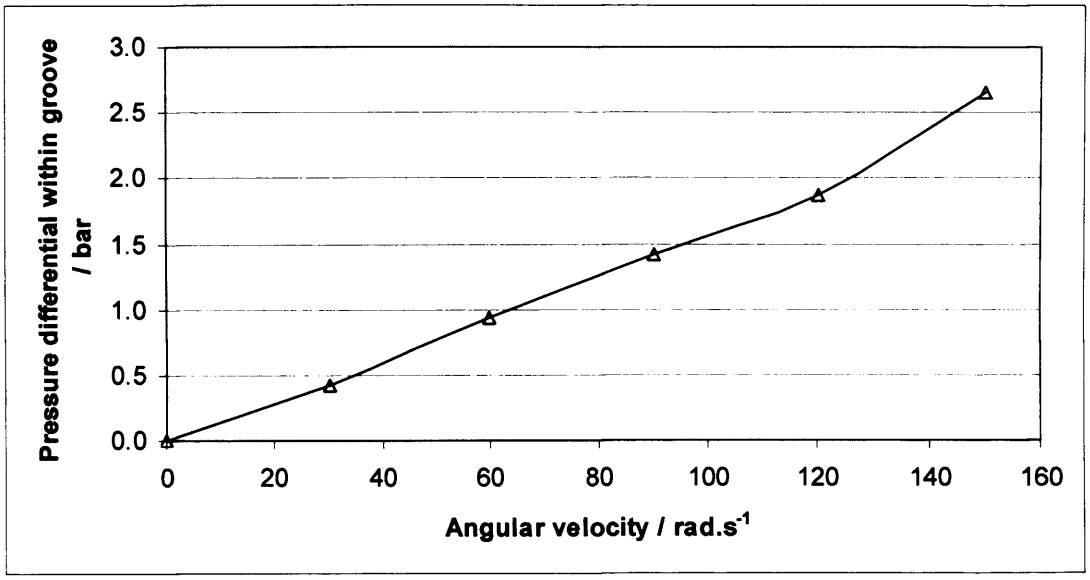

Figure 5.11 Pressure differential within the groove at angle of 0.0307°

Models run with a shallower groove exhibited a greater variance of pressure across the groove, as shown in Figure 5.12.

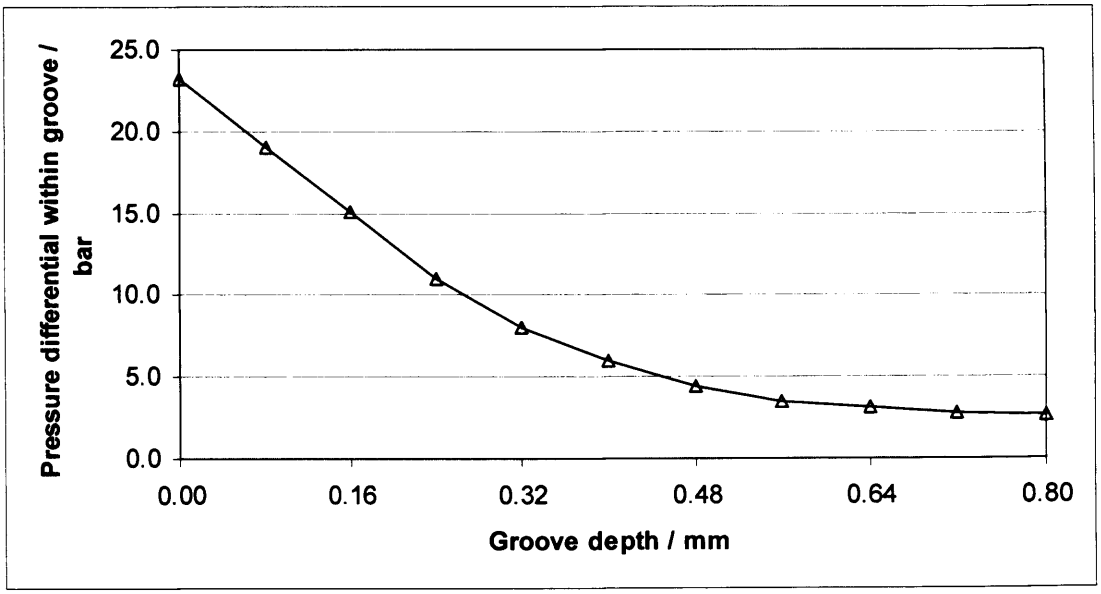

Figure 5.12 Influence of groove depth on maximum pressure differential within groove. Rotation of 150 rad.s^{-1}. Angle of slipper 0.0307°

5.3.4 Leakage

The angle of tilt was observed to have an influence upon the rate of leakage from the slipper. Figure 5.13 shows that under dynamic conditions, as the angle of tilt increased, the leakage was observed to decrease, before increasing again towards maximum tilt. Again, a direct comparison was made with Bergada's theory. Here a small difference between the results was evident. This was due to Bergada's theory modelling radial flow only, with the CFD model considering a more complex flow pattern. For static conditions, the leakage was observed to increase with an increase in tilt. The relative angular velocity was also observed to have an influence on the rate of leakage. An example of this is shown in Figure 5.14 where the leakage from a tilted slipper, operating at 20μm central clearance, is shown to reduce as the rotational velocity increases. For a perfectly flat slipper, this leakage was more constant, reducing only slightly for a significant increase in velocity.

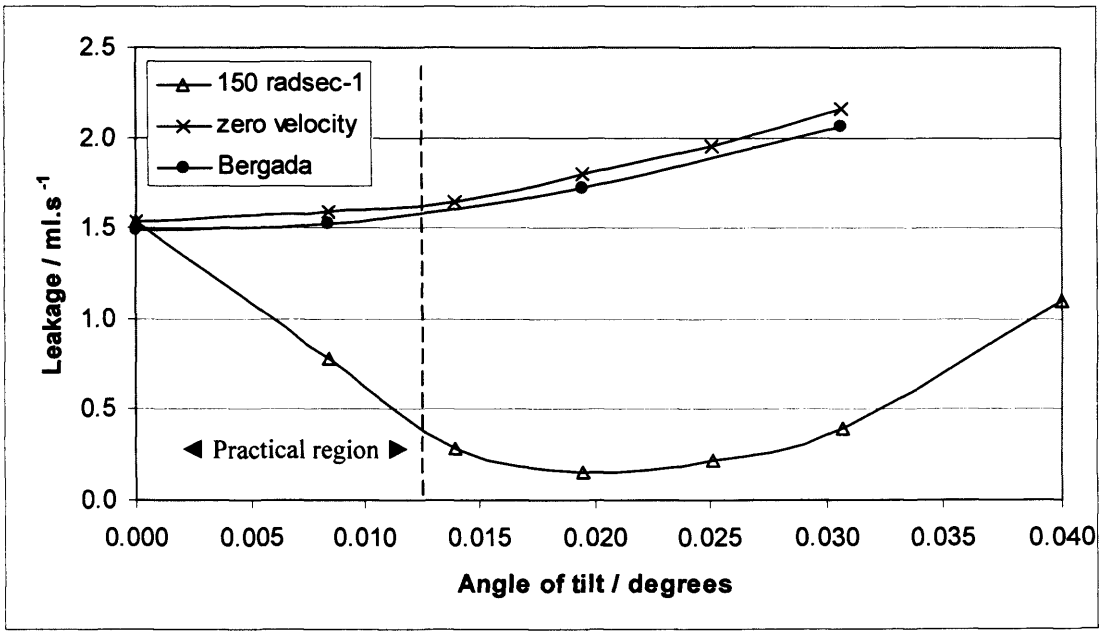

Figure 5.13 Leakage of tilted slipper with and without tangential velocity component

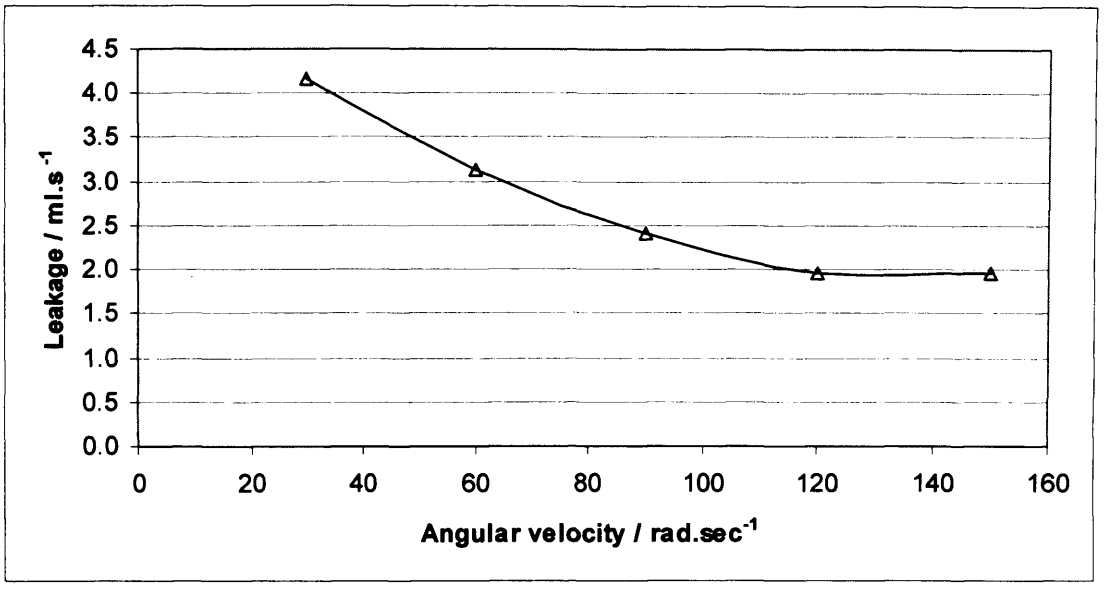

Figure 5.14 Effect of velocity on leakage rate. Slipper with tilt of 0.0307°

5.3.5 Groove location

The rate leakage from the slipper was found to be dependent upon the radial location of the groove. Presented in Figure 5.15 are the leakage rates for a range of groove locations, for a slipper clearance of 10μm. There is a clear trend that moving the groove towards the peripheral of the slipper tends to reduce the leakage. The leakage from a slipper with no groove, and with a clearance of 10μm was found to be 0.422 $ml.s^{-1}$. The presence of a groove, regardless of location, noticeably increased leakage. For a 10μm clearance, this increase was between 7.9 and 14.3%, depending on the location of the groove. Replicating the geometry of the slipper tested in Chapter 4, with a centrally located groove, resulted in an increase of 10.1% over an otherwise identical single land slipper. At increased clearances, however, the leakage rates were higher and as such the presence of a groove had a reduced influence on the increase in flow rate across the slipper face.

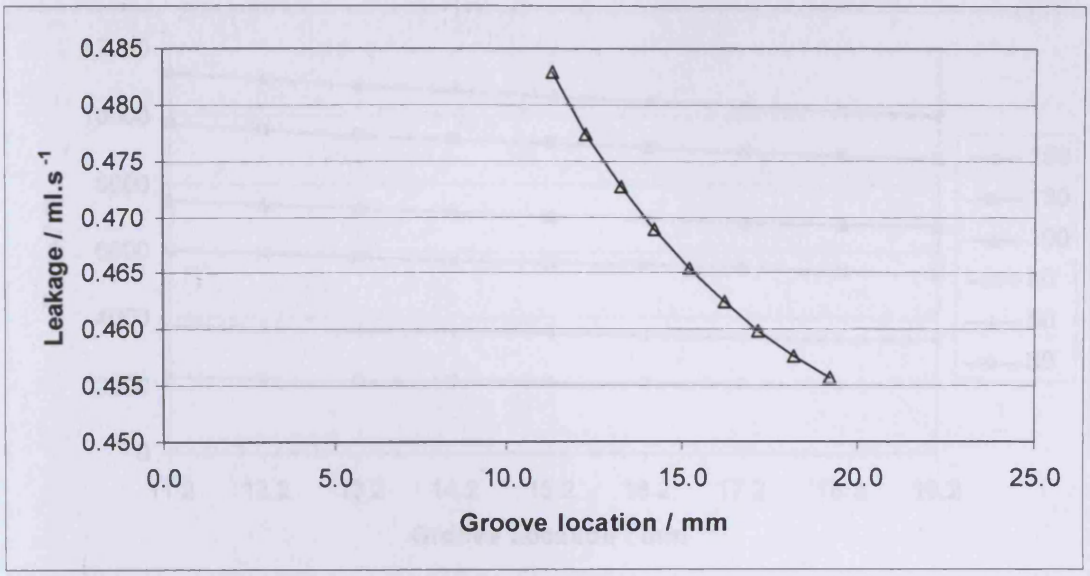

Figure 5.15 Leakage at difference groove locations 150 bar 10μm clearance. Flat slipper with groove depth 0.8mm.

The location of the groove also had an effect on the pressure within it, as shown in Figure 5.16. As there was a negligible pressure drop across the groove in a radial location, the location of the groove also had an influence on the overall hydrostatic lift generated by the slipper, as shown in Figure 5.17.

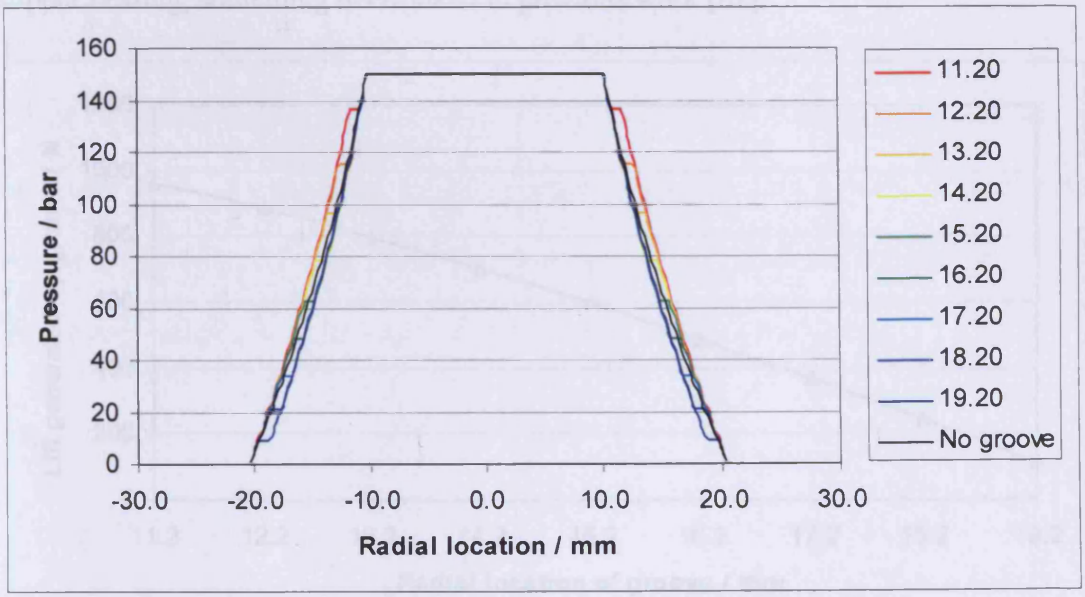

Figure 5.16 Pressure profile across the slipper face at different groove locations with an inlet pressure of 150 bar

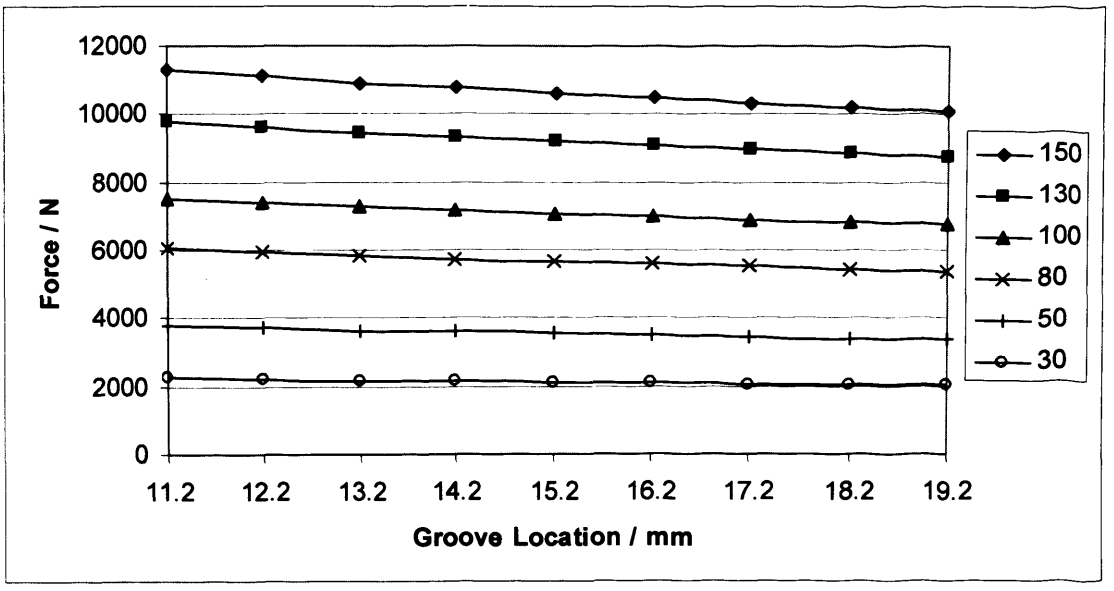

Figure 5.17 Lift generated by flat slipper at different groove locations

Although the effective area of the groove increased as the groove moved towards the outside edge, there was a reduction in pressure within the groove, and hence the lift generated by the groove was observed to reduce, as shown in Figure 5.18. This is clear evidence that the groove does contribute to the hydrostatic lift generated by the slipper bearing, something overlooked in previous work [61].

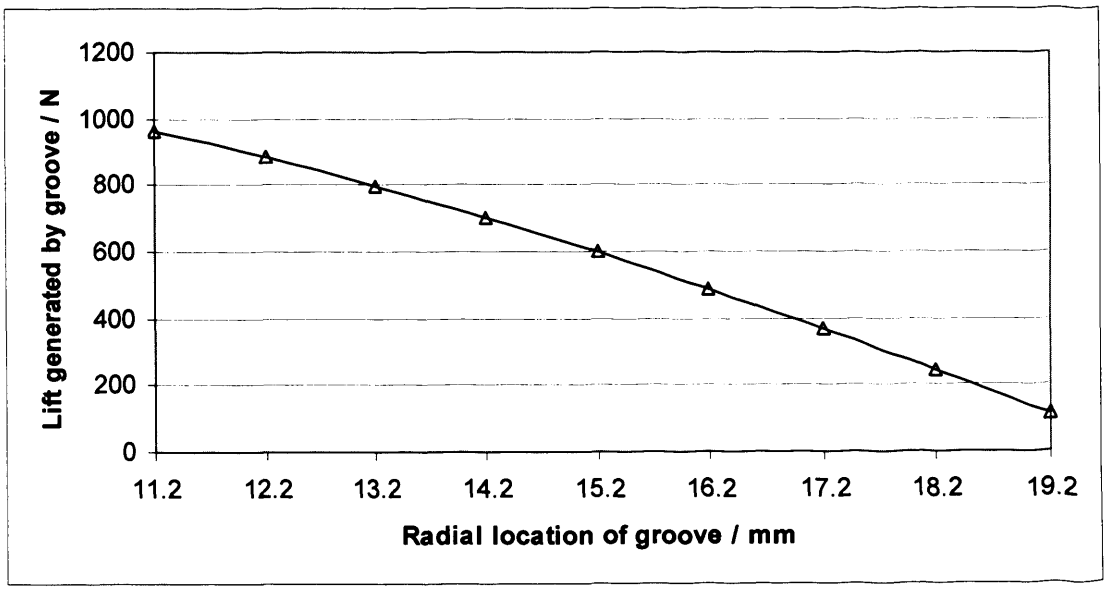

Figure 5.18 Lift generated by groove. Depth of groove 0.8mm.

5.3.6 Modelling of variable clearances

Figure 5.19 illustrates the flow rate through a flat slipper as the clearance varies sinusoidally between 20μm and 31μm, with an angular velocity of 60 radians per second.

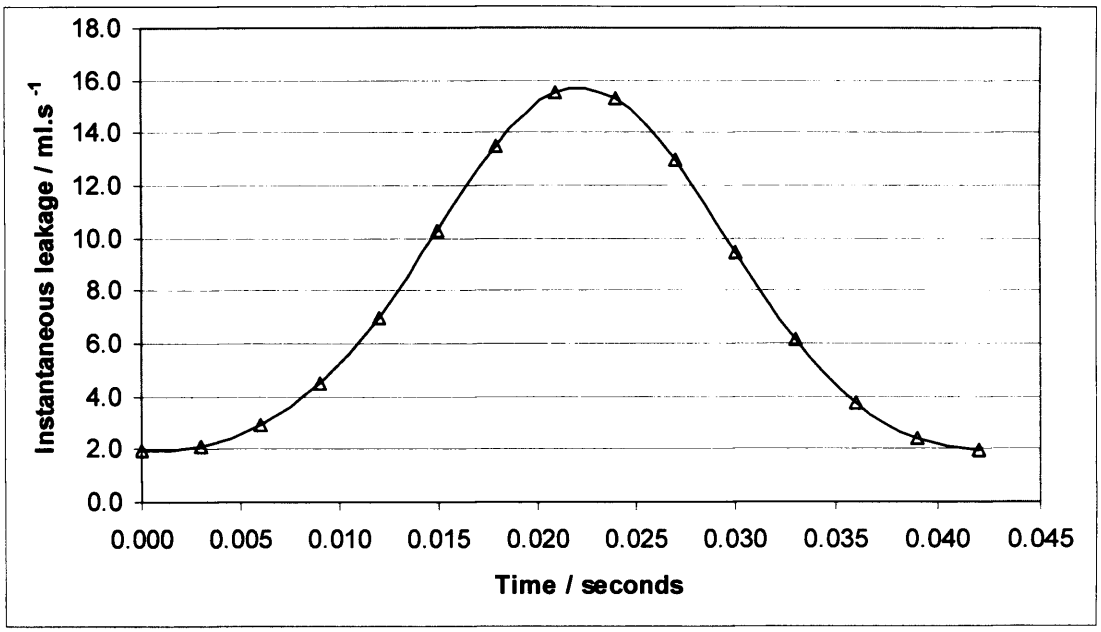

Figure 5.19 Flow rate with varying clearance

With the same variation of clearance, the trend of leakage against angular velocity for both a tilted and flat slipper is shown in Figure 5.20. A curve similar to the one shown in Figure 5.19 was produced for each angular velocity, and hence the flow rates shown in Figure 5.20 are the mean flow rates, and are therefore directly comparable to the leakage rates determined experimentally under dynamic conditions.

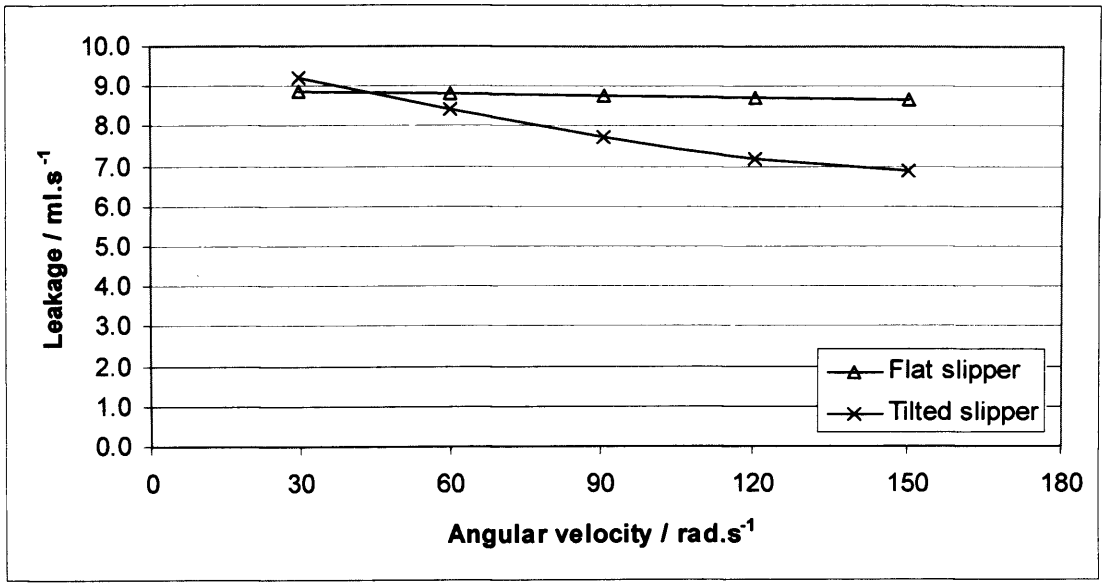

Figure 5.20 Influence of angular velocity on leakage with run-out

The viscosity of the fluid considered within these dynamic CFD models was adjusted to take into account the heating effect of the oil experienced experimentally. As the mean temperature recorded during the experimental tests was 45°C, a kinematic viscosity of 26.4mm^2.s^{-1} was assumed within "FLUENT" [88].

5.4 Discussion

Under stationary conditions, the pressure around the groove was found to be constant when the slipper was flat. This was an expected outcome resulting from the symmetry of only radial flow occurring. The pressure profile across the face of the slipper, as shown in Figure 5.5, demonstrated an excellent correlation with the theory developed by Bergada [60].

From the results obtained, there was always a small pressure differential within the groove for a tilted slipper. This pressure differential was found to be greatest at high angular velocities, with the highest pressure occurring at the part of the groove closest to the trailing edge of the slipper. Both the minimum and maximum pressures within the groove tended to increase with an increase in angular velocity. However the maximum pressure increased more than the minimum, thus increasing the pressure differential across the groove. For the operating conditions studied, the maximum pressure differential occurred for the most tilted slipper, at the highest angular velocity. This pressure differential was 2.66 bar. For all tests using a full depth groove, negligible differences in pressure were present across the width of the groove.

Reducing the depth of the groove was observed to increase the pressure differential within the groove. This was due to the reduction in flow area, thus preventing full equalisation of pressure. The largest impact on groove pressure differential was seen at the smallest groove depths. As such, it is envisioned that increasing the depth beyond 0.8mm would provide little reduction in the pressure differential found within the groove. The CFD models also suggested that the restoring moment acting upon the slipper reduced with an increase in groove depth. This was because the potential

area of high pressure towards the trailing edge of the slipper vented into the groove. This equalisation of pressure caused the minimum pressure within the groove to increase. This suggested that the slipper could operate in a tilted position with more stability than a slipper without a groove.

An increase in groove depth was seen to increase the leakage rate from the slipper. However, the increase in leakage reduced at higher groove depths, and there was no significant change for a groove deeper than 0.32mm.

Under static conditions, flow tended to increase with an increase of slipper inclination. For tilted slippers, the leakage was found to reduce with an increase in angular velocity. This was similar to the experimental findings, although there was a greater reduction in the leakage under the CFD simulations.

For a flat slipper, it was shown that introducing a groove tended to increase the leakage flow rate. Positioning the groove in the location as found in the test apparatus in Chapter 4 created an increase in leakage of approximately 10% when compared to a single-landed slipper. It was found that the closer to the pool the groove was located, the greater the leakage rate of oil. The lift produced by the slipper was also shown to be highest with the groove located at the smallest radius. Although the area of a groove closer to the peripheral of the slipper was larger, the pressure within it was lower. This relationship meant that the lift generated by a groove reduced as the groove was moved radially outwards. It was observed that for two different groove locations, the pressure profile before the smaller groove and after the larger groove was very similar. This is shown in Figure 5.21, and illustrates why the overall lift

generated by a slipper reduced as the groove moves towards the peripheral of the slipper.

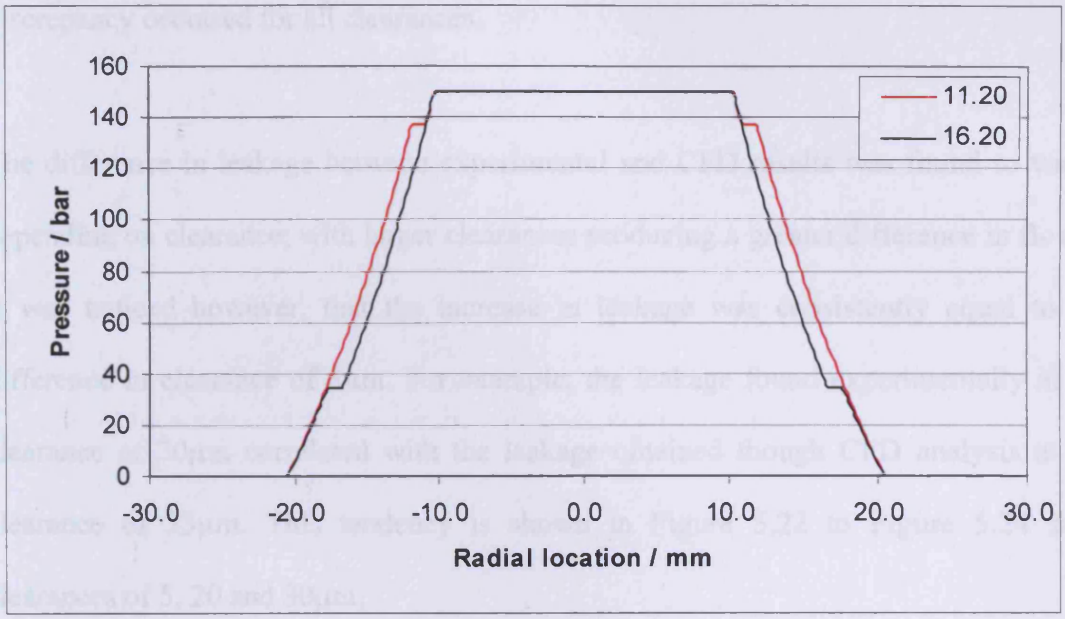

Figure 5.21 Pressure profiles for two groove locations

The results obtained through CFD analysis enabled a validation of the experimental test apparatus developed in Chapter 4. Flow rates obtained through CFD analysis were initially compared with values obtained through theory developed by Bergada (Appendix A.1). These showed an excellent correlation, with a difference of less than 2% for all clearances, thus providing a high level of confidence in the CFD results. The static CFD profiles generated for the pressure characteristics beneath the slipper also exhibited a high level of agreement with those produced by Bergada. For the tilted condition, a small discrepancy was evident between the CFD results and those obtained through theory developed by Bergada. This was due to Bergada's theory only considering radial flow. As such, it is predicted that greater angles of tilt would provide a lower level of correlation.

When comparing leakage flow rates, it was evident that the leakage rates obtained experimentally were greater than the values obtained through CFD analysis. This discrepancy occurred for all clearances.

The difference in leakage between experimental and CFD results was found to vary depending on clearance, with larger clearances producing a greater difference in flow. It was noticed however, that the increase in leakage was consistently equal to a difference in clearance of 3μm. For example, the leakage found experimentally at a clearance of 30μm correlated with the leakage obtained though CFD analysis at a clearance of 33μm. This tendency is shown in Figure 5.22 to Figure 5.24 for clearances of 5, 20 and 30μm.

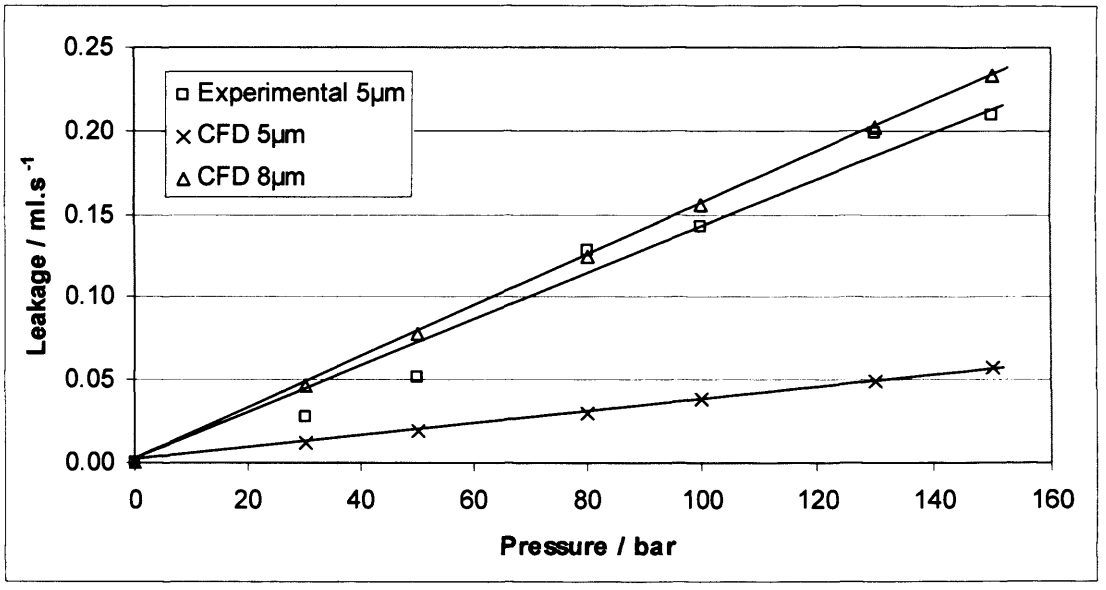

Figure 5.22 Comparison between experimental and CFD leakage rates for a slipper with a 5μm clearance

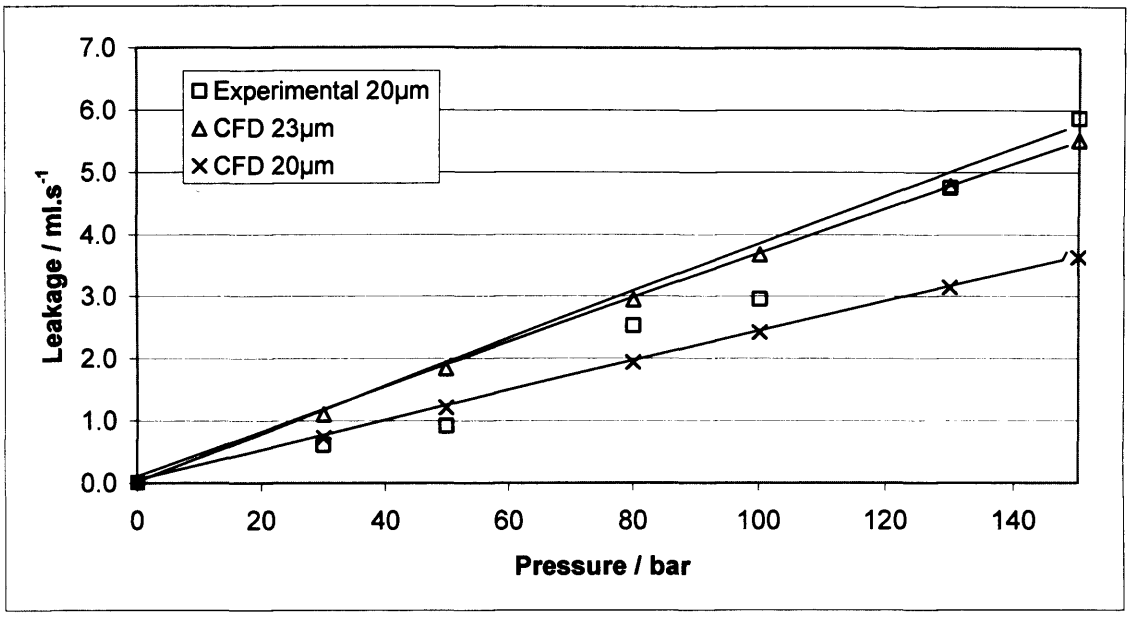

Figure 5.23 Comparison between experimental and CFD leakage rates for a slipper with a 20μm clearance

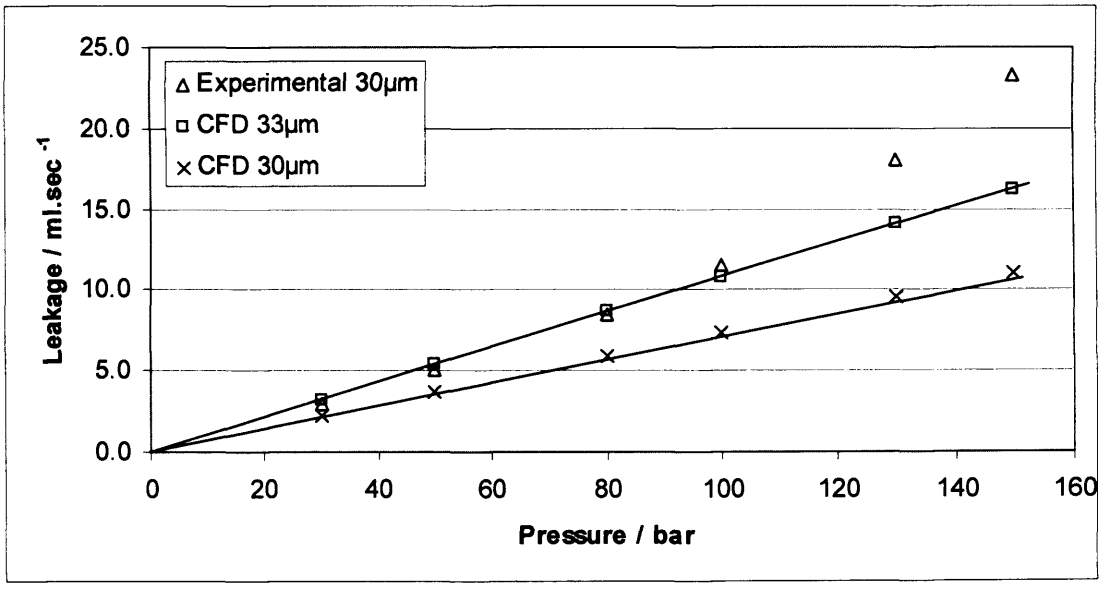

Figure 5.24 Comparison between experimental and CFD leakage rates for a slipper with a 30μm clearance

As this discrepancy was systematic, and observed to be repeatable for all clearances, it is suggested that there was an error in the measurement of the clearance between the

slipper and swash plate. The simplest explanation was an inaccurate zeroing of the displacement sensors. This could have occurred if the slipper was not in contact with the swash plate when the zero displacement reading was taken. This hypothesis was checked; however the correct zero reading was found to be repeatable, and was observed after running each set of tests.

A more likely explanation was due to the surface roughness of the slipper and swash plate surfaces. The roughness profiles shown in Figure 4.16 and Figure 4.17 suggest that surface asperities of both faces prevented full contact, and thus a small gap was present between the slipper and swash plate upon contact. Since the eddy current transducers measured the mean distance to the swash plate the surface, this would have led to subsequent operating clearances having a flow rate characteristic of a slightly larger gap. Referring to the surface profiles, the discrepancy of 3μm in the results seems reasonable: Here the distance between the mean material level and most prominent surface peaks was approximately 1μm for the slipper and 3μm for the swash plate. There is also a possibility that the surfaces were not completely flat. In addition to these factors, the possibility of the slipper deforming under load would have also contributed to the small flow discrepancies observed.

Had there been an error in the actual calibration of each transducer, a proportional error would have been evident, and thus the constant 3μm disparity in clearance would not have been apparent throughout the range of clearances. The possibility of the temperature of the oil influencing the experimental results was considered. Whilst variation in the temperature of the oil may have had a small influence on the results, the difference in results would not have followed the consistent trend outlined above,

and the fact that consistent results were obtained suggests that an error in perceived clearance was the most likely cause. It is accepted that the temperature of the oil could have been a contributory factor however. As the pressure was measured prior to the slipper pool, the pressure within the pool would have been lower than that of the measured value due to a pressure drop across the lubricating orifice. This would have resulted in a lower flow rate than expected. This effect was considered minimal as the pressure drop through the lubricating orifice was deemed to be very small.

The discrepancy in clearance was also identified in the results for a tilted slipper as shown in Figure 5.25.

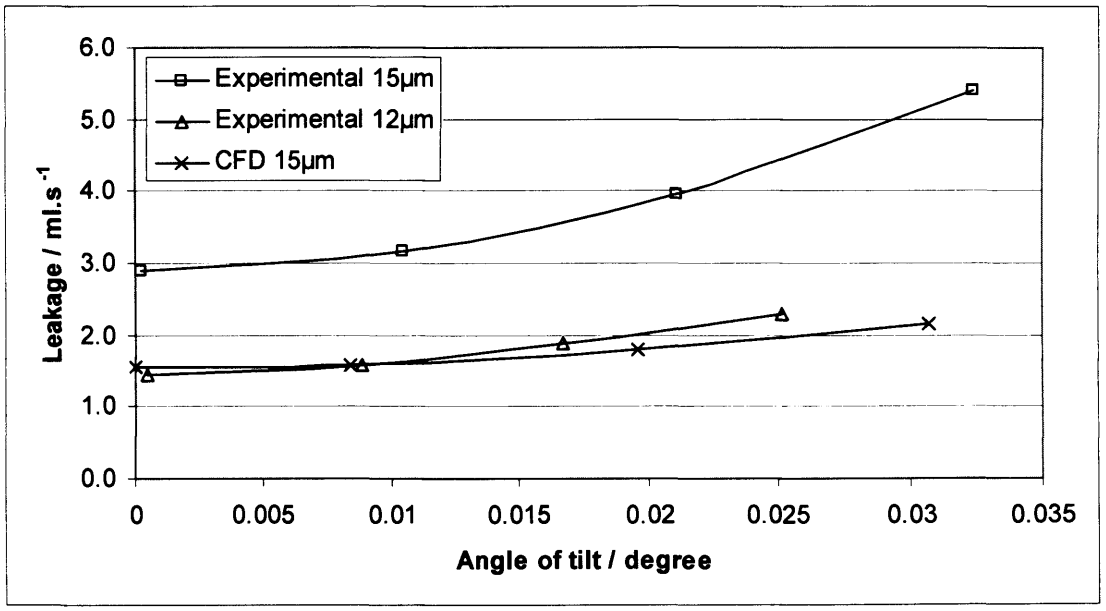

Figure 5.25 Comparison between experimental and CFD results for a tilted slipper

Pressures measured experimentally were found to correlate well with the CFD pressure profiles. An example of this correlation is shown in Figure 5.26, where experimentally measured pressures are superimposed on a CFD generated profile for a clearance of 15µm. Also shown in Figure 5.26 is a pressure profile determined using

theory developed by Bergada. This correlates well with both the experimental and CFD pressure profiles.

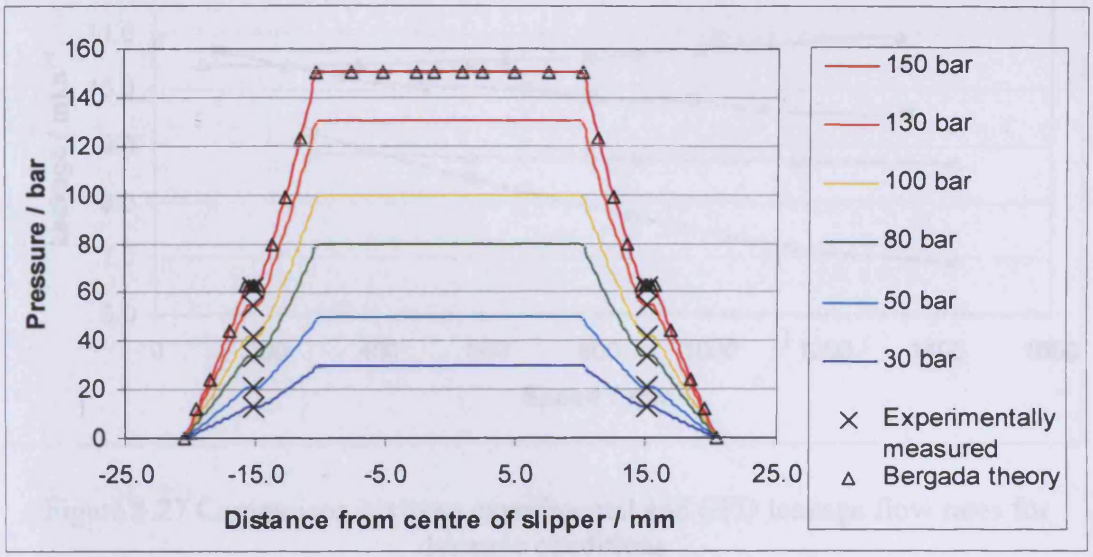

Figure 5.26 Comparison between experimental and CFD pressures

For dynamic conditions, the CFD models predicted a pressure increase within the groove for an increase in rotational velocity. This was also apparent during the experimental tests, although the pressure increase observed was not as great as that predicted by the CFD simulations.

The leakage rates calculated for dynamic conditions via CFD analysis exhibited an excellent likeness to those recorded experimentally. Although lower, the CFD results demonstrated a very similar trend to the experimental values, and therefore provide a high level of validation of the test apparatus, and suggest that the CFD is an appropriate tool for slipper design. Both sets of results shown in Figure 5.27 indicate that for a tilted slipper, the flow rate reduced as the relative speed increased. Both methods suggested a steady leakage rate for a completely flat slipper, regardless of rotational velocity.

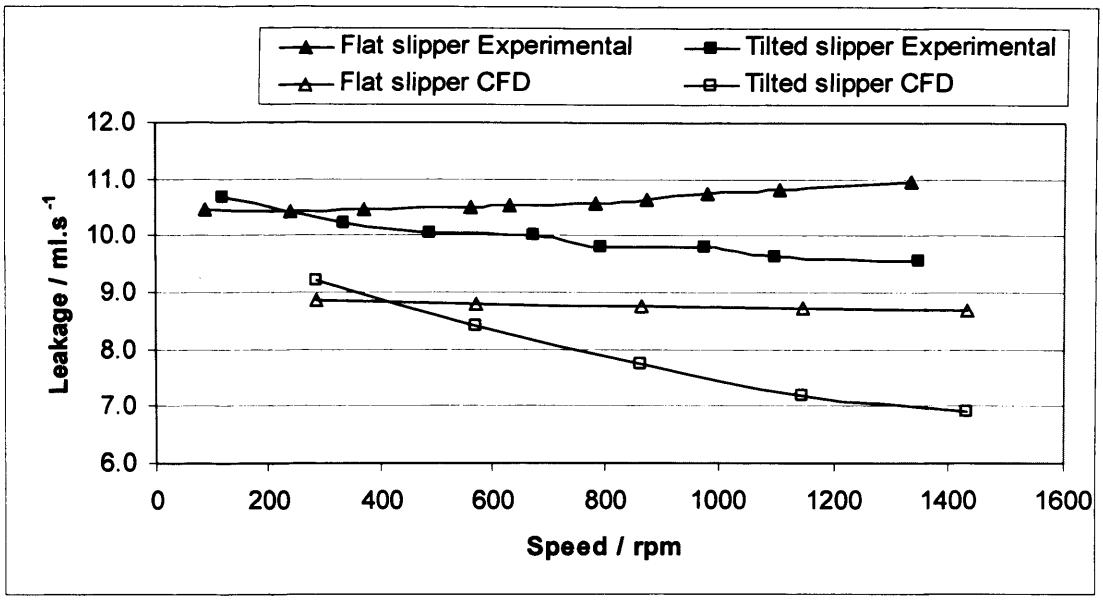

Figure 5.27 Comparison between experimental and CFD leakage flow rates for dynamic conditions

It is clear that the presence of a groove has an effect upon the operation of a slipper. It appears that a groove enables the slipper to operate with a greater level of tilt, as the restoring moment is reduced. In addition, it appears that the groove geometry used experimentally in Chapter 4, is sufficient to enable the groove to work efficiently. This is clear by the fact that negligible pressure differentials were evident within the groove for a wide range of clearances and angles of tilt. It is proposed that increasing the groove depth further would have little impact upon the pressure equalisation within the groove, but would reduce the structural rigidity of the slipper and thus enable it to deform more.

5.5 Conclusions

The main conclusions of the work presented in this chapter are:

1. As a slipper tilts, a restoring moment is generated due to a hydrodynamic effect. This moment tends to restore the slipper to a flat position. The level of pressure, and hence restoring moment, is greatest at large angles of tilt, and when the slipper and swash plate have a high relative velocity.

2. The groove acts to equalise the pressure built up at the trailing edge, thus stabilising the slipper. With a groove, the slipper appears to be more able to operate at an angle to the swash plate. This is because the pressure built up at the trailing edge reduces, thus reducing the restoring moment.

3. The depth of the groove was shown to influence the groove's ability to equalise the pressure around it. Reducing the depth of the groove significantly increased the pressure differential found under tilted conditions. Shallower grooves were therefore associated with greater restoring moments, meaning that the slipper was less able to remain tilted with a shallow groove.

4. The location of the groove on the face of the slipper was found to influence the potential leakage flow rate. In addition, it was seen to influence the hydrostatic lift generated by the slipper.

5. Under static conditions, tilt increased the leakage rate from the slipper, for a given central clearance. Under dynamic conditions, however, a slipper with a

greater leading edge clearance was seen to exhibit a smaller leakage rate than a perfectly flat slipper.

6. CFD results provided a good correlation with the experimental data collected. However a small discrepancy was identified in the leakage flow rate which was attributed to the surface roughness and flatness of the slipper and swash plate.

Chapter 6. Conclusions and Further Work

6.1 Conclusions

In Chapter 3 a three-dimensional CFD model of an axial piston pump was presented. All major leakage paths were considered within this model except the leakage between each piston and its corresponding bore. To model this leakage a separate 2-D axis-symmetric model of a single piston was presented. These models indicated that the pump leakage was dominated by the clearance between the cylinder barrel and port plate. Thus a small increase in clearance would have a significant impact on the volumetric efficiency of the pump.

The pressure within selected piston bores was measured experimentally, and a pressure ripple was noted with a frequency corresponding to pistons entering the discharge port. The ripple was due to an equalisation of pressure: The low pressure within a cylinder rapidly increased upon entry to the discharge port. This equalisation of pressure therefore reduced the pressure within the cylinders already in the discharge port.

An experimental test apparatus was designed and developed to analyse the leakage from a slipper. The test rig used a unique design to enable accurate control and measurement over the position of the slipper. Using a series of opposing screws, the clearance and angle could be adjusted whilst the slipper was under hydraulic load, thus enabling complete control over the position of the slipper.

The leakage was successfully measured under both static and dynamic conditions. When the slipper was at a large angle to the swash plate, an increase in rotational velocity produced a downward trend in leakage. This trend was observed both

experimentally and through the CFD analysis. For a flat slipper the leakage rates were less affected by velocity. Here both the experimental and CFD analyses suggested that the leakage was largely unaffected by a tangential velocity component.

The pressure within the slipper groove was measured experimentally in four locations. For most operating conditions no difference was identified between these readings, suggesting that the pressure around the circumference of the groove remained constant. For large angles, a pressure differential up to 2 bar was apparent. However, as the CFD analyses showed, this differential would have been significantly higher without the groove.

A series of CFD models demonstrated how the behaviour of a slipper is influenced by the existence of a groove. The leakage flow rate from a slipper, which is clearly of importance from an efficiency point of view, was shown to be influenced by both the presence and location of a groove. The groove was also shown to reduce the restoring moment of the slipper under tilted conditions, thus enabling the slipper to operate with a larger angle of tilt than an otherwise identical single-land slipper. The reduction in restoring moment occurred because the hydrodynamic pressure built up towards the trailing edge of the slipper was able to vent around the groove to the leading edge of the slipper. The CFD results showed that a groove depth of 0.8mm was sufficient for this size of slipper, and that any increase in depth would produce little reduction in pressure differential around the groove. Increasing the depth further would potentially however, reduce the rigidity of the slipper enabling more deformation to occur.

6.2 Further Work

The aim of the work in this thesis was to analyse the leakage characteristics and slipper operation of an axial piston pump. In achieving this aim, a number of aspects have been identified that would benefit from further development.

6.2.1 Axial piston pump analysis

A full CFD model of a pump was developed; with leakage paths modelled using a porous mesh technique. This model was fully dynamic and developed an overall pressure as a function of output flow. When the computing power is available, this model could be extended to incorporate the work presented in chapter 5 within a single model. In addition, a mesh dense enough to model cavitation effects could be applied to the geometry when computing power permits.

6.2.2 Experimental investigation of slipper behaviour

6.2.2.1 Flow measurement under dynamic conditions

A new test apparatus was developed to investigate the operating characteristics of a grooved slipper. The measurement of pressure and flow rate was straightforward for the static conditions. Measuring the flow of oil under dynamic conditions was more time consuming. To eliminate the heating effect, a cooling mechanism could be introduced, to prevent the heating of the bearings. This, however, would require a significant time of development, as the bearings were lubricated by the oil flowing through the slipper. Also it should be stated that successful results were obtained using the existing test apparatus, although they were time consuming to obtain for uniform temperature conditions. If further work is to be undertaken on this apparatus however, these recommendations should be considered.

6.2.2.2 Temperature measurement

Potentially, thermocouples could be installed on the face of the slipper to provide a continuous temperature measurement. This would replace the infrared thermometer used during this work.

6.2.2.3 Force measurement

An additional modification is required to enable satisfactory force measurements to be obtained. The current design of the test apparatus meant that a moment on each load cell was unavoidable. Therefore further work needs to be undertaken to either implement load cells insensitive to moments, or to redesign the test apparatus to avoid moments at the location of the load cells.

6.2.2.4 Slipper geometry

The slipper used within the test rig was well characterised for a wide range of operating conditions. An experimental investigation into alternative slipper geometries, including groove location would be of benefit, and could be compared to the results obtained during this investigation.

6.2.2.5 Water-based fluids

Since the test apparatus was manufactured from stainless steel and aluminium, there is scope for repeating the work carried out in this study using water-based fluids.

6.2.3 CFD modelling of the slipper

Although beyond the realm of the current CFD package available, it may be possible in future developments to model the film of fluid beneath the slipper with a self adjusting clearance based upon the pressure applied in the cylinder bore.

References

1 **Dobchuk, J.W., Burton, R.T., Nikiforuk, P.N. and Ukrainetz, P.R.** Mathematical modelling of a variable displacement axial piston pump. *Fluid Power Systems and Technology*, 1999, **6**, 1-8.

2 **Milestone, W.D., Solomon, A. and Olsen, G.** The kinematic analysis of axial-piston pumps. *Mechanism and Machine Theory*, 1983, **18**(6), 475-479.

3 **Zhang, X., Cho, J., Nair, S.S. and Manring, N.D.** Damping on the swash plate of an axial-piston pump. *Proceedings of the American Control Conference*, pp. 3590-3594Illinois, 2000).

4 **Kaliafetis, P. and Costopoulos, T.** Modelling and simulation of an axial piston variable displacement pump with pressure control. *Mechanical Machine Theory*, 1995, **30**(4), 599-612.

5 **Wieczorek, U. and Ivantysynova, M.** CASPAR - A computer aided design tool for axial piston machines. *Bath Workshop on Power Transmission and Motion Control*, pp. 113-126 Bath, UK, 2000).

6 **Ivantysynova, M.** A new approach to the design of sealing and bearing gaps of displacement machines. *Proceedings of the Fourth JHPS International Symposium on Fluid Power*, pp. 45-50 Tokyo, 1999).

7 **Huang, C. and Ivantysynova, M.** An advanced gap flow model considering piston micro motion and elastohydrodynamic effect. *4th Fluid Power Net International*Sarasota, FL, USA, 2006).

8 **Ivantysynova, M. and Lasaar, R.** An investigation into micro- and macrogeometric design of piston / cylinder assembly of swash plate machines. *International Journal of Fluid Power*, 2004, **5**(1), 23-36.

9 **Lasaar, R.** The influence of the microscopic and macroscopic gap geometry on the energy dissipation in the lubricating gaps of displacement machines. *1st Fluid Power Net International PhD Symposium*, pp. 101-116Hamburg, 2000).

10 **Lasaar, R. and Ivantysynova, M.** Gap geometry variations in displacement machines and their effect on the energy dissipation. *International Conference on Fluid Power Transmission and Control* pp. 296-301Hangzhou, China, 2001).

11 **Armbruster, C., Botelle, E. and Lebrun, M.** Modelling an axial piston hydraulic pump. *International Conference on Hydraulics and Pneumatics*, 2003, **18**, 479-489.

12 **Gilardino, L., Mancò, S., Nervegna, F. and Viotto, F.** An experience in simulation: The case of a variable displacement axial piston pump. *JFPS International Symposium on Fluid Power*, pp. 85-91Yokohama, Japan, 1996).

13 **Edge, K.A. and Vaughan, N.D.** Investigation of the effects of swashplate angle and suction timing on the noise generation potential of an axial piston pump. *Fluid Power Systems and Technology*, 1998, **5**, 77-82.

14 **Harrison, A.M. and Edge, K.A.** Reduction of axial piston pump pressure ripple. *Proceedings of the IMechE*, 2000, **214**(I), 53-63.

15 **Yamaguchi, A.** Studies on the characteristics of axial plunger pumps and motors. *Bulletin of the JSME*, 1966, **9**(34), 305-313.

16 **Wiklund, P. and Svedberg, G.C.** Using computational fluid dynamics (CFD) to analyse the inlet flow of an axial piston pump. *Scandinavian International Conference on Fluid Power*, pp. 45-59Sweden, 1997).

17 **Wiklund, P. and Svedberg, G.C.** 3D-CFD, a possibility to analyse piston pump flow dynamics. *Bath International Fluid Power Workshop*Bath, UK, 1997).

18 **Fey, C.G., Totten, G.E. and Sun, Y.H.** Analysis of common failure modes of axial piston pumps. *Hydraulic Failure Analysis: Fluids, Components, and System Effects* (American Society for Testing & Materials, 2001).

19 **K A Edge, K.A. and de Freitas, F.J.T.** A study of pressure fluctuations in the suction lines of positive displacement pumps *Proceedings of the Institution of Mechanical Engineers, Part B: Management and Engineering Manufacture*, 1985, **199**(B4), 211-217.

20 **Edge, K.A. and Wing, T.J.** The measurement of the fluid borne pressure ripple characteristics of hydraulic components. *Proceedings of the Institution of Mechanical Engineers, Part B: Management and Engineering Manufacture*, 1983, **197**, 247-254.

21 **Manring, N.D.** The discharge flow ripple of an axial-piston swash-plate type hydrostatic pump. *Journal of Dynamic Systems, Measurement, and Control*, 2000, **122**, 263-268.

22 **Jun, Z. and Yi, W.** Research for pressure and flow pulsating characteristic of swash plate axial piston pump with even pistons. *International Conference on Fluid Power Transmission and Control* pp. 325-327Hangzhou, 1985).

23 Masuda, K. and Ohuchi, H. Noise reduction of a variable piston pump with even number of cylinders. *JFPS International Symposium on Fluid Power*, pp. 91-96Yokohama, Japan, 1996).

24 Helgestad, B.O., Foster, K. and Bannister, F.K. Pressure transients in an axial piston hydraulic pump. *Proceedings of the Institute of Mechanical Engineers*, 1974, **188**(17), 189-199.

25 Martin, M.J. and Taylor, R. Optimised port plate timing for an axial piston pump. *The Fifth International Fluid Power Symposium*, pp. 51-66 (BRHA Fluid Engineering, University of Durham, UK, 1978).

26 Manring, N.D. Valve-plate design for an axial piston pump operating at low displacements. *Journal of Mechanical Design*, 2003, **125**, 200-207.

27 Manring, N.D. and Zhang, Y. The improved volumetric-efficiency of an axial-piston pump utilizing a trapped-volume design. *Journal of Dynamic Systems, Measurement, and Control*, 2001, **123**, 479-487.

28 Karkoub, M.A., Gad, O.E. and Rabie, M.G. Predicting axial piston pump performance using neural networks. *Mechanism and Machine Theory*, 1999, **34**, 1211-1226.

29 Manring, N.D. Designing a control and containment device for cradle-mounted, axial-actuated swash plates. *Journal of Mechanical Design*, 2002, **124**, 456-464.

30 **Manring, N.D.** Designing a control and containment device for cradle-mounted transverse-actuated swash plates. *Journal of Mechanical Design*, 2001, **123**, 447-455.

31 **Manring, N.D.** The control and containment forces on the swashplate of an axial piston pump utilizing a secondary swash-plate angle. *Proceedings of the American Control Conference*, pp. 4837-4842 Anchorage, 2002).

32 **Manring, N.D. and Dong, Z.** The impact of using a secondary swash-plate angle within an axial piston pump. *Journal of Dynamic Systems, Measurement, and Control*, 2004, **126**, 65-74.

33 **Fairhurst, M.R.** Design analysis of an axial piston pump operating with a water-based fluid *Cardiff School of Engineering*, p. 184 (Cardiff University, 2001).

34 **Halling, J.** *Principles of Tribology*. (The Macmillian Press Ltd, 1975).

35 **Pettersson, U. and Jacobson, S.** Textured surfaces for improved lubrication at high pressure and low
sliding speed of roller / piston in hydraulic motors. *Triboligy International*, 2007, **40**.

36 **Kazama, T. and Yamaguchi, A.** Application of a mixed lubrication model for hydrostatic thrust bearings of hydraulic equipment. *Journal of Tribology*, 1993, **115**, 686-691.

37 **Koc, E., Hooke, C.J. and Li, K.Y.** Slipper balance in axial piston pumps and motors. *Journal of Tribology*, 1992, **114**, 766-773.

38 Manring, N.D. Tipping the cylinder block of an axial-piston swash-plate type hydrostatic machine. *Journal of Dynamic Systems, Measurement, and Control*, 2000, **122**, 216-221.

39 Yamaguchi, A., Sekine, H. and Ishida, S. Bearing / seal characteristics of the film between a valve plate and a cylinder block of axial piston pumps: Effects of fluid types and theoretical discussion. *Journal of Fluid Control*, 1990, **20**(4), 7-29.

40 Kim, J. and Jung, J. Measurement of fluid film thickness on the valve plate in oil hydraulic axial piston pumps (I) Bearing pad effects. *KSME International Journal*, 2003, **17**(2), 246-253.

41 Jacazio, G. and Vatta, F. The block-lift in axial piston hydraulic motors. *Joint ASME / ASCE Bioengineering, Fluids Engineering and Applied Mechanics Conference* Boulder, Colorado, 1981).

42 Bergada, J.M. and Watton, J. A new approach towards the understanding of the flow in small clearnces applicable to hydraulic pump pistons with pressure balancing grooves. *JFPS International Symposium on Fluid Power*, pp. 259-264Nara, Japan, 2002).

43 Bergada, J.M. and Watton, J. A new approach towards the understanding of the flow in small clearances applicable to hydraulic pump pistons with pressure balancing grooves. *International Symposium on Fluid Control, Measurement, and Visualisation*Sorrento, Italy, 2003).

44 Yamaguchi, A. Motion of pistons in piston-type hydraulic machines (3rd report: Exponential function-type piston). *JSME*, 1976, **19**(130), 413-419.

45 Sadashivappa, K., Singaperumal, M. and Narayanasamy, K. On the efficiency of the axial piston motor considering piston form deviations. *Mechatronics*, 1996, **6**(3), 283-301.

46 Tanaka, K., Nakahara, T. and Kyogoku, K. Half-frequency whirl of pistons in axial piston pumps and motors under mixed lubrication. *Proceedings of the IMechE*, 2003, **217**(Part J), 93-102.

47 Hooke, C.J. and Kakoullis, Y.P. The lubrication of slippers in axial piston pumps. *The Fifth International Fluid Power Symposium*, pp. 13-26 (BRHA Fluid Engineering, University of Durham, UK, 1978).

48 Fisher, M.J. A theoretical determination of some characteristics of a tilted hydrostatic slipper bearing. *The British Hydromechanics Research Association*, 1962, **RR728**.

49 Safar, Z.S. and Mote, C.D. Analysis of hydrostatic thrust bearings under non-axisymmetric operation. *Wear*, 1979, **61**, 9-20.

50 Safar, Z.S. Design of tilted hydrostatic thrust bearings. *Wear*, 1981, **70**, 243-248.

51 Iboshi, N. and Yamaguchi, A. Characteristics of a slipper bearing for swash plate type axial piston pumps and motors, 1st report, Theoretical analysis. *Bulletin of the JSME*, 1982, **25**(210), 1921-1930.

52 Iboshi, N. and Yamaguchi, A. Characteristics of a slipper bearing for swash plate type axial piston pumps and motors, 2nd report, Experiment. *Bulletin of the JSME*, 1983, **26**(219), 1583-1589.

53 **Takahashi, K., Ishizawa, S. and Wang, Z.** Viscous flow between parallel disks with a time varying gap width and a central fluid source. *JFPS International Symposium on Fluid Power* Tokyo, Japan, 1989).

54 **Harris, R.M., Edge, K.A. and Tilley, D.G.** Predicting the behaviour of slipper pads in swashplate-type axial piston pumps. *ASME Winter Annual Meeting* (ASME, New Oeleans, Louisiana, 1993).

55 **Harris, R.M., Edge, K.A. and Tilley, D.G.** Slipper pads in swashplate-type axial piston pumps. *Journal of Dynamic Systems, Measurement, and Control*, 1996, **118**, 41-47.

56 **Manring, N.D.** Slipper tipping within an axial-piston swash-plate type hydrostatic pump. *Fluid Power Systems and Technology*, 1998, **5**, 169-175.

57 **Kazama, T. and Yamaguchi, A.** Experiment on mixed lubrication of hydrostatic thrust bearings for hydraulic equipment. *Journal of Tribology*, 1995, **117**, 399-402.

58 **Canbulut, F., Yildirim, S. and Sinanoğlu, C.** Design of an artificial neural network for analysis of frictional power loss of hydrostatic slipper bearings. *Tribology letters*, 2004, **17**(4), 887-899.

59 **Canbulut, F., Sinanoğlu, C., Yildirim, S. and Koc, E.** Design of neural network model for analyising hydrostatic circular recessed bearings with axial piston pump slipper. *Industrial Lubrication amd Tribology*, 2004, **56**(5), 288-299.

60 Bergada, J.M. and Watton, J. Axial piston pump slipper balance with multiple lands. *ASME International Mechanical Engineering Congress & Exposition*, pp. 69-74 (ASME, New Orleans, Louisiana, 2002).

61 Koc, E. and Hooke, C.J. Considerations in the design of partially hydrostatic slipper bearings. *Tribology International*, 1997, **30**(11), 815-823.

62 Hooke, C.J. and Kakoullis, Y.P. The effects of a centrifugal load and ball friction on the lubrication of slippers in axial piston pumps. *International Fluid Power Symposium* Cambridge, England, 1981).

63 Hooke, C.J. and Li, K.Y. The lubrication of overclamped slippers in axial piston pumps - centrally loaded behaviour. *Proceedings of the IMechE*, 1988, **202**, 287-293.

64 Koc, E. and Hooke, C.J. A description of an on-line clearance (Oil film thickness) measurement technique developed - An application to slipper bearings. *ASME Modelling Measurement and Control*, 2000, **69**(2), 19-34.

65 Hooke, C.J. and Li, K.Y. The lubrication of slippers in axial piston pumps and motors - the effects of tilting couples. *Proceedings of the IMechE*, 1989, **203**, 343-350.

66 Koc, E. and Hooke, C.J. Investigation into the effects of orifice size, offset and overclamp ratio on the lubrication of slipper bearings. *Tribology International*, 1996, **29**(4), 299-305.

67 Hooke, C.J. and Kakoullis, Y.P. The effects of non-flatness on the performance of slippers in axial piston pumps. *Proceedings of the IMechE*, 1983, **197C**, 239-247.

68 Manring, N.D., Johnson, R.E. and Cherukuri, H.P. The impact of linear deformations on stationary hydrostatic thrust bearings. *Journal of Tribology*, 2002, **124**, 874-877.

69 Manring, N.D., Wray, C.L. and Dong, Z. Experimental studies on the performance of slipper bearings within axial-piston pumps. *Journal of Tribology*, 2004, **126**, 511-518.

70 Bergada, J.M. and Watton, J. Force and flow through hydrodynamic slippers with grooves. *8th International Symposium on Fluid Control, Measurement and Visualisation*Chengdu, China, 2005).

71 Bergada, J.M. and Watton, J. Optimisation of the lift characteristics of an axial piston pump grooved slipper. *JFPS International Symposium on Fluid Power*Tsukuba, Japan, 2005).

72 Li, K.Y. and Hooke, C.J. A note on the lubrication of composite slippers in water-based axial piston pumps and motors. *Wear*, 1991, **147**, 431-437.

73 Li, Z. Development of hydraulic pump to operate with raw water. *Proceedings of ASME Fluids Engineering Division Summer Meeting* Washington DC, USA, 1998).

74 Nie, S.L., Huang, G.H. and Li, Y.P. Tribological study on hydrostatic slipper bearing with annular orifice damper for water hydraulic axial piston motor. *Tribology International*, 2006, **39**, 1342-1354.

75 **Shudong, Y., Zuyao, Y., Xiaofeng, H. and Zhuangyun, L.** Study on slippers for raw water hydraulic axial piston pumps and motors. *International Symposium on Fluid Power Transmission and Control* Harbin, China, 1999).

76 **Dong, W., Zhuangyun, L. and Yuquan, Z.** Study of the key problems in a water hydraulic piston pump and its applications. *Industrial Lubrication and Tribology*, 2001, **53**(5), 211-216.

77 **Pai, R. and Hargreaves, D.J.** Performance of environment-friendly hydraulic fluids and material wear in cavitating conditions. *Wear*, 2002, **252**(11-12), 970-978.

78 **Donders, S. and Backé, W.** Optimisation of high-pressure piston pumps for HFA fluids. *Scandinavian International Conference on Fluid Power*, pp. 123-138 Sweden, 1997).

79 **Tan, A.C.H., Chua, P.S.K. and Lim, G.H.** Fault diagnosis of water hydraulic actuators under some simulated faults. *Journal of Materials Processing Technology*, 2003, **138**, 123-130.

80 **Huanlong, L., Jian, K., Guozhi, W. and Lanying, Y.** Research on the lubrication characteristics of water hydraulic slipper friction pairs. *Proceedings of the Institution of Mechanical Engineers, Part C: Journal of Mechanical Engineering Science*, 2006, **220**(10), 1559-1567.

81 **Fairhurst, M.R. and Watton, J.** CFD analysis of a pump pressure compensator operating with a water-based fluid. *Power Transmission and Motion Control* (Professional Engineering Publishing Ltd, Bath, 2001).

82 **Massey, B. and Ward-Smith, J.** *Mechanics of Fluids.* (Stanley Thornes Ltd, 1998).

83 **Ivantysynova, M.** Temperaturfeld im Schmierspalt zwischen Kolben und Zylinder einer Axialkolbenmaschine. *Maschinenbautechnik*, 1985, **34**(12), 532 - 535.

84 **Ivantysyn, J. and Ivantysynova, M.** *Hydrostatic Pumps and Motors, principles, designs, performance, modelling, analysis, control and testing.* (Akademia Books International, New Dehli, 2001).

85 **Watton, J.** Fluid Power Systems, modelling, simulation analog and microcomputer control. (Prentice Hall, 1989).

86 **Yamaguchi, A. and Ishikawa, T.** Characteristics of displacement mechanisms in axial piston pumps. *Bulletin of the JSME*, 1979, **22**(165), 356-361.

87 **Micro-Epsilon**. http://www.micro-epsilon.com. p. Documentation on eddyNCDT3010 Sensor System (Micro-Epsilon Messtechnik GmbH, 2006).

88 **Shell**. Shell Tellus Hydraulic Oils Data Sheet. p. 3 (Shell, 2003).

89 **Deutschman, A.D., Michels, W.J. and Wilson, C.E.** *Machine design theory and practice.* (Macmillan Publishing Co., Inc., 1975).

90 **Moot, R.L.** *Machine elements in mechanical design.* (Charles E. Merrill Publishing Company, 1985).

91 **SKF-Group**. http://www.skf.com. p. Bearing data and specifications. Interactive Engineering Catalogue (SKF, 2006).

Appendix A

A.1 Paper currently under review

Leakage and groove pressure of an axial piston pump slipper with multiple lands

JM Bergada[1], JM Haynes[2], J Watton[2]

[1] Fluid Mechanics Department ETSEIT UPC , Colon 11 Terrassa 08222, Spain.
Tel. 0034-937398771. Fax. 0034-937398101. **bergada@mf.upc.edu**

[2] Cardiff School of Engineering. Cardiff University. Queen's Buildings.
The parade PO Box 925 Cardiff CF24 0YF Wales UK.Cardiff University UK
Tel. 0044-2920874797. **wattonj@cardiff.ac.uk**

Abstract

The paper presents a new analytical method, based on Reynolds equation of lubrication, to evaluate the leakage and pressure distribution for an axial piston pump slipper taking into account the effect of grooves. The equations consider slipper spin and tilt and are extended to be used for a generic slipper with any number of grooves. A test rig has been designed and used to check experimentally the applicability of the theoretical equations. Comparisons between theoretical and experimental results show a good agreement. The new theory can predict slipper leakage and pressure inside the groove with a high level of accuracy, especially at low slipper tilts that exist in practice. Experimentally, it is demonstrated that although a groove maintains a constant pressure along its path, under some conditions a pressure differential exists inside the groove. The effect of tangential velocity on groove pressure and slipper leakage is then studied experimentally, showing that as the rotational speed increases, there is a small decrease in leakage and a small increase in the average pressure inside the groove.

Key words: axial piston slipper, multiple lands, Reynolds equation solution

Nomenclature

h slipper general height (m).

h_{01} slipper pocket central clearance (m).

h_{02} slipper first land central clearance (m).

h_{03} slipper groove central clearance (m).

k_1, k_3, k_5, k_7, k_L,C constants (Nm).

k_2, k_4, k_6, k_8, k_M constants (Pa).

P_i general pressure (Pa).

P_{inlet} pressure at the slipper central pocket for a radius r_0 (Pa).

Q_i generalised flow (m^3/s).

r slipper generic radius (m).

r_0 slipper central pocket orifice radius (m).

r_1 inner land inside radius (m).

r_2 inner land outside radius (m).

r_3 outer land inside radius (m).

r_4 outer land outside radius (m).

r_m average radius between land borders (m).

r_{m1} average radius between slipper pocket borders (m).

r_{m2} average radius between inner land borders (m).

r_{m3} average radius between groove borders (m).

r_{m4} average radius between outer land borders (m).

u general linear velocity (m/s).

α slipper tilt angle (rad)

μ fluid dynamic viscosity. (Kg/m s).

θ slipper angle (rad).

ω slipper angular velocity, slipper spin (rad/s).

1. Introduction

Flow rates through small gaps in positive displacement pumps are usually considered to be laminar. In the majority of cases the effect of pressure balancing grooves cut on pistons and slippers has been neglected. The effect of the groove on the flow and pressure distribution is not expected to give a completely different pattern from previous work using single-land theory. The theory developed in this paper is a step forward towards a better understanding of the effect. The main piston and slipper assembly that originated this study is shown in figure 1. This is one of nine pistons from a pump with a maximum volumetric displacement of 0,031 dm^3 /rev. It will be seen that the slipper design uses two full lands. An alternative approach is to include additional slots cut across the second land to balance the groove pressure and outlet pressure, but the approach selected seems to be the corporate design philosophy of the particular pump manufacturer.

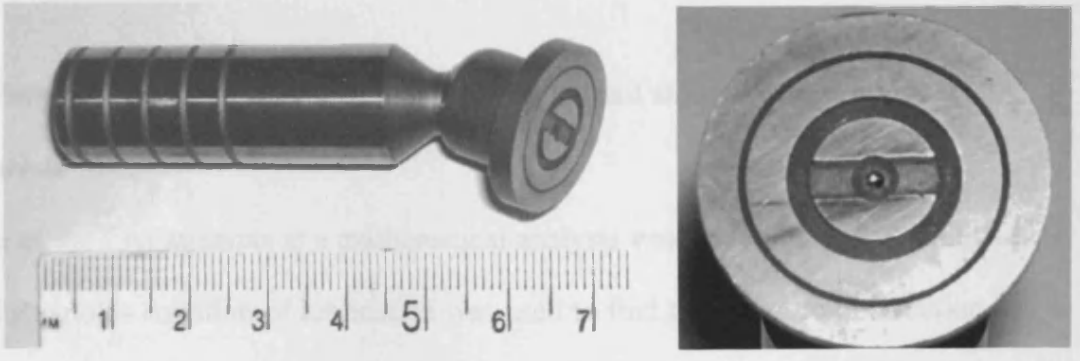

Figure 1. Piston and slipper assembly [Courtesy Oilgear Towler UK Ltd]

There have been many publications in this general subject area over the past 30 years, many concerned with improving the performance of piston pumps and motors. Most of the work has focused on analyzing the forces and torques over the slipper, both

experimentally and analytically [1-3, 5-10, 15-17, 19, 20,]. The effects of slipper spin, tangential velocity, tilt, slipper non-flatness, inlet orifice, and conditions for metal to metal contact, among others, were investigated. The performance of composite slippers working with water-based fluids was studied in [11]. The torque created on the spherical piston slipper interface and its effect onto the slipper dynamic performance was studied in [4, 12, 13]. Slipper dynamic performance over one complete revolution was investigated by [14, 18] finding a huge variation on slipper central clearance and tilt depending on piston connection with tank or outlet ports. The performance of slippers with grooves was reported by [2, 15, 16, 21], in which it was found that a groove brought stability to the slipper dynamics. In all these cases, the second land was vented and therefore the pressure on the groove was reported to be atmospheric. As a result the groove itself was not creating lift. It was also reported that for a given central clearance, reducing the number of lands give a reduction in leakage. Despite of the amount of work developed on slippers, no evidence has been found of any research focused on finding the leakage and groove pressure at different slipper tilts, or for a double land slipper.

2. Flow and pressure distribution on multiple land slippers, mathematical analysis

One of the first attempts at a mathematical analysis was undertaken by Kakoulis [21], and Reynolds equation of lubrication was used to find the pressure distribution below the slipper. Kakoulis assumed the angular pressure distribution to be much smaller than the radial pressure distribution. He also assumed that the pressure along the groove which separates the two lands of the slipper is atmospheric pressure. Therefore the inner land of the slipper was assumed to produce hydrostatic and hydrodynamic

lift, when tilt exists, while the slipper outer land was assumed to produce just hydrodynamic lift. Therefore the groove itself was assumed to produce no lift. In the work by Kakoulis, the second land was vented but in the present case it is not. It will be demonstrated that these assumptions are inappropriate and both slipper lands and the groove produce hydrostatic and hydrodynamic lift. The resolution of Reynolds equation in which radial and angular pressure distribution is taken into account [1, 5, 16, 17, 20] has been performed via solving the differential equation as a power series. A crucial aspect of the method proposed is based on linking the first direct integration of the Reynolds equation with the flow leakage differential equation. It is appropriate to say that until now no attempt has been made to explain the two land slipper behaviour both mathematically and experimentally. As will be demonstrated later, the method proposed allows the behaviour of the slipper grooves and second land to be defined without the necessity of having the second land vented. The basis of the theory was outlined in Bergada and Watton [22, 23]. Consider figure 2 :

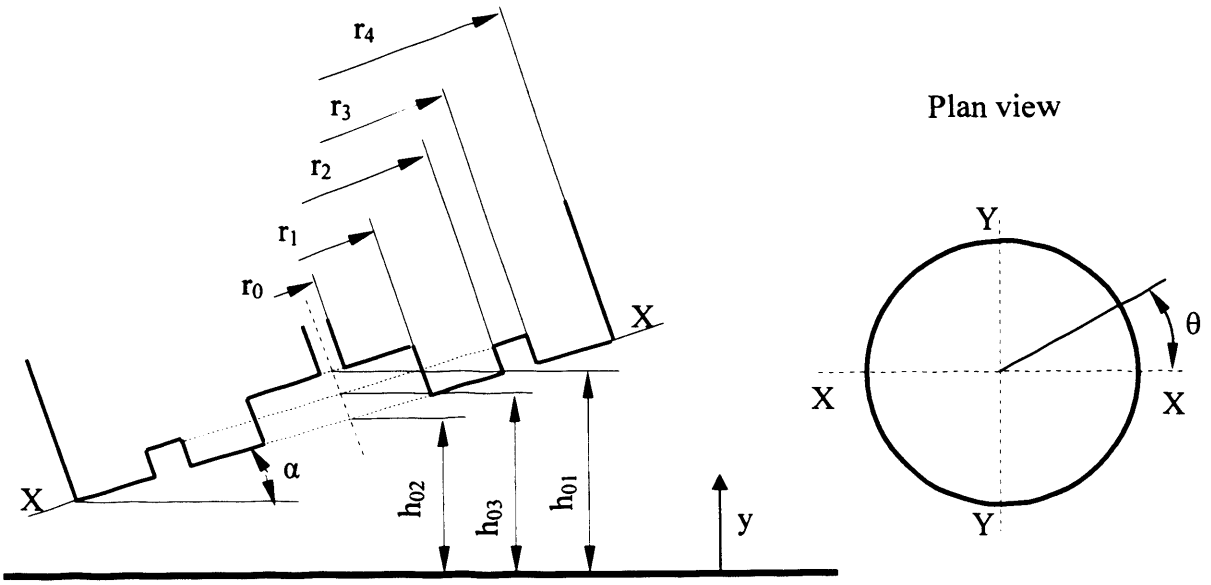

Figure 2. Slipper main parameters.

The following assumptions are then made:

- Flow will be considered laminar.
- The slipper plate clearance is not uniform; the slipper is tilted.
- The fluid is hydraulic mineral oil ISO 32.
- Steady conditions are considered.
- Slipper spin is taken into account.
- Flow will be considered as radial.
- Slipper pocket, groove and slipper lands are flat.
- The only relative movement between slipper/swash plate is slipper spin.

Reynolds equation applicable to this study is given as:

$$\frac{\partial}{\partial r}\left(r h^3 \frac{\partial p}{\partial r}\right) = 6\mu\omega r \frac{\partial h}{\partial \theta} \tag{1}$$

The film thickness in the clearance is given by:

$$h = h_0 + \alpha r_m \cos\theta \tag{2}$$

The average radius between land ends is used, and the film thickness is:

$$\frac{\partial h}{\partial \theta} = -\alpha r_m \sin\theta \tag{3}$$

The first integration of the differential equation (1) will then give:

$$\frac{\partial p}{\partial r} = \frac{-3\mu\omega\alpha r_m \sin\theta\ r}{(h_0 + \alpha r_m \cos\theta)^3} + \frac{k_1}{r(h_0 + \alpha r_m \cos\theta)^3} \tag{4}$$

The second integration gives:

$$p = \frac{-3\mu\omega\alpha r_m \sin\theta\ r^2}{2(h_0 + \alpha r_m \cos\theta)^3} + \frac{k_1}{(h_0 + \alpha r_m \cos\theta)^3}\ln(r) + k_2 \tag{5}$$

The slipper leakage through a generic radius will be:

$$Q_{leakage} = \int_0^{2\pi}\int_0^h u\, r\, dy\, d\theta \tag{6}$$

Assuming Poiseulle flow, the velocity distribution is given by:

$$u = \frac{1}{\mu}\frac{dp}{dr}\frac{y}{2}(y-h) \tag{7}$$

then

$$Q_{leakage} = \int_0^{2\pi}\int_0^h \frac{1}{\mu}\frac{dp}{dr}\frac{y}{2}(y-h)r\,dy\,d\theta \tag{8}$$

Substituting the pressure distribution versus radius, equation (4), into equation (8) and after some integration and rearrangement gives :

$$Q_{leakage} = \int_0^{2\pi} -\frac{1}{12\mu}\left[-3\mu\omega\alpha r_m \sin\theta\, r^2 + k_1\right]d\theta \tag{9}$$

It must be remembered at this point that a second integration cannot be performed since the unknown constant k_1 depends on the angular position θ. Nevertheless for a tilted slipper with several lands as shown in figure 2, and assuming that the flow and pressure distribution in the slipper pocket and groove behave in the same way as in a conventional land, then equations (5) and (9) can be applied to each slipper land obtaining:

Slipper pocket: $r_0 < r < r_1$

$$p_1 = \frac{-3\mu\omega\alpha\, r_{m1}\sin\theta\, r^2}{2\left(h_{01} + \alpha r_{m1}\cos\theta\right)^3} + \frac{k_1}{\left(h_{01} + \alpha r_{m1}\cos\theta\right)^3}\ln(r) + k_2$$

(10)

$$Q_{leakage\,1} = \int_0^{2\pi} -\frac{1}{12\mu}\left[-3\mu\omega\alpha r_{m1}\sin\theta\, r^2 + k_1\right]d\theta$$

(11)

$$r_{m1} = \frac{r_1 + r_0}{2}$$

(12)

First land: $r_1 < r < r_2$

$$p_2 = \frac{-3\mu\omega\alpha\, r_{m2} \sin\theta\ r^2}{2\left(h_{02} + \alpha\, r_{m2}\cos\theta\right)^3} + \frac{k_3}{\left(h_{02} + \alpha\, r_{m2}\cos\theta\right)^3}\ln(r) + k_4$$

(13)

$$Q_{leakage2} = \int_0^{2\pi} -\frac{1}{12\mu}\left[-3\mu\omega\alpha\, r_{m2}\sin\theta\, r^2 + k_3\right]d\theta$$

(14)

$$r_{m2} = \frac{r_2 + r_1}{2}$$

(15)

Slipper groove: $r_2<r<r_3$

$$p_3 = \frac{-3\mu\omega\alpha\, r_{m3} \sin\theta\ r^2}{2\left(h_{03} + \alpha\, r_{m3}\cos\theta\right)^3} + \frac{k_5}{\left(h_{03} + \alpha\, r_{m3}\cos\theta\right)^3}\ln(r) + k_6$$

(16)

$$Q_{leakage3} = \int_0^{2\pi} -\frac{1}{12\mu}\left[-3\mu\omega\alpha\, r_{m3}\sin\theta\, r^2 + k_5\right]d\theta$$

(17)

$$r_{m3} = \frac{r_3 + r_2}{2}$$

(18)

Second land: $r_3<r<r_4$

$$p_4 = \frac{-3\mu\omega\alpha\, r_{m4} \sin\theta\ r^2}{2\left(h_{04} + \alpha\, r_{m4}\cos\theta\right)^3} + \frac{k_7}{\left(h_{04} + \alpha\, r_{m4}\cos\theta\right)^3}\ln(r) + k_8$$

(19)

$$Q_{leakage4} = \int_0^{2\pi} -\frac{1}{12\mu}\left[-3\mu\omega\alpha\, r_{m4}\sin\theta\, r^2 + k_7\right]d\theta$$

(20)

$$r_{m4} = \frac{r_4 + r_3}{2}$$

(21)

The boundary conditions necessary to determine the constants will be:

$r = r_0 \quad p_1 = p_{inlet}$

(22)

$r = r_1 \quad p_1 = p_2 \quad Q_{leakage\ 1} = Q_{leakage\ 2}$

$r = r_2 \quad p_2 = p_3 \quad Q_{leakage\ 2} = Q_{leakage\ 3}$

$r = r_3 \quad p_3 = p_4 \quad Q_{leakage\ 3} = Q_{leakage\ 4}$

$r = r_4 \quad p_4 = p_{outlet}$

After appropriate mathematical development, the value of the constants is found and presented in the appendix. A key feature of the analysis is that it allows a generalised set of equations to be developed for the constants and from these generalised equations the value of any constant for a slipper with any number of lands can be determined. Since all constants are given as a function of the parameter k_1 the generic equation for this parameter will be presented first. It must be remembered that $1< i <n$ where n is the number of lands, including grooves and the slipper pocket. Notice that the minimum value of n is 2. From the appendix, the generic equation for the constant k_1 will be:

$$k_1 = \frac{p_{tank} - p_{inlet} - \frac{3\mu\omega\alpha\sin\theta}{2}\left[\sum_{i=1}^{i=n}\frac{r_{mi}\left(r_{i-1}^2 - r_i^2\right)}{\left(h_{0i} + \alpha r_{mi}\cos\theta\right)^3}\right] - 3\mu\omega\alpha\sin\theta\left[\sum_{i=1}^{i=(n-1)}\frac{\ln\left(\frac{r_{i+1}}{r_i}\right)\left[\sum_{j=1}^{j=i} r_j^2\left(r_{m(j+1)} - r_{mj}\right)\right]}{\left(h_{0(i+1)} + \alpha r_{m(i+1)}\cos\theta\right)^3}\right]}{\sum_{i=1}^{i=n}\frac{\ln\left(\frac{r_i}{r_{(i-1)}}\right)}{\left(h_{0i} + \alpha r_{mi}\cos\theta\right)^3}}$$

(23)

The generic equation for the odd constants k_3, k_5, k_7.....will be:

$$k_L = 3\mu\omega\alpha\,\mathrm{Sin}\theta\left(\sum_{j=1}^{j=\left(\frac{L-1}{2}\right)}\left[r_j^2\left[r_{m(j+1)} - r_{mj}\right]\right]\right) + k_1$$

(24)

The value of "L" will have to be odd and between $3 \le L \le (2n-1)$. The generic equation for the even constants k_2, k_4, k_6, k_8 ....will be:

$$k_M = P_{inlet} + \left\{ \sum_{i=1}^{i=\left(\frac{M-2}{2}\right)} \left(\frac{\ln\left(\frac{r_i}{r_{(i-1)}}\right)}{\left(h_{0i} + \alpha r_{mi}\cos\theta\right)^3} \right) - \frac{\ln r_{\left(\frac{M-2}{2}\right)}}{\left(h_{0(M/2)} + \alpha\, r_{m(M/2)}\cos\theta\right)^3} \right\} k_1 +$$

$$+ \frac{3\mu\omega\alpha\sin\theta}{2} \left\{ \sum_{i=1}^{i=\left(\frac{M-2}{2}\right)} \left(\frac{r_{mi}\left(r_{i-1}^2 - r_i^2\right)}{\left(h_{0i} + \alpha r_{mi}\cos\theta\right)^3} \right) + \frac{r_{m(M/2)}\, r_{\left(\frac{M-2}{2}\right)}^2}{\left(h_{0(M/2)} + \alpha r_{m(M/2)}\cos\theta\right)^3} \right\} +$$

$$+ 3\mu\omega\alpha\sin\theta \left\{ \sum_{i=1}^{i=\left(\frac{M-4}{2}\right)} \left(\frac{\left[\sum_{j=1}^{j=i}\left[r_j^2\left(r_{m(j+1)} - r_{mj}\right)\right]\right]\ln\left(\frac{r_{i+1}}{r_i}\right)}{\left(h_{0(i+1)} + \alpha r_{m(i+1)}\cos\theta\right)^3} \right) - \frac{\sum_{j=1}^{j=\left(\frac{M-2}{2}\right)}\left(r_j^2\left(r_{m(j+1)} - r_{mj}\right)\right)}{\left(h_{0(M/2)} + \alpha r_{m(M/2)}\cos\theta\right)^3} \ln r_{\left(\frac{M-2}{2}\right)} \right\}$$

(25)

The values of the variable "M" in equation (25) must be even, and between $2 \le M \le 2n$. When producing the explicit equations based on the generic equations given here it must be remembered that in a summation $\sum_{\text{lower limit}}^{\text{upper limit}}$ then if the upper limit has a value smaller than the lower limit it means that the value of the entire term is zero. Substituting the different constants into the equations for the pressure distribution at different lands, (10), (13), (16) and (19), yields explicit equations for the pressure distribution at each land. Further details are presented in the appendix. A generic equation is presented here which is capable of generating the pressure distribution equations for a slipper with any number of lands.

$$p_i = p_{inlet} + k_1\left[\frac{\ln\left(\frac{r}{r_{i-1}}\right)}{\left(h_{0i}+\alpha r_{mi}\cos\theta\right)^3}+\sum_{j=2}^{j=i}\frac{\ln\left(\frac{r_{j-1}}{r_{j-2}}\right)}{\left(h_{0(j-1)}+\alpha r_{m(j-1)}\cos\theta\right)^3}\right]+$$

$$\frac{3\mu\omega\alpha\sin\theta}{2}\left[\frac{r_{mi}\left[r_{i-1}^2-r^2\right]}{\left(h_{0i}+\alpha r_{mi}\cos\theta\right)^3}+\sum_{j=2}^{j=i}\frac{r_{m(j-1)}\left[r_{j-2}^2-r_{j-1}^2\right]}{\left(h_{0(j-1)}+\alpha r_{m(j-1)}\cos\theta\right)^3}\right]+$$

$$3\mu\omega\alpha\sin\theta\left[\frac{\left[\sum_{j=2}^{j=i}r_{j-1}^2\left[r_{mj}-r_{m(j-1)}\right]\right]}{\left(h_{0i}+\alpha r_{mi}\cos\theta\right)^3}\ln\left(\frac{r}{r_{i-1}}\right)+\sum_{j=3}^{j=i}\left[\frac{\ln\left(\frac{r_{j-1}}{r_{j-2}}\right)\left[\sum_{k=3}^{k=i}r_{k-2}^2\left[r_{m(k-1)}-r_{m(k-2)}\right]\right]}{\left(h_{0(j-1)}+\alpha r_{m(j-1)}\cos\theta\right)^3}\right]\right]$$

(26)

When substituting the constants into the leakage equations, (11), (14), (17) and (20), the same equation for the leakage flow is found:

$$Q_{leakage} = -\int_0^{2\pi}\frac{k_1}{12\,\mu}\,d\theta$$

(27)

Due to the complexity of the integral, equation (27) must be integrated numerically to determine the leakage.

3. Test rig

In order to experimentally validate the equations developed, the test rig represented in figure 3 was constructed.

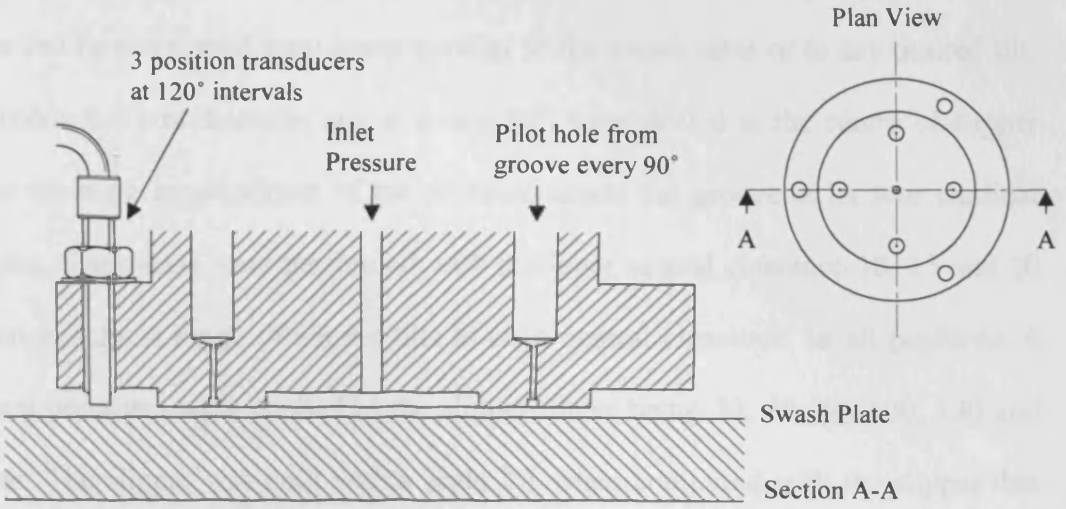

a) Cross section of the slipper area

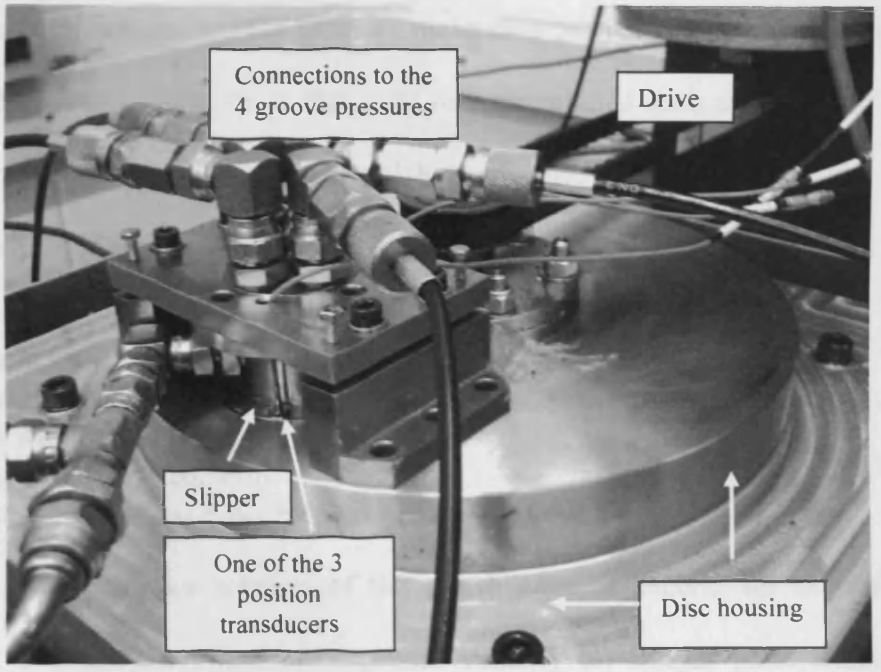

b) Slipper, disc housing and drive system

Figure 3 Experimental apparatus

Three position transducers, having a measurement accuracy of 0.5 microns, were attached to the slipper at 120° intervals. These sensors require non-ferrous measuring face for optimum performance and therefore the housing assembly was manufactured from aluminium while the slipper assembly was manufactured from stainless steel. The slipper is held in position using four screws and the required slipper orientation

was achieved by turning four additional positioning screws. Using this method the slipper can be positioned completely parallel to the swash plate or to any desired tilt. Four holes, 0.5 mm diameter and at every 90°, were drilled at the centre of slipper groove allowing measurement of the pressure inside the groove at its four cardinal positions. Static tests were performed with a slipper central clearance 10, 15 and 20 microns and for a range of slipper tilts at each central clearance. In all positions, 6 different pressures were applied to the slipper, these being 30, 50, 80, 100, 130 and 150 bar. The slipper was built with a scale 2:1 when compared with the slipper that initiated this project, shown in figure 1. This was done to be able to physically locate both the position sensors and the pressure measuring points. However, the size of the test rig slipper is not unlike those that exist in larger pumps such as the set of pistons and slippers supplied by Oilgear Towler UK to the authors for reference. The test rig slipper dimensions are:

- Orifice radius r_0 = 1mm
- Inner land inside radius r_1 = 10,15mm
- Inner land outside radius r_2 = 14,7mm
- Groove width = 1mm
- Outside radius r_4 = 20,5mm
- When $\alpha = 0$; then: $h_{01} = h_{02} + 1{,}4$ mm; $h_{03} = h_{02} + 0.8$ mm.

Since the test rig allows rotation of the swash plate, a second set of tests were performed to study the effect of tangential velocity on slipper plate leakage and slipper groove pressure distribution. The variable-speed tests were performed for a single central clearance of 15 microns and for a single tilt of 0.035°. A set of swash plate turning speeds were studied in the range 0 to 1350 rpm, the maximum turning speed corresponding to a tangential velocity on the slipper main axis of 13 m/s.

The test conditions considered should be put into context with those that would probably exist for the test slipper when used in a real pump application. Slipper force

is not considered in this paper, but a calculation can be made using existing lubrication theory [24, 25]. It is assumed that :

- the maximum pump pressure would be 350bar
- the fluid viscosity $\mu = 0.032 Ns/m^2$
- the pocket pressure is marginally different from the pump pressure
- the swash plate angle is 20^o
- the pressure distribution across the slipper is approximated by an equivalent logarithmic decay passing through the centre of the groove

The hydrostatic force generated on the slipper is then 23kN. The force balance across the slipper and piston is then determined by the pump manufacturer, perfect force balance occurring for a piston diameter of 28.9mm. If an additional hydrodynamic force is required then this will not be greater than typically 5% of the hydrodynamic force, and is based upon well-established design knowledge. There is no explicit theory for determining the hydrodynamic lift for a circular slipper, but a good approximation can be made by using square plain bearing theory with side leakage effects taken into account [25]. It will be further assumed that:

- a square plain bearing of equivalent area, 36.3mm x 36.3mm, applies
- the bearing central clearance h_o = 10micron
- a side leakage compensating factor of 0.44 applies [25]
- a tangential velocity of 13m/s still applies

The bearing tilt is then calculated to be equivalent to a 0.26 microns increase from the trailing edge to the leading edge. This gives a square bearing tilt angle of 0.00041^o and therefore smaller by a factor of 12.2 compared with the minimum non-zero value

of 0.005° that was set in the tests. Even if all the slipper lift force was created by hydrodynamic effects, a condition that would not normally occur with a non-blocked slipper orifice, the tilt angle would still only be 0.0079°.

4. Results

4.1 Analytical and experimental results under static conditions, slipper leakage

Leakage at every slipper angular position can be studied using equation (27), once the numerical integration is done. This results in figure 4 from where can clearly be seen that as tilt increases the difference between the front and back leakage also increases. What is most remarkable is that for the range of slipper spin speed values studied the total leakage does not depend upon the slipper turning speed; it just depends upon the pressure differential, the slipper central gap and tilt. Figure 5 represents the leakage given as a percentage of increase versus the slipper non tilted position. It is evident that leakage increases with slipper tilt and for a given central clearance such an increase does not depend on the pressure differential applied to the slipper.

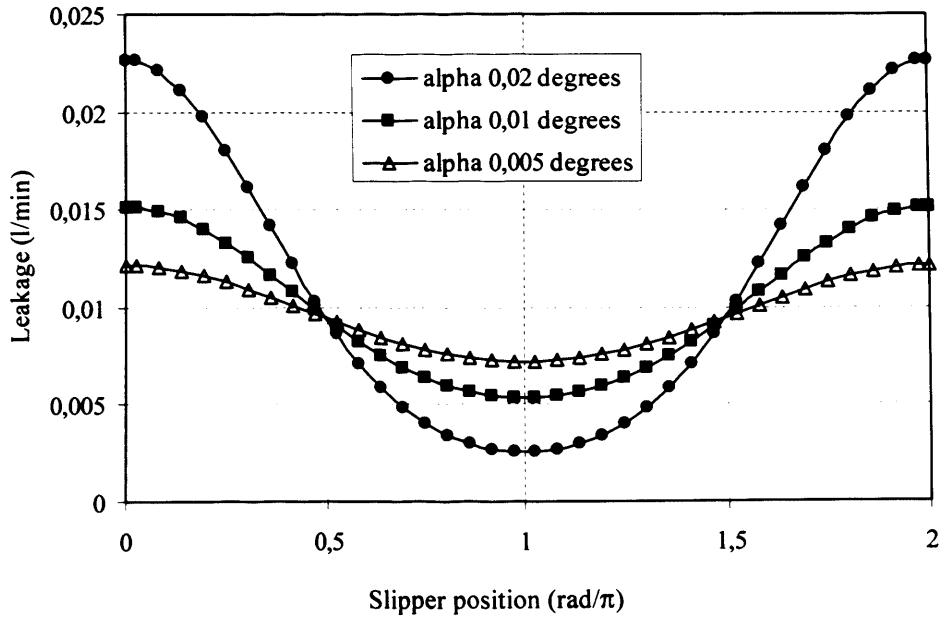

Figure 4. Leakage flow, (analytical), central distance h_{02} = 15 microns, P_{inlet} = 100 bar

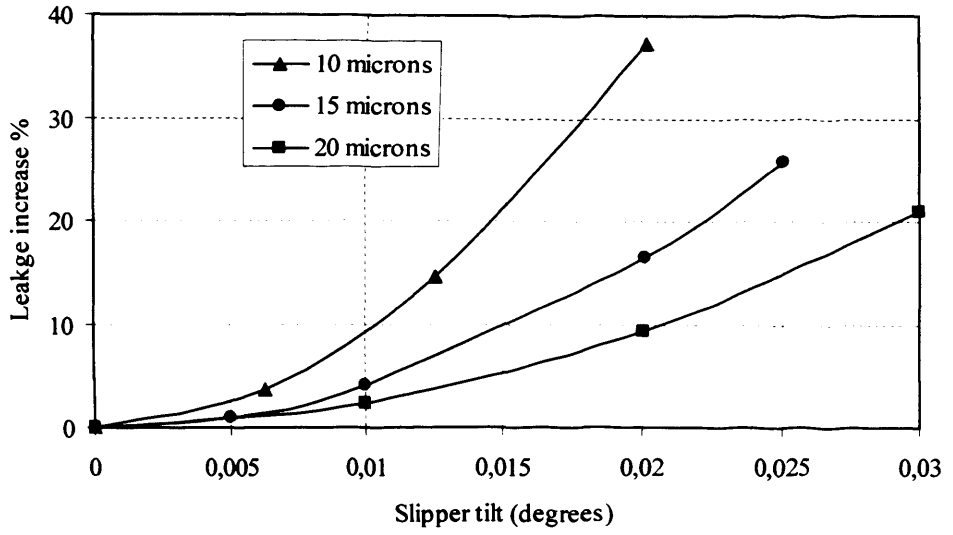

Figure 5 Slipper leakage percentage increase versus non tilt slipper. Analytical

Some of the experimental leakage results are shown in figures 6(a), (b), (c) for the three central clearances of 10, 15 and 20 microns, and for a range of slipper tilts and inlet pressures. It can clearly be noticed that as the tilt increases the leakage also increases. This leakage increases as inlet pressure is increased. These experimental results correspond to the theory presented here. It is also very interesting to point out that at a central clearance of 10 microns, and for any given pressure, the leakage seems to first increase and then decrease with slipper tilt, as shown in figure 6(a). The explanation of this anomalous behaviour is to be found when realizing that at some clearances and tilts the flow at the entrance of the slipper first land changes from reattached to separated, reducing the flow section and therefore reducing the flow.

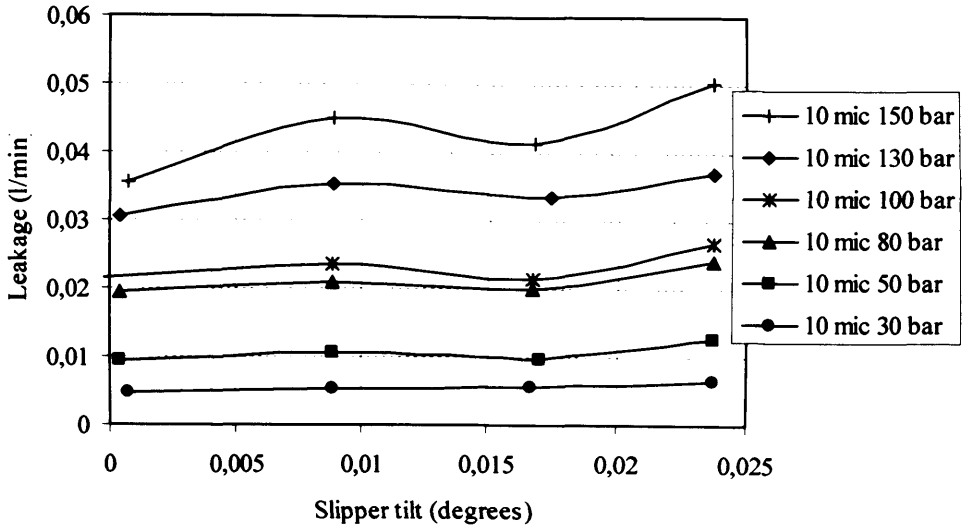

Figure 6(a) Leakage as a function of slipper tilt and inlet pressure.
Experimental, central clearance 10 microns.

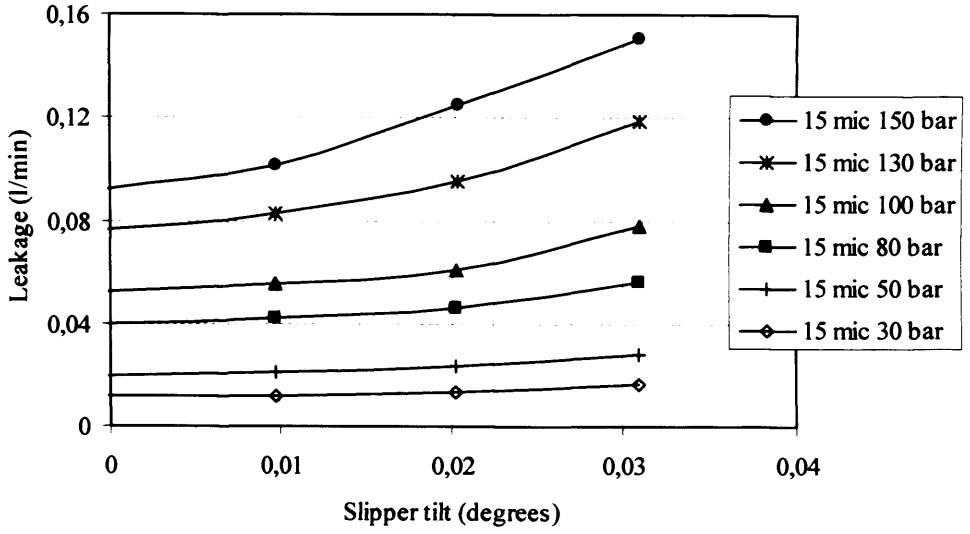

Figure 6(b) Leakage as a function of slipper tilt and inlet pressure.
Experimental, central clearance 15 microns.

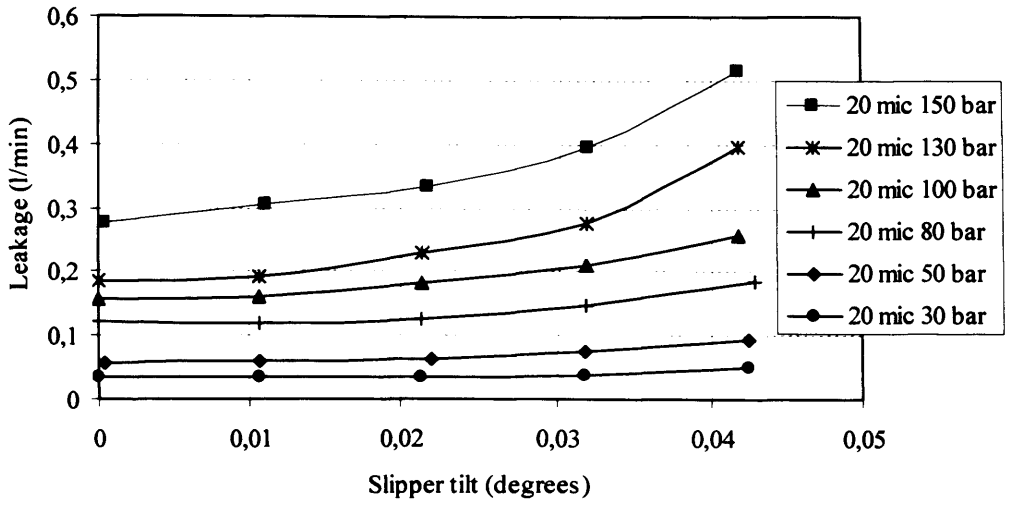

Figure 6(c) Leakage as a function of slipper tilt and inlet pressure.
Experimental., central clearance 20 microns.

According to the theory presented the leakage increase, given as a percentage of non tilted slipper leakage, should be independent on inlet pressure, as shown in figure 5. When leakage in figure 6 is represented as a percentage of the non tilted slipper it can be seen that for a given central clearance, all the different curves can be brought together. Therefore figure 7 presents the trend curve for all the central clearances studied which are compared with the theoretical predictions. It can be seen that a good agreement is found, especially at low tilts which probably exist in practice. From these results it can be stated that leakage percentage increase versus a non tilted slipper is mostly independent on the inlet pressure. Nevertheless it has been found experimentally that as the inlet pressure increases the percentage increase trend line curve tends to slightly increase.

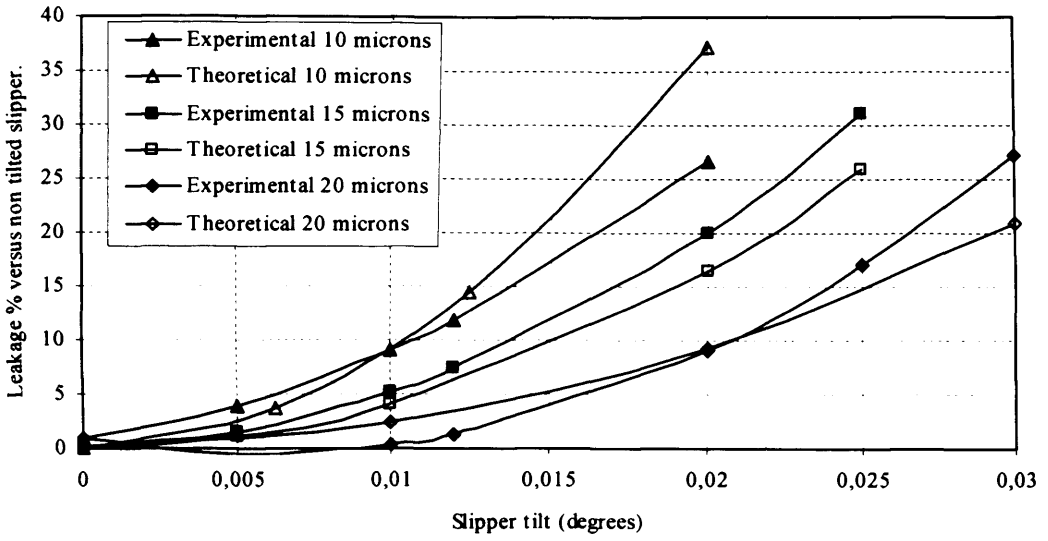

Figure 7 Comparison experimental and theoretical leakages, given as a percentage of the non tilted slipper leakage.

4.2 Analytical and experimental results under static conditions, Pressure distribution

Regarding the pressure distribution, the equations presented are capable of predicting the pressure at all points below the slipper, as is represented in figure 8. It has to be said that due to the consideration of radial flow at all points, the theoretical pressure differential inside the slipper groove is higher than what has been found experimentally. In fact the experiments have revealed that the pressure inside the groove is mostly constant for the set of tilts and central clearances studied. For a given central clearance the groove pressure, although constant at all four pick up points, tends to decrease as the tilt increases. This is shown in figure 9(a), (b), (c). Also represented in figure 9 is the theoretical pressure variation. In agreement with the theory, the pressure inside the groove does change with angular position. The pressure at angle $\theta = 0$ is computed, see figure 2, and represents the analytical minimum pressure on the slipper groove. Theoretically the pressure inside the groove increases

for a tilted slipper as the slipper clearance decreases, and the question arises as to which of the range of theoretical pressures is likely to appear experimentally. Thanks to the experimentation undertaken it can be said that the minimum theoretical pressure is the most likely to appear in reality. A well-designed groove geometry allows flow from the theoretical groove high pressure points to move almost instantaneously towards the groove theoretical low pressure points, thus equalising the pressure within the groove. It can then be concluded that for the groove studied, a rate of momentum exchange exists between fluid particles at the top of the groove. From figure 9 it is noticed that for smaller central clearances the pressure decay with slipper tilt inside the groove is higher. A very good agreement between theory and experimentation is found under all conditions studied.

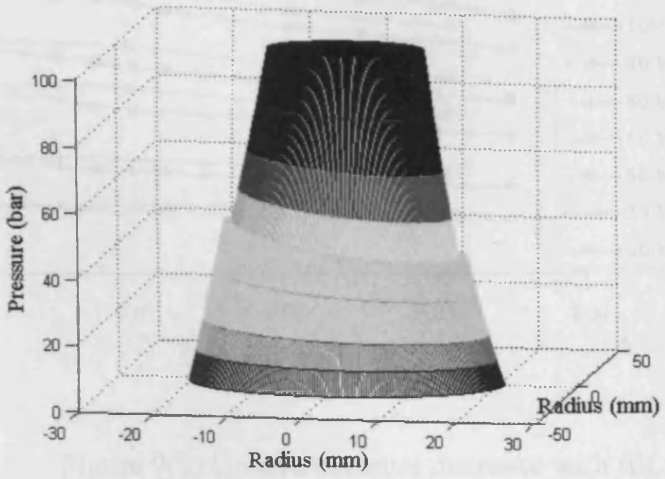

Figure 8, Theoretical pressure distribution below the slipper.
h_{02}=15 microns α =0,01 deg ω = 25,12 rad/s

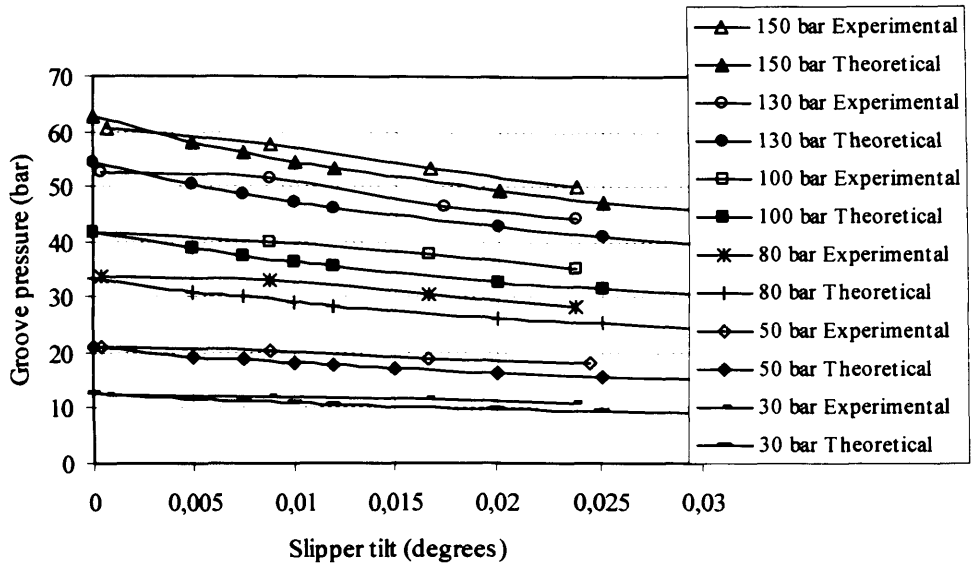

Figure 9(a) Groove pressure decrease with tilt.
Comparison experimental and analytical results. 10 microns central clearance.

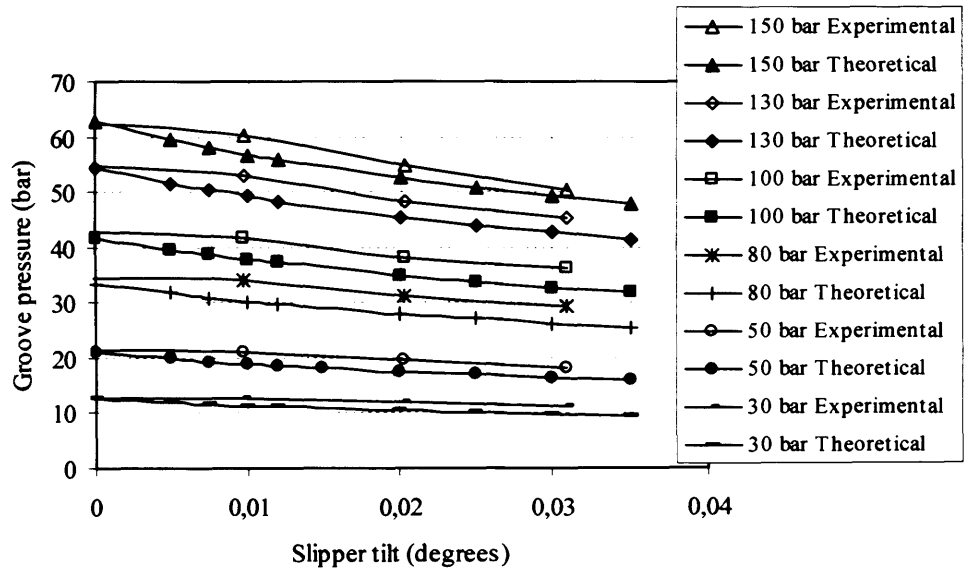

Figure 9(b) Groove pressure decrease with tilt.
Comparison experimental and analytical results. 15 microns central clearance.

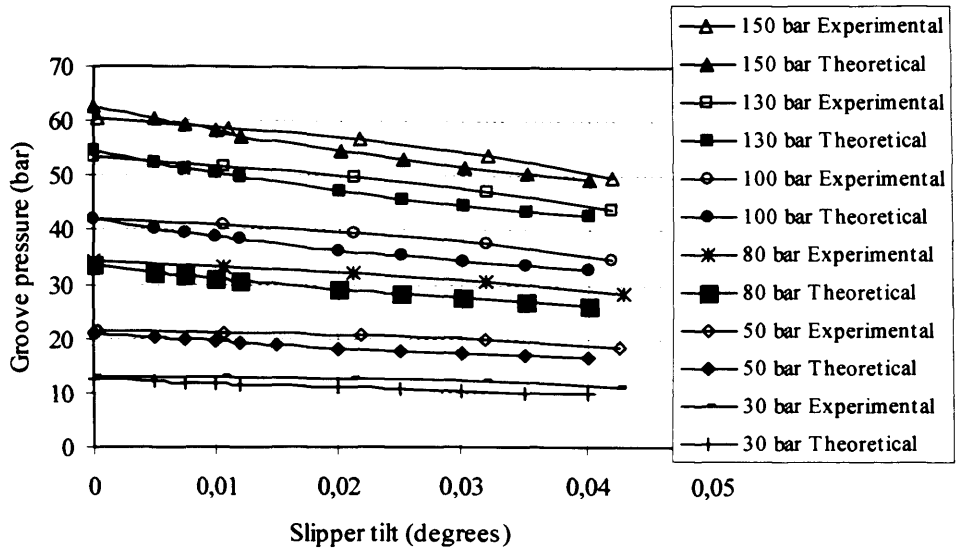

Figure 9(c) Groove pressure decrease with tilt.
Comparison experimental and analytical results. 20 microns central clearance.

For the slipper with groove studied, and when working under expected operating conditions, the pressure inside the groove is maintained constant. However it has been found experimentally that as the tilt and slipper inlet pressure increases, some pressure differential inside the groove can be expected. To illustrate this point figure 10 is presented, showing that when the slipper is operating outside the normal working conditions, the flow circulation around the groove and therefore the momentum exchange around the groove is not enough to maintain constant pressure. Figure 10 also demonstrates that if the groove depth is decreased then a much bigger pressure differential inside the groove is to be expected. Notice that an increase of inlet pressure also creates higher pressure differential inside the groove.

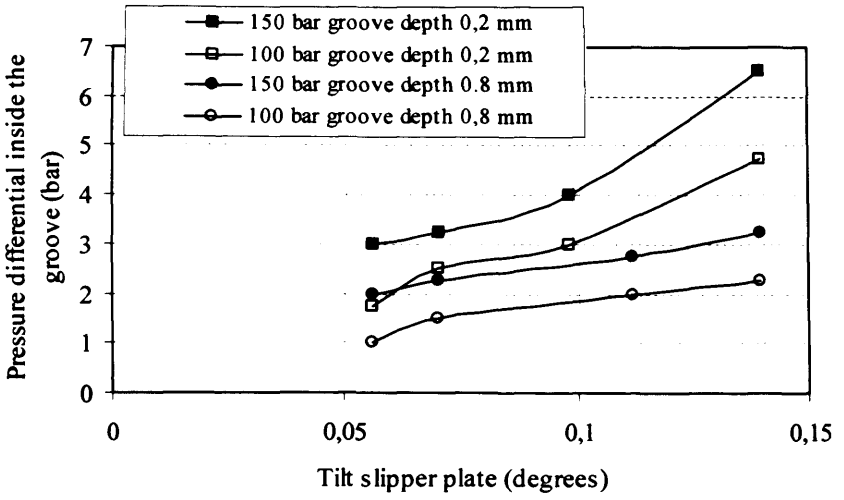

Figure 10 Operating conditions under which pressure differential inside the groove can be expected. Experimental.

4.3 The effect of pump turning speed on slipper leakage and groove pressure

To experimentally study the effect of the pump turning speed on the slipper leakage and pressure distribution inside the groove, the test rig presented in figure 3 was again used. In this case the plate below the slipper, representing the swash plate in practice, was able to be turned at different rotational speeds between 0 and 1350 rpm. This is opposite to the real pump method of operation using a fixed swash plate but the effect is the same. A single slipper central clearance of 15 microns was studied with a slipper tilt of 0.035°. For each turning speed a set of inlet pressures of 30, 50, 80, 100, 130 and 150 bar were studied.

The effect of swash plate turning speed on leakage and groove pressure is represented in figures 11 and 12. Figure 11 presents slipper leakage for several swash plate turning speeds, where it is noticed that the slipper leakage decreases as the turning speed increases. This result is understandable when it is realised that the flow created by the swash plate rotation acts against the radial flow tending to leave the slipper at $\theta = 0$ degrees, see figure 2, and pushes the radial flow towards $\theta = 180$ degrees. As is demonstrated in figure 4, the maximum flow around the slipper is expected to be at $\theta = 0$ and therefore the swash plate movement will prevent a normal evolution of the slipper flow in this direction. This results in a decrease of slipper leakage with increased turning speed.

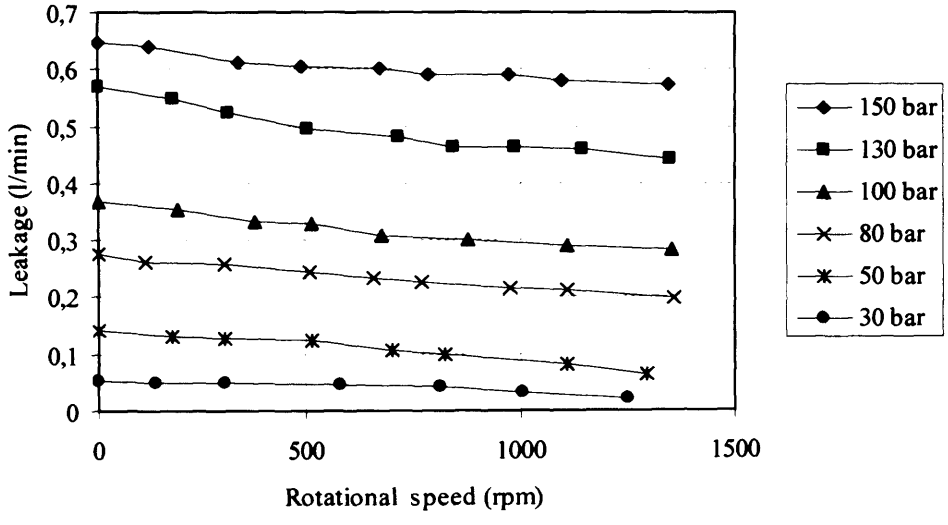

Figure 11. Slipper leakage as a function of pump turning speed.
Central clearance 15 microns, slipper tilt 0.035°. Experimental.

Figure 12 Demonstrates that as the turning speed increases the average pressure inside the groove also increases. In fact it has also been seen during the experimental work that the pressure differential inside the groove slightly increases with increased turning speed and also with inlet pressure, although the maximum pressure

differential found in all the experiments performed never exceeded 1.5bar. Therefore it demonstrates that even when rotational speed is considered, the groove under study allows a good momentum interchange between fluid particles around the groove.

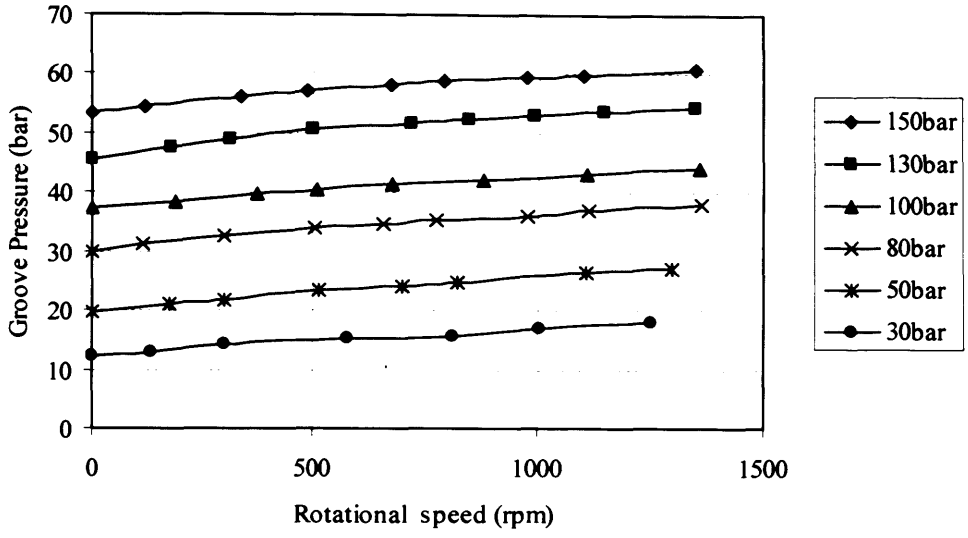

Figure 12. Average pressure inside the groove when the slipper turns along the swash plate. Central clearance 15 microns, slipper tilt 0.035°. Experimental

6 Conclusions

A new set of equations have been developed to take into account the effect of grooves cut on slippers, slipper tilt and rotational speed. The equations have been generalised to be used for a slipper with any number of lands. Results were achieved for slipper tilts far beyond those that would exist in practice, had the test slipper geometry been used in a pump application.

The equations can be used to evaluate the leakage at slipper tilts of the order likely to be met in practice, and with sufficient accuracy for design purposes. It does seem from the tests that the effect of slipper tilt on leakage is negligible for a real pump application using the test slipper.

It has been found experimentally that leakage increases as the slipper tilt increases and for a given central clearance, such an increase is mostly independent of inlet pressure. This is predicted by the theory. Theoretical and experimental results show a good agreement especially at low slipper tilt. However the increase will be negligible for practical slipper angles in the real pump application.

Although the theory predicts some pressure differential inside the groove, it has been found experimentally that under normal working conditions, and for the slipper groove studied, the pressure remains constant around the groove. Such a constant pressure then decays as slipper tilt increases and theoretical predictions and experimental results show a very good agreement.

It has been experimentally demonstrated that the well-chosen groove depth resulted in a constant pressure around the groove and therefore a groove needs to be properly designed to avoid a pressure differential effect.

As the slipper turns relative to the swash plate, the leakage decreases as the rotational speed increases, while the average groove pressure increases with an increase in rotational speed. A very small pressure differential inside the groove is detected as the rotational speed increases. The theory developed is therefore valuable in that it can predict the maximum leakage flow possible.

Confidence in the predictions is given by the fact that the slipper tilts chosen for the experimental tests were an order of magnitude higher than those expected in a pump,

should it have pistons matched to the test slipper. In fact the very small slipper tilts expected in practice are extremely difficult to set experimentally.

Further work is needed on experimental validation of tangential velocity effects with reference to force and torque distribution when the slipper position and tilt are precisely known.

Appendix

The expressions for the different constants are given as a function of the first constant k_1

$$k_1 = \frac{p_{tank} - p_{inlet} - \frac{3\mu\omega\alpha\sin\theta}{2}\left[\frac{r_{m1}\left(r_0^2 - r_1^2\right)}{\left(h_{01} + \alpha r_{m1}\cos\theta\right)^3} + \frac{r_{m2}\left(r_1^2 - r_2^2\right)}{\left(h_{02} + \alpha r_{m2}\cos\theta\right)^3} + \frac{r_{m3}\left(r_2^2 - r_3^2\right)}{\left(h_{03} + \alpha r_{m3}\cos\theta\right)^3} + \frac{r_{m4}\left(r_3^2 - r_4^2\right)}{\left(h_{04} + \alpha r_{m4}\cos\theta\right)^3}\right]}{\frac{\ln\left(\frac{r_1}{r_0}\right)}{\left(h_{01} + \alpha r_{m1}\cos\theta\right)^3} + \frac{\ln\left(\frac{r_2}{r_1}\right)}{\left(h_{02} + \alpha r_{m2}\cos\theta\right)^3} + \frac{\ln\left(\frac{r_3}{r_2}\right)}{\left(h_{03} + \alpha r_{m3}\cos\theta\right)^3} + \frac{\ln\left(\frac{r_4}{r_3}\right)}{\left(h_{04} + \alpha r_{m4}\cos\theta\right)^3}} +$$

$$- \frac{3\mu\omega\alpha\sin\theta\left[\frac{r_1^2\left(r_{m2} - r_{m1}\right)\ln\left(\frac{r_2}{r_1}\right)}{\left(h_{02} + \alpha r_{m2}\cos\theta\right)^3} + \frac{\left[r_1^2\left(r_{m2} - r_{m1}\right) + r_2^2\left(r_{m3} - r_{m2}\right)\right]\ln\left(\frac{r_3}{r_2}\right)}{\left(h_{03} + \alpha r_{m3}\cos\theta\right)^3} + \frac{\left[r_1^2\left(r_{m2} - r_{m1}\right) + r_2^2\left(r_{m3} - r_{m2}\right) + r_3^2\left(r_{m4} - r_{m3}\right)\right]\ln\left(\frac{r_4}{r_3}\right)}{\left(h_{04} + \alpha r_{m4}\cos\theta\right)^3}\right]}{\frac{\ln\left(\frac{r_1}{r_0}\right)}{\left(h_{01} + \alpha r_{m1}\cos\theta\right)^3} + \frac{\ln\left(\frac{r_2}{r_1}\right)}{\left(h_{02} + \alpha r_{m2}\cos\theta\right)^3} + \frac{\ln\left(\frac{r_3}{r_2}\right)}{\left(h_{03} + \alpha r_{m3}\cos\theta\right)^3} + \frac{\ln\left(\frac{r_4}{r_3}\right)}{\left(h_{04} + \alpha r_{m4}\cos\theta\right)^3}}$$

(28)

$$k_3 = 3\,\mu\,\omega\,\alpha\,\sin\theta\,r_1^2\left[r_{m2} - r_{m1}\right] + k_1$$

(29)

$$k_5 = 3\,\mu\,\omega\,\alpha\,\sin\theta\left[r_1^2\left[r_{m2} - r_{m1}\right] + r_2^2\left[r_{m3} - r_{m2}\right]\right] + k_1$$

(30)

$$k_7 = 3\,\mu\,\omega\,\alpha\,\sin\theta\left[r_1^2\left[r_{m2} - r_{m1}\right] + r_2^2\left[r_{m3} - r_{m2}\right] + r_3^2\left[r_{m4} - r_{m3}\right]\right] + k_1$$

(31)

$$k_2 = p_{inlet} + \frac{3\mu\omega\alpha r_{m1}\sin\theta}{(h_{01}+\alpha r_{m1}\cos\theta)^3}\frac{r_0^2}{2} - \frac{k_1}{(h_{01}+\alpha r_{m1}\cos\theta)^3}\ln r_0$$

(32)

$$k_4 = p_{inlet} + k_1\left[\frac{\ln\left(\frac{r_1}{r_0}\right)}{(h_{01}+\alpha r_{m1}\cos\theta)^3} - \frac{\ln r_1}{(h_{02}+\alpha r_{m2}\cos\theta)^3}\right] + \frac{3\mu\omega\alpha\sin\theta}{2}\left[\frac{r_{m1}\left[r_0^2-r_1^2\right]}{(h_{01}+\alpha r_{m1}\cos\theta)^3} + \frac{r_{m2}r_1^2}{(h_{02}+\alpha r_{m2}\cos\theta)^3}\right]$$
$$-\frac{3\mu\omega\alpha\sin\theta r_1^2\left[r_{m2}-r_{m1}\right]}{(h_{02}+\alpha r_{m2}\cos\theta)^3}\ln r_1$$

(33)

$$k_6 = p_{inlet} + k_1\left[\frac{\ln\left(\frac{r_1}{r_0}\right)}{(h_{01}+\alpha r_{m1}\cos\theta)^3} + \frac{\ln\left(\frac{r_2}{r_1}\right)}{(h_{02}+\alpha r_{m2}\cos\theta)^3} - \frac{\ln r_2}{(h_{03}+\alpha r_{m3}\cos\theta)^3}\right]$$
$$+\frac{3\mu\omega\alpha\sin\theta}{2}\left[\frac{r_{m1}\left[r_0^2-r_1^2\right]}{(h_{01}+\alpha r_{m1}\cos\theta)^3} + \frac{r_{m2}\left[r_1^2-r_2^2\right]}{(h_{02}+\alpha r_{m2}\cos\theta)^3} + \frac{r_{m3}r_2^2}{(h_{03}+\alpha r_{m3}\cos\theta)^3}\right]$$
$$+3\mu\omega\alpha\sin\theta\left[\frac{r_1^2\left[r_{m2}-r_{m1}\right]\ln\left(\frac{r_2}{r_1}\right)}{(h_{02}+\alpha r_{m2}\cos\theta)^3} - \frac{r_1^2\left[r_{m2}-r_{m1}\right]+r_2^2\left[r_{m3}-r_{m2}\right]}{(h_{03}+\alpha r_{m3}\cos\theta)^3}\ln r_2\right]$$

(34)

$$k_8 = p_{inlet} + k_1\left[\frac{\ln\left(\frac{r_1}{r_0}\right)}{(h_{01}+\alpha r_{m1}\cos\theta)^3} + \frac{\ln\left(\frac{r_2}{r_1}\right)}{(h_{02}+\alpha r_{m2}\cos\theta)^3} + \frac{\ln\left(\frac{r_3}{r_2}\right)}{(h_{03}+\alpha r_{m3}\cos\theta)^3} - \frac{\ln r_3}{(h_{04}+\alpha r_{m4}\cos\theta)^3}\right]$$
$$+\frac{3\mu\omega\alpha\sin\theta}{2}\left[\frac{r_{m1}\left[r_0^2-r_1^2\right]}{(h_{01}+\alpha r_{m1}\cos\theta)^3} + \frac{r_{m2}\left[r_1^2-r_2^2\right]}{(h_{02}+\alpha r_{m2}\cos\theta)^3} + \frac{r_{m3}\left[r_2^2-r_3^2\right]}{(h_{03}+\alpha r_{m3}\cos\theta)^3} + \frac{r_{m4}r_3^2}{(h_{04}+\alpha r_{m4}\cos\theta)^3}\right]$$
$$+3\mu\omega\alpha\sin\theta\left[\frac{r_1^2\left[r_{m2}-r_{m1}\right]\ln\left(\frac{r_2}{r_1}\right)}{(h_{02}+\alpha r_{m2}\cos\theta)^3} + \frac{r_1^2\left[r_{m2}-r_{m1}\right]+r_2^2\left[r_{m3}-r_{m2}\right]}{(h_{03}+\alpha r_{m3}\cos\theta)^3}\ln\left(\frac{r_3}{r_2}\right) - \frac{r_1^2\left[r_{m2}-r_{m1}\right]+r_2^2\left[r_{m3}-r_{m2}\right]+r_3^2\left[r_{m4}-r_{m3}\right]}{(h_{04}+\alpha r_{m4}\cos\theta)^3}\ln r_3\right]$$

(35)

When substituting the different constants into the equations for the pressure distribution at different lands, equations (10), (13), (16) and (19), explicit equations for the pressure distribution at each land are obtained and take the following form.

$$p_1 = p_{inlet} + \frac{k_1 \ln\left(\frac{r}{r_0}\right)}{(h_{01} + \alpha r_{m1}\cos\theta)^3} + \frac{3\mu\omega\alpha r_{m1}\sin\theta}{(h_{01} + \alpha r_{m1}\cos\theta)^3}\left[\frac{r_0^2}{2} - \frac{r^2}{2}\right]$$

(36)

$$p_2 = p_{inlet} + k_1\left[\frac{\ln\left(\frac{r_1}{r_0}\right)}{(h_{01} + \alpha r_{m1}\cos\theta)^3} + \frac{\ln\left(\frac{r}{r_1}\right)}{(h_{02} + \alpha r_{m2}\cos\theta)^3}\right] + \frac{3\mu\omega\alpha\sin\theta}{2}\left[\frac{r_{m1}\left[r_0^2 - r_1^2\right]}{(h_{01} + \alpha r_{m1}\cos\theta)^3} + \frac{r_{m2}\left[r_1^2 - r^2\right]}{(h_{02} + \alpha r_{m2}\cos\theta)^3}\right]$$
$$+ \frac{3\mu\omega\alpha\sin\theta r_1^2\left[r_{m2} - r_{m1}\right]}{(h_{02} + \alpha r_{m2}\cos\theta)^3}\ln\left(\frac{r}{r_1}\right)$$

(37)

$$p_3 = p_{inlet} + k_1\left[\frac{\ln\left(\frac{r_1}{r_0}\right)}{(h_{01} + \alpha r_{m1}\cos\theta)^3} + \frac{\ln\left(\frac{r_2}{r_1}\right)}{(h_{02} + \alpha r_{m2}\cos\theta)^3} + \frac{\ln\left(\frac{r}{r_2}\right)}{(h_{03} + \alpha r_{m3}\cos\theta)^3}\right]$$
$$+ \frac{3\mu\omega\alpha\sin\theta}{2}\left[\frac{r_{m1}\left[r_0^2 - r_1^2\right]}{(h_{01} + \alpha r_{m1}\cos\theta)^3} + \frac{r_{m2}\left[r_1^2 - r_2^2\right]}{(h_{02} + \alpha r_{m2}\cos\theta)^3} + \frac{r_{m3}\left[r_2^2 - r^2\right]}{(h_{03} + \alpha r_{m3}\cos\theta)^3}\right]$$
$$+ 3\mu\omega\alpha\sin\theta\left[\frac{r_1^2\left[r_{m2} - r_{m1}\right]\ln\left(\frac{r_2}{r_1}\right)}{(h_{02} + \alpha r_{m2}\cos\theta)^3} + \frac{r_1^2\left[r_{m2} - r_{m1}\right] + r_2^2\left[r_{m3} - r_{m2}\right]}{(h_{03} + \alpha r_{m3}\cos\theta)^3}\ln\left(\frac{r}{r_2}\right)\right]$$

(38)

$$p_4 = p_{inlet} + k_1\left[\frac{\ln\left(\frac{r_1}{r_0}\right)}{(h_{01}+\alpha r_{m1}\cos\theta)^3}+\frac{\ln\left(\frac{r_2}{r_1}\right)}{(h_{02}+\alpha r_{m2}\cos\theta)^3}+\frac{\ln\left(\frac{r_3}{r_2}\right)}{(h_{03}+\alpha r_{m3}\cos\theta)^3}+\frac{\ln\left(\frac{r}{r_3}\right)}{(h_{04}+\alpha r_{m4}\cos\theta)^3}\right]$$
$$+\frac{3\mu\omega\alpha\sin\theta}{2}\left[\frac{r_{m1}\left[r_0^2-r_1^2\right]}{(h_{01}+\alpha r_{m1}\cos\theta)^3}+\frac{r_{m2}\left[r_1^2-r_2^2\right]}{(h_{02}+\alpha r_{m2}\cos\theta)^3}+\frac{r_{m3}\left[r_2^2-r_3^2\right]}{(h_{03}+\alpha r_{m3}\cos\theta)^3}+\frac{r_{m4}\left[r_3^2-r^2\right]}{(h_{04}+\alpha r_{m4}\cos\theta)^3}\right]$$
$$+3\mu\omega\alpha\sin\theta\left[\frac{r_1^2\left[r_{m2}-r_{m1}\right]\ln\left(\frac{r_2}{r_1}\right)}{(h_{02}+\alpha r_{m2}\cos\theta)^3}+\frac{r_1^2\left[r_{m2}-r_{m1}\right]+r_2^2\left[r_{m3}-r_{m2}\right]}{(h_{03}+\alpha r_{m3}\cos\theta)^3}\ln\left(\frac{r_3}{r_2}\right)+\frac{r_1^2\left[r_{m2}-r_{m1}\right]+r_2^2\left[r_{m3}-r_{m2}\right]+r_3^2\left[r_{m4}-r_{m3}\right]}{(h_{04}+\alpha r_{m4}\cos\theta)^3}\ln\left(\frac{r}{r_3}\right)\right]$$

(39)

References

[1] Fisher MJ. A theoretical determination of some characteristics of a tilted hydrostatic slipper bearing. B.H.R.A. Rep. RR 728 April 1962.

[2] Böinghoff O. Untersuchen zum Reibungsverhalten der Gleitschuhe in Schrägscheiben-Axialkolbenmascinen. VDI-Forschungsheft 584. VDI-Verlag. 1-46. 1977.

[3] Hooke CJ and Kakoullis YP. The lubrication of slippers on axial piston pumps. 5th International Fluid Power Symposium September 1978, B2-(13-26) Durham, England.

[4] Hooke CJ and Kakoullis YP. The effects of centrifugal load and ball friction on the lubrication of slippers in axial piston pumps. 6th International Fluid Power Symposium, 179-191, Cambridge, England. 1981

[5] Iboshi N and Yamaguchi A. Characteristics of a slipper Bearing for swash plate type axial piston pumps and motors, theoretical analysis. Bulletin of the JSME, Vol 25, No 210, December 1982, 1921-1930.

[6] Iboshi N and Yamaguchi A. Characteristics of a slipper Bearing for swash plate type axial piston pumps and motors, experiment. Bulletin of the JSME, Vol 26, No 219, September 1983. 1583-1589.

[7] Hooke CJ and Kakoullis YP. The effects of non flatness on the performance of slippers in axial piston pumps. Proceedings of the Institution of Mechanical Engineers, December 1983, Vol. 197 C, 239-247.

[8] Hooke CJ and Li KY. The lubrication of overclamped slippers in axial piston pumps centrally loaded behaviour. Proceedings of the Institution of Mechanical Engineers 1988, Vol 202, No C4, 287-293.

[9] Hooke CJ and Li KY. The lubrication of slippers in axial piston pumps and motors. The effect of tilting couples. Proceedings of the Institution of Mechanical Engineers 1989, Vol 203, part C, 343-350.

[10] Takahashi K and Ishizawa S. Viscous flow between parallel disks with time varying gap width and central fluid source. JHPS International Symposium on Fluid Power, Tokyo, March 1989, 407-414.

[11] Li KY and Hooke CJ. A note on the lubrication of composite slippers in water based axial piston pumps and motors. Wear, 147 1991, 431-437.

[12] Koc E, Hooke CJ, Li KY. Slipper balance in axial piston pumps and motors.. Trans ASME, Journal of Tribology, Vol 114, October 1992, 766-772.

[13] Kobayashi S, Hirose M, Hatsue J, Ikeya M. Friction characteristics of a ball joint in the swashplate type axial piston motor. Proc Eighth International Symposium on Fluid Power, J2-565-592, Birmingham, England, 1988.

[14] Harris RM, Edge KA, Tilley DG. Predicting the behaviour of slipper pads in swashplate-type axial piston pumps. ASME Winter Annual Meeting. New Orleans, Louisiana. November 28-December 3, 1993, 1-9.

[15] Koc E and Hooke CJ. Investigation into the effects of orifice size, offset and oveclamp ratio on the lubrication of slipper bearings. Tribology International, Vol. 29, No 4, 299-305, 1996.

[16] Koc E and Hooke CJ. Considerations in the design of partially hydrostatic slipper bearings. Tribology International, Vol 30, No. 11, 815-823, 1997.

[17] Tsuta T, Iwamoto T, Umeda T. Combined dynamic response analysis of a piston-slipper system and lubricants in hydraulic piston pump. Emerging Technologies in Fluids, Structures and Fluid/Structure Interactions. Vol 396 187-194 ASME 1999.

[18] Wieczoreck U and Ivantysynova M. CASPAR-A computer aided design tool for axial piston machines. Proceedings of the Power Transmission Motion and Control International Workshop, PTMC2000, Bath, UK. 2000, 113-126.

[19] Crabtree AB, Manring ND, Johnson RE. Pressure measurements for translating hydrostatic trust bearings. International Journal of Fluid Power. Vol. 6 N 3 November 2005.

[20] Kazama T. Numerical simulation of a slipper model for water hydraulic pumps/motors in mixed lubrication. Proceedings of the 6th JFPS International Symposium on Fluid Power, TSUKUBA 2005. November 7-10, 2005.

[21] Kakoulis YP. Slipper lubrication in axial piston pumps, M.Sc. Thesis University of Birmingham, 1977.

[22] Bergada JM and Watton J. A direct leakage flow rate calculation method for axial pump grooved pistons and slippers, and its evaluation for a 5/95 fluid application. 5th JFPS international Symposium on fluid power, Nara Japan. November 13, 2002.

[23] Bergada JM and Watton J. Axial piston pump slipper balance with multiple lands. ASME International Mechanical Engineering Congress and exposition. IMECE 2002. New Orleans Louisiana November 17-22 2002. Vol 2 paper 39338.

[24] Konami S and Nishiumi T. Hydraulic Control Systems (in Japanese). Published by TDU 1999.

[25] Freeman P. Lubrication and friction. Published by Pitman, 1962

A.2 Axial piston pump analysis

A.2.1 Calibration curves for pressure transducers

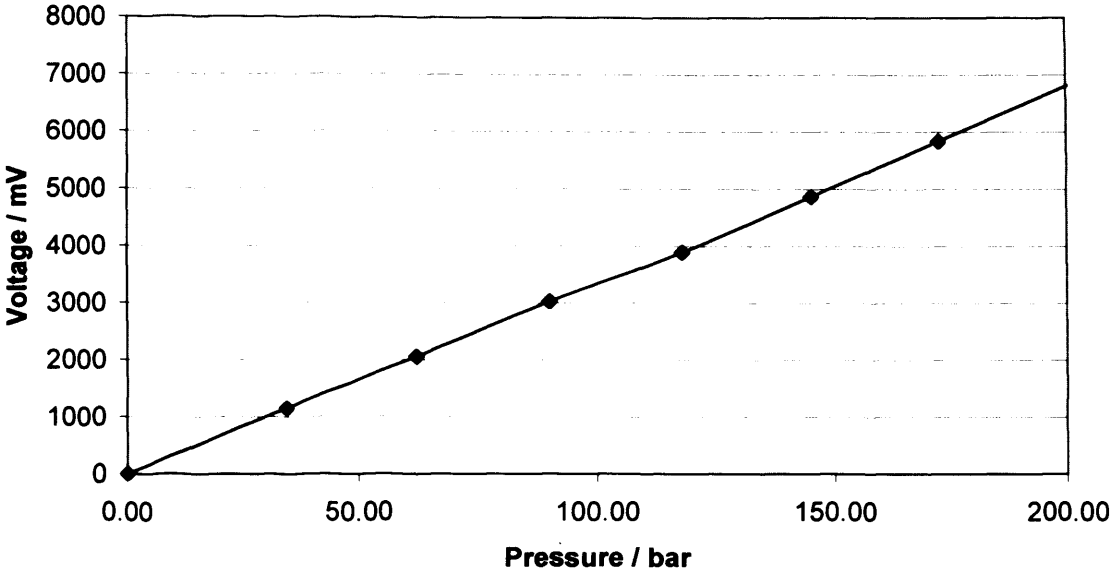

A.2.1.1 Calibration Curve transducer 26767 and charge amplifier #2

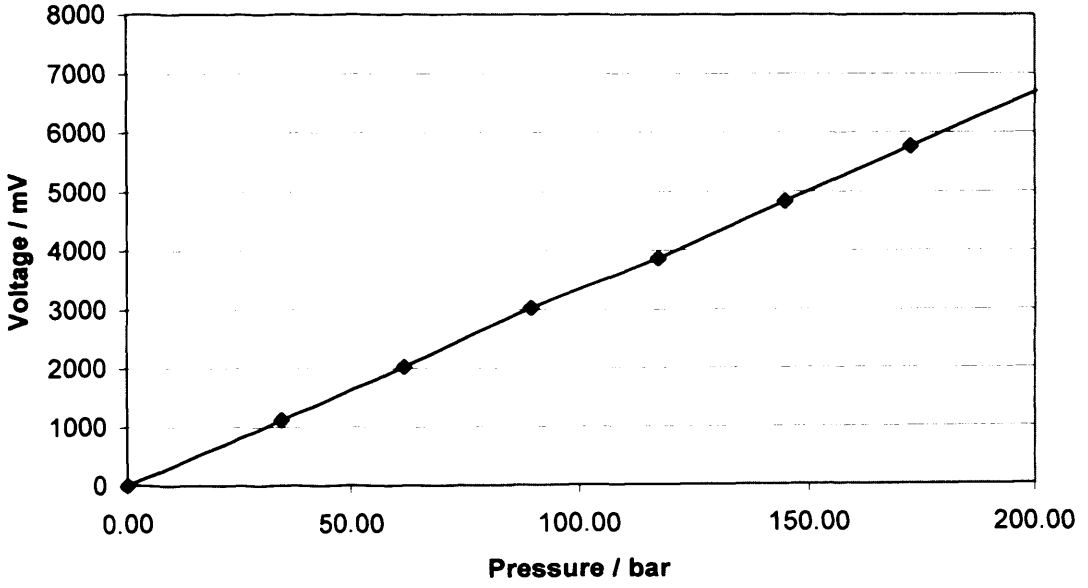

A.2.1.2 Calibration Curve transducer 26768 and charge amplifier #3

A.2.2 Pump model mesh deformation

A.2.2.1 User defined function for motion of pistons

```
/************************************************************************/
/* UDF for defining the motion of a piston in an axial piston pump      */
/* UDF written for use with FLUENT                                      */
/************************************************************************/

#include "udf.h"

DEFINE_CG_MOTION(Piston_Motion_1,dt,vel,omega,time,dtime)
        {
                real pi;
                real beta;
                real radius;
                real w;
                real theta;
                real t;
                t = CURRENT_TIME ;
                pi = 3.141592654 ;
                beta = 0.34906585 ;
                radius = 0.0306 ;
                w = 150 ;
                theta = t * w ;
                vel[2] = w*radius*tan(beta)*sin(theta) ;
        }


DEFINE_CG_MOTION(Piston_Motion_2,dt,vel,omega,time,dtime)
        {
                real pi;
                real beta;
                real radius;
                real w;
                real theta;
                real t;
                t = CURRENT_TIME ;
                pi = 3.141592654 ;
                beta = 0.34906585 ;
                radius = 0.0306 ;
                w = 150 ;
                theta = t * w ;
                vel[2] = w*radius*tan(beta)*sin(theta-((40*pi)/180)) ;
        }


DEFINE_CG_MOTION(Piston_Motion_3,dt,vel,omega,time,dtime)
        {
                real pi;
```

```
        real beta;
        real radius;
        real w;
        real theta;
        real t;
        t = CURRENT_TIME ;
        pi = 3.141592654 ;
        beta = 0.34906585 ;
        radius = 0.0306 ;
        w = 150 ;
        theta = t * w ;
        vel[2] = w*radius*tan(beta)*sin(theta-((80*pi)/180)) ;
    }


DEFINE_CG_MOTION(Piston_Motion_4,dt,vel,omega,time,dtime)
    {
        real pi;
        real beta;
        real radius;
        real w;
        real theta;
        real t;
        t = CURRENT_TIME ;
        pi = 3.141592654 ;
        beta = 0.34906585 ;
        radius = 0.0306 ;
        w = 150 ;
        theta = t * w ;
        vel[2] = w*radius*tan(beta)*sin(theta-((120*pi)/180)) ;
    }


DEFINE_CG_MOTION(Piston_Motion_5,dt,vel,omega,time,dtime)
    {
        real pi;
        real beta;
        real radius;
        real w;
        real theta;
        real t;
        t = CURRENT_TIME ;
        pi = 3.141592654 ;
        beta = 0.34906585 ;
        radius = 0.0306 ;
        w = 150 ;
        theta = t * w ;
        vel[2] = w*radius*tan(beta)*sin(theta-((160*pi)/180)) ;
    }
```

```
DEFINE_CG_MOTION(Piston_Motion_6,dt,vel,omega,time,dtime)
    {
        real pi;
        real beta;
        real radius;
        real w;
        real theta;
        real t;
        t = CURRENT_TIME ;
        pi = 3.141592654 ;
        beta = 0.34906585 ;
        radius = 0.0306 ;
        w = 150 ;
        theta = t * w ;
        vel[2] = w*radius*tan(beta)*sin(theta-((200*pi)/180)) ;
    }

DEFINE_CG_MOTION(Piston_Motion_7,dt,vel,omega,time,dtime)
    {
        real pi;
        real beta;
        real radius;
        real w;
        real theta;
        real t;
        t = CURRENT_TIME ;
        pi = 3.141592654 ;
        beta = 0.34906585 ;
        radius = 0.0306 ;
        w = 150 ;
        theta = t * w ;
        vel[2] = w*radius*tan(beta)*sin(theta-((240*pi)/180)) ;
    }

DEFINE_CG_MOTION(Piston_Motion_8,dt,vel,omega,time,dtime)
    {
        real pi;
        real beta;
        real radius;
        real w;
        real theta;
        real t;
        t = CURRENT_TIME ;
        pi = 3.141592654 ;
        beta = 0.34906585 ;
        radius = 0.0306 ;
        w = 150 ;
```

```
        theta = t * w ;
        vel[2] = w*radius*tan(beta)*sin(theta-((280*pi)/180)) ;
    }


DEFINE_CG_MOTION(Piston_Motion_9,dt,vel,omega,time,dtime)
    {
        real pi;
        real beta;
        real radius;
        real w;
        real theta;
        real t;
        t = CURRENT_TIME ;
        pi = 3.141592654 ;
        beta = 0.34906585 ;
        radius = 0.0306 ;
        w = 150 ;
        theta = t * w ;
        vel[2] = w*radius*tan(beta)*sin(theta-((320*pi)/180)) ;
    }
```

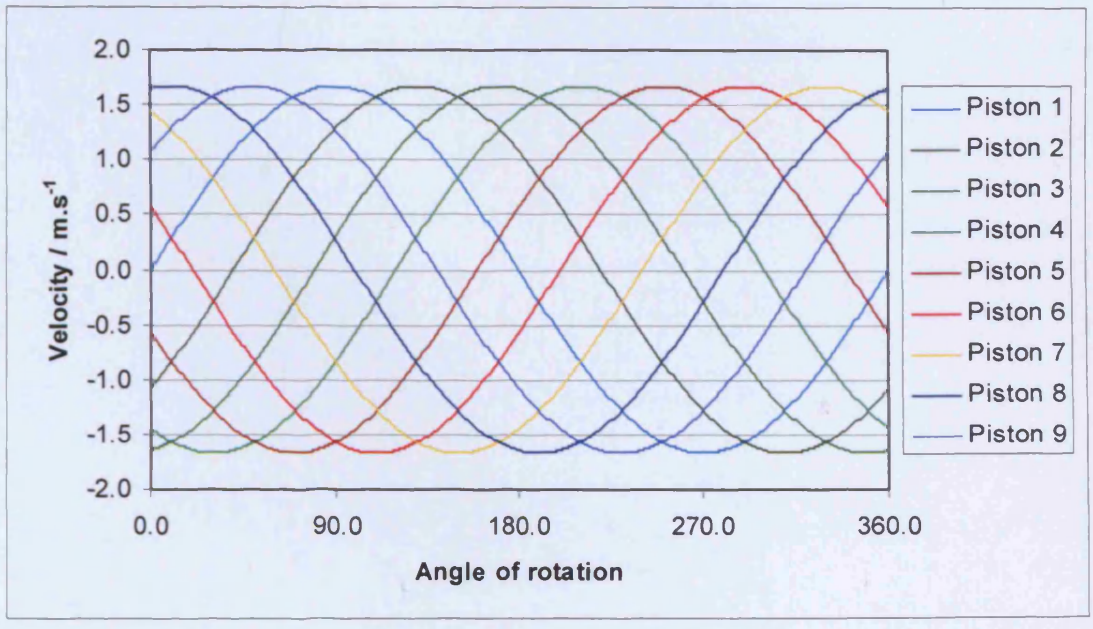

A.2.2.2 Velocity of Pistons

A.2.3 CAD drawings

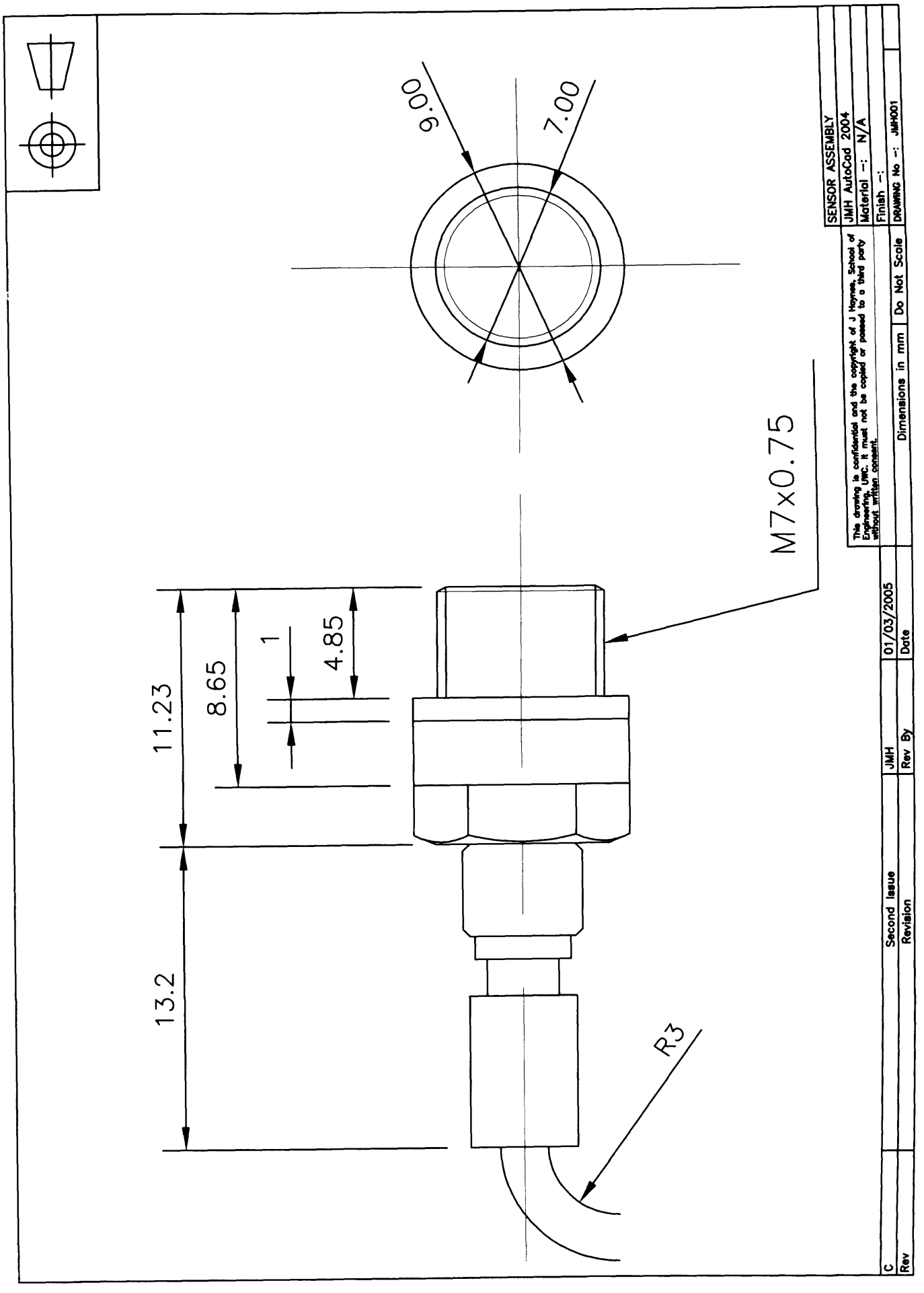
9.00
7.00
M7x0.75
11.23
8.65
1
4.85
13.2
R3
SENSOR ASSEMBLY
JMH AutoCad 2004
Material –: N/A
Finish –:
DRAWING No –: JMH001
This drawing is confidential and the copyright of J Haynes, School of Engineering, UWC. It must not be copied or passed to a third party without written consent.
Do Not Scale
Dimensions in mm
01/03/2005
JMH
Second Issue
C
Rev
Date
Rev By
Revision

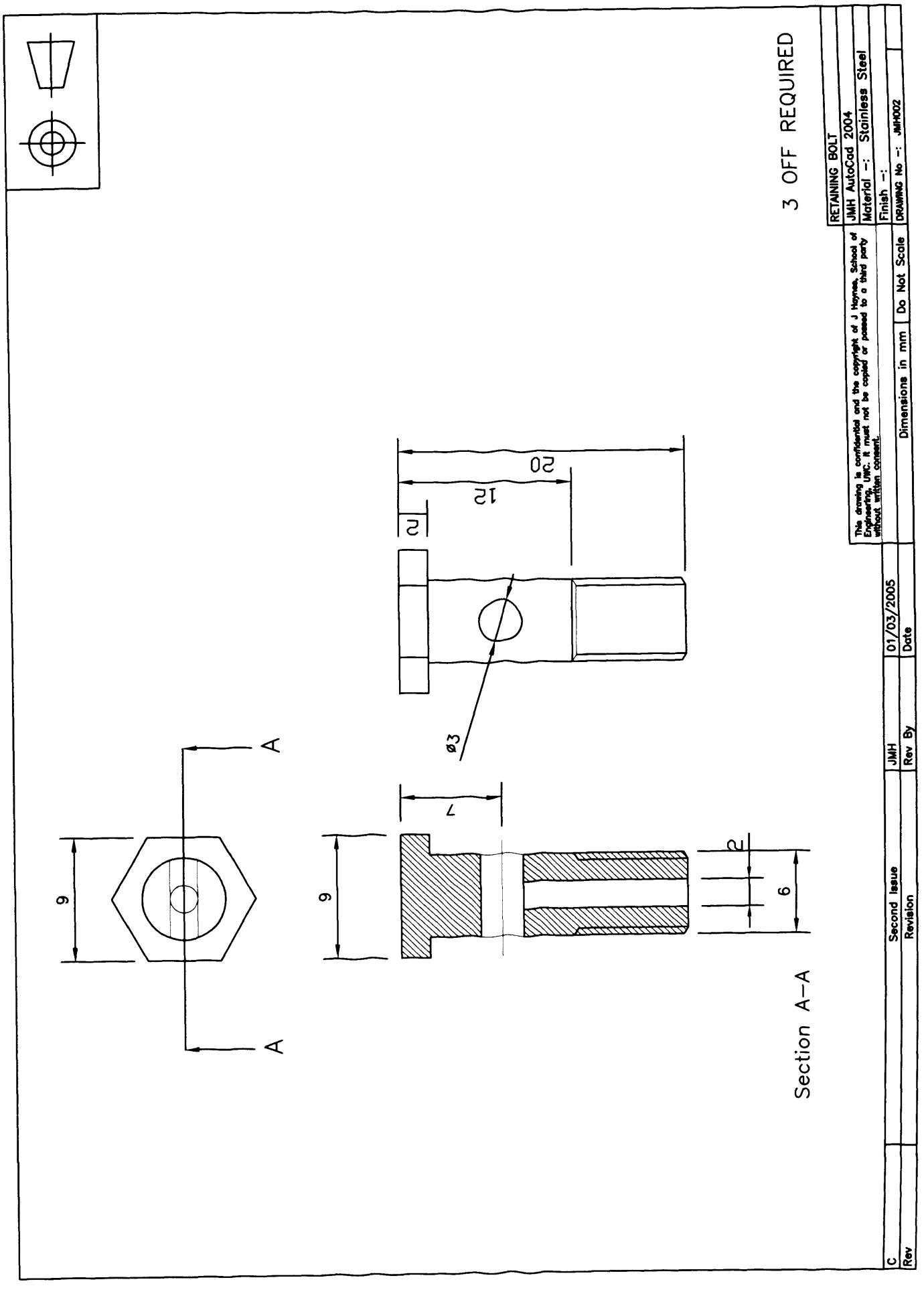
3 OFF REQUIRED
RETAINING BOLT
JMH AutoCad 2004
Material –: Stainless Steel
Finish –:
DRAWING No –: JMH002
This drawing is confidential and the copyright of J Haynes, School of Engineering, UWC. It must not be copied or passed to a third party without written consent.
Dimensions in mm
Do Not Scale
01/03/2005
Date
JMH
Rev By
Second Issue
Revision
C
Rev
20
12
2
ø3
7
9
9
2
6
A
A
Section A–A

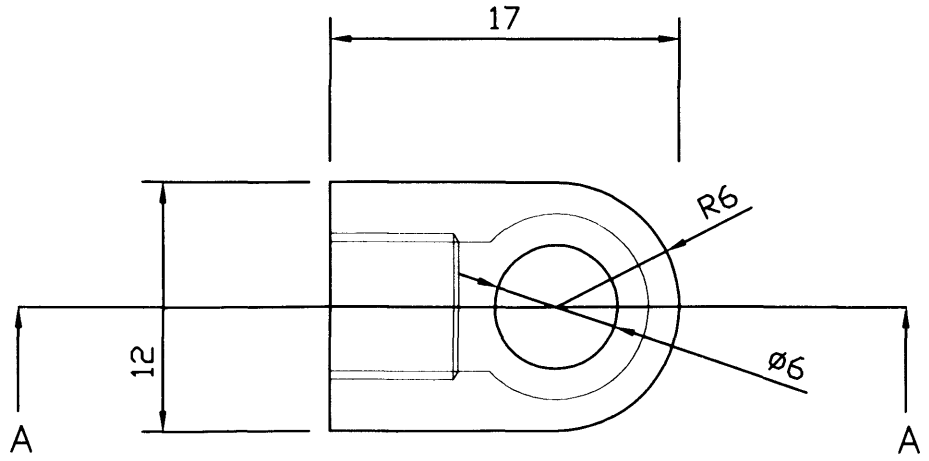

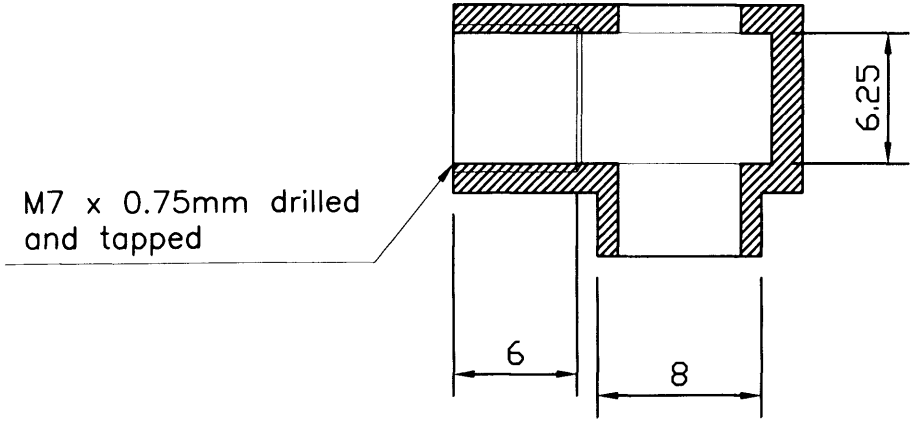

Section A–A

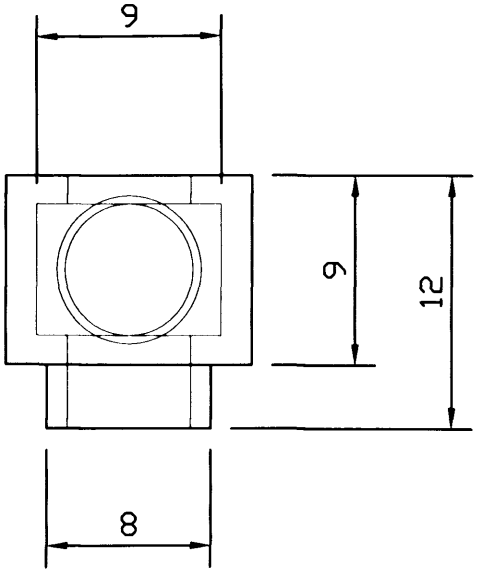

3 OFF REQUIRED

C	Second Issue	JMH	01/03/2005		COLLAR
					JMH AutoCad 2004
					Material –: Stainless Steel
					Finish –:
Rev	Revision	Rev By	Date	Dimensions in mm Do Not Scale	DRAWING No –: JMH003

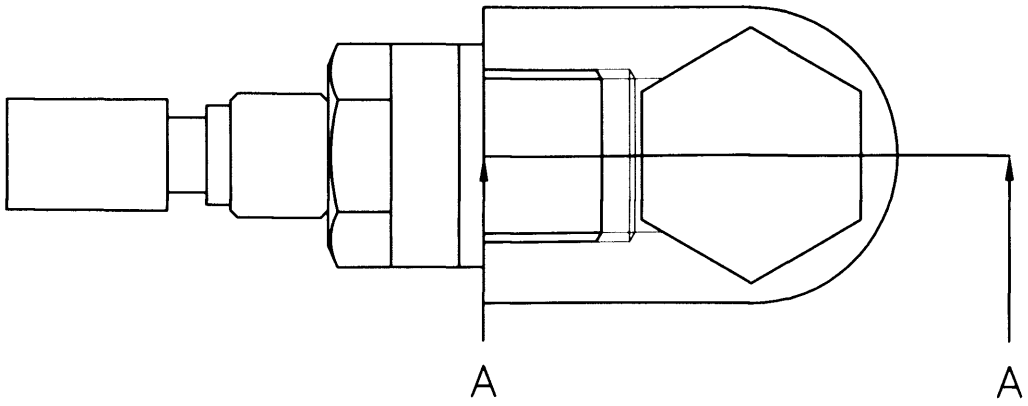

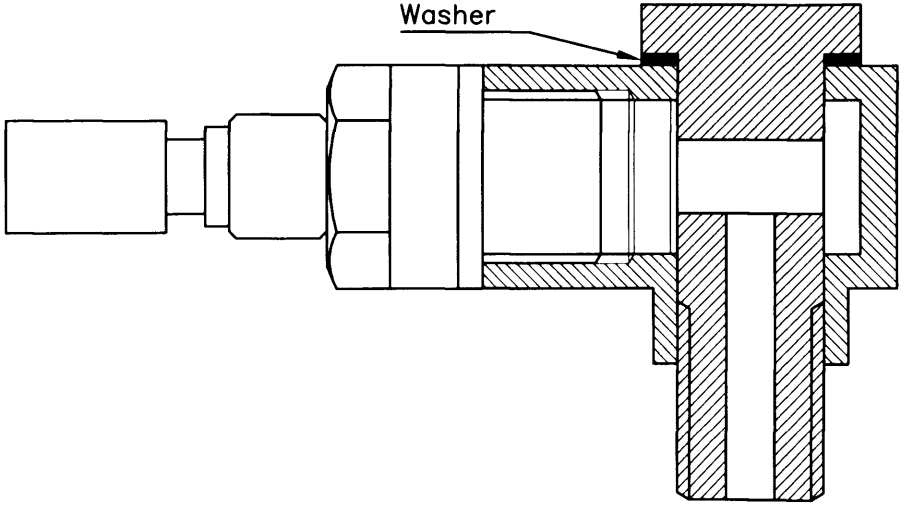

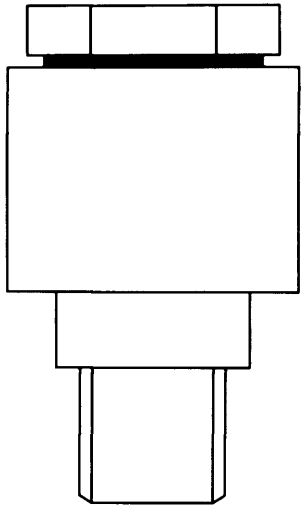

Section A–A

					ASSEMBLED SENSOR HOLDER
				This drawing is confidential and the copyright of J Haynes, School of Engineering, UWC. It must not be copied or passed to a third party without written consent.	JMH AutoCad 2004
					Material –: Stainless Steel
C	Second Issue	JMH	01/03/2005		Finish –:
Rev	Revision	Rev By	Date	Dimensions in mm Do Not Scale	DRAWING No –: JMH004

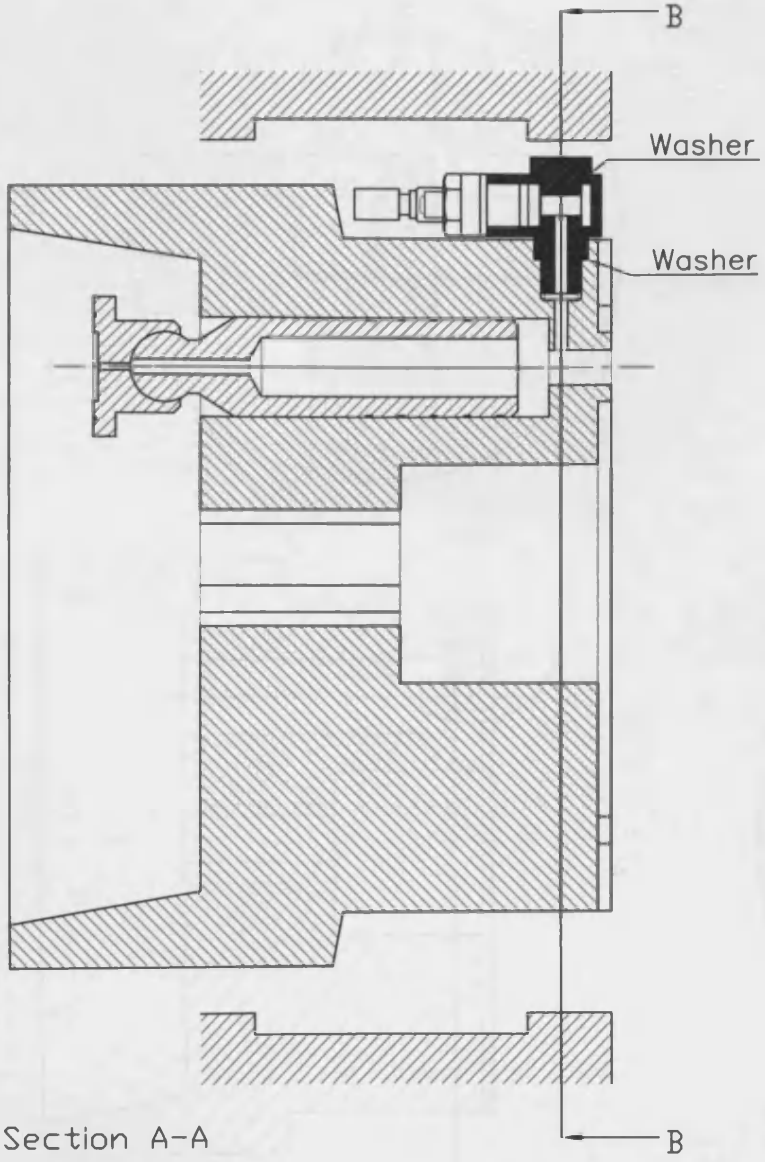

Section A-A

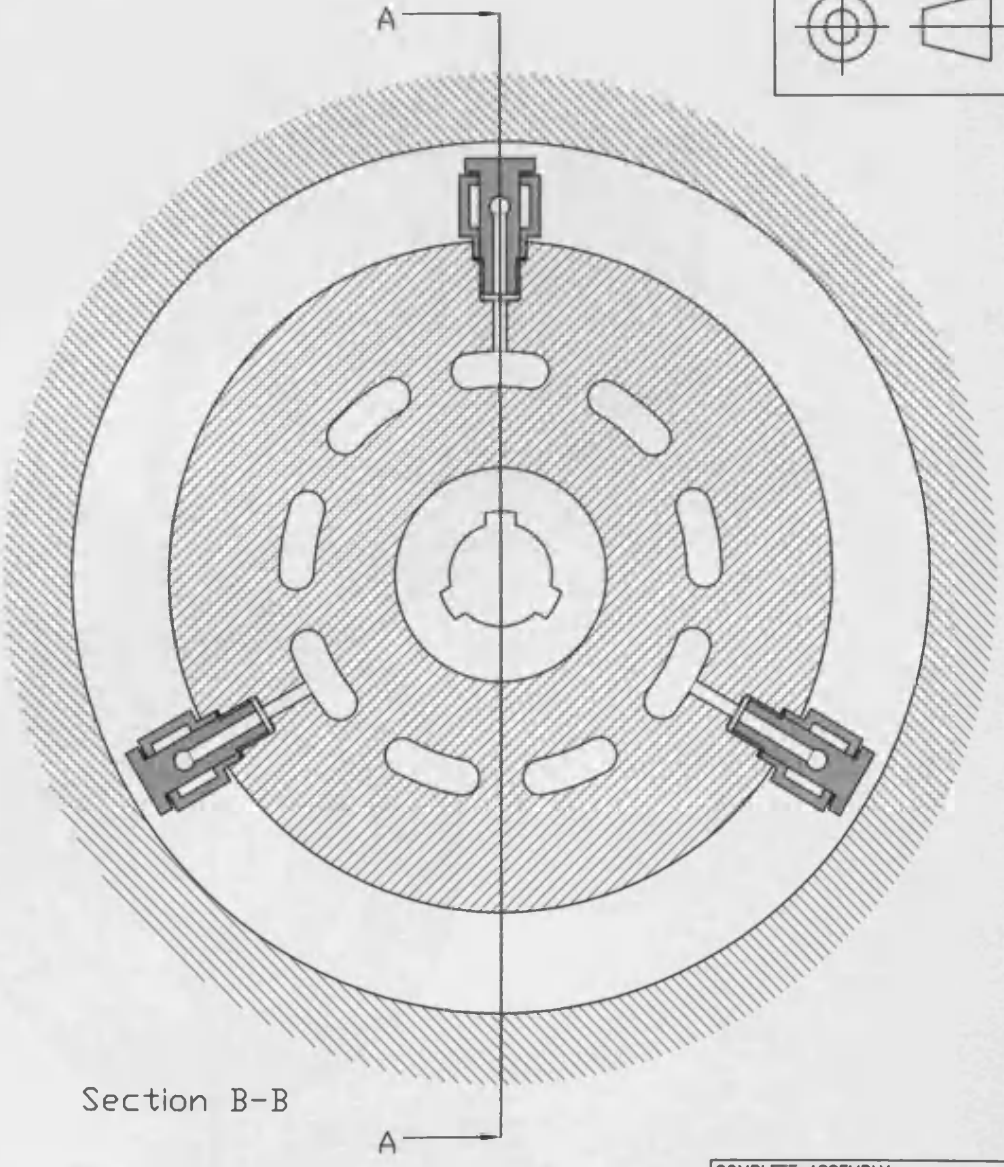

Section B-B

C	Second Issue	JMH	01/03/2005	COMPLETE ASSEMBLY	
Rev	Revision	Rev By	Date	JMH AutoCad 2004	
				Material –: N/A	
				Finish –:	
			Dimensions in mm	Do Not Scale	DRAWING No –: JMH005

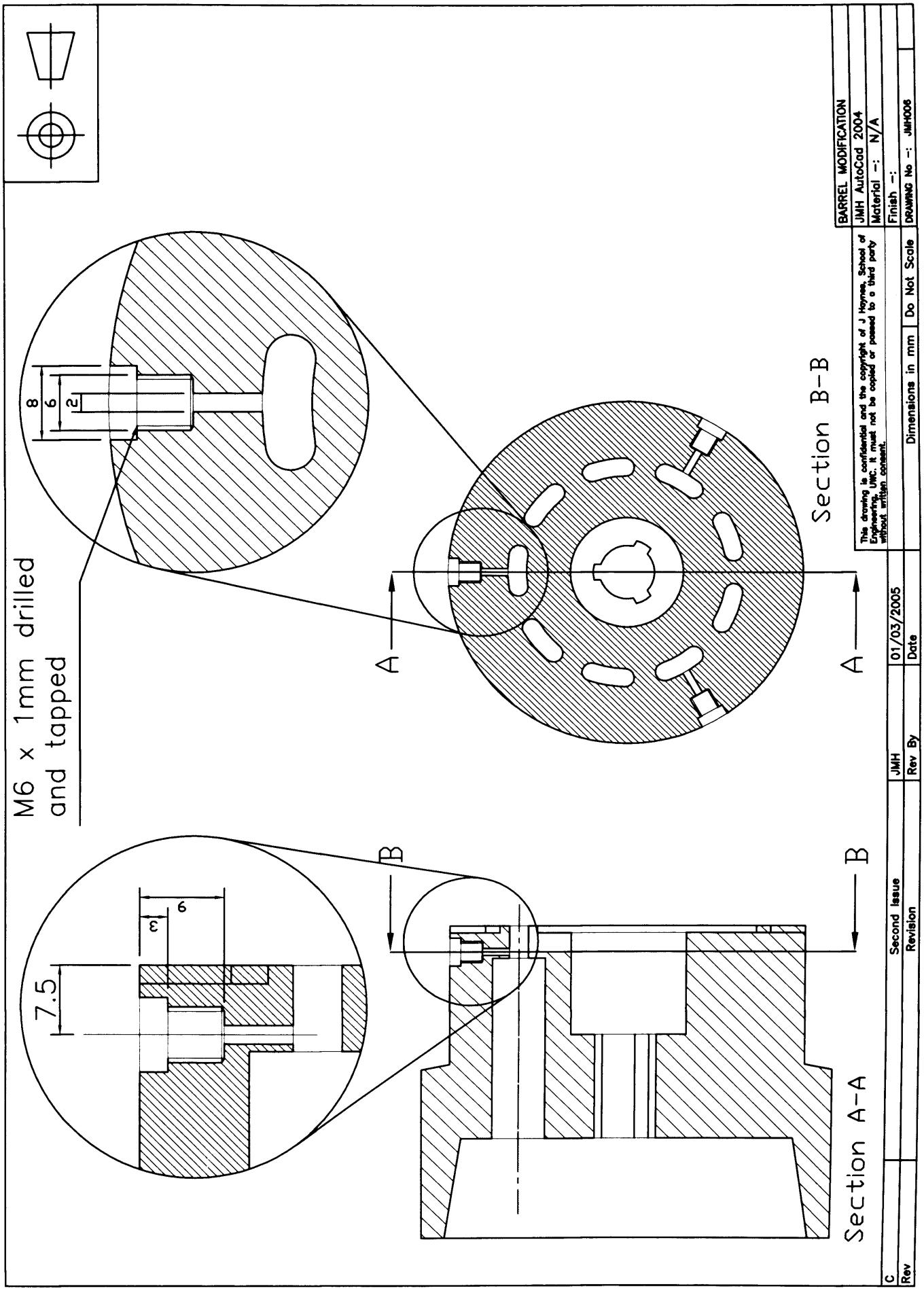
M6 x 1mm drilled
and tapped
8
6
2
Section B-B
A
A
B
B
7.5
3
6
Section A-A
BARREL MODIFICATION
JMH AutoCad 2004
Material –: N/A
Finish –:
DRAWING No –: JMH006
This drawing is confidential and the copyright of J Haynes, School of Engineering, UMC. It must not be copied or passed to a third party without written consent.
Dimensions in mm
Do Not Scale
c
Second Issue
JMH
01/03/2005
Rev
Revision
Rev By
Date

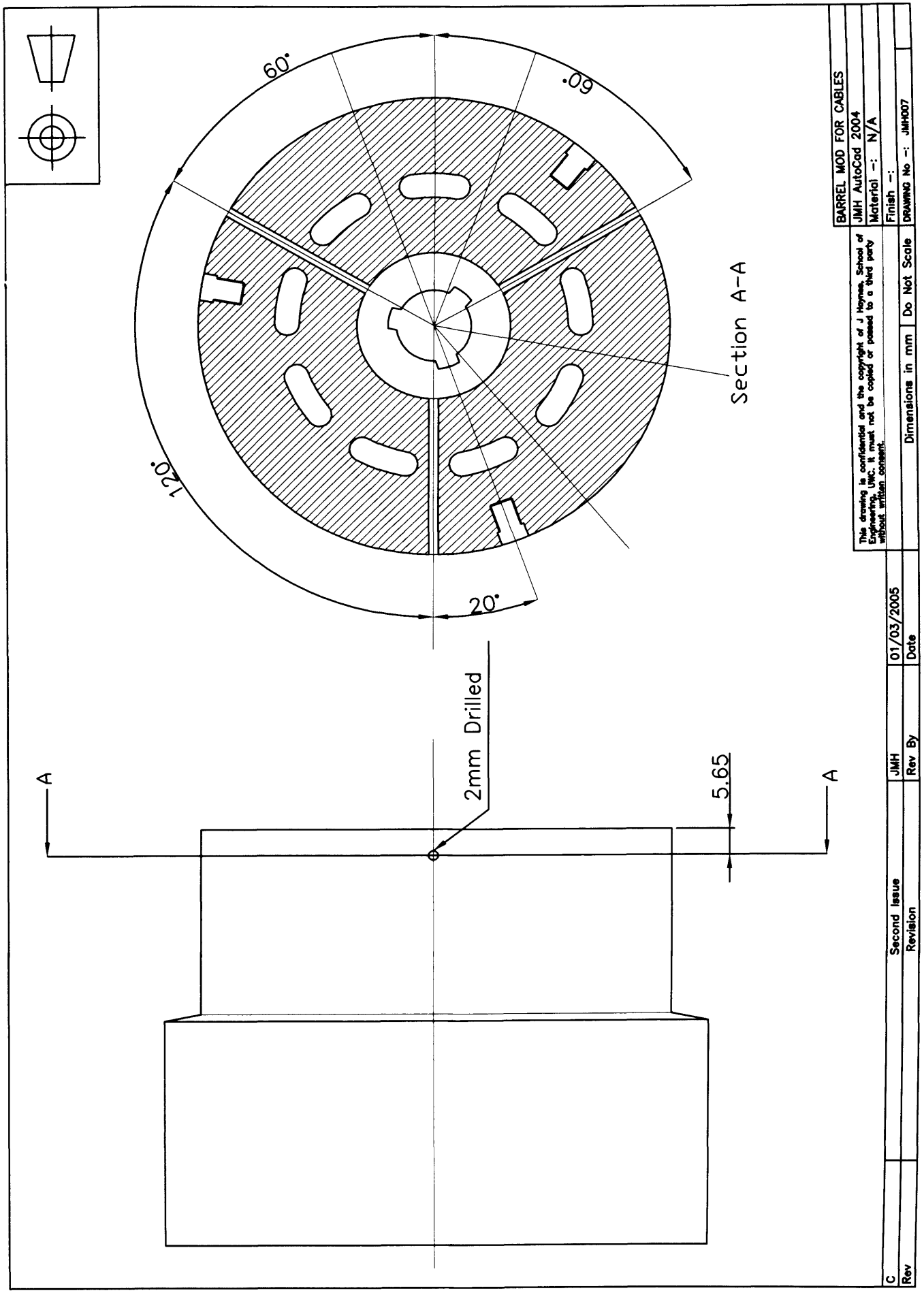
60°
60°
120°
20°
Section A-A
2mm Drilled
5.65
A
A
BARREL MOD FOR CABLES
JMH AutoCad 2004
Material –: N/A
Finish –:
DRAWING No –: JMH007
Dimensions in mm
Do Not Scale
This drawing is confidential and the copyright of J Haynes, School of Engineering, UWC. It must not be copied or passed to a third party without written consent.
C
Second Issue
JMH
01/03/2005
Rev
Revision
Rev By
Date

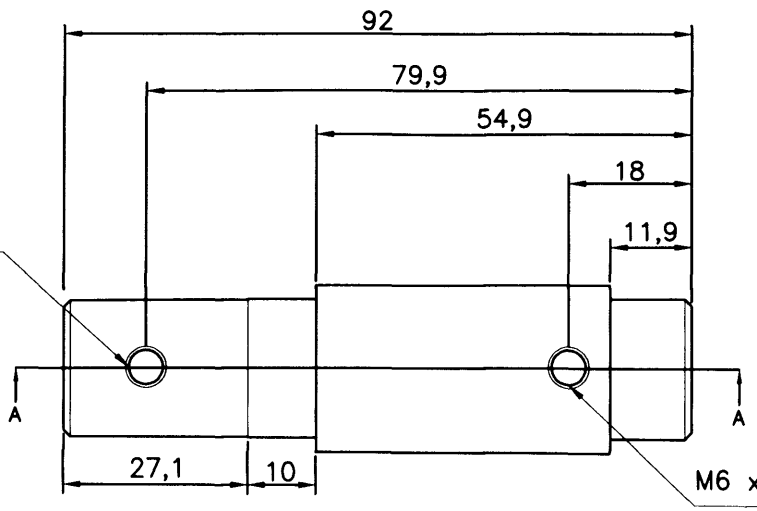

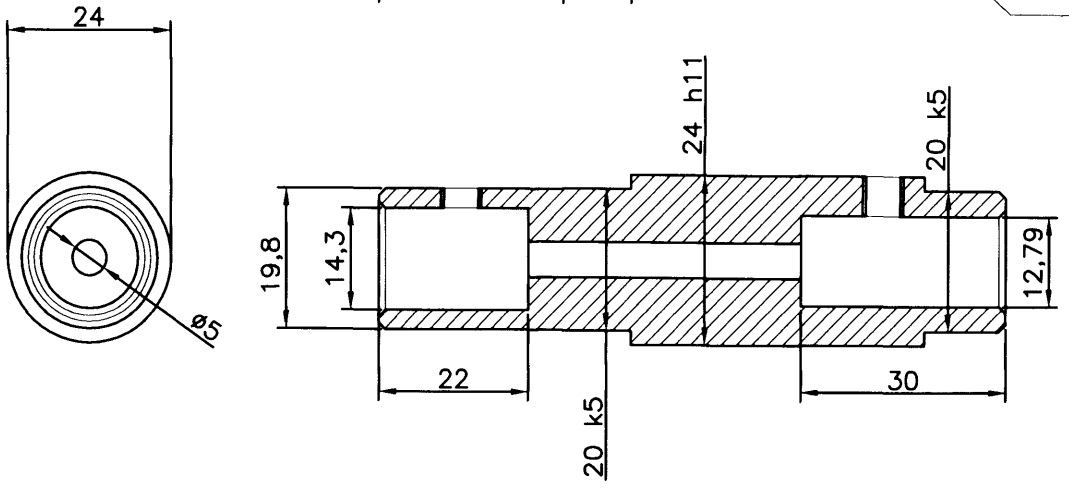

Section A–A

Tolerances:
k5: +0.011mm
+0.002

h11: +0
−0.13

COUPLING

JMH AutoCad 2004

Material –: Silver Steel

Finish –:

DRAWING No –: JMH008

Dimensions in mm | Do Not Scale

Rev	Revision	Rev By	Date
C	Third Issue	JMH	21/04/2005

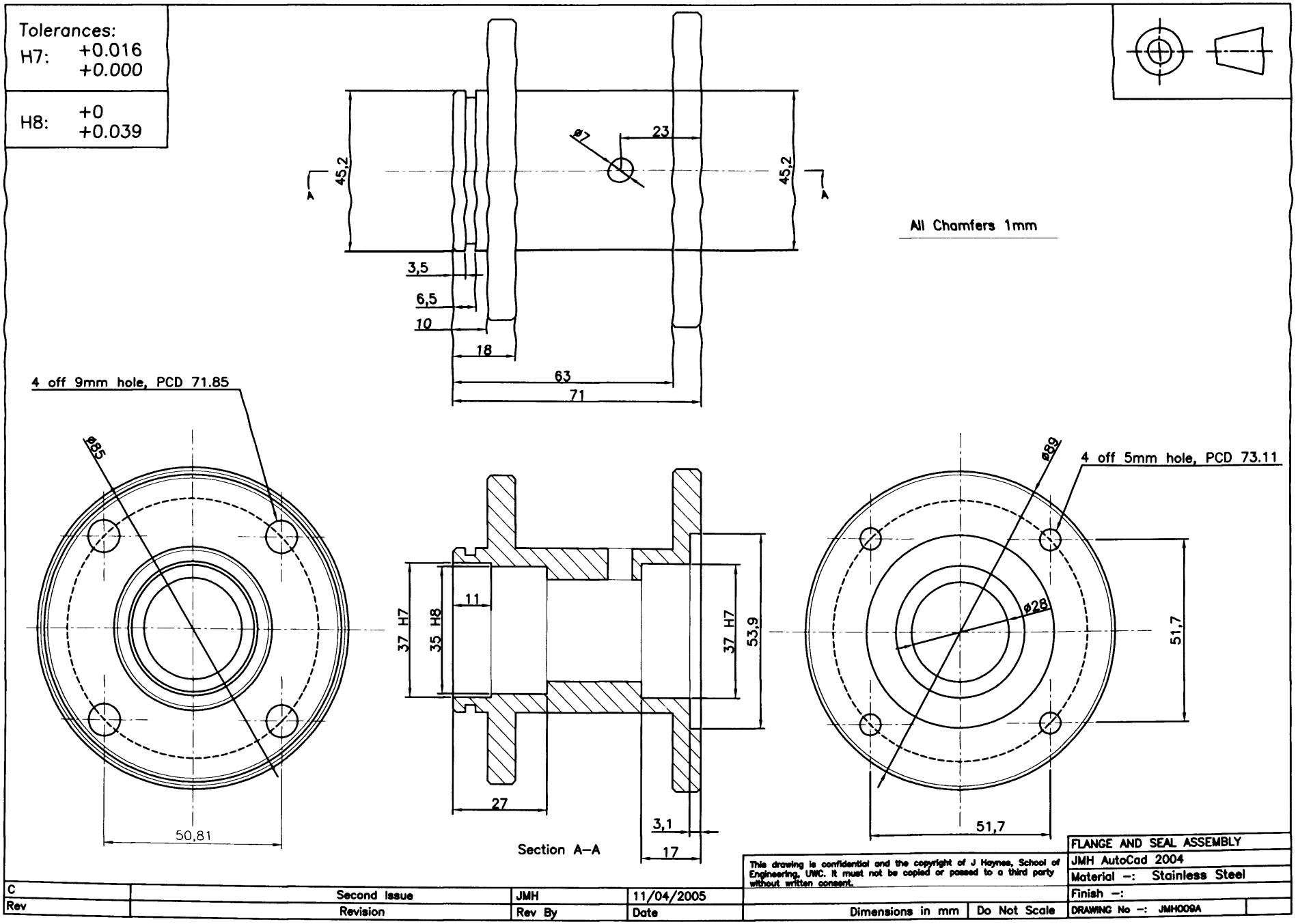
Tolerances:
H7: +0.016 +0.000
H8: +0 +0.039
45,2
ø7
23
45,2
All Chamfers 1mm
3,5
6,5
10
18
63
71
4 off 9mm hole, PCD 71.85
ø85
50,81
37 H7
35 H8
11
27
3,1
17
Section A-A
37 H7
53,9
ø89
4 off 5mm hole, PCD 73.11
ø28
51,7
51,7
This drawing is confidential and the copyright of J Haynes, School of Engineering, UWC. It must not be copied or passed to a third party without written consent.
FLANGE AND SEAL ASSEMBLY
JMH AutoCad 2004
Material –: Stainless Steel
Finish –:
DRAWING No –: JMH009A
C
Second Issue
JMH
11/04/2005
Rev
Revision
Rev By
Date
Dimensions in mm
Do Not Scale

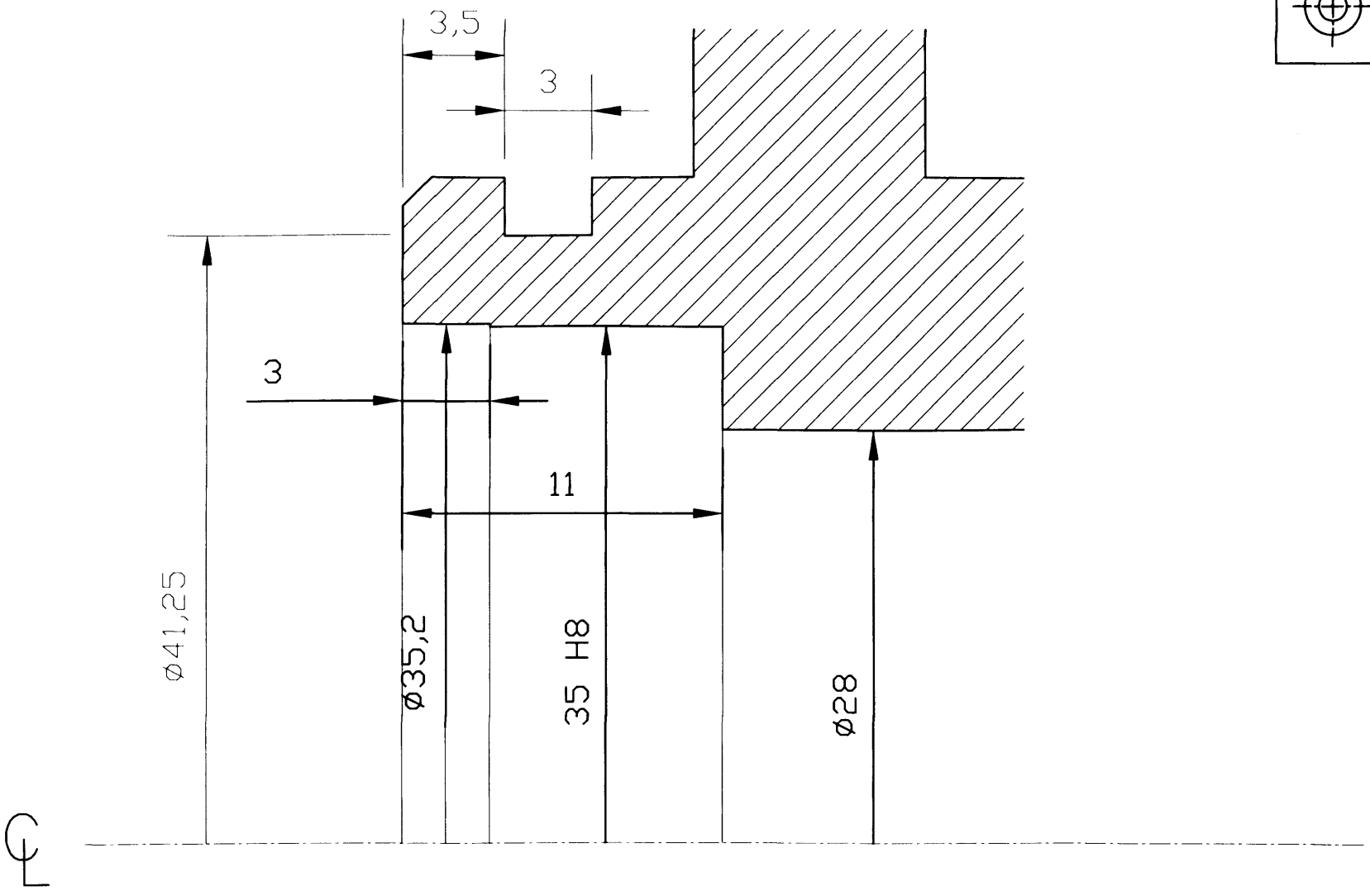

Detail of seal seat, drawing JMH009A

				This drawing is confidential and the copyright of J Haynes, School of Engineering, UWC. It must not be copied or passed to a third party without written consent.		FLANGE AND SEAL ASSEMBLY
						JMH AutoCad 2004
						Material –: Stainless Steel
C	Second Issue	JMH	11/04/2005			Finish –:
Rev	Revision	Rev By	Date	Dimensions in mm	Do Not Scale	DRAWING No –: JMH009B

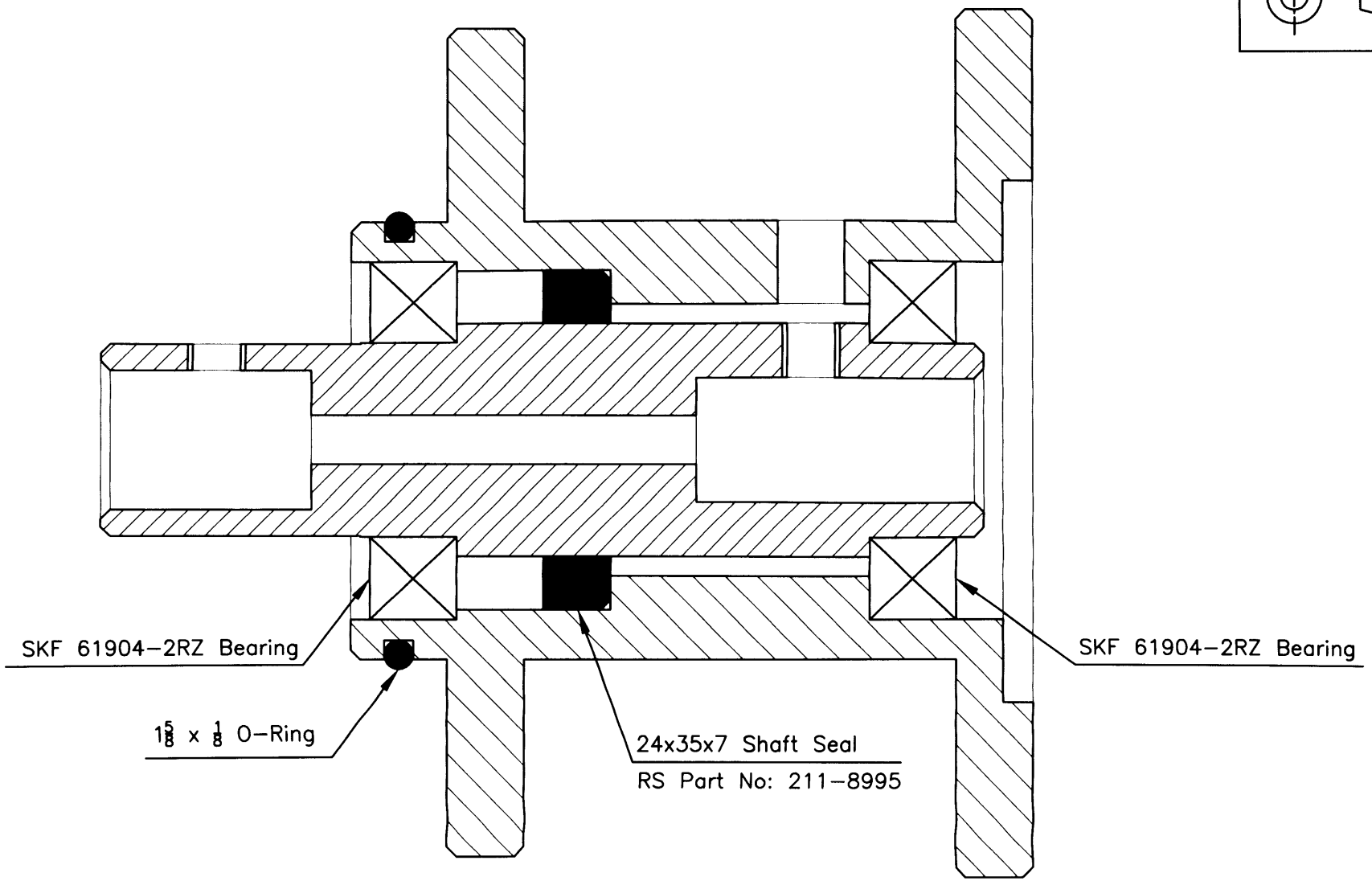

Section through flange and coupling

						FLANGE AND SEAL ASSEMBLY
				This drawing is confidential and the copyright of J Haynes, School of Engineering, UWC. It must not be copied or passed to a third party without written consent.		JMH AutoCad 2004
						Material –: Stainless Steel
C	Second Issue	JMH	11/04/2005			Finish –:
Rev	Revision	Rev By	Date	Dimensions in mm	Do Not Scale	DRAWING No –: JMH010

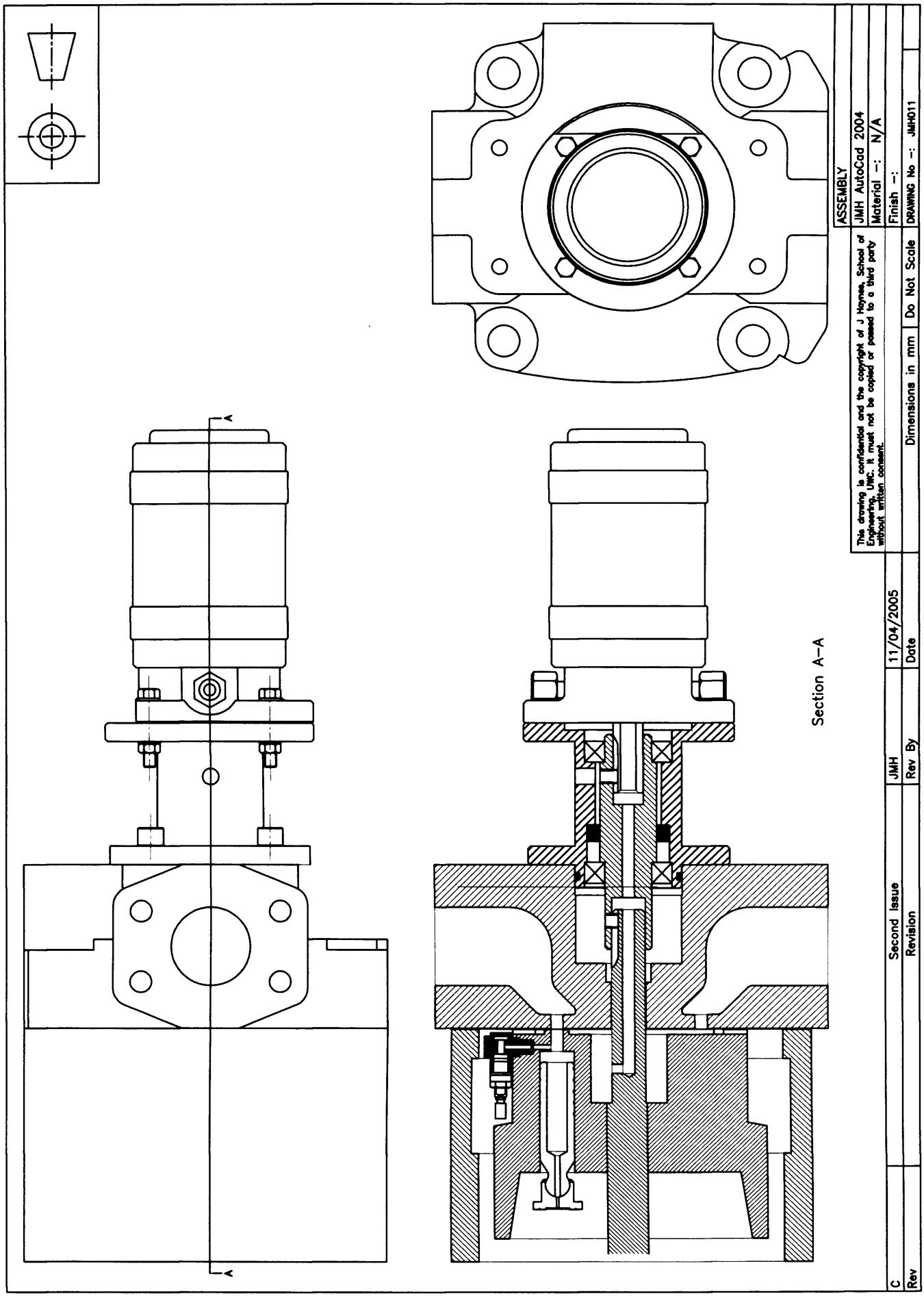
ASSEMBLY
JMH AutoCad 2004
Material –: N/A
Finish –:
DRAWING No –: JMH011
This drawing is confidential and the copyright of J Haynes, School of Engineering, UWC. It must not be copied or passed to a third party without written consent.
Dimensions in mm
Do Not Scale
Second Issue
11/04/2005
JMH
Revision
Date
Rev By
C
Rev
Section A–A

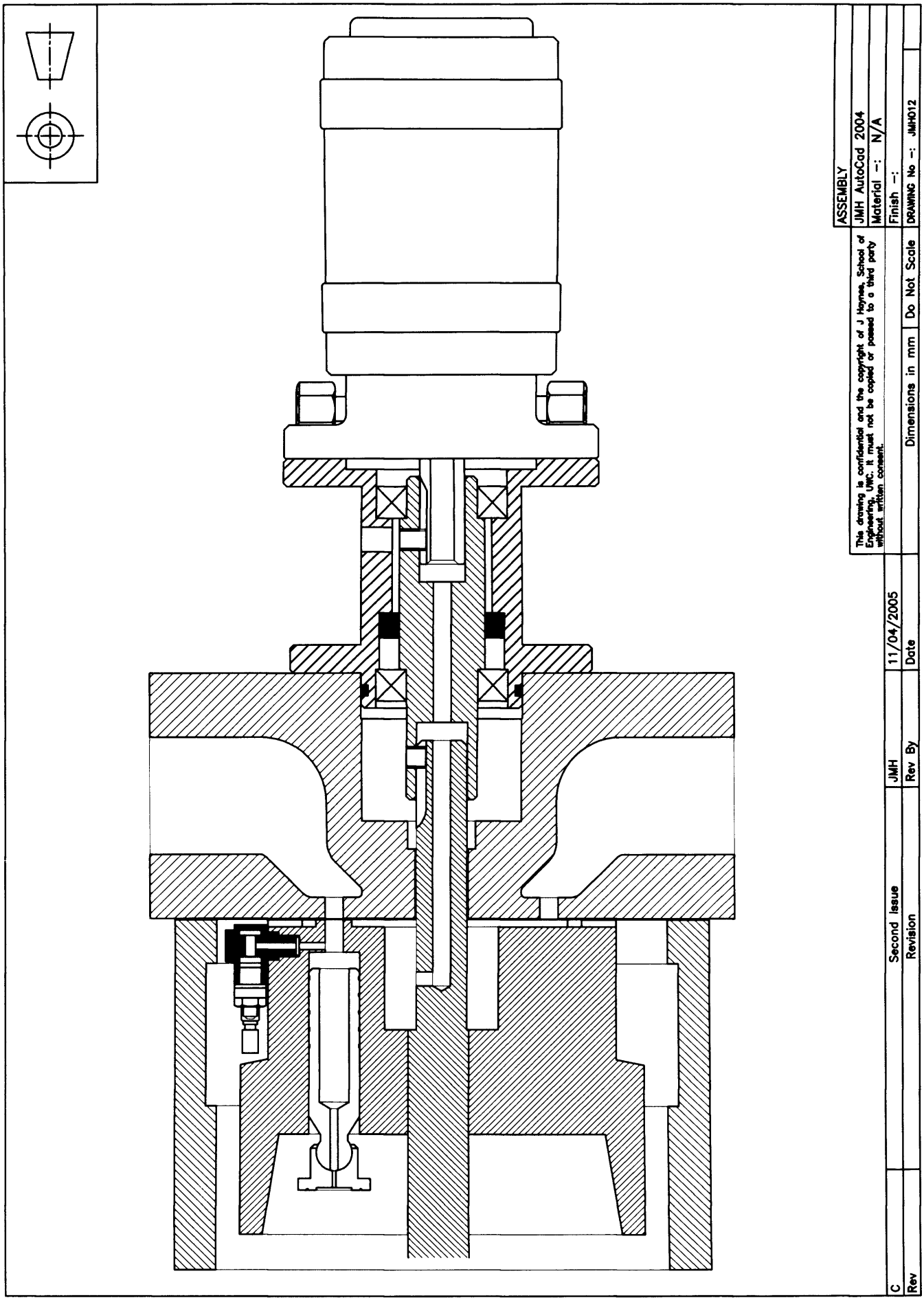
ASSEMBLY
JMH AutoCad 2004
Material –: N/A
Finish –:
DRAWING No –: JMH012
This drawing is confidential and the copyright of J Haynes, School of Engineering, UWC. It must not be copied or passed to a third party without written consent.
Dimensions in mm
Do Not Scale
Second Issue
JMH
11/04/2005
Revision
Rev By
Date
C
Rev

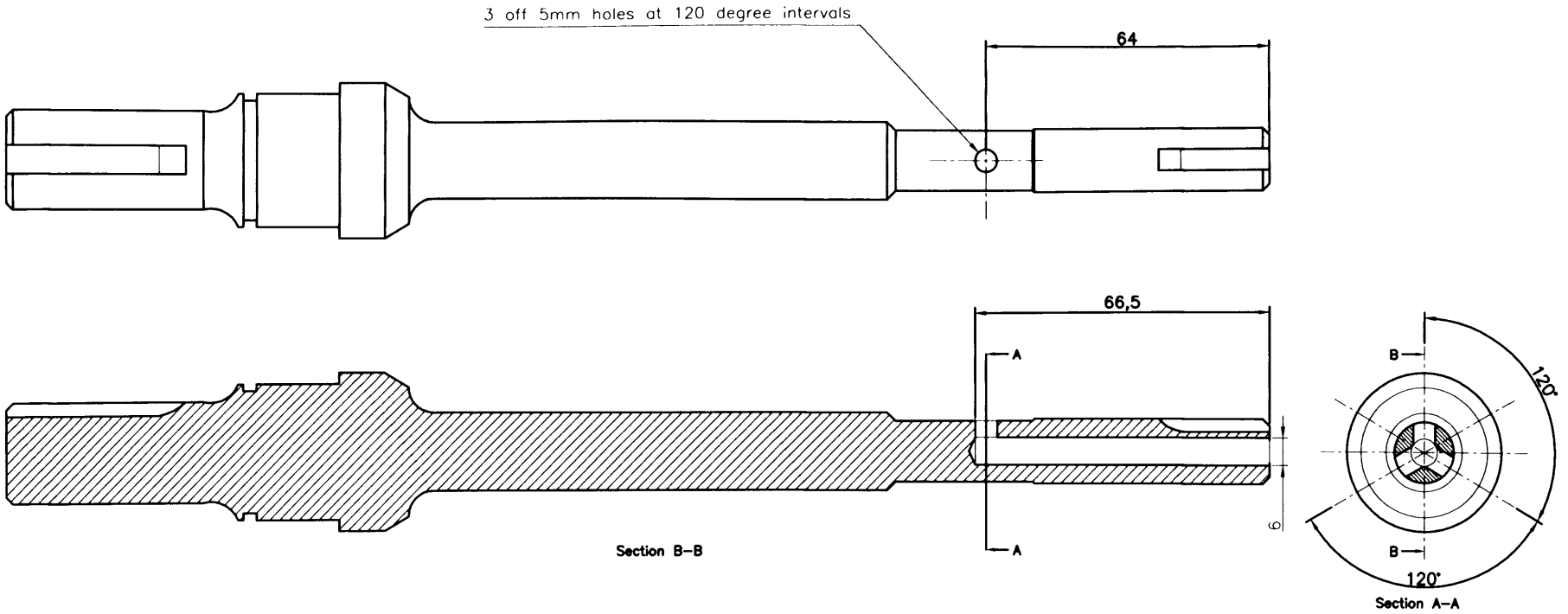

				This drawing is confidential and the copyright of J Haynes, School of Engineering, UWC. It must not be copied or passed to a third party without written consent.		MOD TO PUMP SHAFT
						JMH AutoCad 2004
						Material –: N/A
C	Second Issue	JMH	11/05/2005			Finish –:
Rev	Revision	Rev By	Date	Dimensions in mm	Do Not Scale	DRAWING No –: JMH013

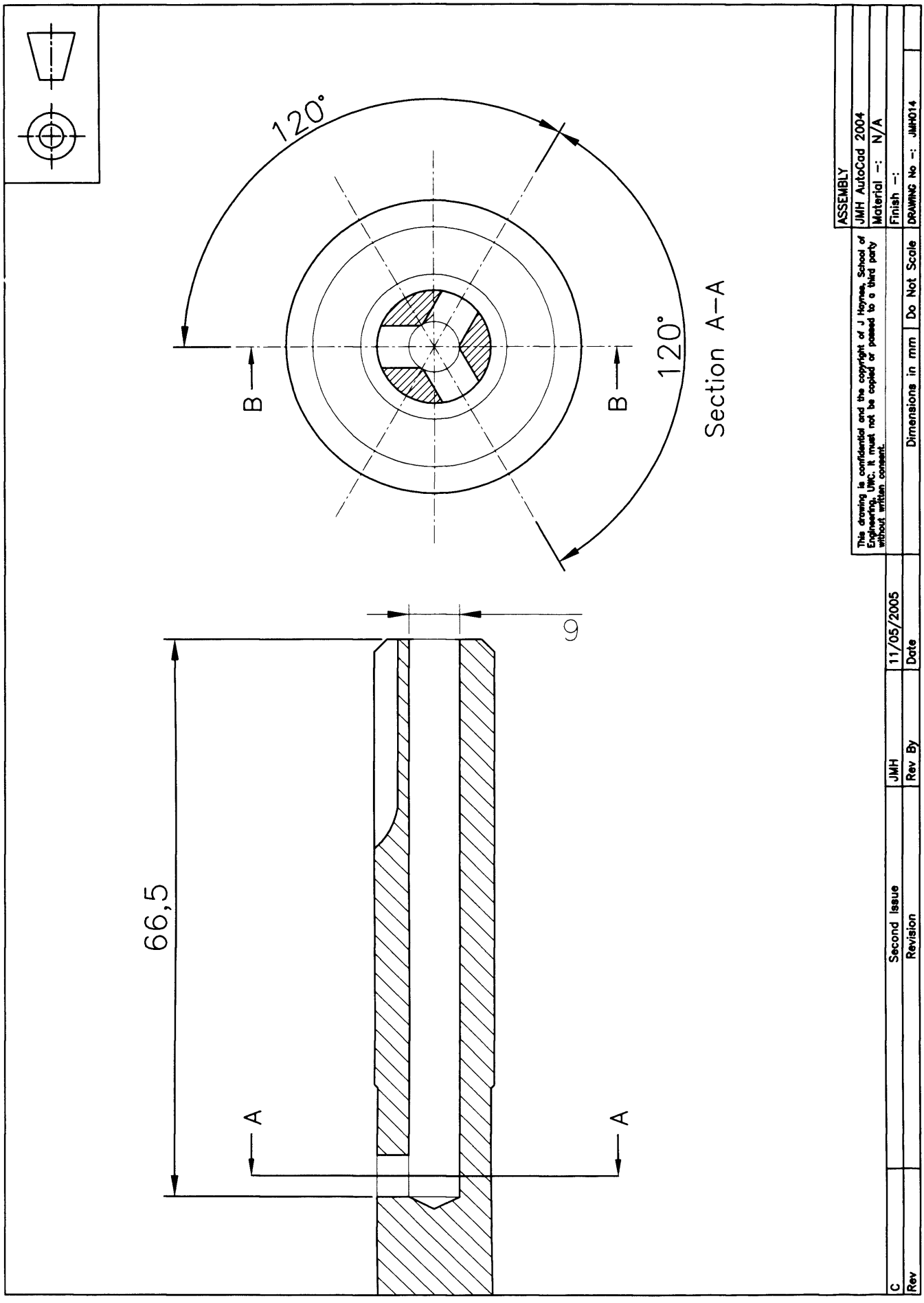
120°
120°
B
B
Section A-A
9
66,5
A
A
ASSEMBLY
JMH AutoCad 2004
Material –: N/A
Finish –:
DRAWING No –: JMH014
This drawing is confidential and the copyright of J Haynes, School of Engineering, UWC. It must not be copied or passed to a third party without written consent.
Dimensions in mm
Do Not Scale
Second Issue
Revision
JMH
Rev By
11/05/2005
Date
C
Rev

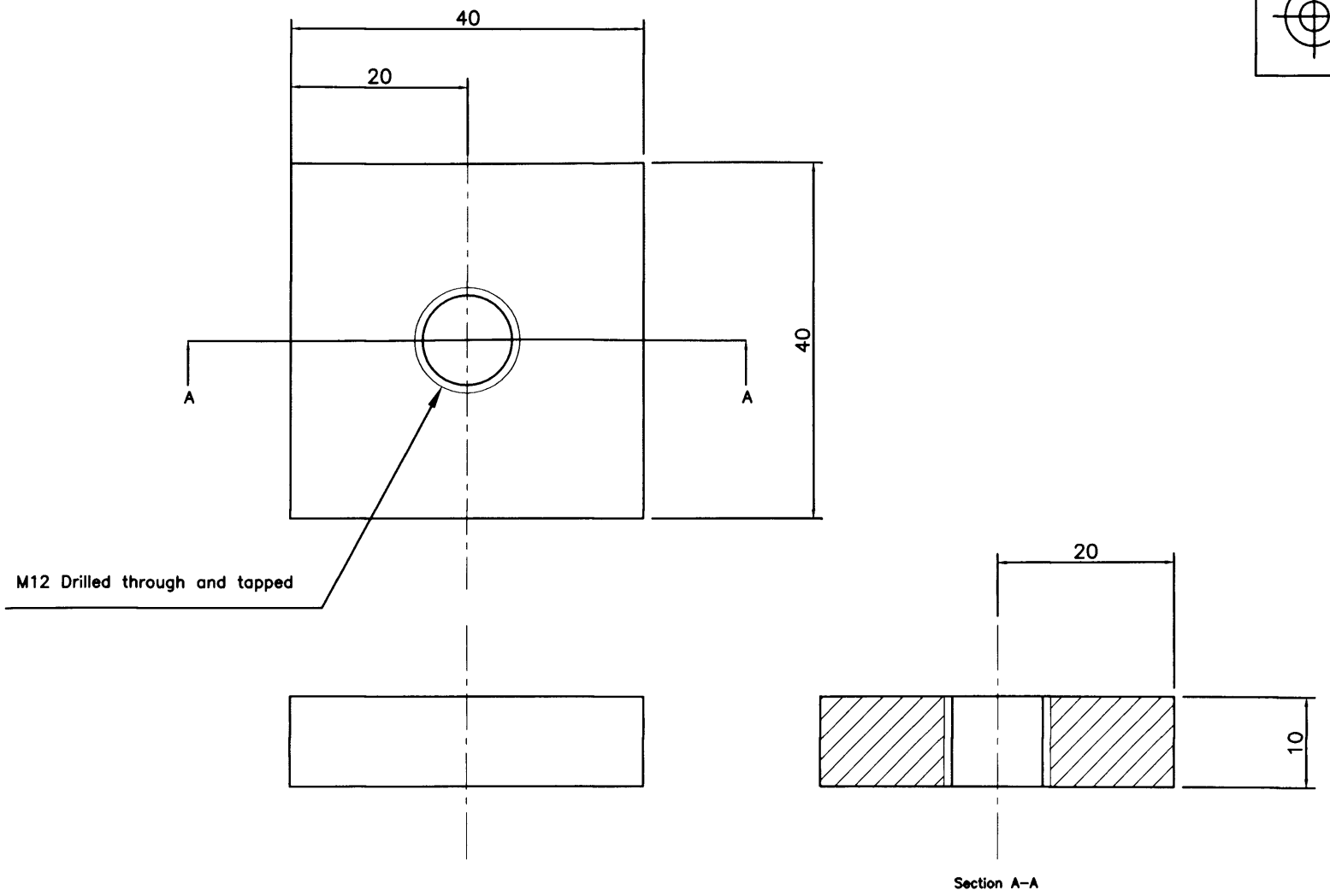

4 OFF REQUIRED

				This drawing is confidential and the copyright of J Haynes, School of Engineering, UWC. It must not be copied or passed to a third party without written consent.		Blocks for Securing Pump
						JMH AutoCad 2004
						Material –: N/A
A	First Issue	JMH	07/09/2005			Finish –:
Rev	Revision	Rev By	Date	Dimensions in mm	Do Not Scale	DRAWING No –: JMH015

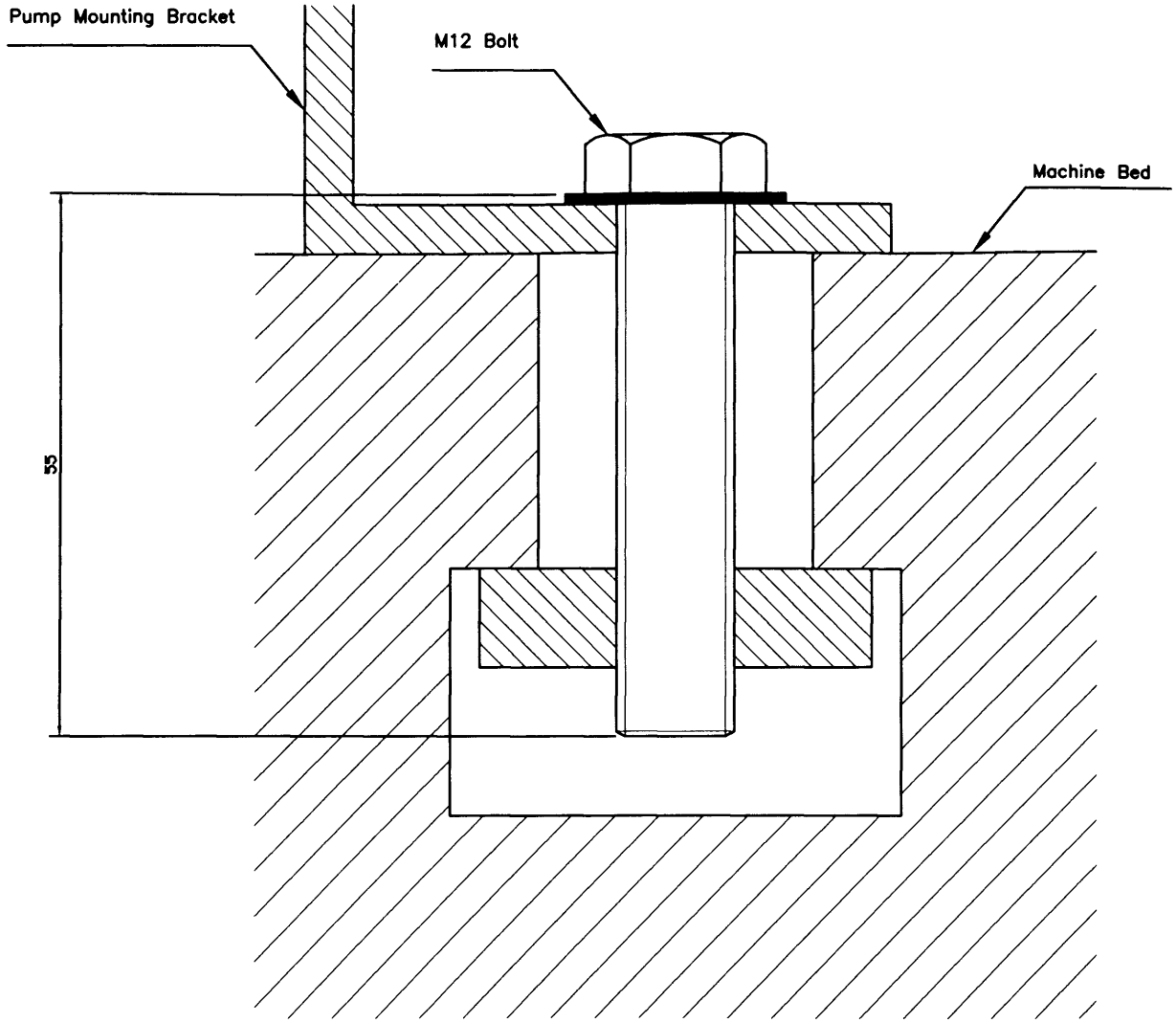

						Blocks for Securing Pump
				This drawing is confidential and the copyright of J Haynes, School of Engineering, UWC. It must not be copied or passed to a third party without written consent.		JMH AutoCad 2004
						Material –: N/A
A	First Issue	JMH	07/09/2005			Finish –:
Rev	Revision	Rev By	Date	Dimensions in mm	Do Not Scale	DRAWING No –: JMH016

A.2.4 Assembly drawings

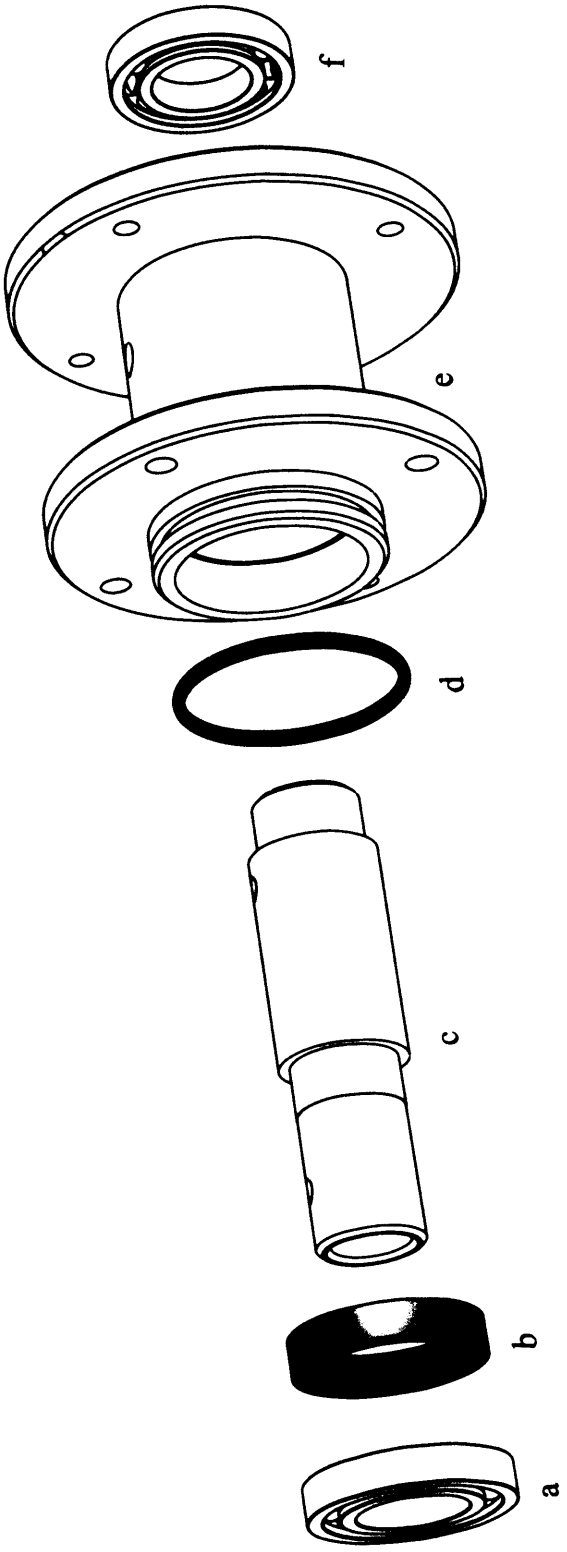

Exploded view of coupling with shaft and seal arrangement
(a) SKF 61904-2RZ bearing, (b) 24x35x7 shaft seal, (c) connecting shaft, (d) 41mm I.D. x 3mm O-ring, (e) flange, (f) SKF 61904-2RZ bearing

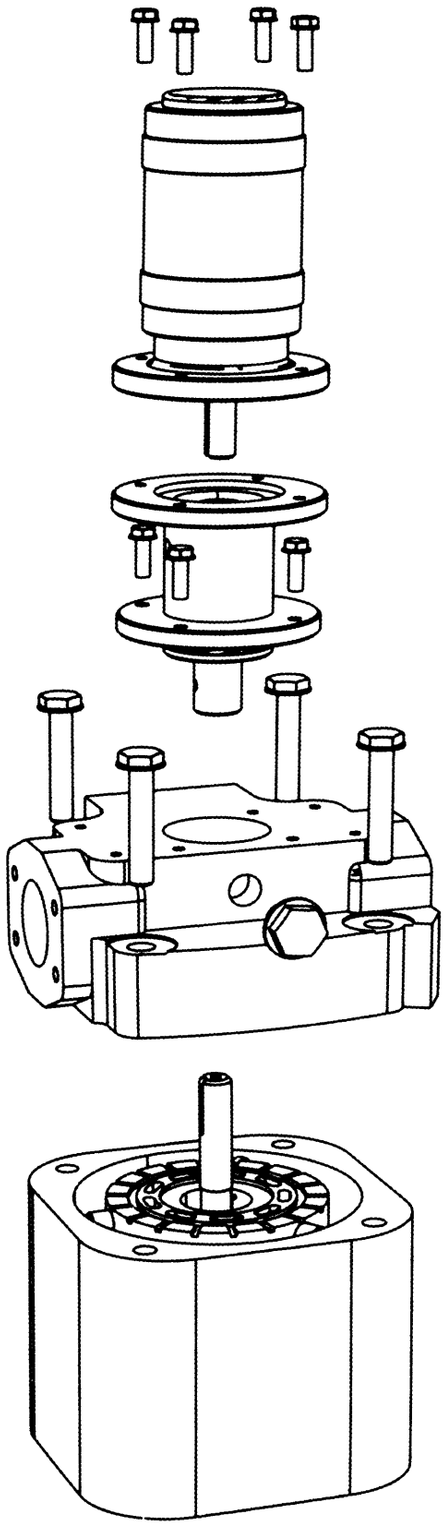

Exploded view of slip ring and connecting coupling

A.3 Slipper test apparatus

A.3.1 Calibration of displacement transducers

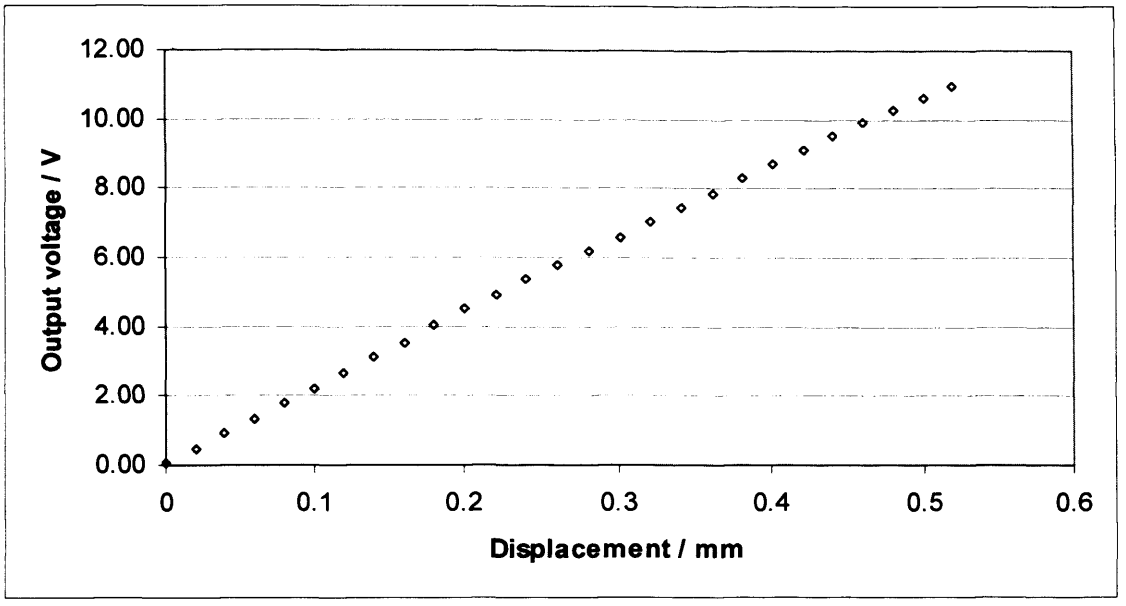

A.3.1.1 Eddy current sensor calibration curve (Sensor serial # 25267)

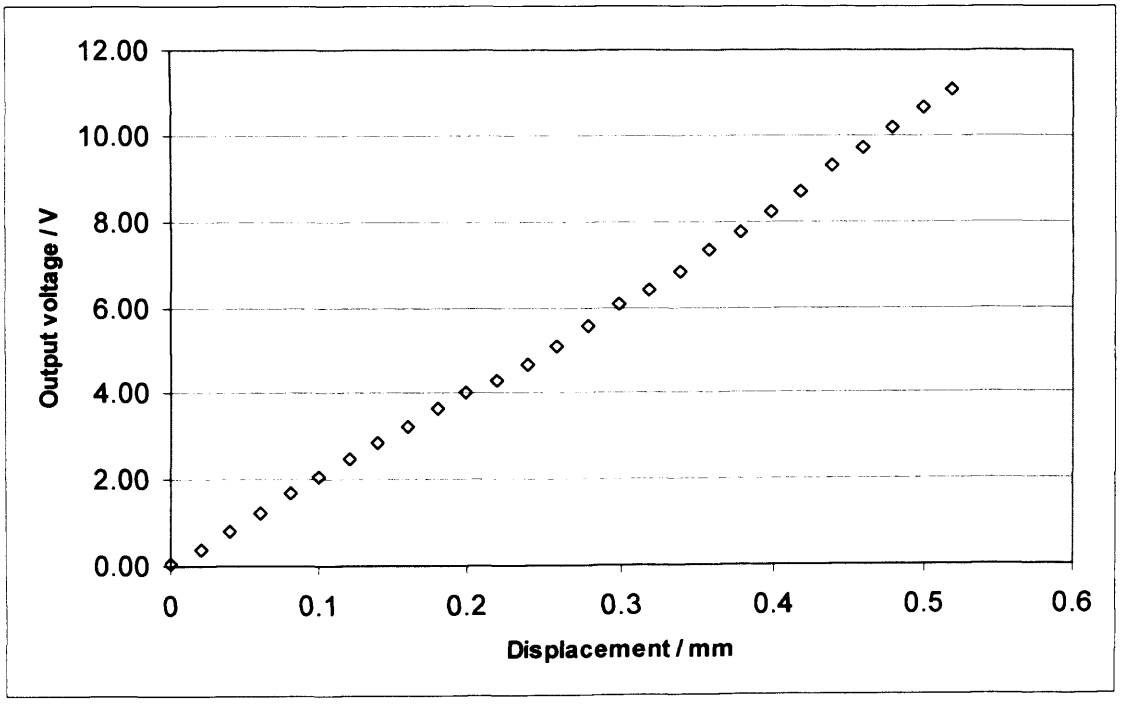

A.3.1.2 Eddy current sensor calibration curve (Sensor serial # 25268)

A.3.2 Retaining bolt tensile tests

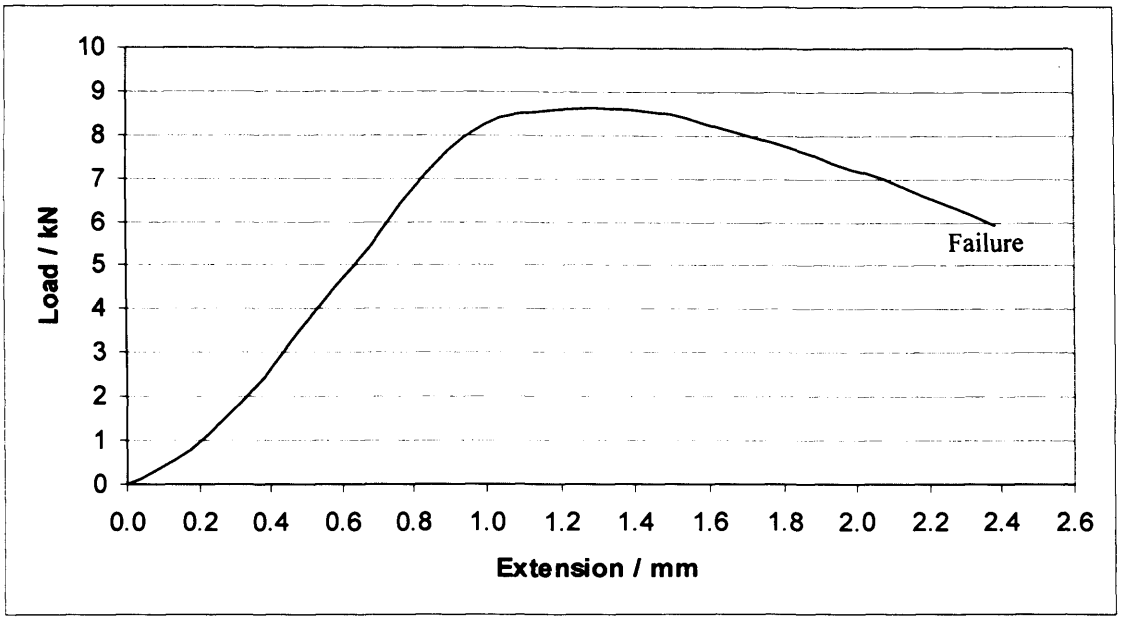

A.3.2.1 Load – deformation characteristics of retaining bolt (M4)

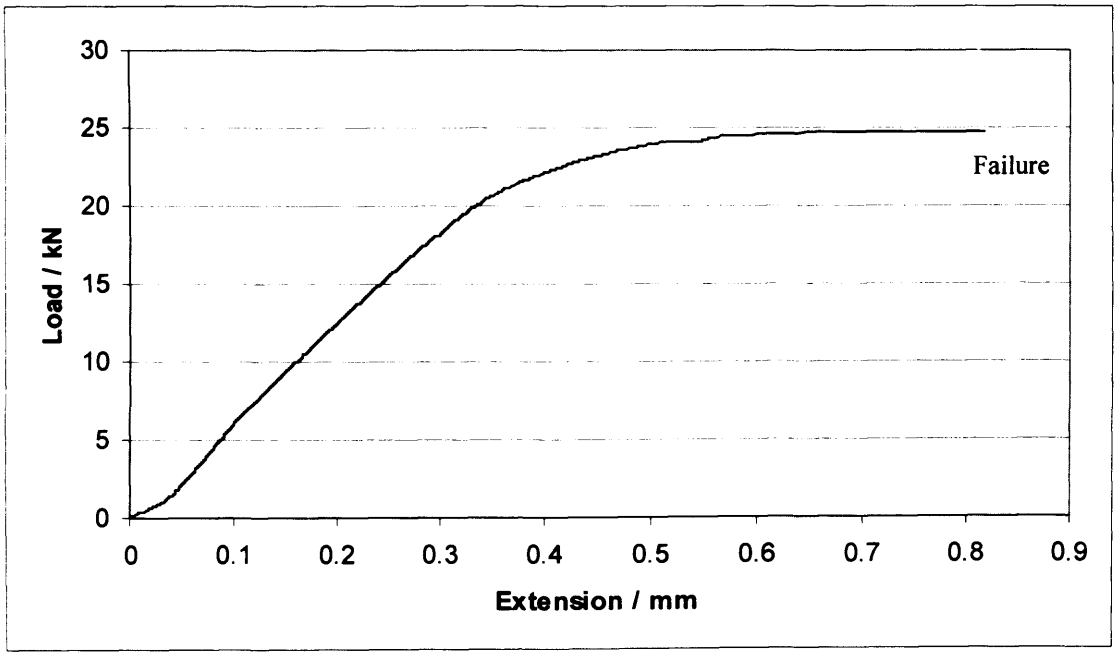

A.3.2.2 Load – deformation characteristics of retaining bolt (M6)

A.3.3 Bearing life calculations

The following section details bearing life calculations performed to confirm that the bearings selected for use within the test apparatus developed in Chapter 4 would have a suitable life expectancy. [89-91]

The basic rating life, L_{10}, for a thrust ball bearing is given by

$$L_{10} = \left(\frac{C_a}{P_{ea}} \right)^{P_L} \quad (1)$$

Where:

L_{10} = the life in millions of revolutions expected by 90% of an identical group of bearings

C_a = the basic dynamic axial load rating

P_{ea} = the dynamic equivalent axial load.

P_L = the exponent of the life equation = 3 for ball bearings and 10/3 for roller bearings

A.3.3.1 SKF 51132M thrust bearing

Since the nominal contact angle, α, of a bearing is 90°, i.e. the bearing can support axial loads only, the dynamic equivalent axial load for the bearing is given by:

$$P_{ea} = F_a \quad 2$$

Where F_a is the applied axial load.

In order to provide satisfactory operation, thrust bearings must be subjected to a minimum load. The required minimum axial load applied is given by the following equation:

$$F_{am} = A\left(\frac{n}{1000}\right)^2 \quad (3)$$

Where:

F_{am} = the minimum axial load applied to the bearing / kN

A = the minimum load factor for the specific bearings

n = rotational speed / rpm

In the case of the thrust bearing in the apparatus, the axial load will be a combination of its preload, and the force exerted upon it by the hydraulic pressure applied to the slipper. The value of A for the bearing, as specified by SKF, is 1.1, with a maximum expected rotational speed of 1500 rpm.

This gives a minimum axial load requirement, F_{am}, of 2.475 kN. This force must be applied to the bearing at all times, so would be in the form of a pre-load.

Assuming a preload of 2.5kN, which can be applied by the tightening of the six preload bolts, and a maximum hydraulic force of 12kN, the maximum expected axial load, F_a, acting on the thrust bearing is 14.5kN.

Thus using combining Equation (1) and (2), yields a value for L_{10} of 461 million revolutions. This equates to 5120 hours of operation under full load and maximum speed conditions.

A.3.3.2 SKF 32206 J2/Q tapered roller bearing

The taped roller bearing experiences an axial load, the preload applied to the thrust bearing. A radial load is also applied to this bearing due to the tension within the belt driving the swash plate.

The basic rating life, L_{10}, for a radial bearing is given by:

$$L_{10} = \left(\frac{C_r}{P_r}\right)^{10/3} \tag{4}$$

Where:

L_{10} = the life in millions of revolutions expected by 90% of an identical group of bearings

C_r = the basic dynamic radial load rating

P_r = the dynamic equivalent radial load.

For a roller bearing, for conditions where $F_a / F_r > e$, the dynamic equivalent radial load for a bearing undergoing constant loading is given by:

$$P_r = XF_r + YF_a \tag{5}$$

Where

X = the radial load factor which is specified as 0.4 by SKF

Y = constant determined from the geometry of the bearing and shown in Equation (6),

F_r = Radial force / N

F_a = Axial force / N

e = A bearing constant which is specified as 0.37 by SKF

$$Y = 0.4\cot\alpha \tag{6}$$

Where α is the bearing half-included outer race angle, which is 14°. Using this value of α with Equation (6) yields a value for Y of 1.60.

Assuming the motor develops full torque at its maximum speed, the applied torque, T, is:

$$T = \frac{P}{\omega} \tag{7}$$

Where:

P = the maximum power developed by the motor / = 2.2kW

ω = angular velocity / rad.s^{-1}

Thus, at 1500 rpm, the torque generated is equal to 14.0Nm. Hence, the tension, F, applied to the belt at this applied torque is:

$$\frac{T}{R_p} = F \tag{8}$$

Where:

R_p = the radius of the driven pulley

Using Equation (8), the maximum tension in the belt is found to be 615N. Therefore, using Equation (5), the dynamic equivalent radial load value, P_r, for the tapered roller bearing, assuming it supported the full tension of the belt, was found to be:

$$P_r = (0.4x615) + (1.6x2500) = 4246N$$

The basic dynamic radial load rating, C_r, provided by SKF, was 50.1kN Thus using Equation (4), the basic life rating of the bearing was determined to be 3740 million revolutions or 41,500 hours.

A.3.3.3 SKF NU2210 ECP cylindrical roller bearing

The basic rating life, L_{10}, for a radial ball bearing is given by:

$$L_{10} = \left(\frac{C_r}{P_r}\right)^3 \tag{9}$$

Although minimal load was expected on this bearing, the calculations will assume a worse case scenario of the bearing supporting the full load exerted by the tension of the belt.

Since no axial load can be applied to this bearing, the dynamic equivalent radial load is simply the radial force applied to the bearing.

The basic dynamic radial load rating was specified by SKF as 90kN. Thus using Equation (9), the expected life was found to be 3.5×10^7 hours.

Based on these calculations, it was concluded that the bearings chosen would provide a sufficient life span for use within the test apparatus. It is probable that the bearings exceeded the life span required; however the bearings were originally considered for their dimensions.

A.3.4 Photographs of components within the test apparatus

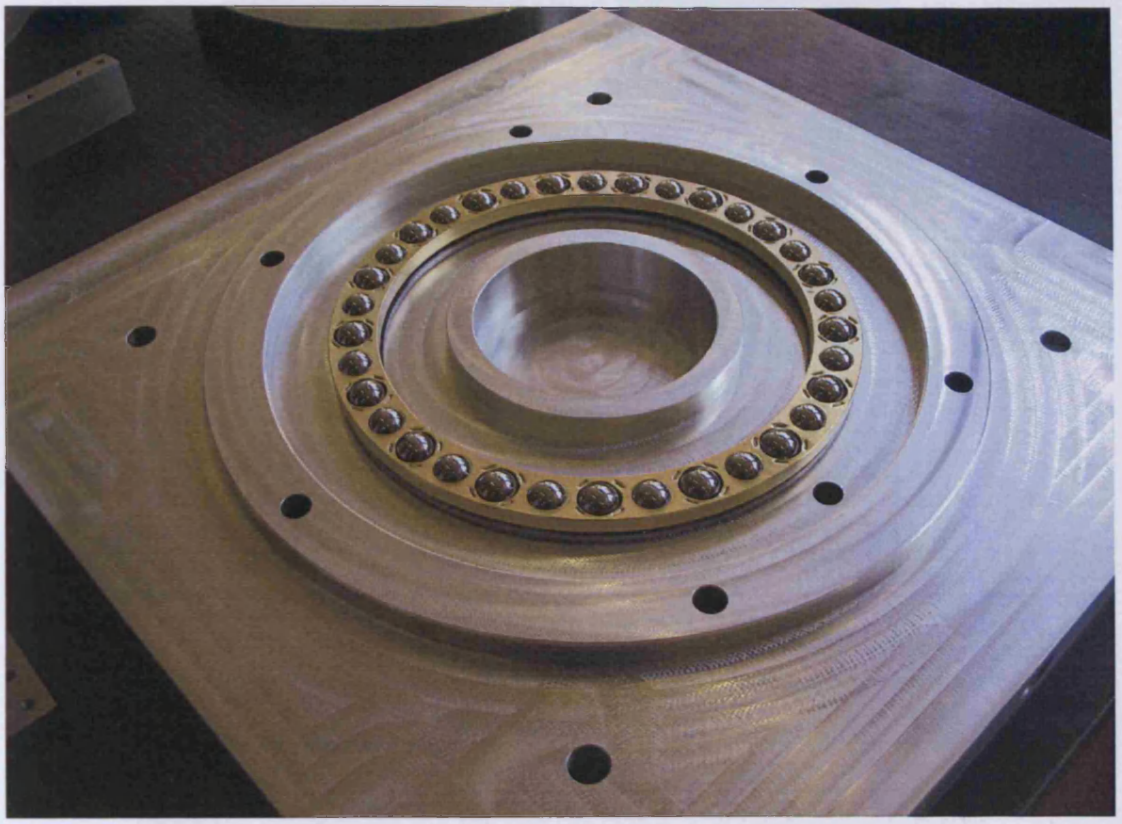

Base plate and thrust bearing

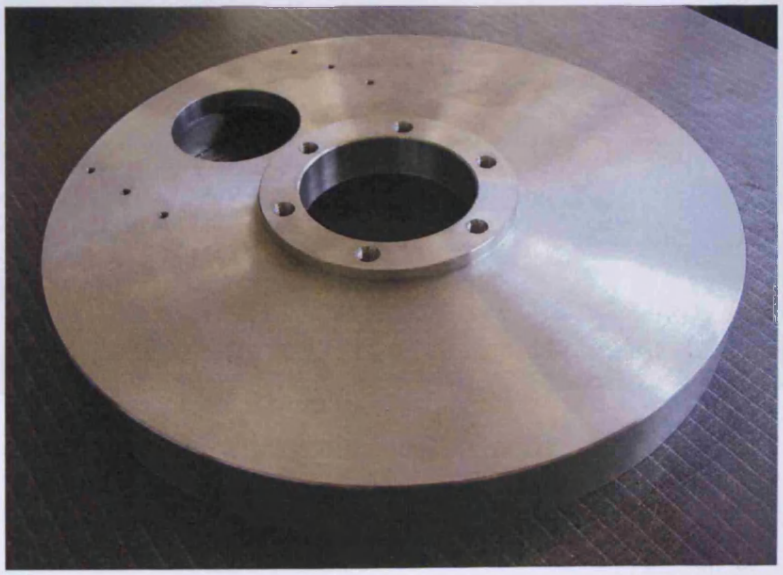

Disc housing

Test slipper

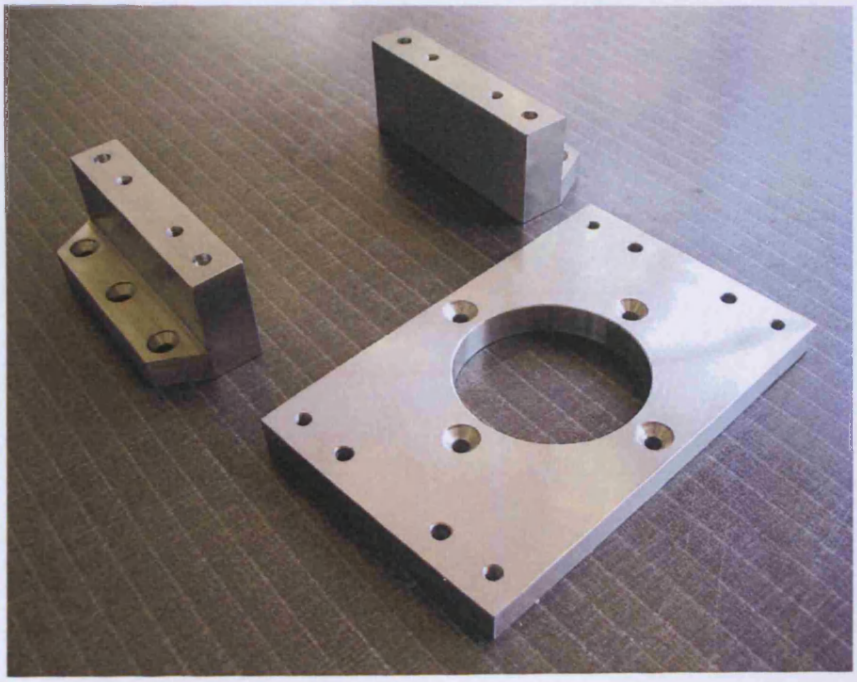

Tilting plate and supports

A.3.5 CAD drawings

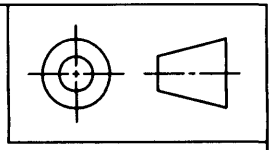

① Base Plate – See Drawing JMH019

② Disk – See Drawings JMH020 and JMH021

③ Top Plate – See Drawing JMH022

④ Bearing Flange – See Drawing JMH023

⑤ ⑥ ⑦ SKF Bearings – See Drawing JMH024

⑧ ⑨ ⑩ See Drawing JMH024

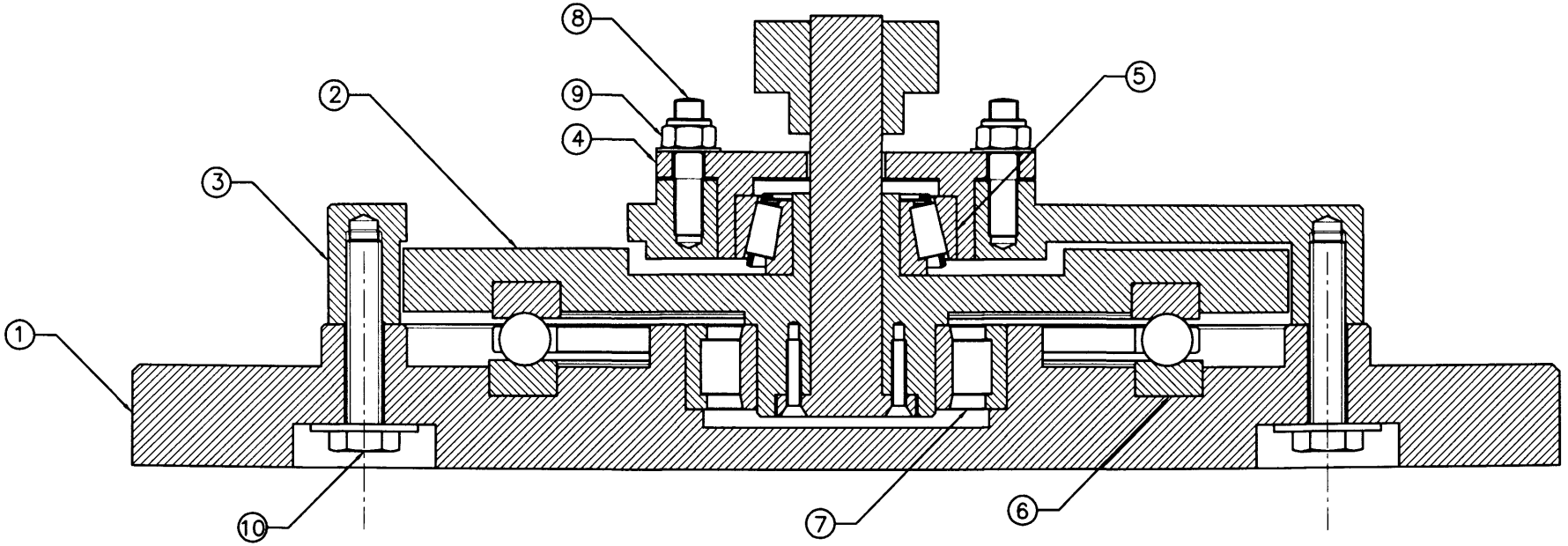

					Assembly Drawing / Part List
				This drawing is confidential and the copyright of J Haynes, School of Engineering, UWC. It must not be copied or passed to a third party without written consent.	JMH AutoCad 2004
A	Second Issue	JMH	28/02/2006		Material –: Various
Rev	Revision	Rev By	Date	Dimensions in mm Do Not Scale	Finish –:
					DRAWING No –: JMH017

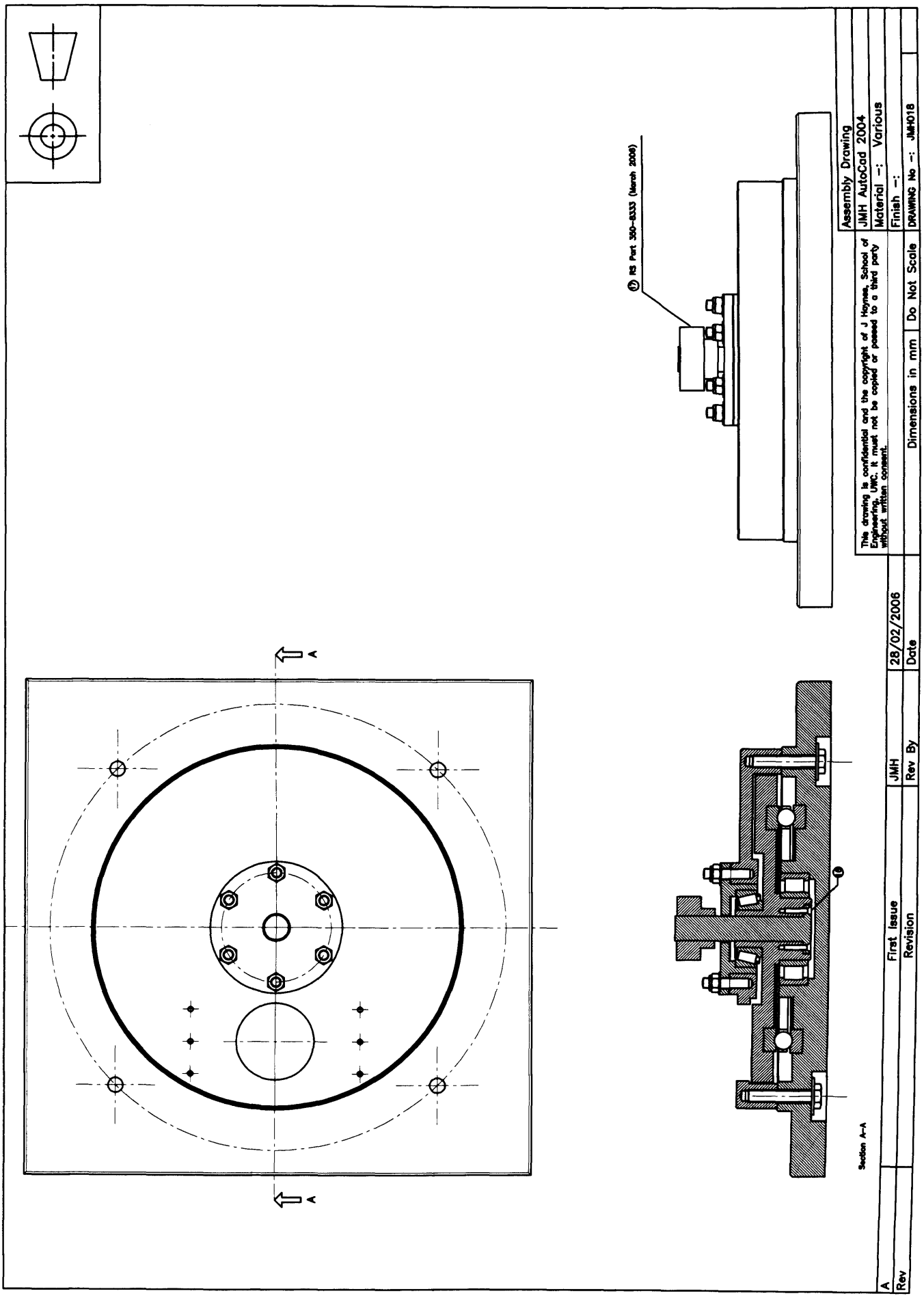
RS Part 350-8333 (March 2006)
Assembly Drawing
JMH AutoCad 2004
Material –: Various
Finish –:
DRAWING No –: JMH018
This drawing is confidential and the copyright of J Haynes, School of Engineering, UMC. It must not be copied or passed to a third party without written consent.
Dimensions in mm
Do Not Scale
A
Rev
First Issue
Revision
JMH
Rev By
28/02/2006
Date
Section A–A

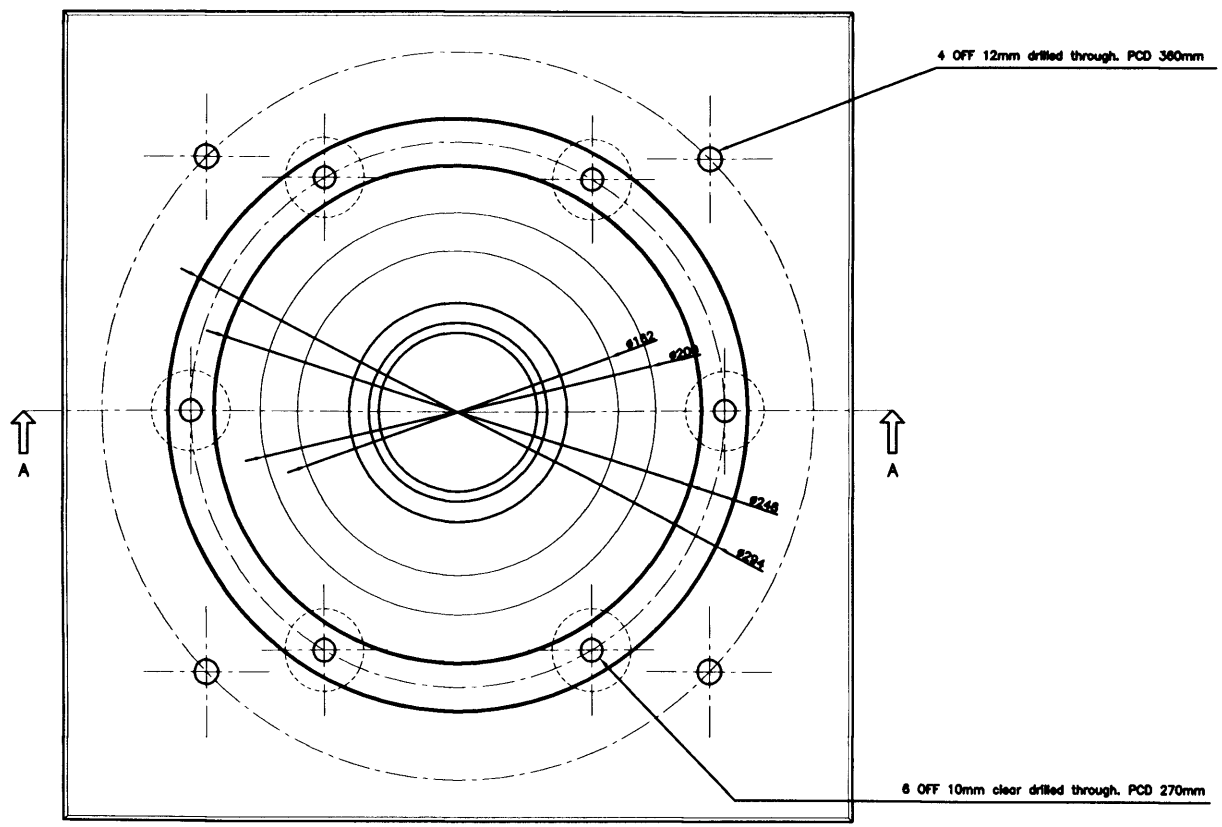

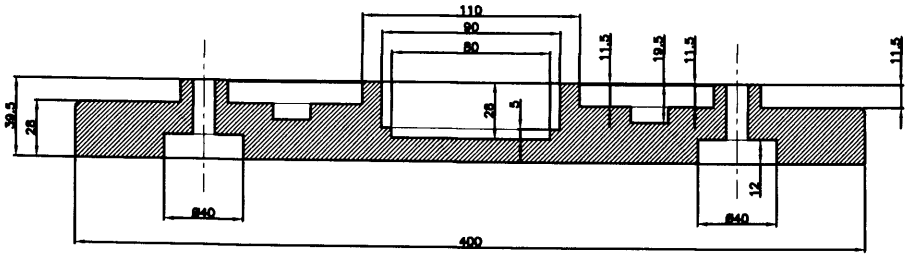

Section A–A

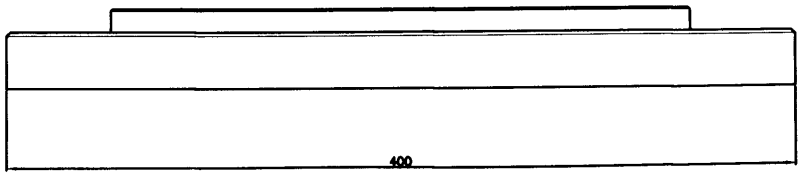

A	Second Issue	JMH	28/02/2006	This drawing is confidential and the copyright of J Haynes, School of Engineering, UWC. It must not be copied or passed to a third party without written consent.	Base Plate
Rev	Revision	Rev By	Date		JMH AutoCad 2004
					Material –: Aluminium
					Finish –:
				Dimensions in mm Do Not Scale	DRAWING No –: JMH019

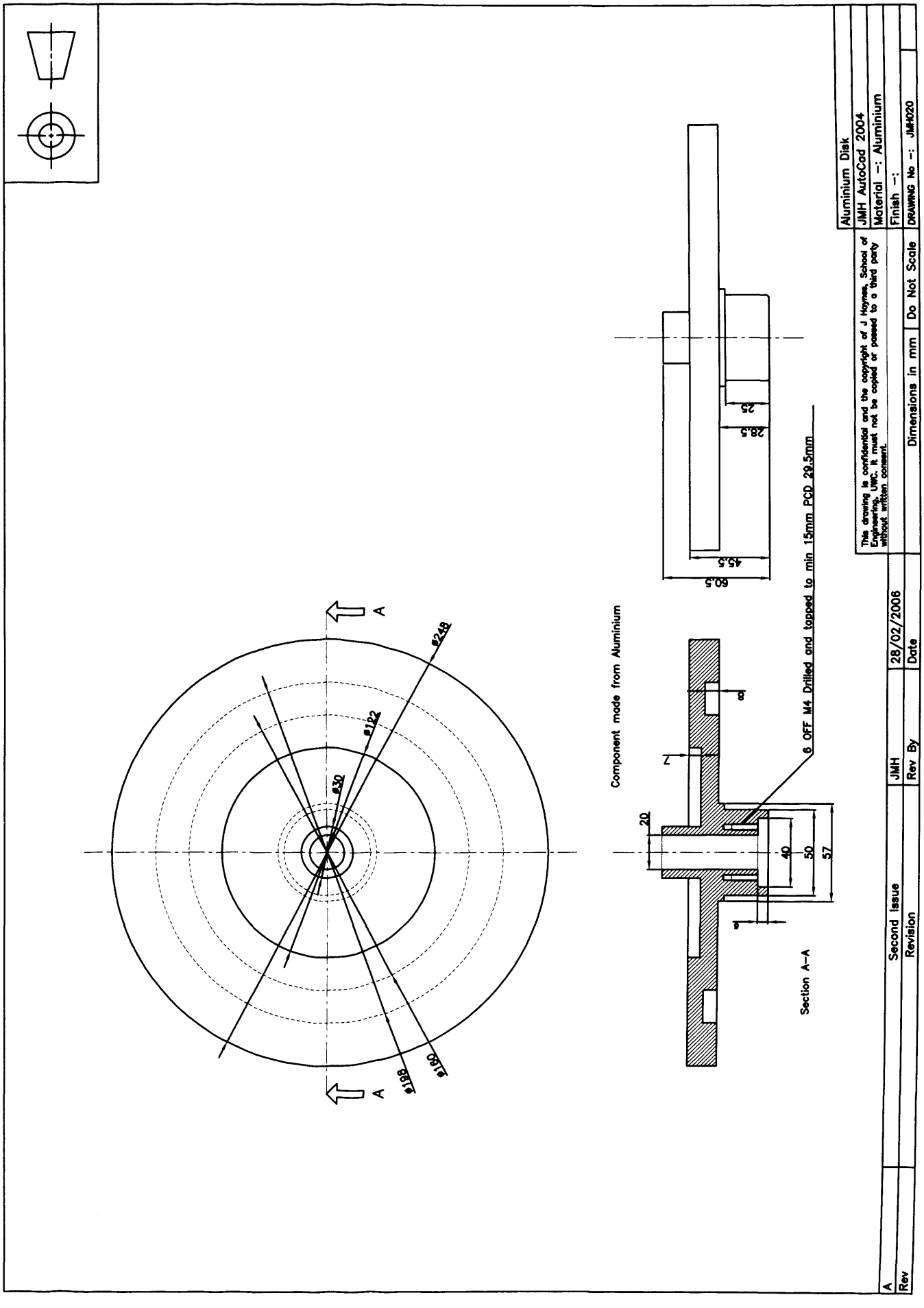
Aluminium Disk
JMH AutoCad 2004
Material –: Aluminium
Finish –:
DRAWING No –: JMH020
This drawing is confidential and the copyright of J Haynes, School of Engineering, UNC. It must not be copied or passed to a third party without written consent.
Dimensions in mm
Do Not Scale
Second Issue
JMH
28/02/2006
Revision
Rev By
Date
A
Rev
Component made from Aluminium
6 OFF M4 Drilled and tapped to min 15mm PCD 29.5mm
Section A-A
A
A
ø248
ø122
ø30
ø198
ø180
60.5
45.5
28.5
25
20
7
8
40
50
57
4

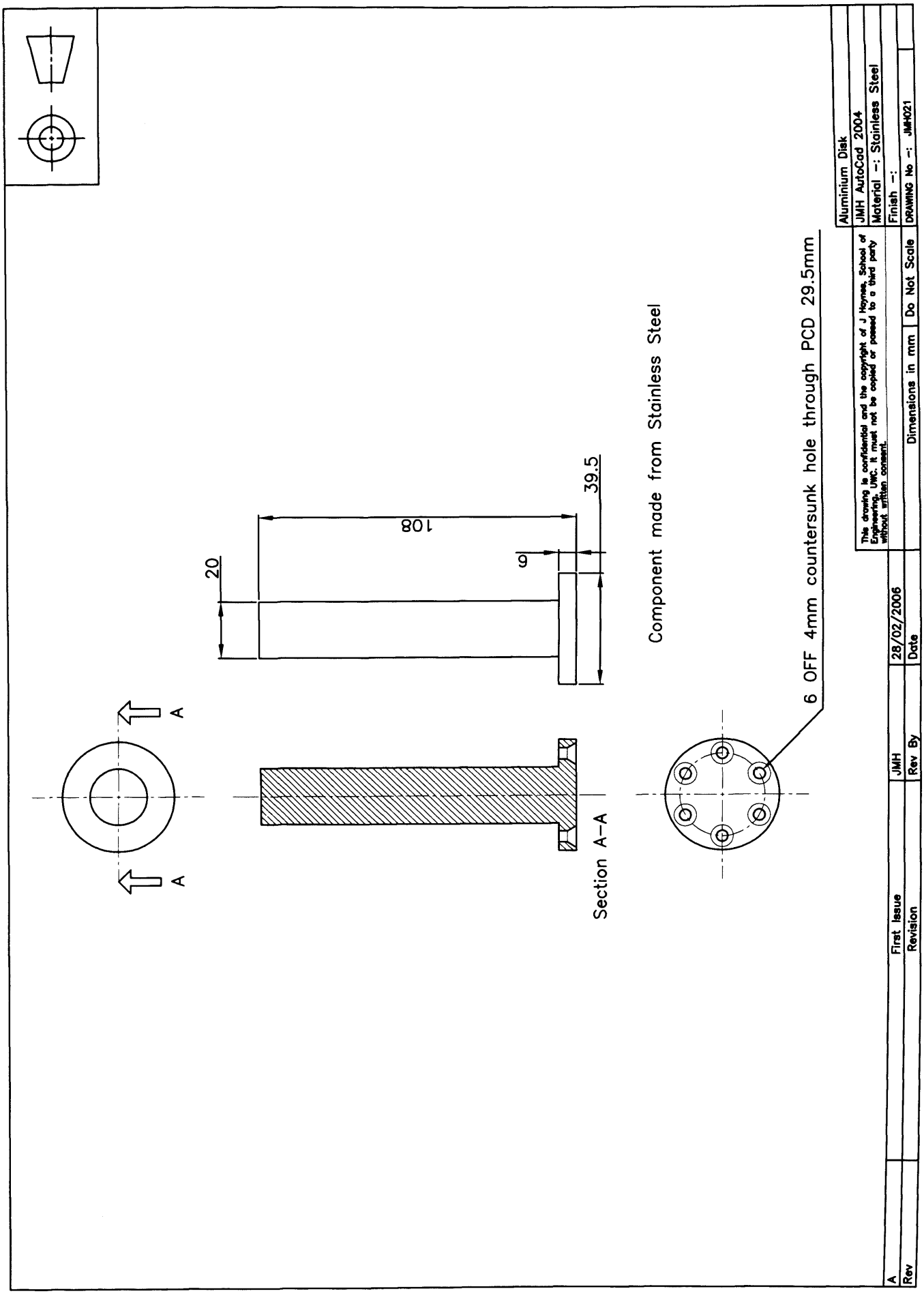
6 OFF 4mm countersunk hole through PCD 29.5mm
Component made from Stainless Steel
108
39.5
6
20
A
A
Section A-A
Aluminium Disk
JMH AutoCad 2004
Material –: Stainless Steel
Finish –:
DRAWING No –: JMH021
Dimensions in mm
Do Not Scale
28/02/2006
Date
JMH
Rev By
First Issue
Revision
A
Rev

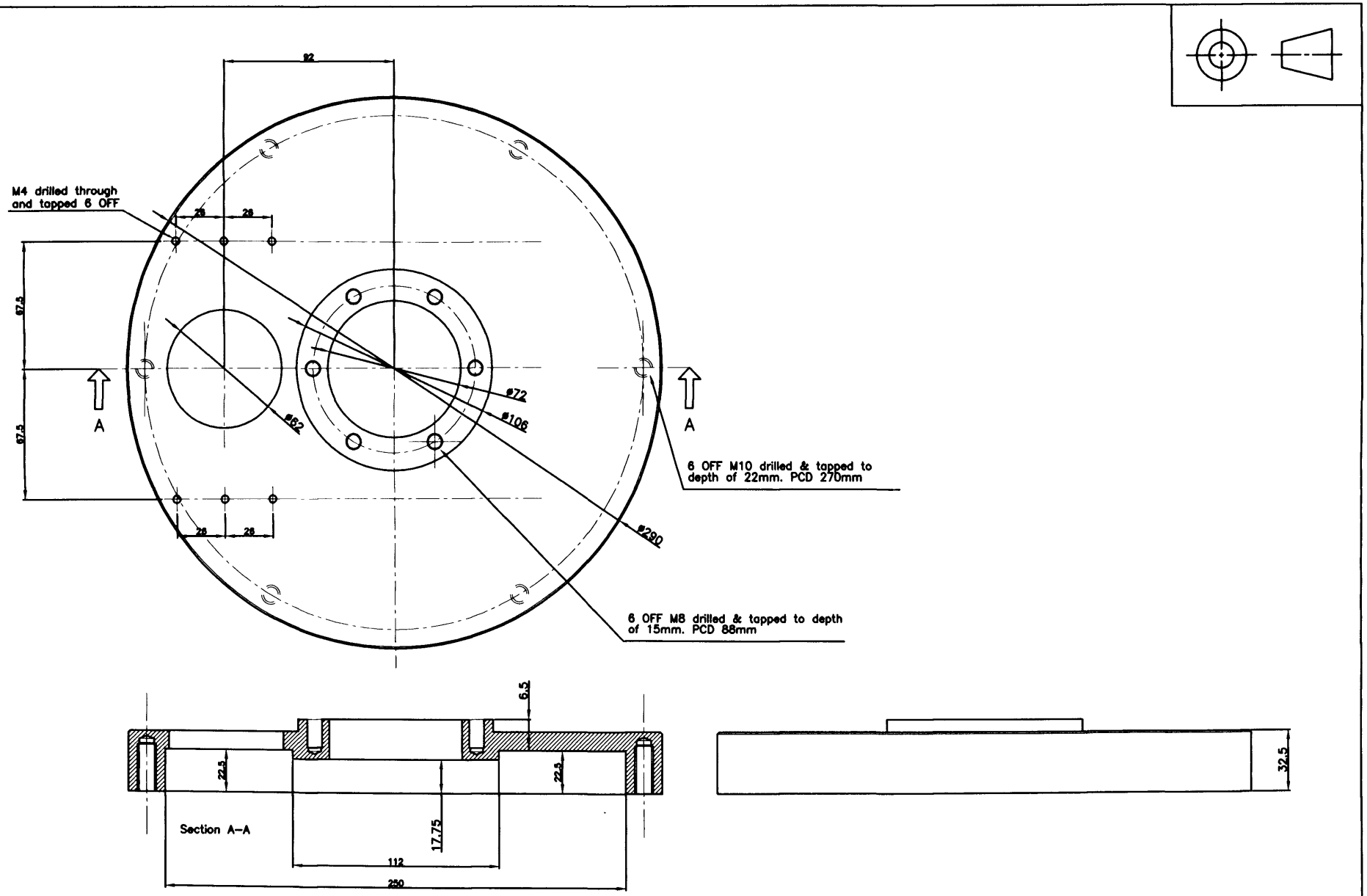

A	Second Issue	JMH	28/02/2006	Dimensions in mm	Do Not Scale
Rev	Revision	Rev By	Date		

Top Plate
JMH AutoCad 2004
Material –: Stainless Steel
Finish –:
DRAWING No –: JMH022

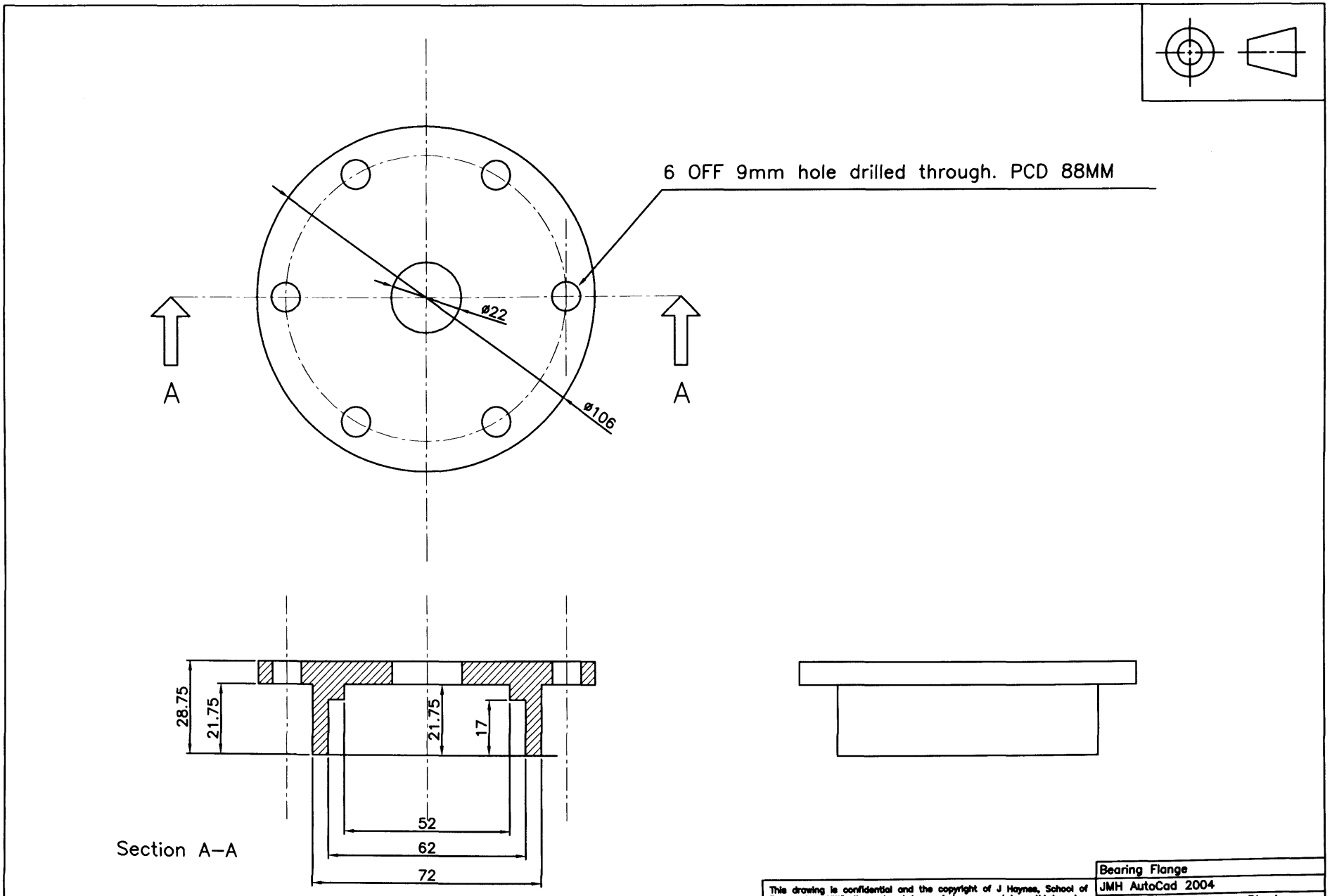

A	Second Issue	JMH	28/02/2006	This drawing is confidential and the copyright of J Haynes, School of Engineering, UWC. It must not be copied or passed to a third party without written consent.	Bearing Flange
					JMH AutoCad 2004
					Material –: Stainless Steel
					Finish –:
Rev	Revision	Rev By	Date	Dimensions in mm Do Not Scale	DRAWING No –: JMH023

⑤ SKF 32206 J2/Q Tappered Roller Bearing

⑥ SKF 51132 M Thrust Bearing

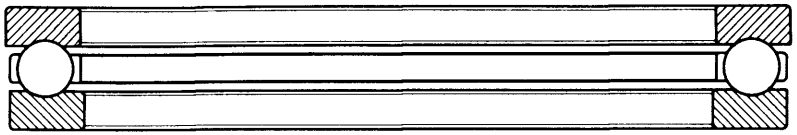

NOTE: Unequal Race Diameters

⑦ SKF NU2210 ECP Cylindrical Roller Bearing

⑧ M8 Threaded Stud 6 OFF

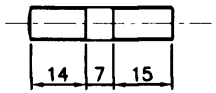

⑨ M8 Ni–Lock Nut 6 OFF

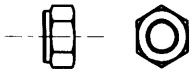

⑩ M10 x 52mm 6 OFF

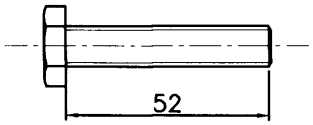

⑪ 1/8 – 1/8 BSP Fitting 4 OFF

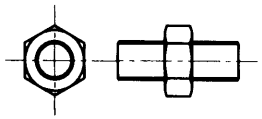

⑫ M4 x 25mm countersunk 4 OFF

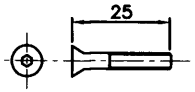

⑬ M4x0.5 x 22mm 4 OFF

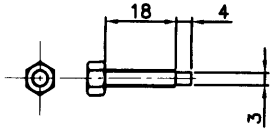

⑭ M6 x 30mm 4 OFF

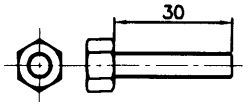

⑮ M4 countersunk x 22mm 6 OFF

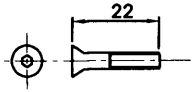

⑯ M4 countersunk x 21mm 6 OFF

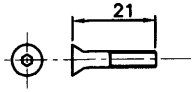

⑰ RS 350–8333 Pulley

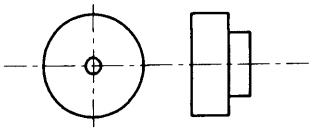

Bearings / Bolts			
JMH AutoCad 2004			
Material –:			
Finish –:			
DRAWING No –: JMH024	Dimensions in mm	Do Not Scale	

Rev	Revision	Rev By	Date
A	Second Issue	JMH	28/02/2006

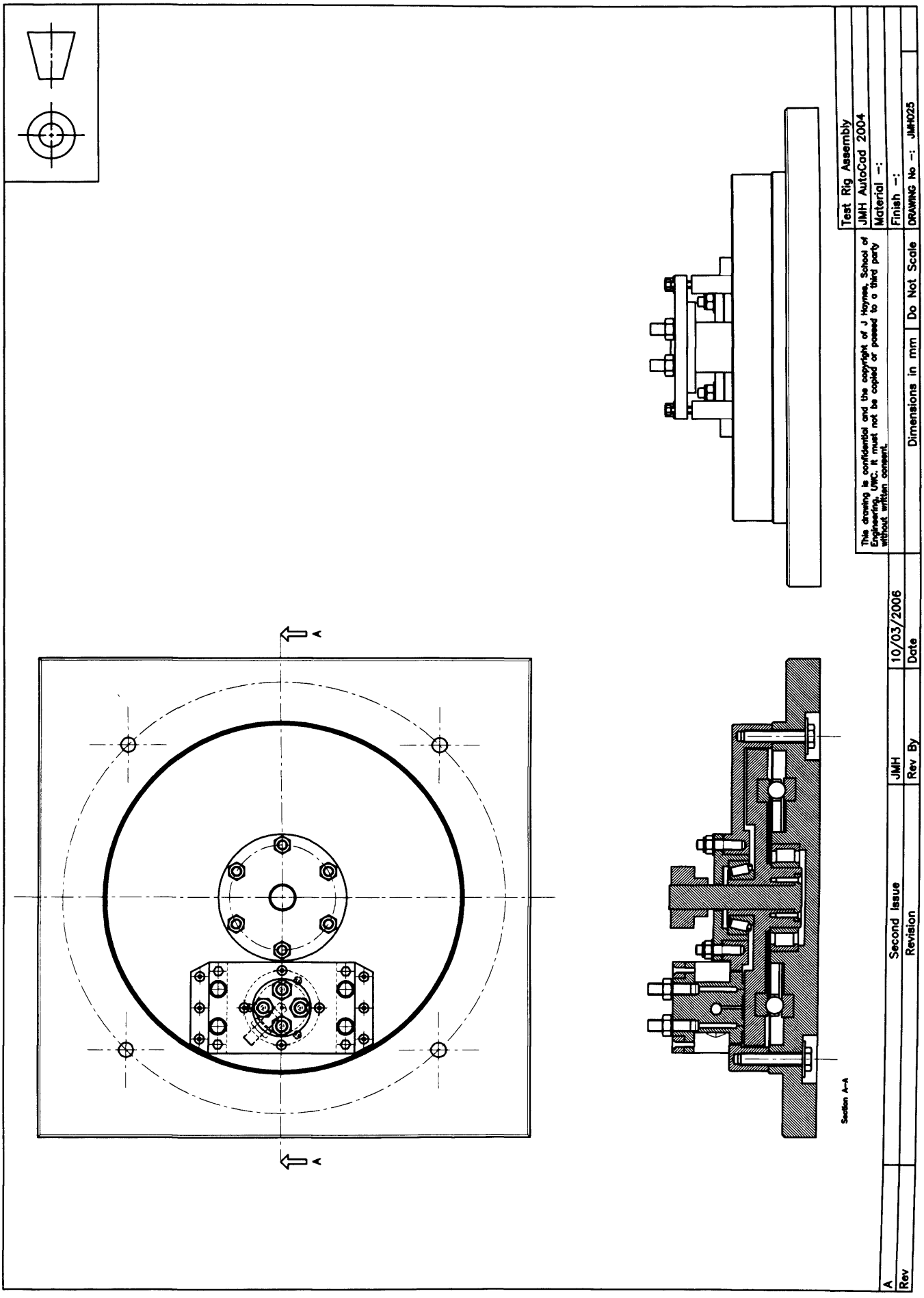
Test Rig Assembly
JMH AutoCad 2004
Material –:
Finish –:
DRAWING No –: JMH025
This drawing is confidential and the copyright of J Haynes, School of Engineering, UWC. It must not be copied or passed to a third party without written consent.
Dimensions in mm
Do Not Scale
A
Second Issue
JMH
10/03/2006
Rev
Revision
Rev By
Date
Section A–A

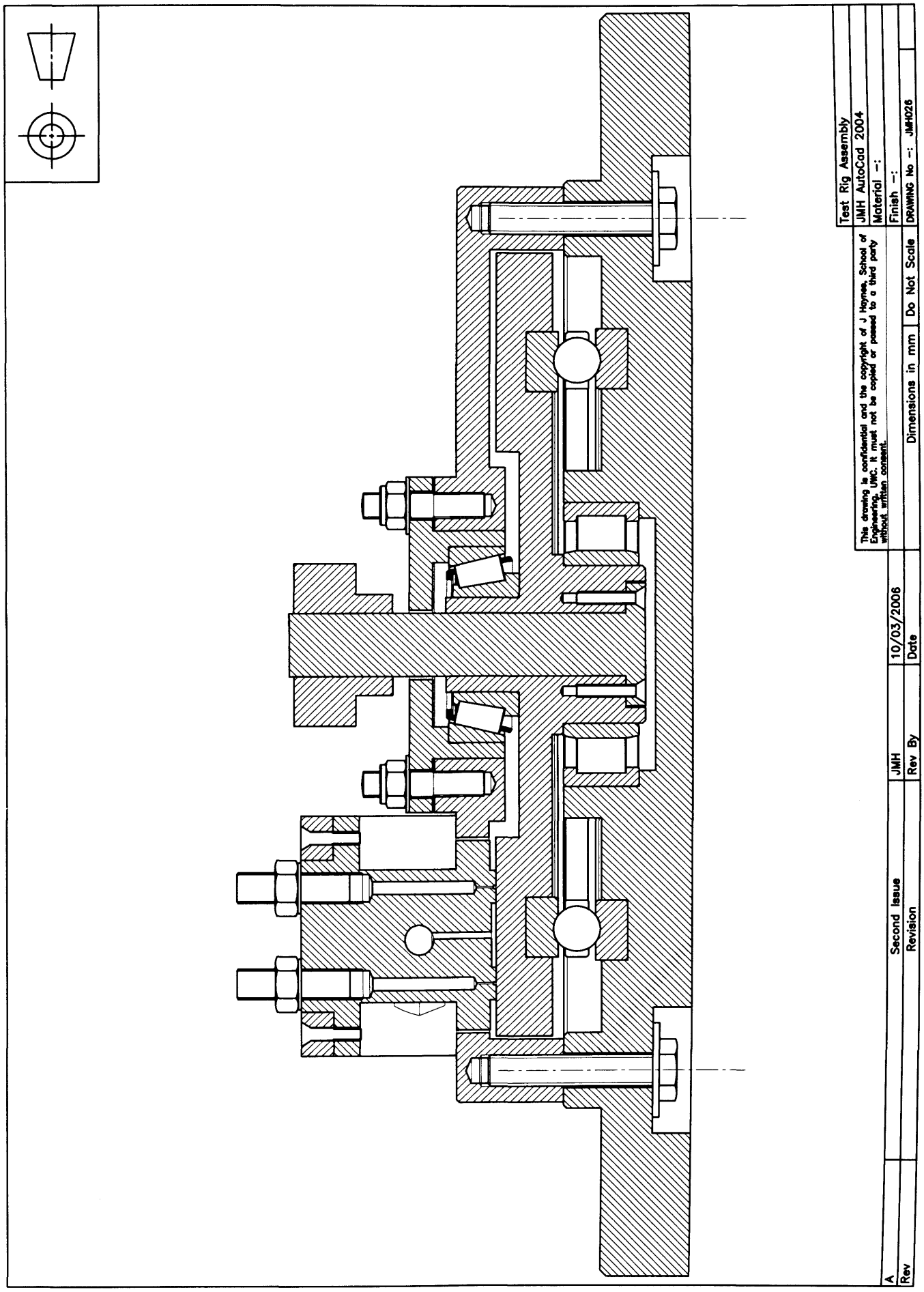
Test Rig Assembly
JMH AutoCad 2004
Material –:
Finish –:
DRAWING No –: JMH026
This drawing is confidential and the copyright of J Haynes, School of Engineering, UWC. It must not be copied or passed to a third party without written consent.
Dimensions in mm
Do Not Scale
A
Second Issue
JMH
10/03/2006
Rev
Revision
Rev By
Date

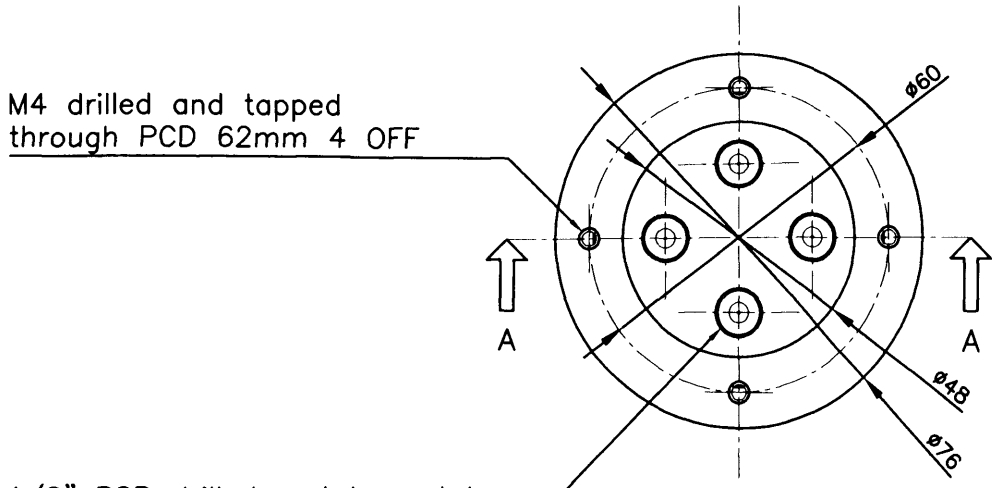

For details of slipper face geometry, see Drawing JMH032

See Drawing JMH028 for more details

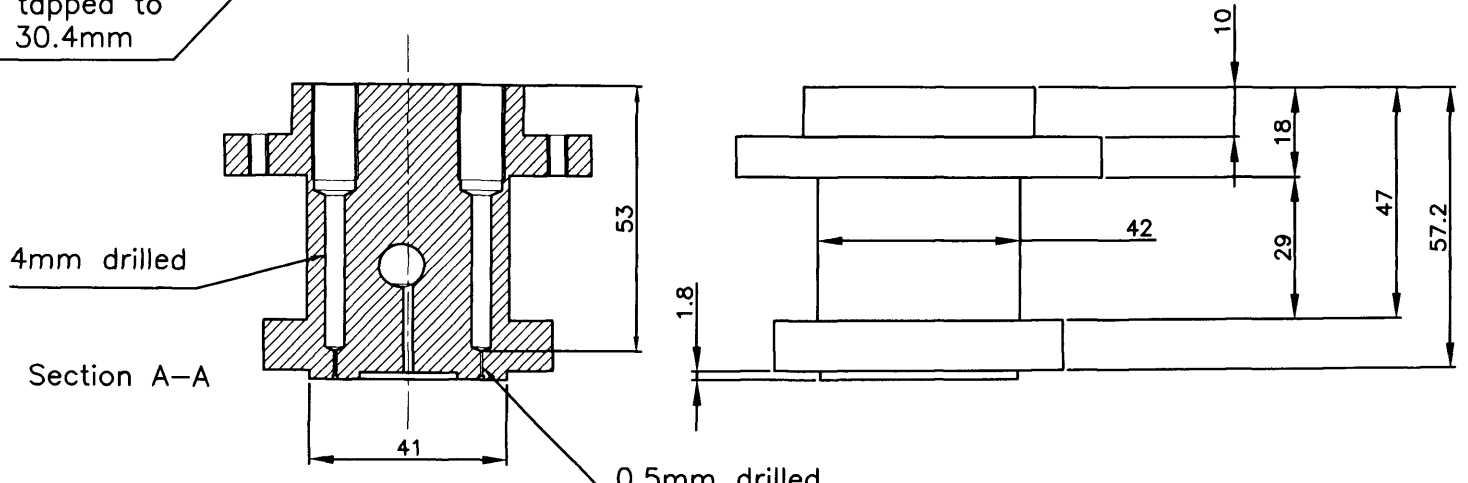

A	Second Issue	JMH	10/03/2006	This drawing is confidential and the copyright of J Haynes, School of Engineering, UWC. It must not be copied or passed to a third party without written consent.		Slipper Assembly
						JMH AutoCad 2004
						Material –: Stainless Steel
Rev	Revision	Rev By	Date	Dimensions in mm	Do Not Scale	Finish –:
						DRAWING No –: JMH027

For use with Drawing JMH027

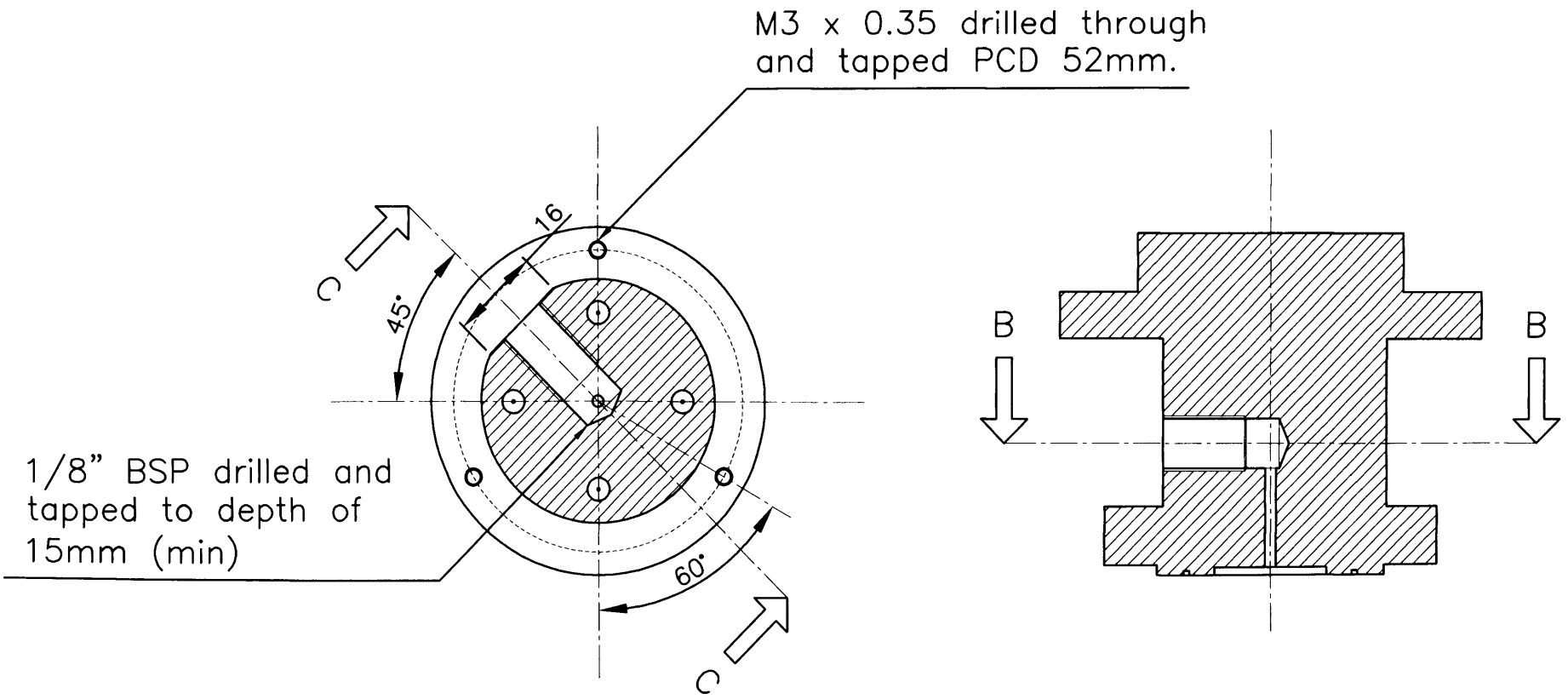

Section B–B

Section C–C

					Slipper Assembly
				This drawing is confidential and the copyright of J Haynes, School of Engineering, UWC. It must not be copied or passed to a third party without written consent.	JMH AutoCad 2004
					Material –: Stainless Steel
A	Second Issue	JMH	10/03/2006		Finish –:
Rev	Revision	Rev By	Date	Dimensions in mm Do Not Scale	DRAWING No –: JMH028

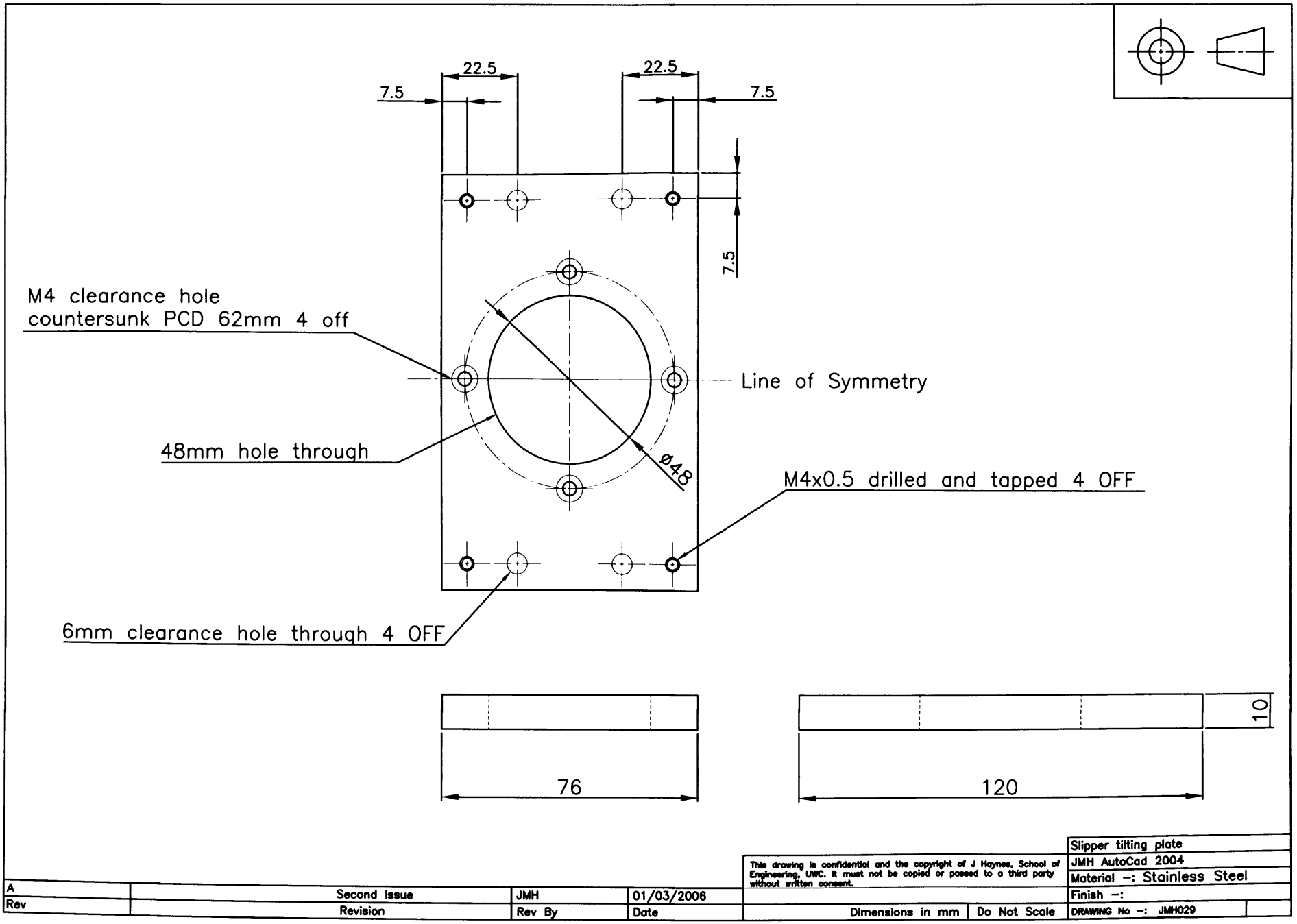

					Slipper tilting plate
				This drawing is confidential and the copyright of J Haynes, School of Engineering, UWC. It must not be copied or passed to a third party without written consent.	JMH AutoCad 2004
A	Second Issue	JMH	01/03/2006		Material –: Stainless Steel
Rev	Revision	Rev By	Date		Finish –:
				Dimensions in mm Do Not Scale	DRAWING No –: JMH029

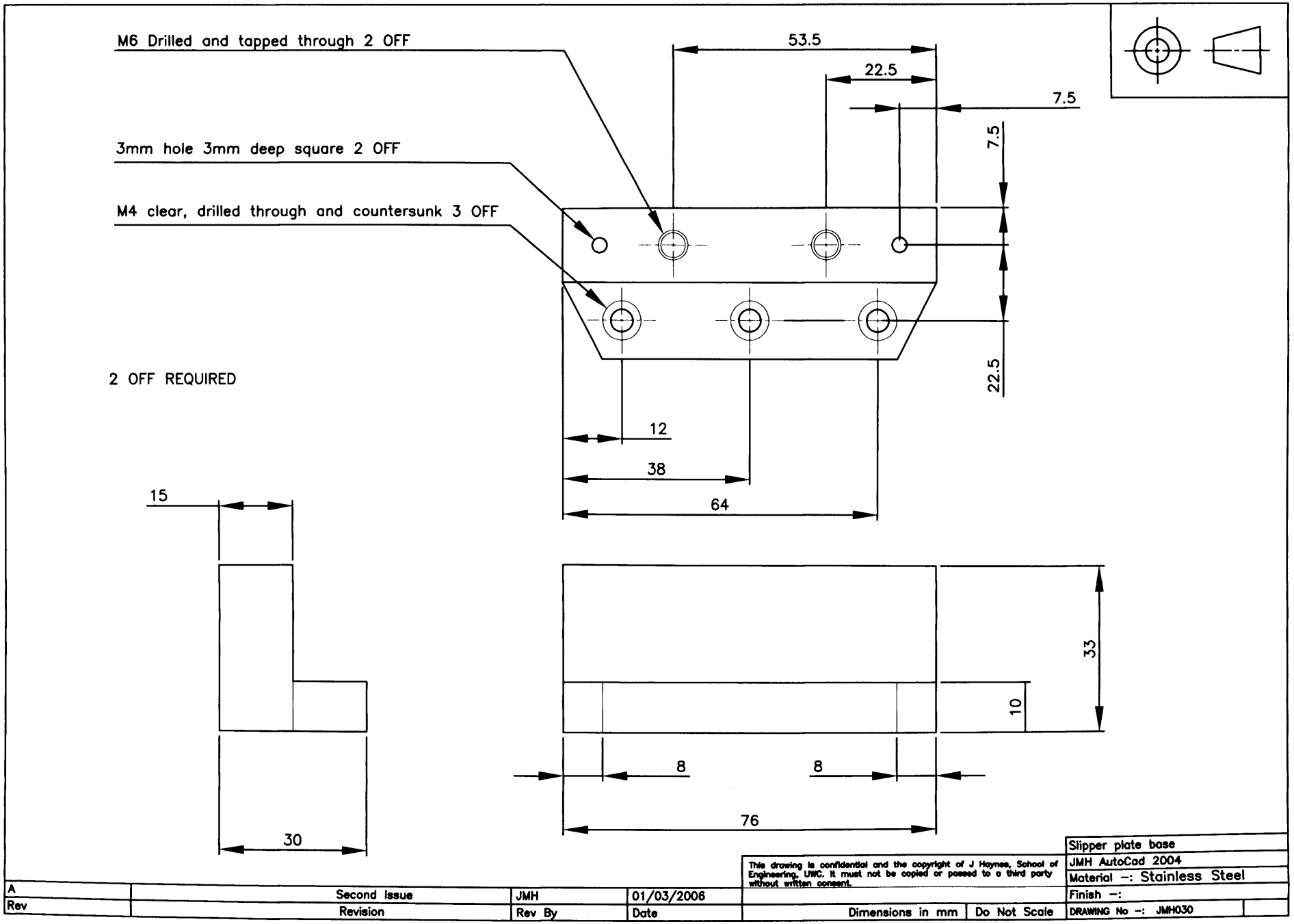

A	Second Issue	JMH	01/03/2006	This drawing is confidential and the copyright of J Haynes, School of Engineering, UWC. It must not be copied or passed to a third party without written consent.	Slipper plate base
					JMH AutoCad 2004
					Material –: Stainless Steel
Rev	Revision	Rev By	Date	Dimensions in mm Do Not Scale	Finish –:
					DRAWING No –: JMH030

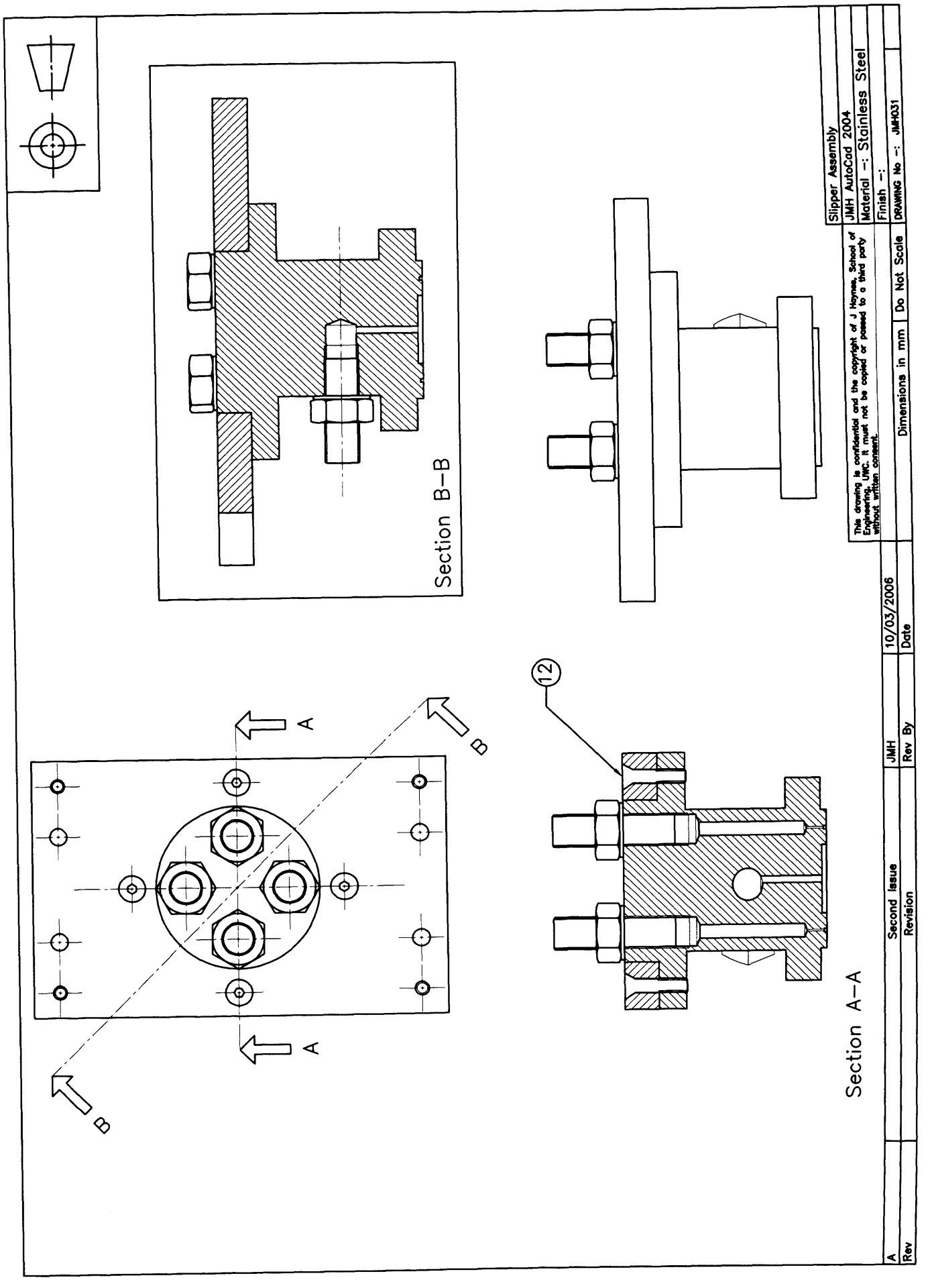
Section B–B
Section A–A
A
B
A
B
12
Slipper Assembly
JMH AutoCad 2004
Material –: Stainless Steel
Finish –:
DRAWING No –: JMH031
This drawing is confidential and the copyright of J Haynes, School of Engineering, UWC. It must not be copied or passed to a third party without written consent.
Dimensions in mm
Do Not Scale
10/03/2006
JMH
Second Issue
A
Rev
Date
Rev By
Revision

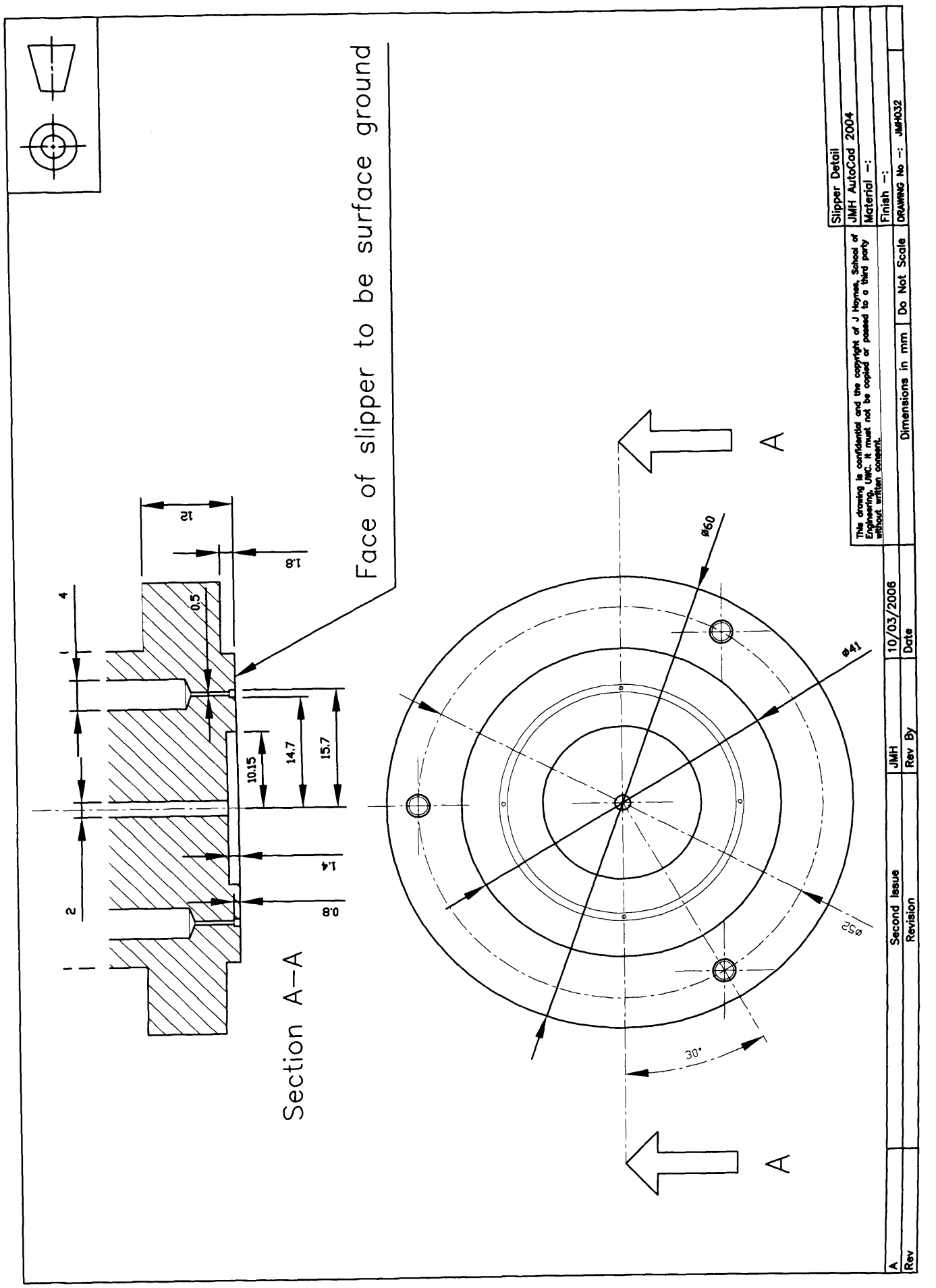
Face of slipper to be surface ground
Section A–A
A
A
Ø60
Ø41
Ø52
30°
12
1.8
0.5
4
1
2
10.15
14.7
15.7
1.4
0.8
Slipper Detail
JMH AutoCad 2004
Material –:
Finish –:
DRAWING No –: JMH032
This drawing is confidential and the copyright of J Haynes, School of Engineering, UMC. It must not be copied or passed to a third party without written consent.
Dimensions in mm
Do Not Scale
10/03/2006
JMH
Second Issue
A
Rev
Revision
Rev By
Date

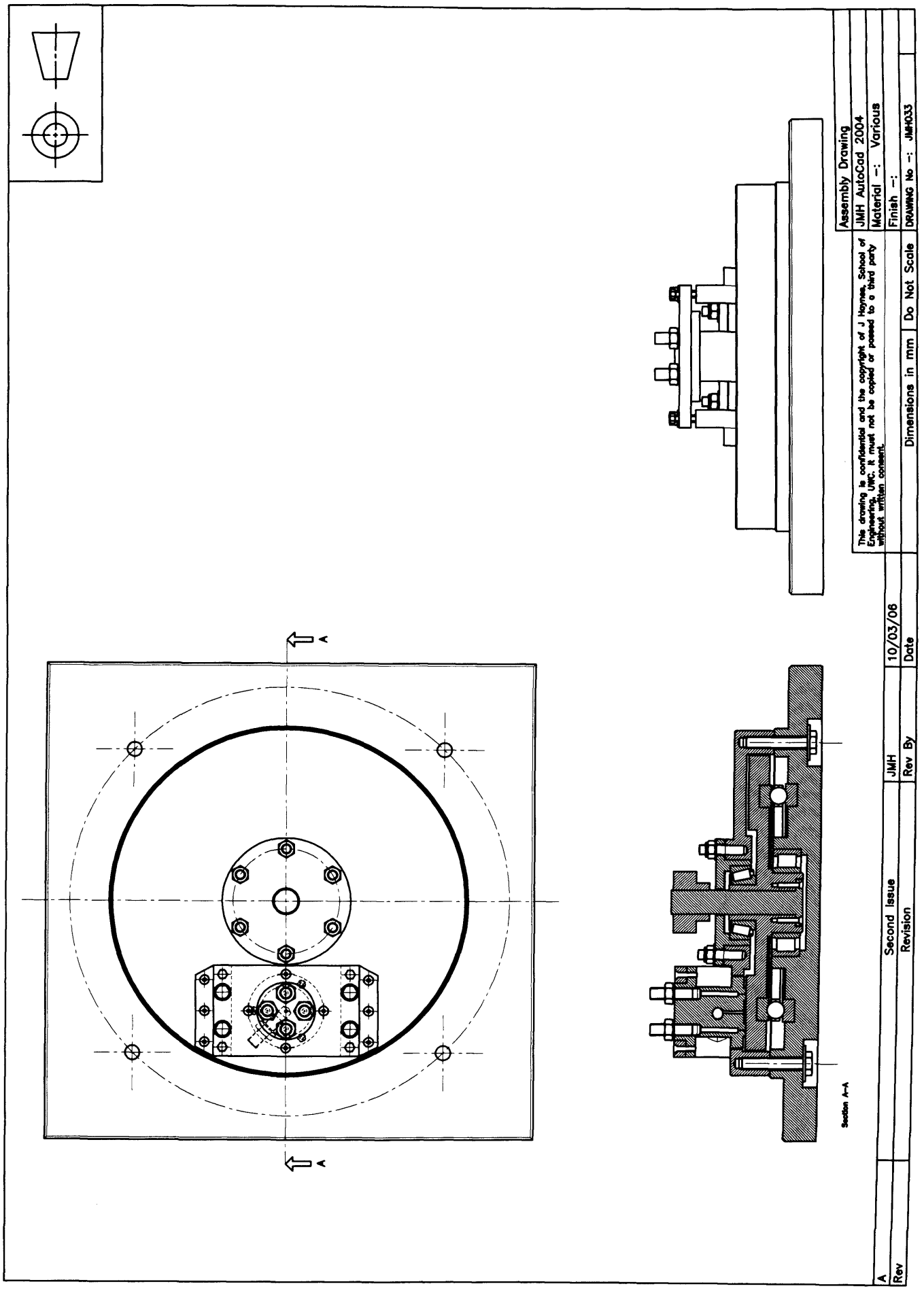
Assembly Drawing
JMH AutoCad 2004
Material –: Various
Finish –:
DRAWING No –: JMH033
This drawing is confidential and the copyright of J Haynes, School of Engineering, UWC. It must not be copied or passed to a third party without written consent.
Dimensions in mm
Do Not Scale
Second Issue
Revision
JMH
Rev By
10/03/06
Date
A
Rev
Section A-A

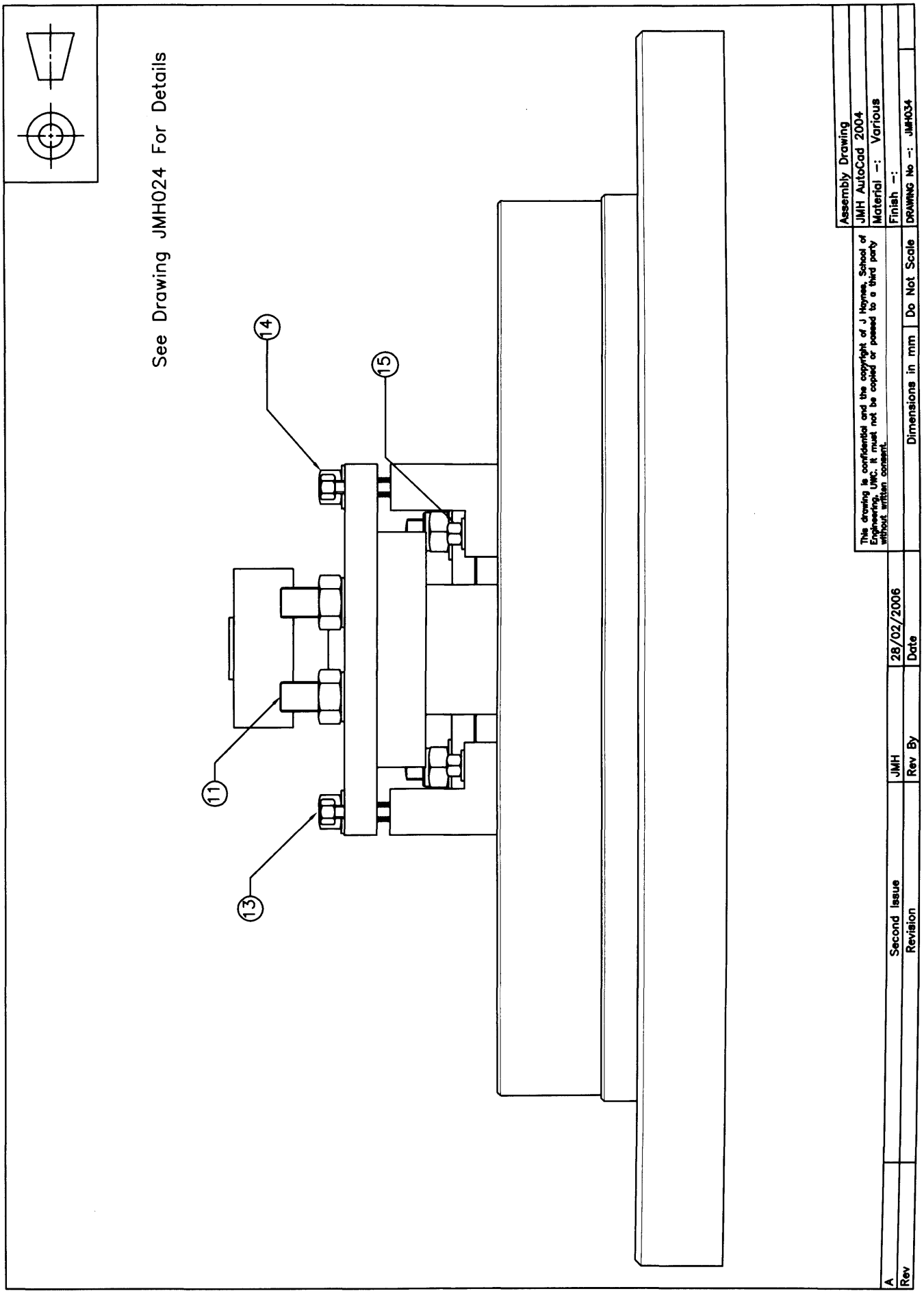
See Drawing JMH024 For Details
14
15
11
13
Assembly Drawing
JMH AutoCad 2004
Material –: Various
Finish –:
DRAWING No –: JMH034
This drawing is confidential and the copyright of J Haynes, School of Engineering, UWC. It must not be copied or passed to a third party without written consent.
Dimensions in mm
Do Not Scale
A
Second Issue
JMH
28/02/2006
Rev
Revision
Rev By
Date

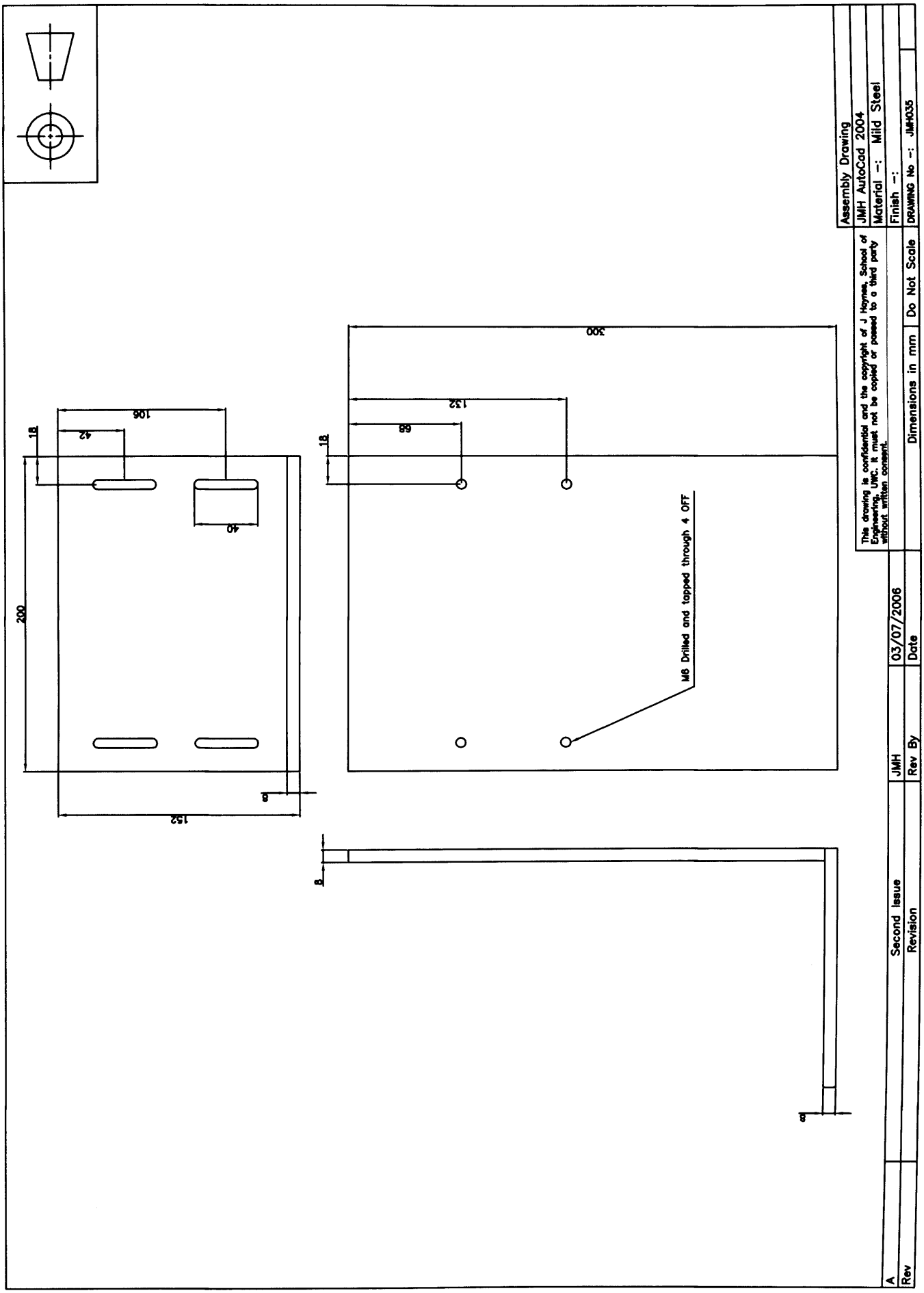
Assembly Drawing
JMH AutoCad 2004
Material –: Mild Steel
Finish –:
DRAWING No –: JMH035
This drawing is confidential and the copyright of J Haynes, School of Engineering, UWC. It must not be copied or passed to a third party without written consent.
Dimensions in mm
Do Not Scale
Second Issue
Revision
JMH
Rev By
03/07/2006
Date
A
Rev
300
132
68
18
106
42
40
200
152
8
M6 Drilled and tapped through 4 OFF

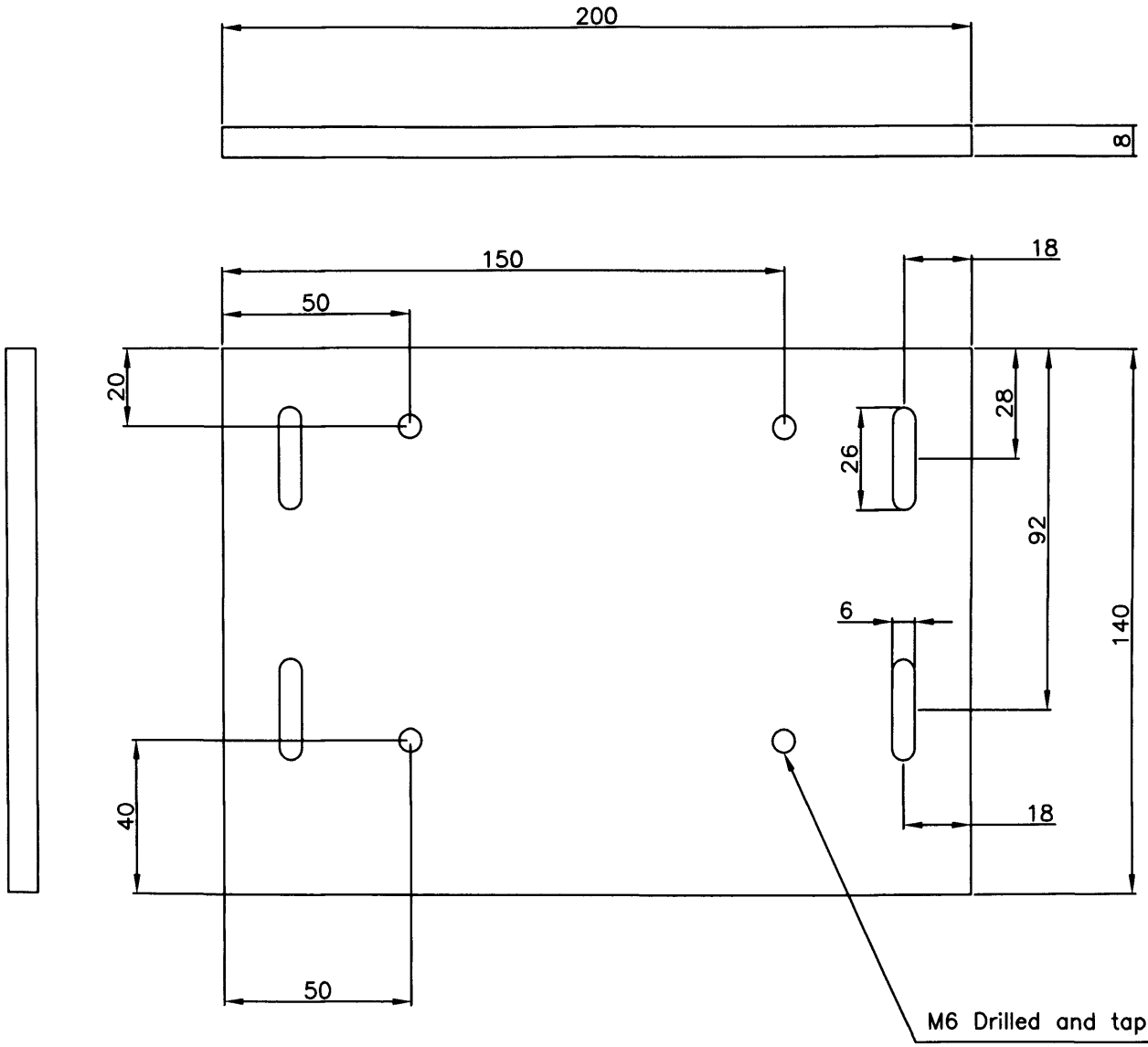

				This drawing is confidential and the copyright of J Haynes, School of Engineering, UWC. It must not be copied or passed to a third party without written consent.	Assembly Drawing
					JMH AutoCad 2004
					Material –: Mild Steel
A	Second Issue	JMH	03/07/2006		Finish –:
Rev	Revision	Rev By	Date	Dimensions in mm Do Not Scale	DRAWING No –: JMH036

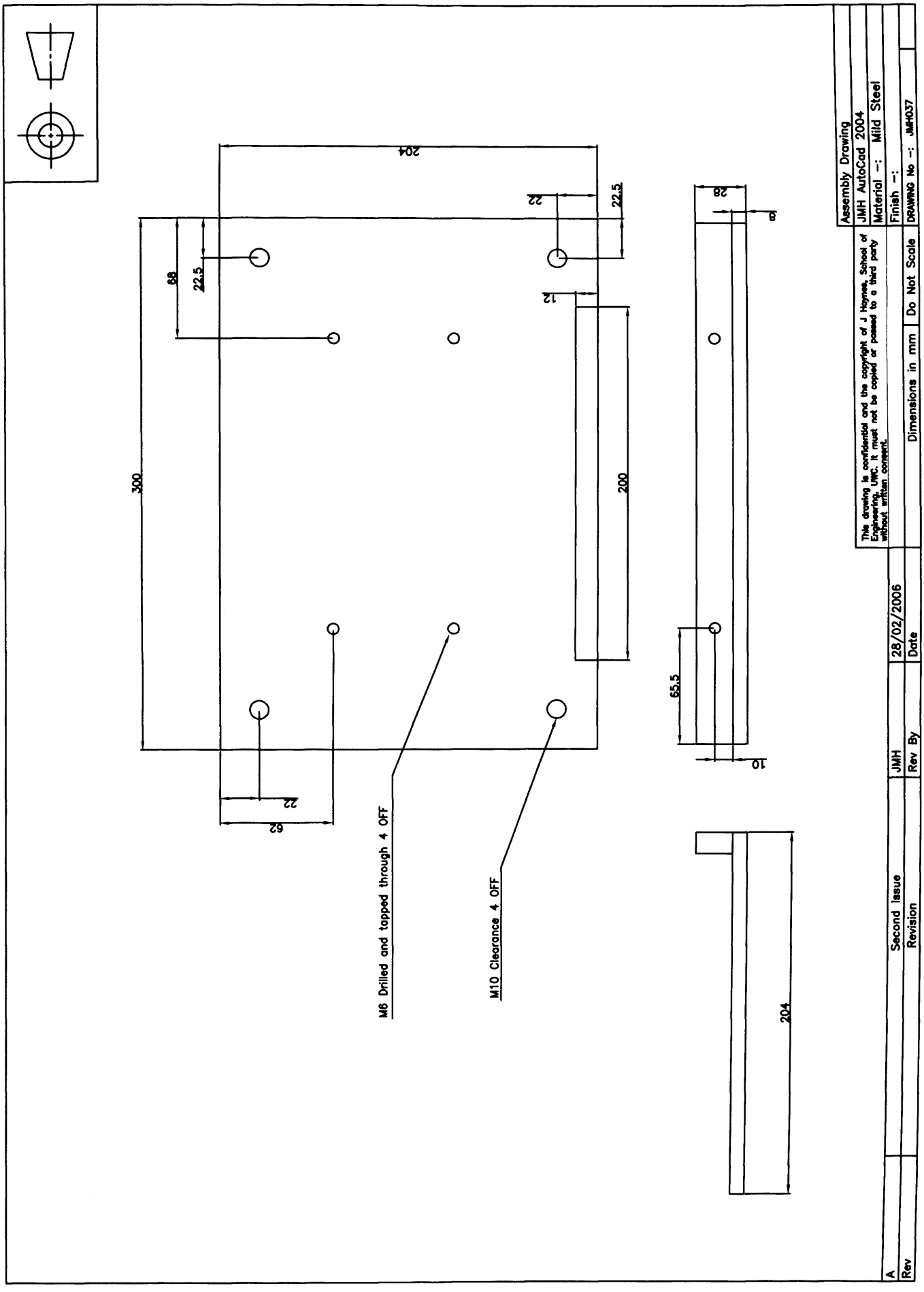
204
22
22.5
68
22.5
12
300
200
28
8
65.5
10
22
62
M6 Drilled and tapped through 4 OFF
M10 Clearance 4 OFF
204
Assembly Drawing
JMH AutoCad 2004
Material –: Mild Steel
Finish –:
DRAWING No –: JMH037
This drawing is confidential and the copyright of J Haynes, School of Engineering, UWC. It must not be copied or passed to a third party without written consent.
Dimensions in mm
Do Not Scale
28/02/2006
Date
JMH
Rev By
Second Issue
Revision
A
Rev

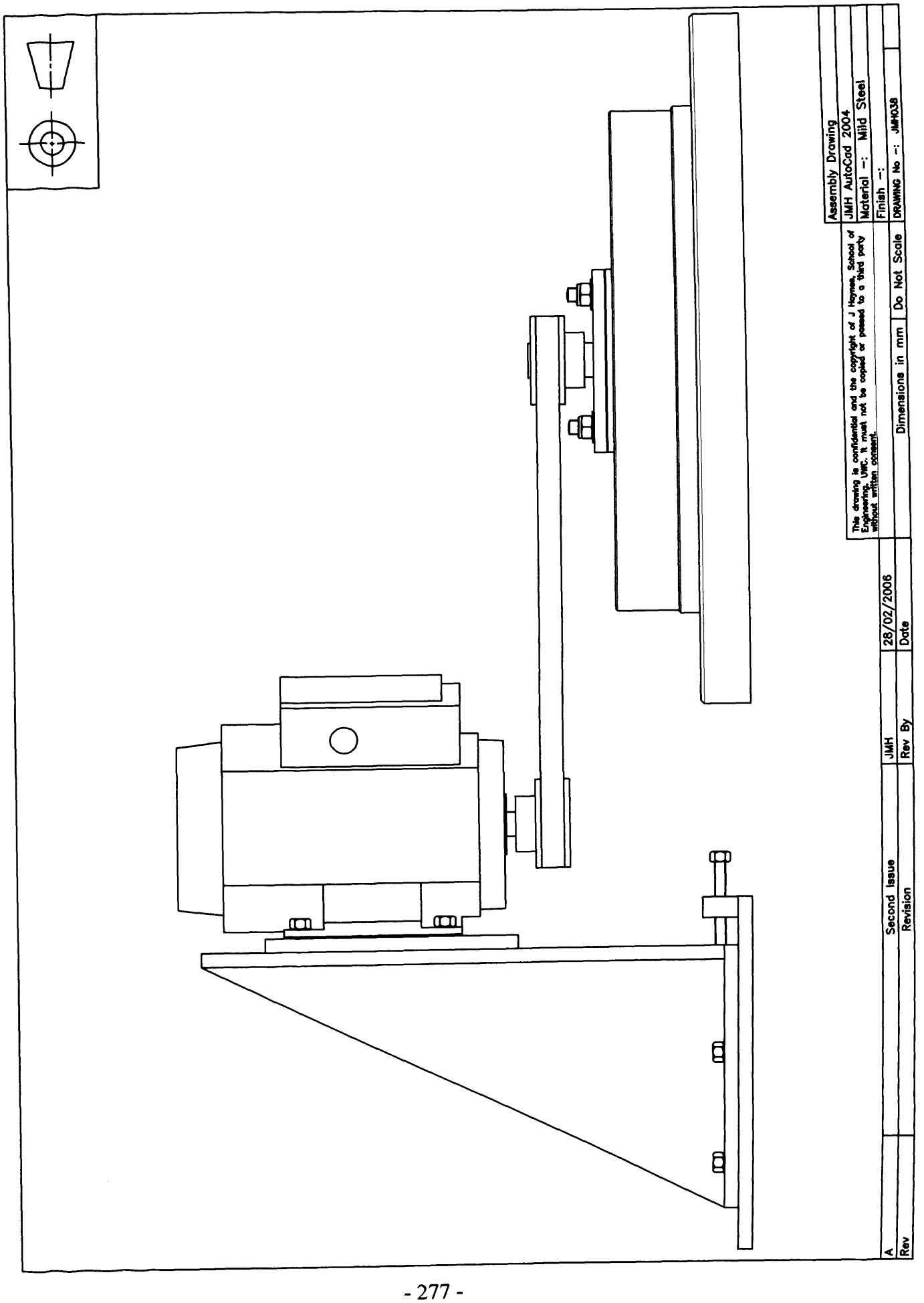
Assembly Drawing
JMH AutoCad 2004
Material –: Mild Steel
Finish –:
DRAWING No –: JMH038
This drawing is confidential and the copyright of J Haynes, School of Engineering, UWC. It must not be copied or passed to a third party without written consent.
Dimensions in mm
Do Not Scale
Second Issue
Revision
JMH
Rev By
28/02/2006
Date
A
Rev

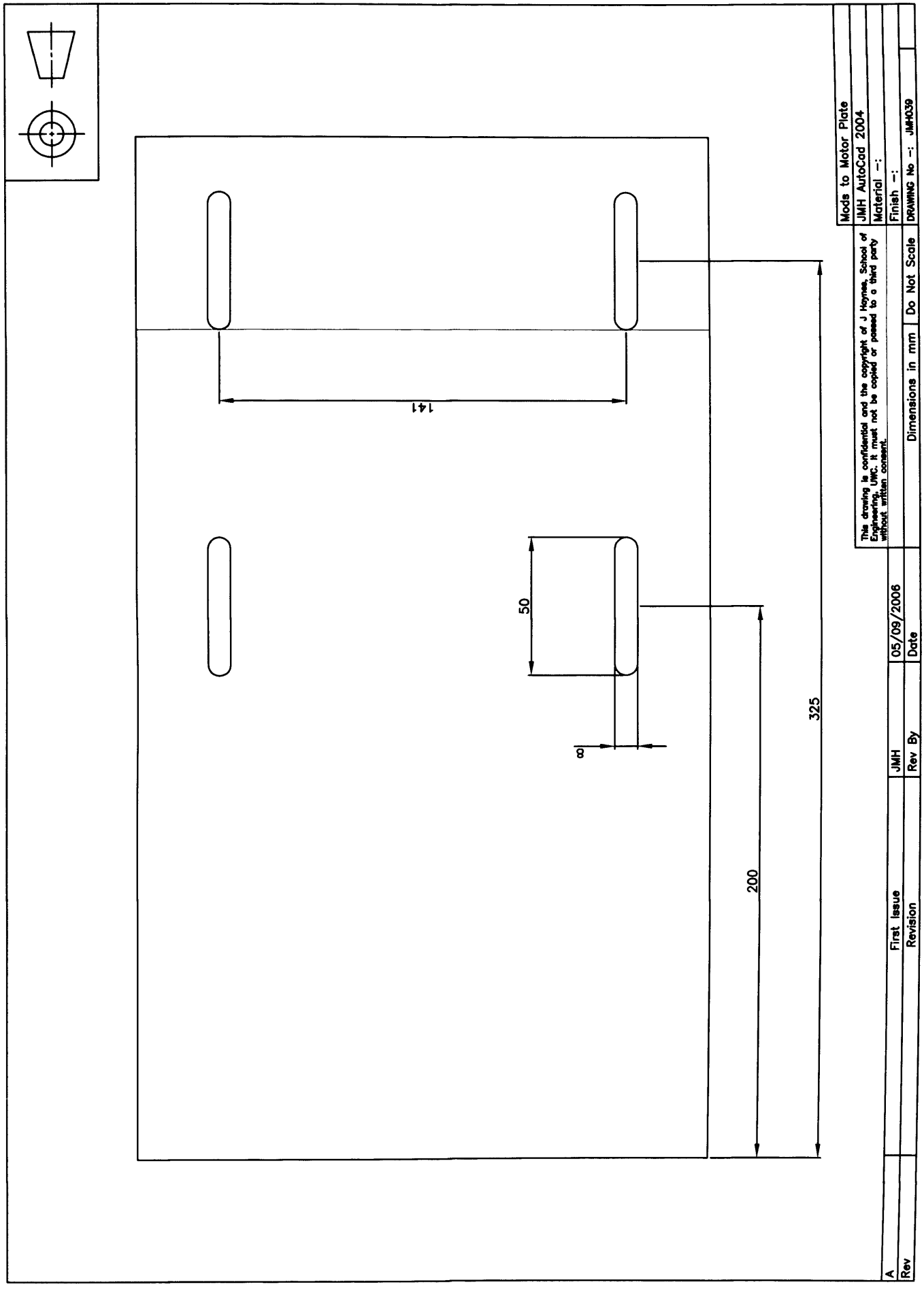
141
50
8
325
200
Mods to Motor Plate
JMH AutoCad 2004
Material –:
Finish –:
DRAWING No –: JMH039
This drawing is confidential and the copyright of J Haynes, School of Engineering, UWC. It must not be copied or passed to a third party without written consent.
Dimensions in mm
Do Not Scale
A
First Issue
JMH
05/09/2006
Rev
Revision
Rev By
Date

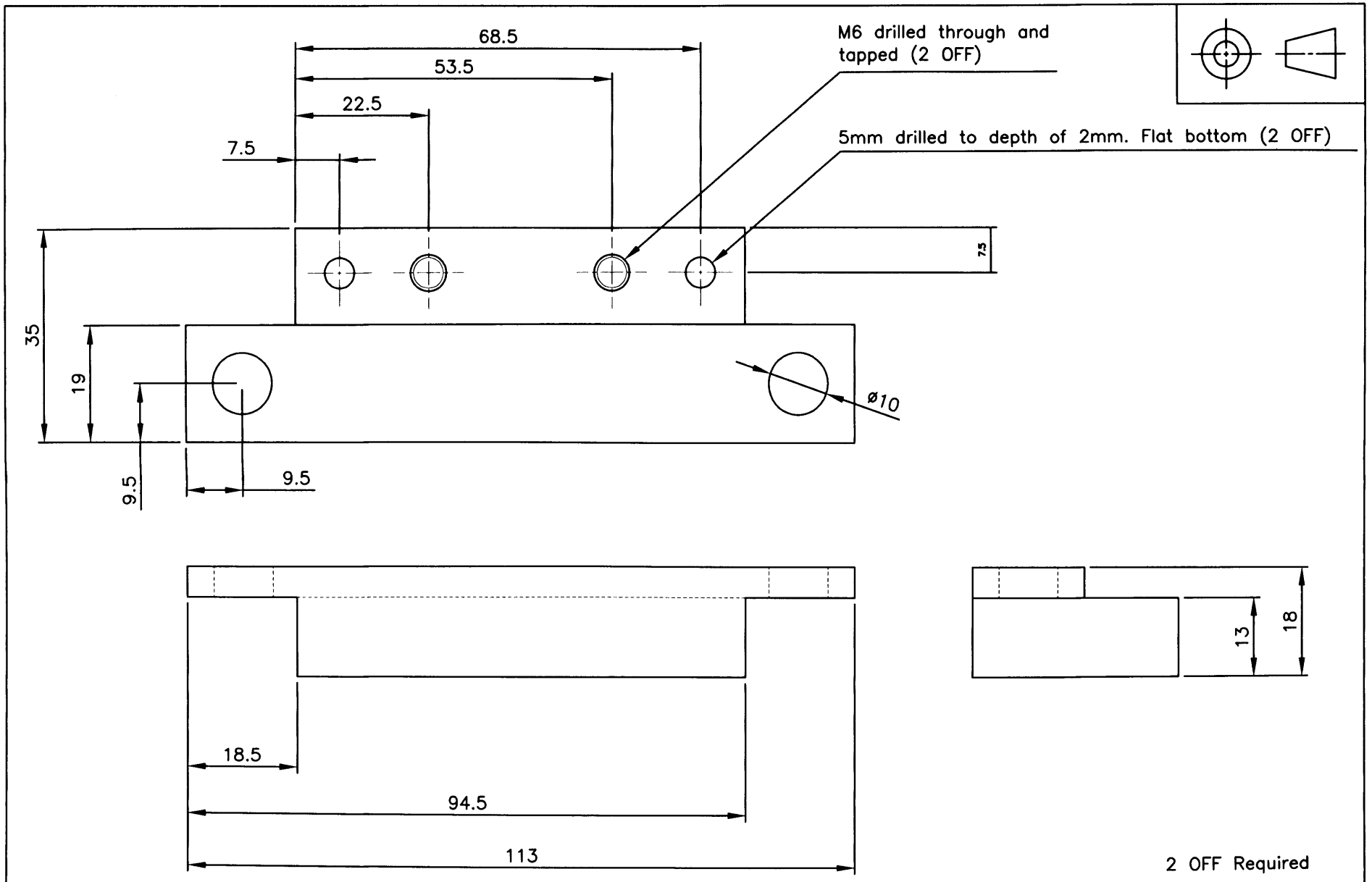

A	First Issue	JMH	04/11/2006	This drawing is confidential and the copyright of J Haynes, School of Engineering, UWC. It must not be copied or passed to a third party without written consent.	Force Transducer Mounting Plate
Rev	Revision	Rev By	Date	Dimensions in mm Do Not Scale	JMH AutoCad 2004
					Material –: Stainless Steel
					Finish –:
					DRAWING No –: JMH040

Modification to JMH036 2 OFF Required

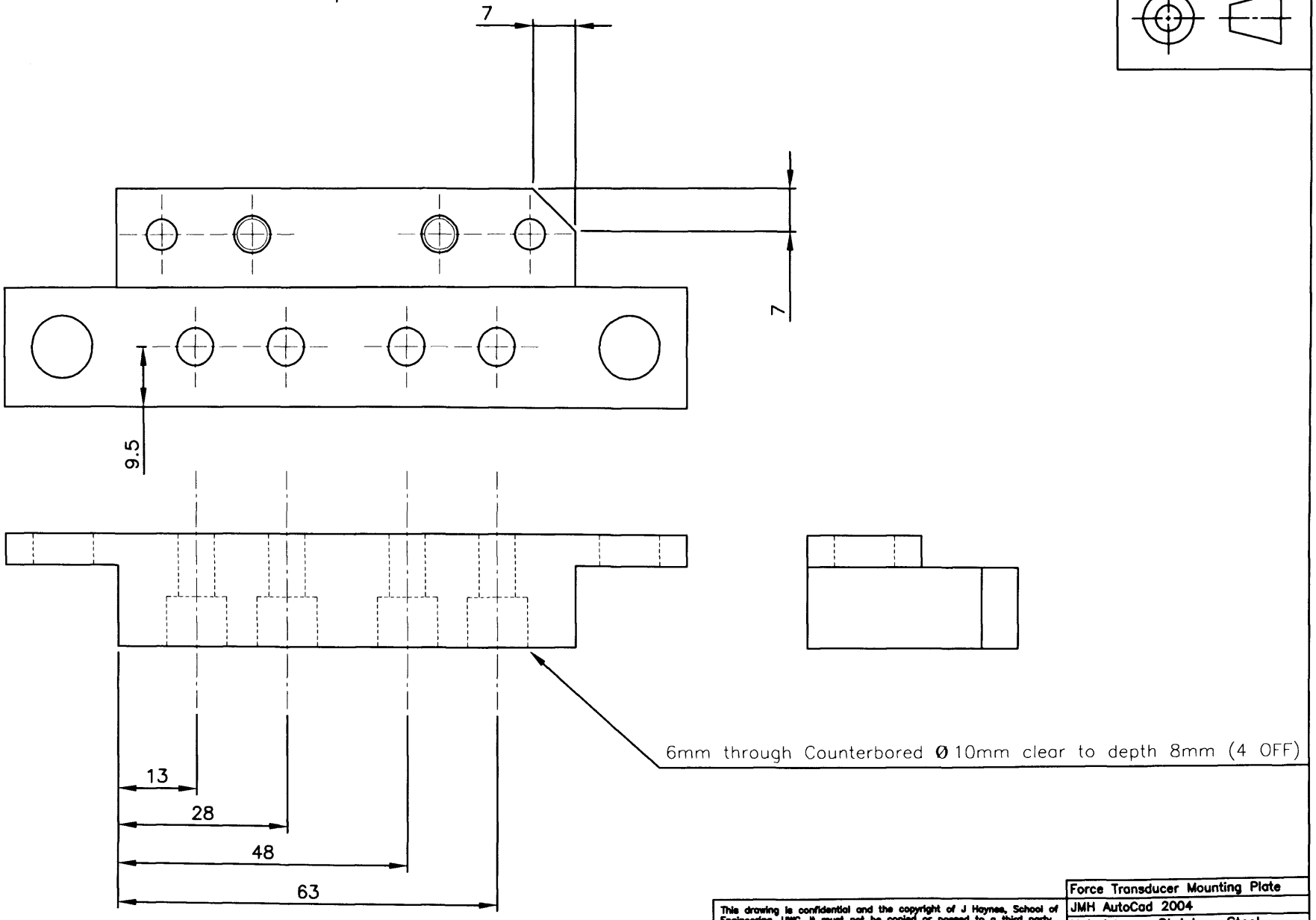

A	First Issue	JMH	05/12/2006	This drawing is confidential and the copyright of J Haynes, School of Engineering, UWC. It must not be copied or passed to a third party without written consent.	Force Transducer Mounting Plate
Rev	Revision	Rev By	Date		JMH AutoCad 2004
					Material –: Stainless Steel
					Finish –:
				Dimensions in mm Do Not Scale	DRAWING No –: JMH041

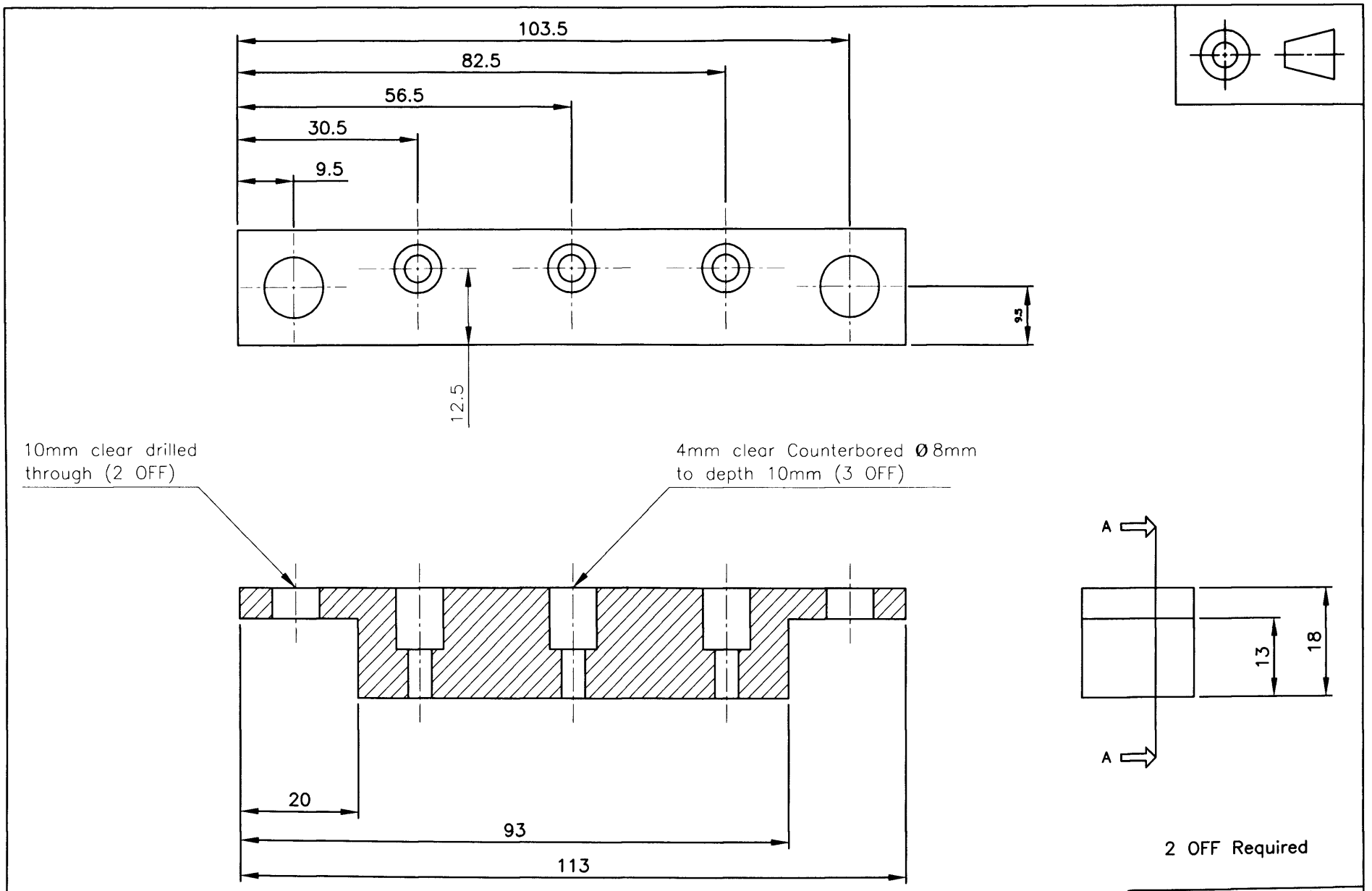

A	First Issue	JMH	04/11/2006	This drawing is confidential and the copyright of J Haynes, School of Engineering, UWC. It must not be copied or passed to a third party without written consent.	Force Transducer Mounting Plate
Rev	Revision	Rev By	Date	Dimensions in mm Do Not Scale	JMH AutoCad 2004
					Material –: Stainless Steel
					Finish –:
					DRAWING No –: JMH042

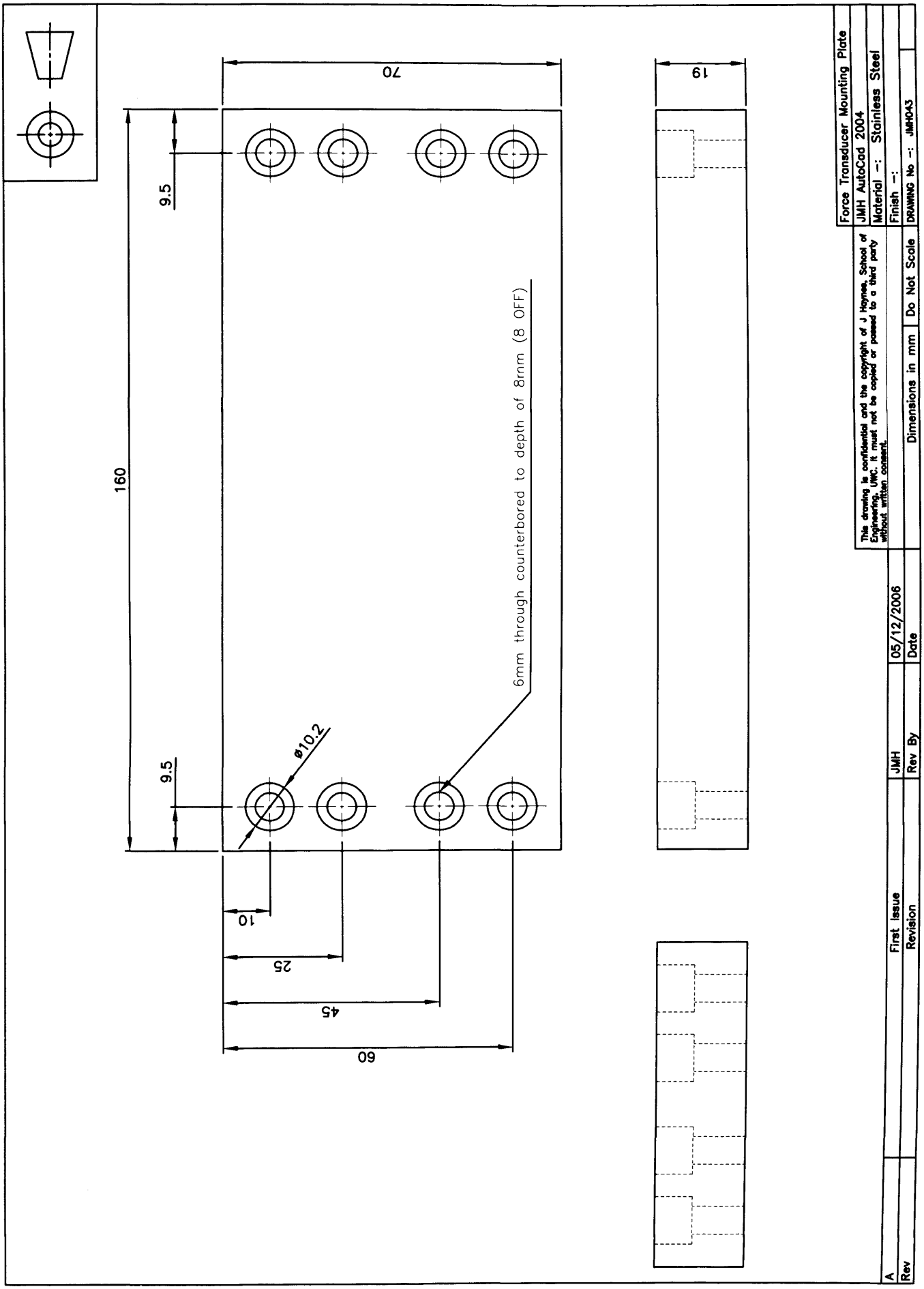
70
19
9.5
160
9.5
6mm through counterbored to depth of 8mm (8 OFF)
ø10.2
10
25
45
60
Force Transducer Mounting Plate
JMH AutoCad 2004
Material –: Stainless Steel
Finish –:
DRAWING No –: JMH043
This drawing is confidential and the copyright of J Haynes, School of Engineering, UWC. It must not be copied or passed to a third party without written consent.
Dimensions in mm
Do Not Scale
A
Rev
First Issue
Revision
JMH
Rev By
05/12/2006
Date

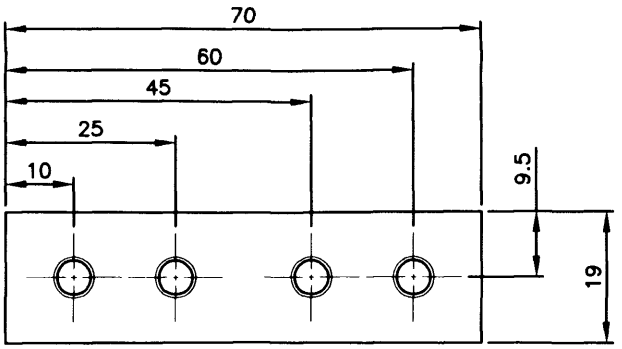

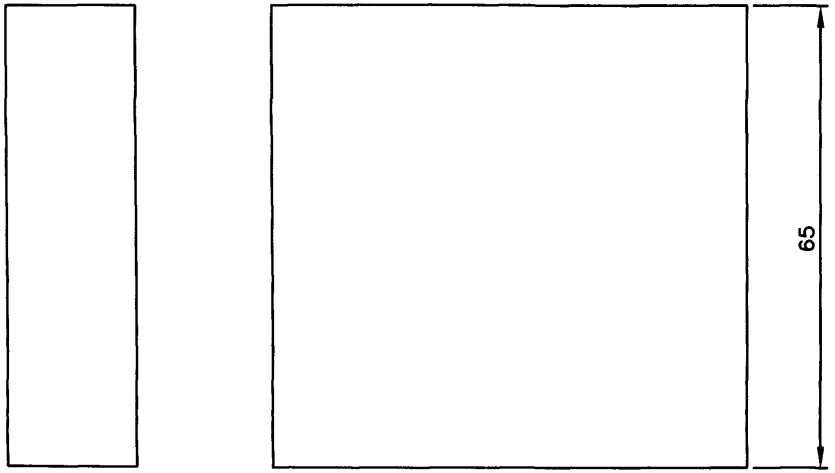

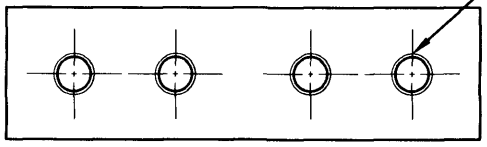

2 OFF REQUIRED

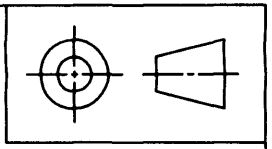

					Force Transducer Mounting Plate
				This drawing is confidential and the copyright of J Haynes, School of Engineering, UWC. It must not be copied or passed to a third party without written consent.	JMH AutoCad 2004
					Material –: Stainless Steel
A	First Issue	JMH	05/12/2006		Finish –:
Rev	Revision	Rev By	Date	Dimensions in mm Do Not Scale	DRAWING No –: JMH044

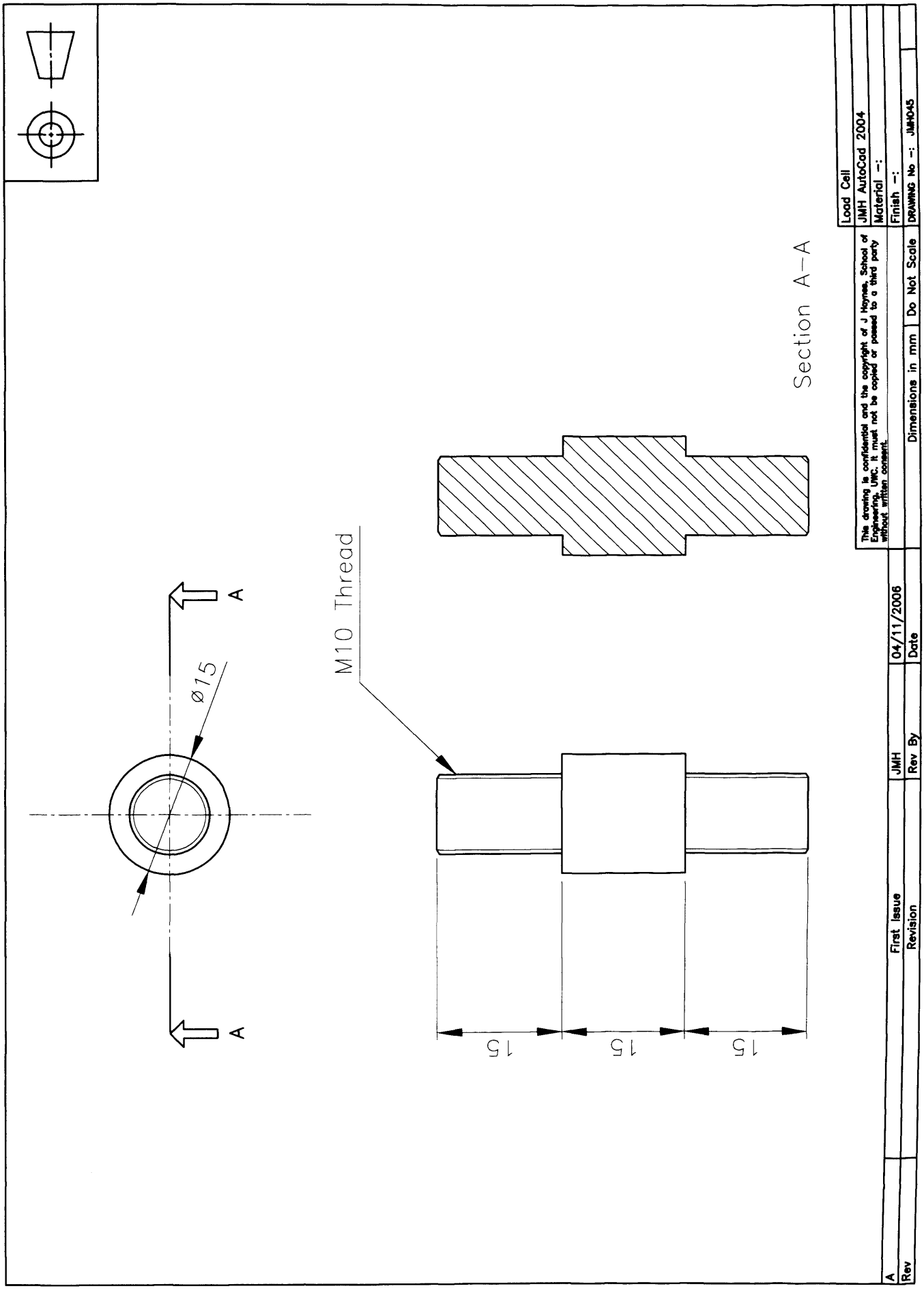
Load Cell
JMH AutoCad 2004
Material –:
Finish –:
DRAWING No –: JMH045
This drawing is confidential and the copyright of J Haynes, School of Engineering, UWC. It must not be copied or passed to a third party without written consent.
Dimensions in mm
Do Not Scale
A
First Issue
JMH
04/11/2006
Rev
Revision
Rev By
Date
Section A–A
M10 Thread
Ø15
A
A
15
15
15

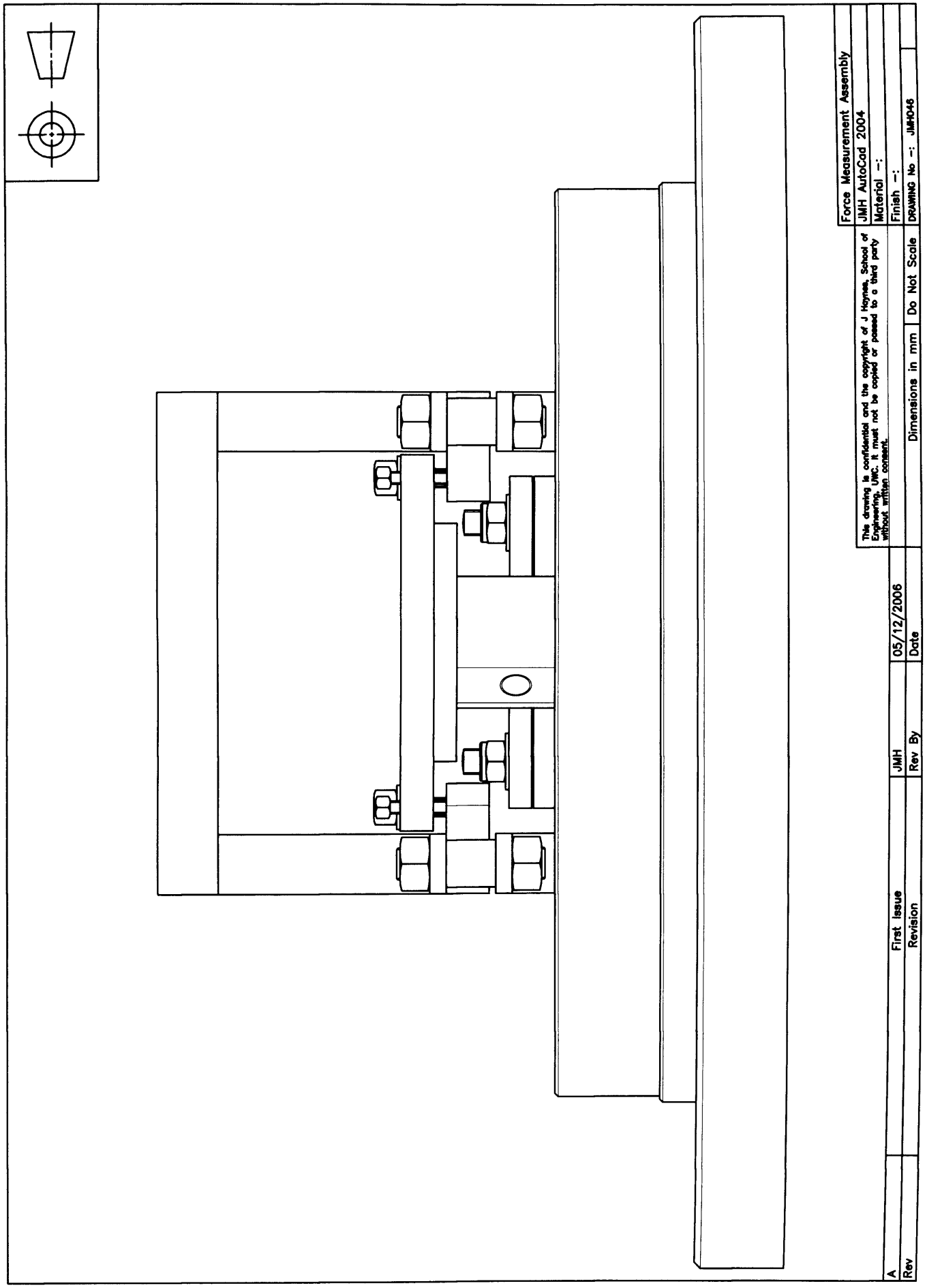
Force Measurement Assembly
JMH AutoCad 2004
Material –:
Finish –:
DRAWING No –: JMH046
This drawing is confidential and the copyright of J Haynes, School of Engineering, UWC. It must not be copied or passed to a third party without written consent.
Dimensions in mm
Do Not Scale
A First Issue JMH 05/12/2006
Rev Revision Rev By Date

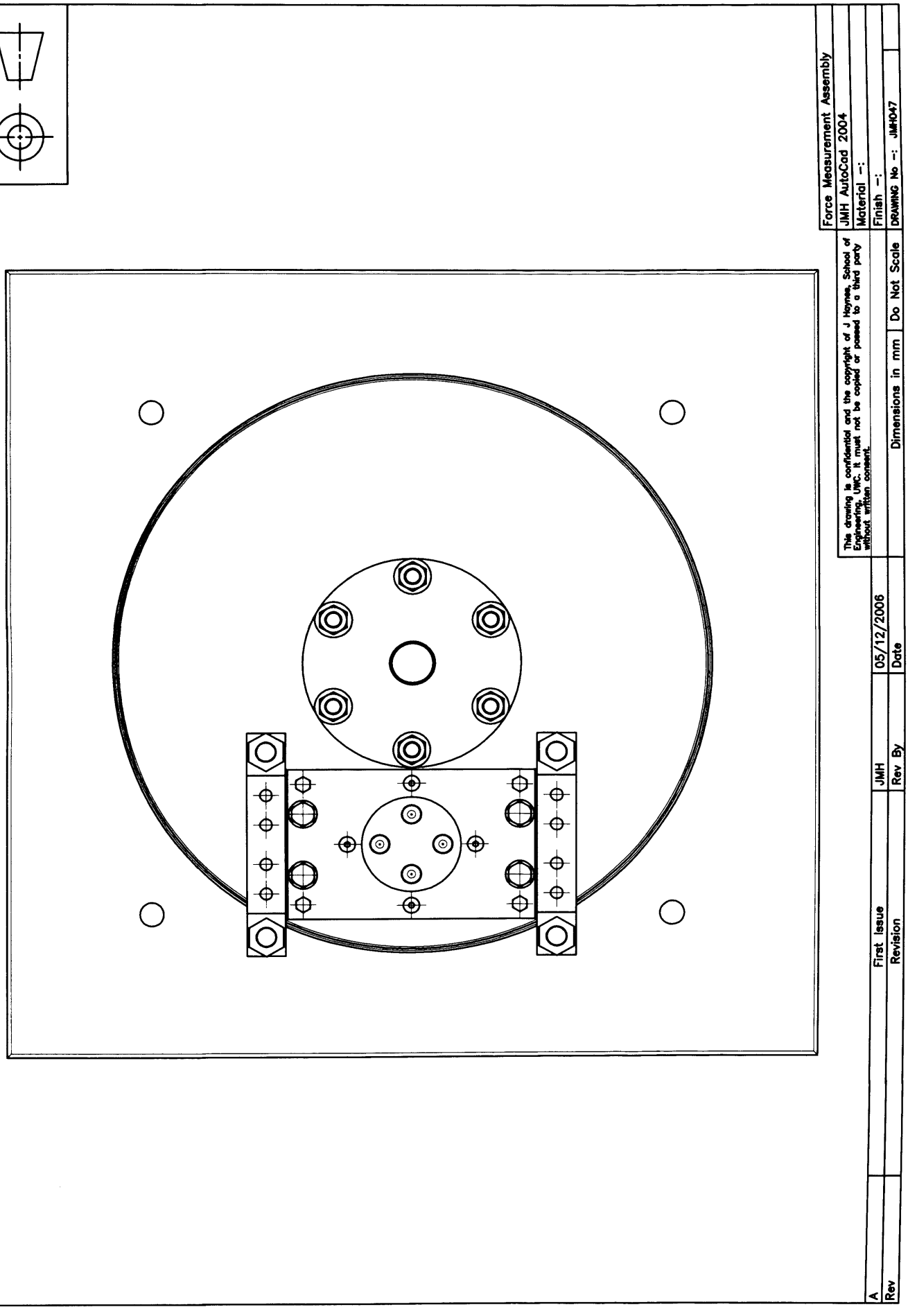
Force Measurement Assembly
JMH AutoCad 2004
Material –:
Finish –:
DRAWING No –: JMH047
This drawing is confidential and the copyright of J Haynes, School of Engineering, UWC. It must not be copied or passed to a third party without written consent.
Dimensions in mm
Do Not Scale
A
First Issue
JMH
05/12/2006
Rev
Revision
Rev By
Date

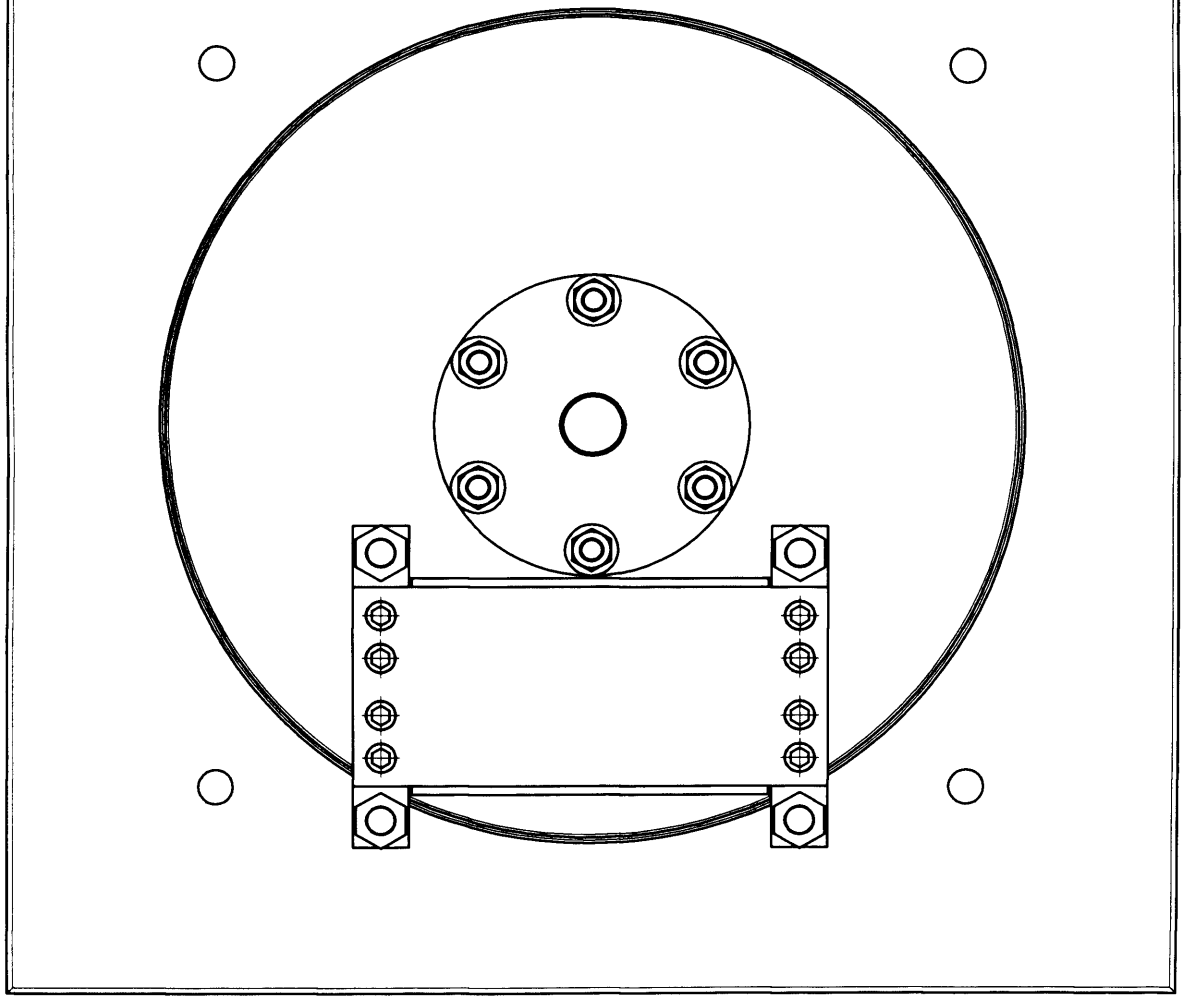

Force Measurement Assembly
JMH AutoCad 2004
Material –:
Finish –:
DRAWING No –: JMH045
Dimensions in mm | Do Not Scale
Date 05/12/2006
Rev By JMH
First Issue
Revision
A
Rev

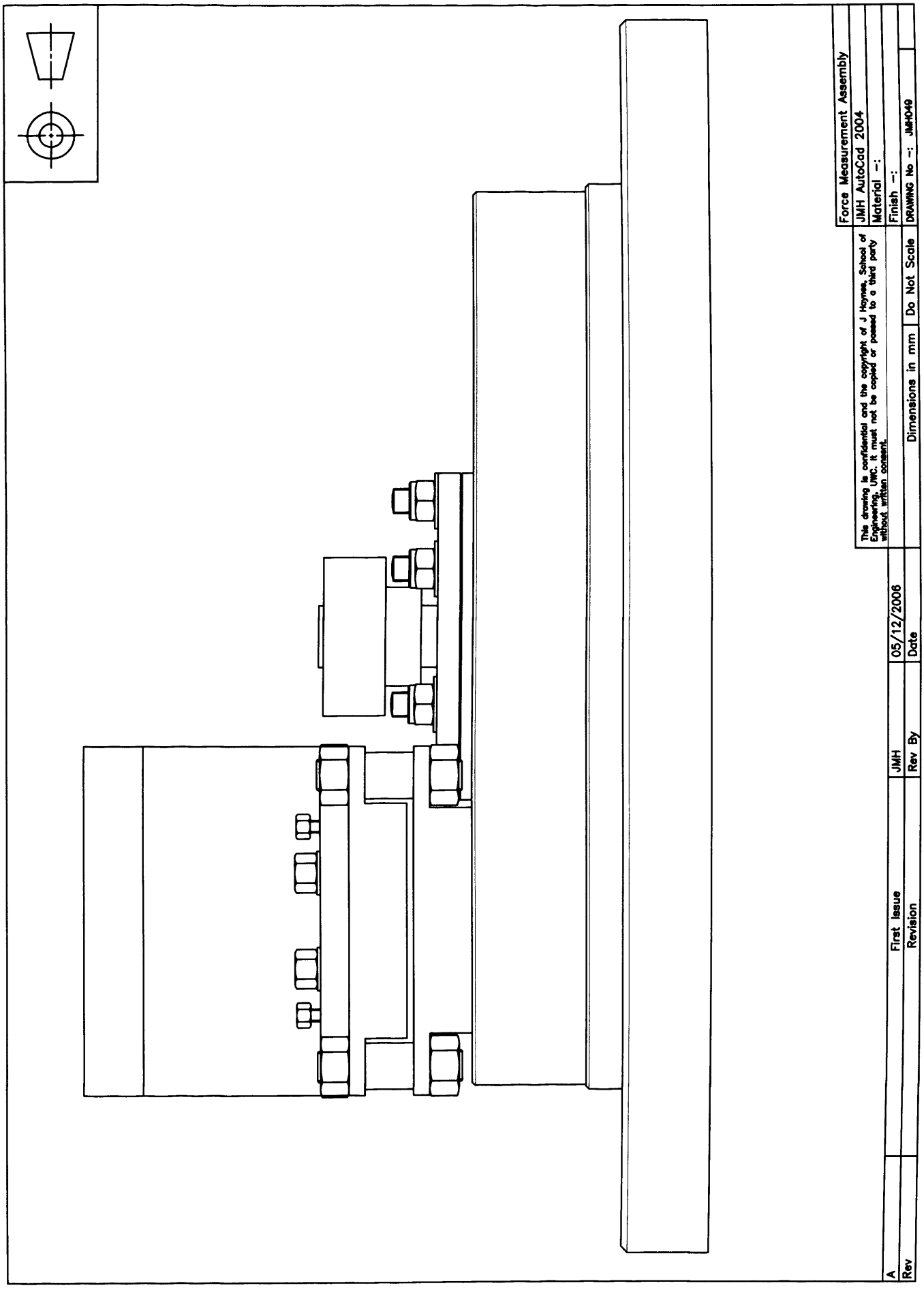
Force Measurement Assembly
JMH AutoCad 2004
Material –:
Finish –:
DRAWING No –: JMH049
This drawing is confidential and the copyright of J Haynes, School of Engineering, UWC. It must not be copied or passed to a third party without written consent.
Dimensions in mm
Do Not Scale
A
First Issue
JMH
05/12/2006
Rev
Revision
Rev By
Date

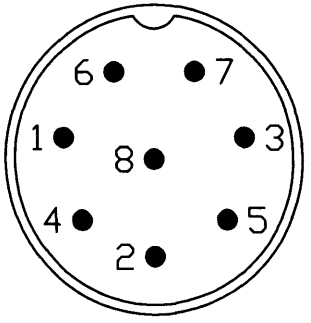

PIN	Colour	Assignment
1	White	0V
6	Green	+24V
2	Brown	+15V
4	Yellow	-15V
5	Grey	0V
3	Green	Signal voltage output
7	Blue	0V
8	Red	Signal current output

NB: As viewed from solder pin on female connector

					Plug Connections
				This drawing is confidential and the copyright of J Haynes, School of Engineering, UWC. It must not be copied or passed to a third party without written consent.	JMH AutoCad 2004
					Material –:
A	First Issue	JMH	05/12/2006		Finish –:
Rev	Revision	Rev By	Date	Dimensions in mm Do Not Scale	DRAWING No –: JMH050

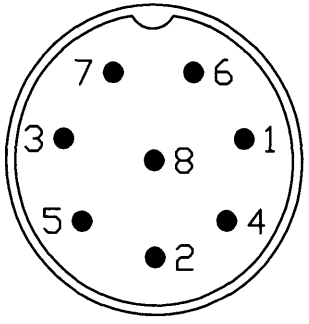

PIN	Colour	Assignment
1	White	0V
6	Green	+24V
2	Brown	+15V
4	Yellow	-15V
5	Grey	0V
3	Green	Signal voltage output
7	Blue	0V
8	Red	Signal current output

NB: As viewed on ready installed plug

A	First Issue	JMH	05/12/2006	Plug Connections	
Rev	Revision	Rev By	Date	JMH AutoCad 2004	
				Material –:	
				Finish –:	
			Dimensions in mm Do Not Scale	DRAWING No –: JMH051	

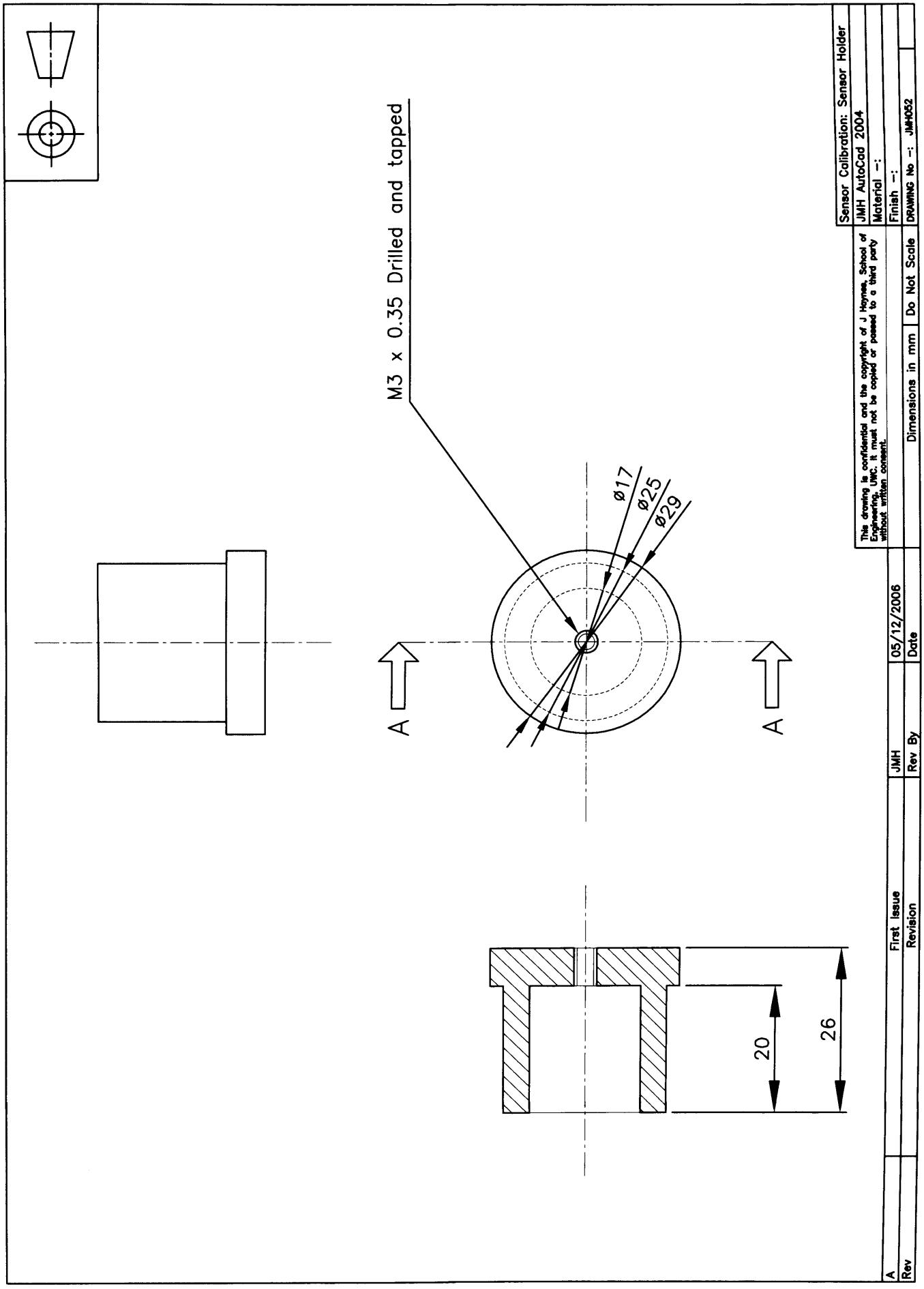
M3 x 0.35 Drilled and tapped
ø17
ø25
ø29
A
A
20
26
Sensor Calibration: Sensor Holder
JMH AutoCad 2004
Material –:
Finish –:
DRAWING No –: JMH052
This drawing is confidential and the copyright of J Haynes, School of Engineering, UWC. It must not be copied or passed to a third party without written consent.
Dimensions in mm
Do Not Scale
A
First Issue
JMH
05/12/2006
Rev
Revision
Rev By
Date

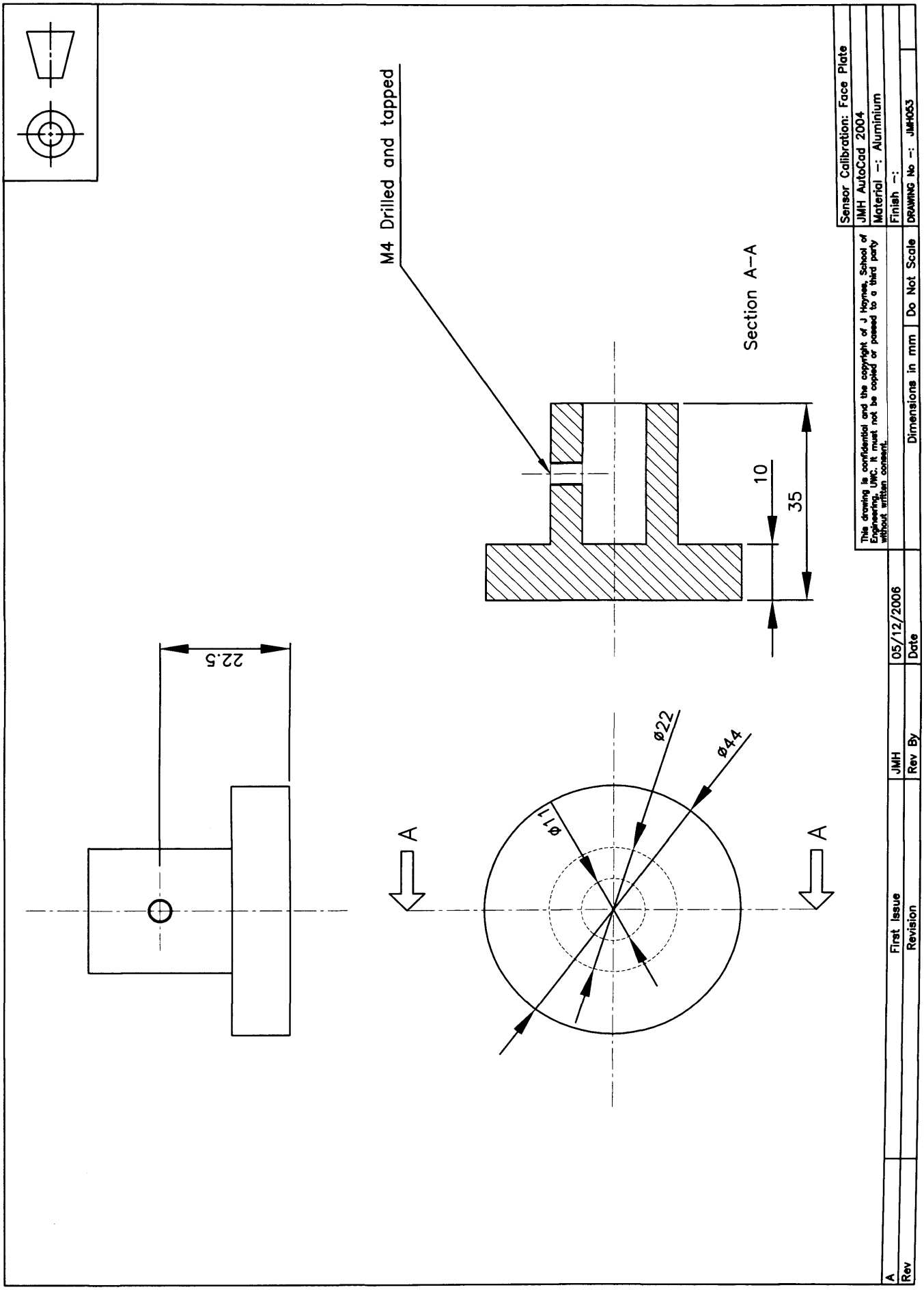
M4 Drilled and tapped
Section A–A
10
35
22.5
ø22
ø44
ø11
A
A
Sensor Calibration: Face Plate
JMH AutoCad 2004
Material –: Aluminium
Finish –:
DRAWING No –: JMH063
This drawing is confidential and the copyright of J Haynes, School of Engineering, UWC. It must not be copied or passed to a third party without written consent.
Dimensions in mm
Do Not Scale
A
First Issue
JMH
05/12/2006
Rev
Revision
Rev By
Date

A.3.6 Assembly drawings

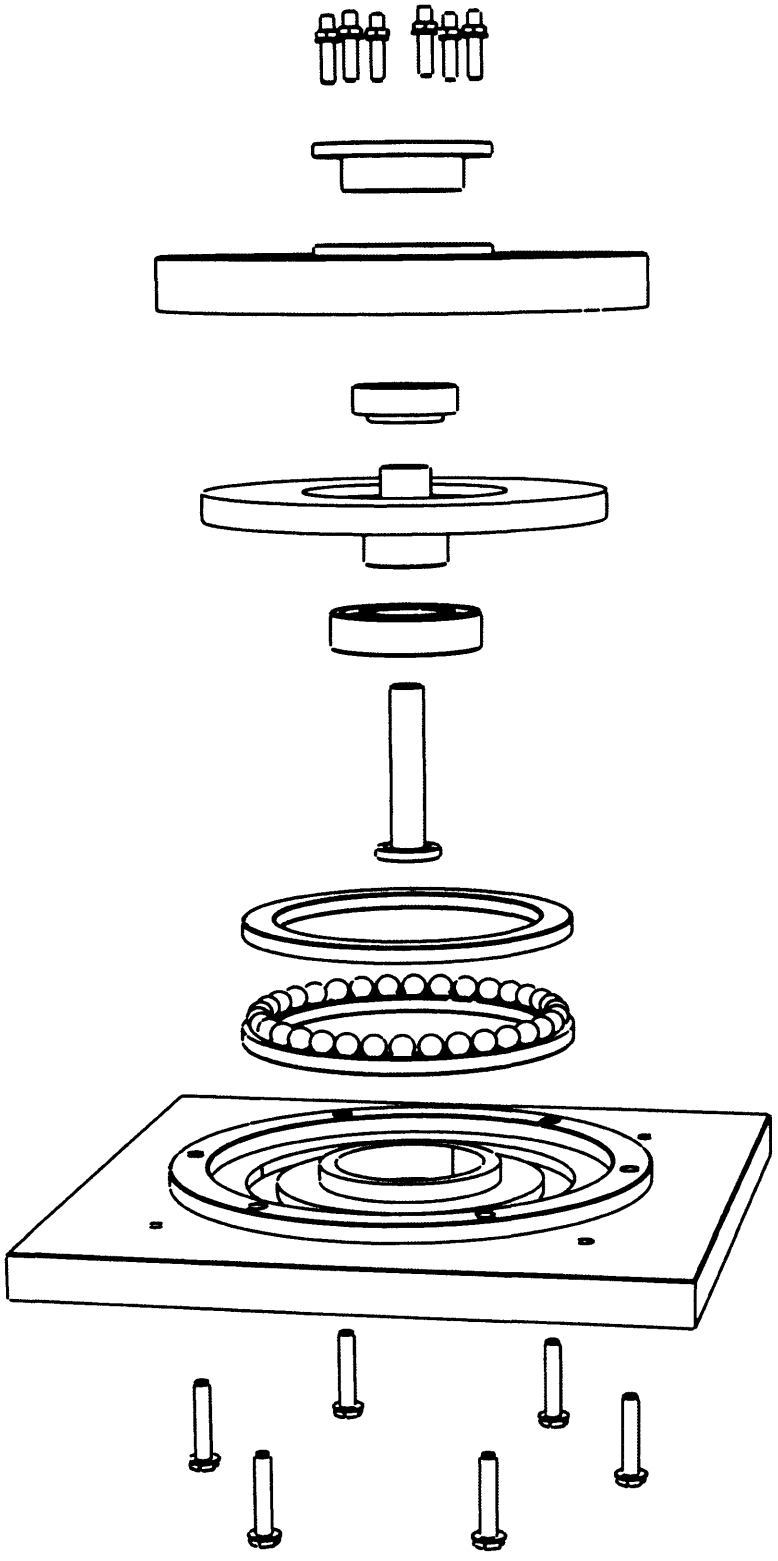

Test apparatus bearing assembly

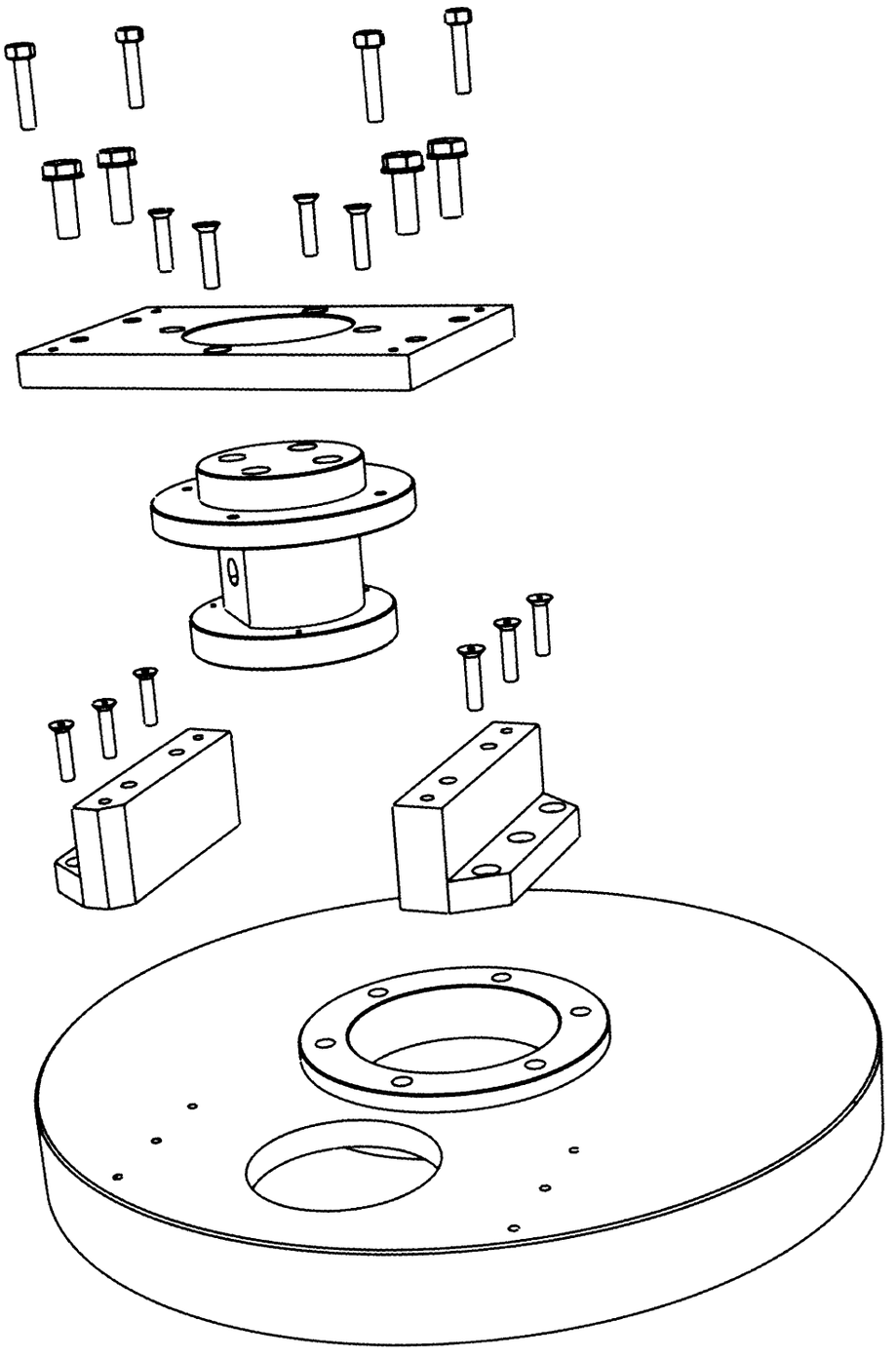

Slipper tilt mechanism assembly

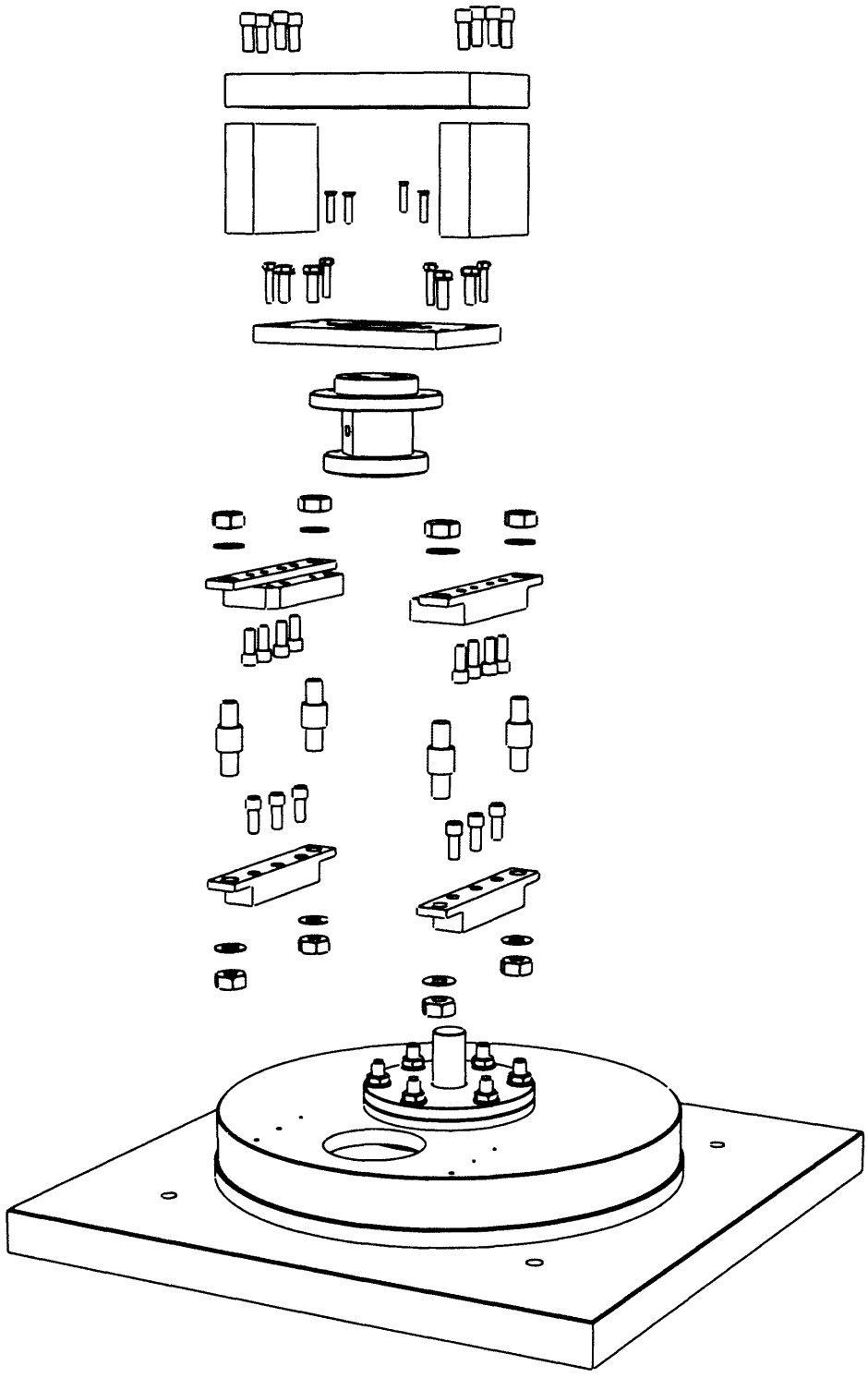

Slipper tilt mechanism with load cells

A.4 CFD analysis of slipper behaviour

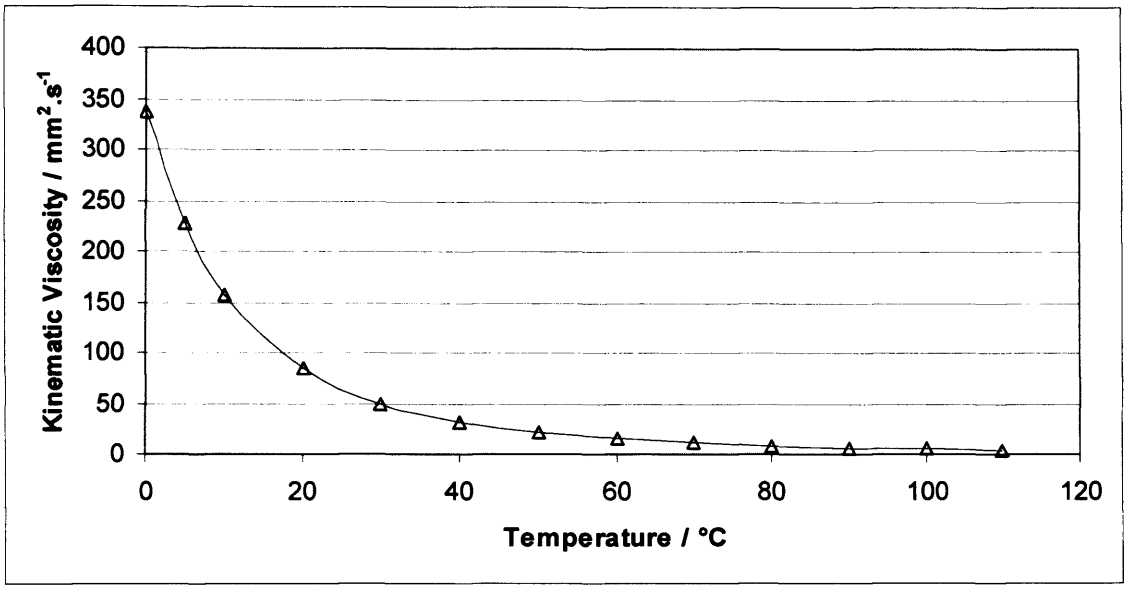

A.4.1 Kinematic viscosity of shell tellus ISO32 hydraulic oil

A.4.2 User defined function for varying clearance CFD models

```
/************************************************************************/
/* UDF for defining the velocity of motion in z direction for run out of 11 microns  */
/* with an angular velocity of 150 rad.sec-1. Initial condition zero deformation      */
/* UDF applied to lower face of volume                                                */
/* UDF written for use with FLUENT                                                    */
/************************************************************************/

#include "udf.h"

DEFINE_CG_MOTION(Slipper_Motion_1,dt,vel,omega,time,dtime)

    {
        real pi;
        real runnout;
        real w;
        real theta;
        real t;
        t = CURRENT_TIME ;
        pi = 3.141592654 ;
        runnout = 0.000011 ;
        w = 150 ;
        theta = t * w ;

        vel[2] = -0.5*w*runnout*sin(theta) ;
    }
```